

This item was submitted to Loughborough's Institutional Repository (<https://dspace.lboro.ac.uk/>) by the author and is made available under the following Creative Commons Licence conditions.



For the full text of this licence, please go to:  
<http://creativecommons.org/licenses/by-nc-nd/2.5/>

## Thesis Access Form

Copy No.....Location.....

Author.....

Title.....

Status of access OPEN / RESTRICTED / CONFIDENTIAL

Moratorium Period:.....years, ending...../.....200.....

Conditions of access approved by (CAPITALS):.....

Supervisor (Signature).....

Department of.....

**Author's Declaration:** *I agree the following conditions:*

Open access work shall be made available (in the University and externally) and reproduced as necessary at the discretion of the University Librarian or Head of Department. It may also be digitised by the British Library and made freely available on the Internet to registered users of the EThOS service subject to the EThOS supply agreements.

*The statement itself shall apply to ALL copies including electronic copies:*

**This copy has been supplied on the understanding that it is copyright material and that no quotation from the thesis may be published without proper acknowledgement.**

**Restricted/confidential work:** All access and any photocopying shall be strictly subject to written permission from the University Head of Department and any external sponsor, if any.

Author's signature.....Date.....

users declaration: for signature during any Moratorium period (Not Open work): <i>I undertake to uphold the above conditions:</i>			
Date	Name (CAPITALS)	Signature	Address

CERTIFICATE OF ORIGINALITY

This is to certify that I am responsible for the work submitted in this thesis, that the original work is my own except as specified in acknowledgments or in footnotes, and that neither the thesis nor the original work contained therein has been submitted to this or any other institution for a degree.

..... ( Signed )

..... ( Date )

# **AUTOMATED DESIGN OF TRABECULAR STRUCTURES**

By

**Ettore Ramin**

Doctoral thesis submitted in partial fulfilment of the requirements for  
the award of Doctor of Philosophy of Loughborough University

**February 26, 2010**

© by Ettore Ramin 2010

---

## INDEX

<b>Abstract.....</b>	<b>6</b>
<b>Acknowledgments.....</b>	<b>8</b>
<b>Glossary.....</b>	<b>9</b>
<b>Nomenclature.....</b>	<b>12</b>
 <b>CHAPTER 1 - LITERATURE REVIEW -.....</b>	 <b>15</b>
1.1 Introduction to Computed-Aided Design.....	15
1.1.1 Solid Modelling.....	19
1.1.1.1 Constructive Solid Geometry.....	22
1.1.1.2 Boundary representation.....	24
1.2 Principles of the Additive Manufacturing Processes.....	26
1.2.1 Liquid Monomer Based Processes.....	29
1.2.1.1 Stereolithography.....	29
1.2.2 Molten Material Based.....	31
1.2.2.1 Fused Deposition Modelling.....	31
1.2.2.2 Multi Jet Modelling.....	32
1.2.3 Powder Based.....	33
1.2.3.1 Selective Laser Sintering.....	33
1.2.3.2 Three Dimensional Printing.....	35
1.2.4 Laminate Based Processes.....	36
1.2.4.1 Laminate Object Manufacturing.....	36
1.3 Tissue Engineering.....	38
1.3.1 Conventional Manufacturing and Tissue Engineering Scaffolds.....	41
1.3.2 Additive Manufacturing and Tissue Engineering Scaffolds.....	41
1.3.3 TE Scaffold Requirements.....	43
1.4 Trabecular Bone Architecture.....	45
1.5 TE Scaffolds and Computer Aided Design.....	54
1.6 Hypothesis.....	62
1.7 Research Novelty.....	63

<b>CHAPTER 2 - METHODOLOGY -.....</b>	<b>65</b>
2.1 Need for an Automated, Efficient and Flexible Design Method.....	65
2.2 Aim.....	66
2.3 Overview of the Methodology.....	67
2.3.1 Selection of Tissue.....	67
2.3.2 Definition of the 3D Geometrical Element.....	68
2.3.3 Efficiency of the Methodology.....	69
2.3.4 Flexibility of the Methodology.....	71
2.4 Design Variables.....	72
2.4.1 Pore size.....	72
2.4.2 Pore shape.....	73
2.4.3 Pore location.....	74
2.4.4 Rod paths.....	77
2.4.5 Coupling variables.....	78
2.4.6 Volumetric Variables.....	79
2.4.7 Output Variables.....	79
2.4.8 Concept of random variation.....	79
2.5 CAD Requirements.....	80
2.5.1 Programming language requirements.....	81
2.5.2 Application Programming Interface.....	82
2.5.3 CAD Evaluation.....	82
2.5.4 Routines to convert rods into channels.....	83
2.6 Stages of Experiments.....	84
 <b>CHAPTER 3 - AUTOMATED DESIGN IN CUBIC VOLUMES -.....</b>	 <b>86</b>
3.1 Introduction.....	86
3.2 Application of the Methodology.....	86
3.2.1 Pore Size and Shape.....	86
3.2.2 Pore Location.....	87
3.2.3 Coupling Variables.....	88
3.2.4 Rods Paths.....	88
3.2.5 Volumetric Variables.....	89
3.2.6 Output Variables.....	89

3.3 Results.....	89
3.3.1 Case 1.....	89
3.3.2 Case 2.....	90
3.3.3 Case 3.....	91
3.3.4 Case 4.....	93
3.3.5 Case 5.....	94
3.3.6 Case 6.....	96
3.4 Review.....	98

## **CHAPTER 4 - AUTOMATED DESIGN INTEGRATION IN ANATOMICAL**

<b>VOLUMES -.....</b>	<b>102</b>
4.1 Introduction.....	102
4.2 Application of the Methodology.....	103
4.2.1 Pore Size and Shape.....	103
4.2.2 Pore Location.....	104
4.2.3 Coupling Variables.....	109
4.2.4 Rods Paths.....	110
4.2.5 Volumetric Variables.....	111
4.2.6 Output Variables.....	112
4.3 Results.....	112
4.3.1 Case Study 1: Craniofacial Implant.....	113
4.3.2 Case Study 2: Mouse Humerus.....	122
4.4 Review.....	127

## **CHAPTER 5 - POROSITY AND PORE SIZE ANALYSIS IN TRABECULAR BONE**

<b>STRUCTURES -.....</b>	<b>129</b>
5.1 Introduction.....	129
5.2 Methodology of Analysis.....	130
5.2.1 Slicing.....	131
5.2.2 SSL File Structure.....	133
5.2.3 Slice Data Analysis.....	134
5.2.3.1 Template File for Analysis.....	134
5.2.3.2 Input from SSL.....	137
5.2.3.3 Output from SSL.....	138

---

5.3 Results.....	139
5.3.1 Analysis of a Cubic $\mu$ CT Trabecular Bone Sample.....	140
5.3.1.1 Gradients of Trabecular and Sliced Area.....	141
5.3.2 Analysis of a Mouse Humerus $\mu$ CT Trabecular Bone Sample.....	146
5.3.2.1 Gradients of Trabecular and Sliced Area.....	148
5.3.3 Analysis of Cubic ADI Case 5 Sample.....	152
5.3.3.1 Gradients of Trabecular and Sliced Area.....	152
5.3.4 Analysis of Cubic ADI Case 6 Sample.....	157
5.3.4.1 Gradients of Trabecular and Sliced Area.....	157
5.3.5 Analysis of ADI Mouse Humerus Sample.....	162
5.3.5.1 Gradients of Trabecular and Sliced Area.....	163
5.4 Comparison and Assessment of the Analysed Structures.....	167
5.4.1 Comparison between Cubic ADI Case 5 Sample and Cubic $\mu$ CT Sample.....	167
5.4.2 Comparison between Cubic ADI Case 6 Sample and Cubic $\mu$ CT Sample.....	173
5.4.3 Comparison between ADI Mouse Humerus Sample and $\mu$ CT Mouse Humerus Sample.....	179
5.5 Review.....	186
 <b>CHAPTER 6 - AUTOMATED BIO-MIMETIC DESIGN INTEGRATION (ABDI) -189</b>	
6.1 Introduction.....	189
6.2 Methodology.....	190
6.2.1 Discretization of Sliced Area from a Cubic $\mu$ CT Sample.....	193
6.2.2 Mathematical Description of the Problem.....	195
6.2.2.1 Linear Diophantine Equations.....	200
6.2.3 Implementation of a Resolution Algorithm.....	202
6.2.4 Design Implementation.....	208
6.2.4.1 Minimum Zeros Propagation Strategy.....	211
6.2.4.2 Other Design Strategies.....	214
6.2.4.3 Remedies to Incompatibility of Solutions.....	215
6.2.5 Computational Time and File Size.....	217
6.2.6 Export to CAD.....	217
6.3 Results.....	218
6.3.1 ABDI Geometry - Case 1 -.....	220

---



---

6.3.2 ABDI Geometry - Case 2 - .....	227
6.4 Review.....	234
 <b>CHAPTER 7 - DISCUSSION - .....</b>	<b>236</b>
7.1 ADI Methodology (chapter 2).....	236
7.2 Automated Design on Regular Volumes (chapter 3).....	239
7.3 Automated Design on Anatomical Volumes (chapter 4).....	240
7.4 Evaluation and Assessment of Automated Designed Structures (chapter 5).....	243
7.5 Automated Bio-mimetic Design (chapter 6).....	245
7.5.1 Description of the ABDI geometries.....	247
 <b>CHAPTER 8 - CONCLUSIONS - .....</b>	<b>249</b>
 <b>CHAPTER 9 - RECOMMENDATIONS FOR FURTHER WORK - .....</b>	<b>254</b>
 <b>Publications.....</b>	<b>257</b>
<b>References.....</b>	<b>258</b>

## ABSTRACT

Additive manufacturing technologies are enabling newfound degrees of geometrical complexity to be realised, particularly with regards to internal structures. All of these manufacturing technologies are dependant on their prior design in an appropriate electronic form, either by reverse engineering, or, primarily, by computer-aided design.

Within these emerging applications is the design of scaffolds with an intricate and controlled internal structure for bone tissue engineering. There is a consensus that ideal bone scaffold geometry is evident in biological trabecular structures. In their most basic topological form, these structures consist of the non-linear distribution of irregular interconnecting rods and plates of different size and shape.

Complex and irregular architectures can be realised by several scaffold manufacturing techniques, but with little or no control over the main features of the internal geometry, such as size, shape and interconnectivity of each individual element. The combined use of computer aided design systems and additive manufacturing techniques allows a high degree of control over these parameters with few limitations in terms of achievable complexity. However, the design of irregular and intricate trabecular networks in computer aided design systems is extremely time-consuming since manually modelling an extraordinary number of different rods and plates, all with different parameters, may require several days to design an individual scaffold structure. In an attempt to address these difficulties, several other research efforts in this domain have largely focussed on techniques which result in designs which comprise of relatively regular and primitive shapes and do not represent the level of complexity seen biologically. Detailed descriptions of these methods are covered in chapter 1.

An automated design methodology for trabecular structures is proposed by this research to overcome these limitations. This approach involves the investigation of novel software algorithms, which are able to interact with a conventional computer aided design program

and permit the automated design of geometrical elements in the form of rods, each with a different size and shape. The methodology is described in chapter 2 and is tested in chapter 3. Applications of this methodology in anatomical designs are covered in chapter 4.

Nevertheless, complex designed rod networks may still present very different properties compared to trabecular bone geometries due to a lack detailed information available which explicitly detail their geometry. The lack of detailed quantitative descriptions of trabecular bone geometries may compromise the validity of any design methodology, irrespective of automation and efficiency. Although flexibility of a design methodology is beneficial, this may be rendered inadequate when insufficient quantitative data is known of the target structure. In this work a novel analysis methodology is proposed in chapter 5, which may provide a significant contribution toward the characterisation and quantification of target geometries, with particular focus on trabecular bone structures. This analysis methodology can be used either to evaluate existing design techniques or to drive the development of new bio-mimetic design techniques.

This work then progresses to a newly derived bio-mimetic automated design technique, driven by the newly produced quantitative data on trabecular bone geometries. This advanced design methodology has been developed and tested in chapter 6. This has demonstrated the validity of the technique and realised a significant stage of development in the context and scope of this work.

## **ACKNOWLEDGMENTS**

The Author would like to acknowledge the help of several individuals and parties who have aided in the realisation of this work:

First, to Dr. Russell Harris for his supervision throughout the duration of this work, and for having given me the opportunity to undertake my research with the benefit of his help and assistance, both professional and personal.

I would also like to thank the people in the Additive Manufacturing Research Group, with whom I have shared many research experiences and moments of enjoyment over the years.

I thank Lydia and my family for their continued support and encouragement, and my friends Luisa, Oscar and Mulillo for their advice on difficult matters.

## GLOSSARY

<b>2D</b>	Two Dimensional
<b>3D</b>	Three Dimensional
<b>3DP</b>	Three Dimensional Printing
<b>ABDI</b>	Automated Bio-mimetic Design Integration
<b>ABS</b>	Acrylonitrile Butadiene Styrene
<b>ADI</b>	Automated Design Integration
<b>AM</b>	Additive Manufacturing
<b>API</b>	Application Programming Interface
<b>ASCII</b>	American Standard Code for Information Interchange
<b>Basis</b>	set of vectors that can represent every vector in a given vector space by linear combinations
<b>Boolean</b>	set of operations to combine geometric entities
<b>B-spline</b>	Basis spline
<b>B-Rep</b>	Boundary-Representation
<b>CAD</b>	Computer Aided Design
<b>Calcium phosphate</b>	family of inorganic minerals
<b>CAM</b>	Computer Aided Manufacturing
<b>Chondrocytes</b>	cells which constitute cartilage tissue
<b>CLI</b>	Common Layer Interface slicing format
<b>CSG</b>	Constructive Solid Geometry
<b>CT</b>	Computed Tomography
<b>FEA</b>	Finite Element Analysis
<b>FDM</b>	Fused Deposition Modelling
<b>GUI</b>	Graphical User Interface
<b>Histology</b>	study of the microscopic anatomy of cells and tissues
<b>Histomorphometry</b>	quantitative study of the microscopic organization and structure of a tissue
<b>Humerus</b>	upper arm bone
<b>Hydroxyapatite</b>	a calcium phosphate mineral which provides up to seventy percent of bone composition

---

<b>IGES</b>	Initial Graphics Exchange Specification
<i>in vitro</i>	simulated body environment
<i>in vivo</i>	implanted in living organisms
<b>Knot/control points</b>	connection points for each polynomial piece forming a spline curve
<b>LOM</b>	Laminate Object Manufacturing
<b>LM</b>	Layer Manufacturing
<b>μCT</b>	Micro-Computed Tomography
<b>Mandibular condyle</b>	part of the mandible that articulates with the skull
<b>MB</b>	Mega-Byte
<b>MIT</b>	Massachusetts Institute of Technology
<b>MJM</b>	Multi-Jet Modelling
<b>MRI</b>	Magnetic Resonance Imaging
<b>NC</b>	Numerical Control
<b>Non-manifold</b>	solids in which each edge connects to more than two faces
<b>NURBS</b>	Non-Uniform Rational B-Spline
<b>Osteogenesis</b>	process of new bone formation
<b>Osteoporosis</b>	process of bone depletion
<b>PA</b>	polyamide
<b>PC</b>	polycarbonate
<b>PPSU</b>	polyphenylsulphone
<b>Pro-E</b>	Pro-Engineer CAD software
<b>PS</b>	polystyrene
<b>QMC</b>	Queens Medical Centre, Nottingham, UK
<b>RAM</b>	Random Access Memory
<b>RM</b>	Rapid Manufacturing
<b>RP</b>	Rapid Prototyping
<b>Solid</b>	solid volumetric entities in CAD
<b>STEP</b>	Standard for the Exchange of Product model data
<b>STL</b>	Stereolithography file format
<b>SLA</b>	Stereolithography Apparatus
<b>SLC</b>	StereoLithography Contour – slice file format
<b>SLS</b>	Selective Laser Sintering process
<b>SSL</b>	Stratasys Slicing Language
<b>TE</b>	Tissue Engineering

---

---

<b>UV</b>	Ultra Violet
<b>VB</b>	Visual Basic
<b>VBA</b>	Visual Basic for Applications

## NOMENCLATURE

### • Chapter 2

$\vec{v}_1, \vec{v}_2, \dots, \vec{v}_n$	basis vectors of n dimension
$\Re$	set of real numbers
$a_1, a_2, \dots, a_n$	scalar coefficients in $\Re$
$\vec{v}$	generic vector in the vector space
$a, t_1, t_2, t_3, \dots, t_k, b$	subdivisions of the domain $a, b$ for spline curves
$P(\%)$	porosity in percentage.
$V_{voids}$	volume of voids.
$V_{solid}$	volume of solid material.
$V_{implant}$	volume of the implant (with no voids), given by the sum of $V_{solid}$ and $V_{voids}$

### • Chapters 3 and 4

$X_i$	$X$ coordinate of the centre of the $i$ pore in prismatic rod networks
$Y_i$	$Y$ coordinate of the centre of the $i$ pore in prismatic rod networks
$Z_i$	$Z$ coordinate of the centre of the $i$ pore in prismatic rod networks
$a_x$	minimum distance from the $X$ border in prismatic rod networks
$a_y$	minimum distance from the $Y$ border in prismatic rod networks
$a_z$	minimum distance from the $Z$ border in prismatic rod networks
$n_x$	number of rods along $X$ in prismatic rod networks
$n_y$	number of rods along $Y$ in prismatic rod networks
$n_z$	number of rods along $Z$ in prismatic rod networks
$l$	length of the prism.
$w$	width of the prism.
$h$	height of the prism .
$Int$	VB integer function that returns the integer portion of a number
$Rnd$	VB random numbers generator function



---

$X_s$	$X$ coordinate of the middle point defining curved paths in prismatic rod networks
$Y_s$	$Y$ coordinate of the middle point defining curved paths in prismatic rod networks
$Z_s$	$Z$ coordinate of the middle point defining curved paths in prismatic rod networks
$X_c$	$X$ coordinate of the centre of the prismatic volume
$Y_c$	$Y$ coordinate of the centre of the prismatic volume
$Z_c$	$Z$ coordinate of the centre of the prismatic volume
$\Delta x, \Delta y, \Delta z$	size of an internal prism concentric with the prismatic volume.

• **Chapter 5**

$d_1, d_2$	vectors defining two curved co-ordinate lines $u$ and $v$ on anatomical volumes
$u_i$	curvilinear co-ordinate of a generic point $i$ on $u$
$c_u$	spatial resolution on $u$
$n_u^+$	number of rods in the positive side of $u$ for anatomical volumes
$n_u^-$	number of rods in the negative side of $u$ for anatomical volumes
$l_u^-$	length of the negative part of $u$
$l_u^+$	length of the positive part of $u$
$b_u$	minimum distance along $u$ from the border
$v_i$	curvilinear co-ordinate of a generic point $i$ on $v$
$c_v$	spatial resolution on $v$
$n_v^+$	number of rods in the positive side of $v$ for anatomical volumes
$n_v^-$	number of rods in the negative side of $v$ for anatomical volumes
$l_v^-$	length of the negative part of $v$
$l_v^+$	length of the positive part of $v$
$b_v$	minimum distance along $v$ from the border

---

- **Chapter 6**

$A$	area of a closed polyline
$N$	number of vertices of a closed polyline
$x_i$	horizontal co-ordinate of the generic vertex $i$ of a polyline
$y_i$	vertical co-ordinate of the generic vertex $i$ of a polyline

- **Chapter 7**

$Real\_sliced\_area\_tot$	sum of the sliced areas expressed in real values
$tot\_number\_of\_voxels$	number of voxels obtained from the $Real\_sliced\_area\_tot$
$tot\_number\_of\_voxels\_X$	number of voxels obtained by the sum of the number of voxels of each slice along $X$
$tot\_number\_of\_voxels\_Y$	number of voxels obtained by the sum of the number of voxels of each slice along $Y$
$tot\_number\_of\_voxels\_Z$	number of voxels obtained by the sum of the number of voxels of each slice along $Z$
$N$	number of layers along $X$ .
$M$	number of layers along $Y$ .
$P$	number of layers along $Z$ .
$\alpha_{j,i}$	$M$ -group relative to the layer $i$ along $Z$ in the layer $j$ along $X$ .
$D_j$	number of voxels required for the layer $j$ along $X$ .
$C_i$	number of voxels required for the layer $i$ along $Z$ .
$\beta_{j,i}$	$N$ -group relative to the layer $i$ in $Z$ and the $j$ layer in $Y$ .
$E_j$	number of voxels required for the layer $j$ along $Y$ .
$t_{j,i}$	represent the minimum values for either $\alpha_{j,i}$ or $\beta_{j,i}$
$\mathbb{N}$	set of natural numbers
$u$	zeros in the sequence $\alpha_{0,i}, \alpha_{1,i}, \alpha_{2,i}, \alpha_{3,i}, \dots, \alpha_{N-1,i}$ related to a layer $i$ on $Z$
$v$	zeros in the sequence $\beta_{0,i}, \beta_{1,i}, \beta_{2,i}, \beta_{3,i}, \dots, \beta_{M-1,i}$ related to a layer $i$ on $Z$

## CHAPTER 1

### - LITERATURE REVIEW -

#### 1.1 Introduction to Computed-Aided Design

The literature on Computer-Aided Design (CAD) is vast and dates from the late 1950s. This section presents the main developments and the most significant contributions in CAD history and relevant elements in the context of this research work.

The first computer program developed to draw geometrical elements on a display screen was a system called SKETCHPAD, by Ivan Sutherland at the Massachusetts Institute of Technology (MIT), in 1963 (Sutherland, 1963). This software was limited to two dimensional drawings and was capable of introducing constraints among the various geometrical entities. A light pen was used as the input device to draw planar entities directly on the display device. SKETCHPAD also incorporated the first Graphical User Interface (GUI) which allowed the user to interact graphically with the application.

Due to the high costs of early computers and their limited capabilities, first-generation Computer-Aided Design (CAD) systems were typically 2D drafting applications developed internally by large aerospace and automotive companies, often in collaboration with university research groups.

The advent of Numerical Control (NC) machining made the description of mathematically complex shapes necessary. Before NC, master models were produced and refined by skilled model makers, and often the geometries specified in drawings did not coincide with the actual shape of the master. For example, car bodies were designed by tracing cross sections located ten centimeters apart in the master model. Each section was then connected by using plane curves.

Several attempts to mathematically describe complex shapes were made both in Europe and in the US in the late 1950s and early 1960s. In France, Pierre Bézier at Renault developed a type of curve known as a ‘Bézier curve’ (Bézier, 1966; 1967), based on polynomial expressions of different degrees, to represent smooth and complex curves. Generalizations of Bézier curves to two or more dimensions are called Bézier surfaces. A similar type of curve was also developed by Paul de Casteljau at Citroen a few years earlier, along with a recursive formula to automatically compute such curves. This recursive method constitutes an important algorithm for CAD and is known as ‘The de Casteljau algorithm’ (de Casteljau, 1963). Since de Casteljau did not publicly publish the results, the theory of such curves and surfaces became known by Bézier’s name.

In the US, researchers followed an approach based on spline functions (for either curves or surfaces), defined piecewise by polynomial curves of different degrees with predefined smoothness conditions at the knot points (the connection points for each polynomial piece). Splines and Basis-splines (B-splines) were invented in 1946 by Isaac Schoenberg (Schoenberg, 1946). B-splines are splines in which the polynomial pieces form a basis for the set of all polynomial functions of a given degree, smoothness, and domain partition. Since any spline on a given set can be obtained by linear combinations of B-splines (de Boor, 1978), research efforts focused on the investigation of such functions.

On a vector space of  $n$  dimensions and basis vectors  $\vec{v}_1, \vec{v}_2, \dots, \vec{v}_n$ , linear combinations are defined as:

$$\vec{v} = a_1 \vec{v}_1 + a_2 \vec{v}_2 + \dots + a_n \vec{v}_n$$

Where:

$\vec{v}$  = generic vector in the vector space

$a_1, a_2, \dots, a_n$  = scalar coefficients in  $\mathfrak{R}$

Carl de Boor further advanced the theory of B-splines, and in 1972 developed an important algorithm to automatically compute splines and B-splines, which constitutes a generalisation of the de Casteljau algorithm for Bézier curves. This algorithm is still extensively used in CAD programs and it is known as ‘The de Boor algorithm’. A similar recursive method was proposed in the same period by Maurice Cox (Cox, 1972).

The theory of Bèzier curves and B-splines were unified by William Gordon and Richard Riesenfeld in 1974, who demonstrated how Bezièr curves and the de Casteljau algorithm were a special case of B-spline curves and the de Boor algorithm respectively.

A further generalisation of the concept of B-splines to rational B-splines (in which each piece is defined as the ratio of two polynomial functions) was developed by Kenneth Versprille in 1975, following earlier works by Stephen Coons (1968), Robin Forrest (1968) and Riesenfeld (1973). Versprille's work on rational B-splines was later completed by Lewis Knapp (1979).

Versprille and Knapp's work significantly contributed to the development of the most general class of splines, Non-Uniform Rational B-Splines (NURBS), which were invented by Les Piegl and Wayne Tiller (Tiller, 1983; Piegl and Tiller, 1987). The term 'Non-Uniform' refers to a non uniform spacing of the domain of each individual polynomial within the whole domain of the spline. This concept is illustrated in Fig. 1.1.

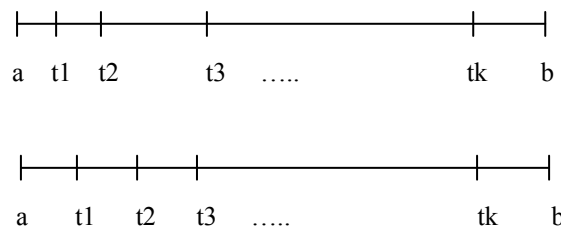
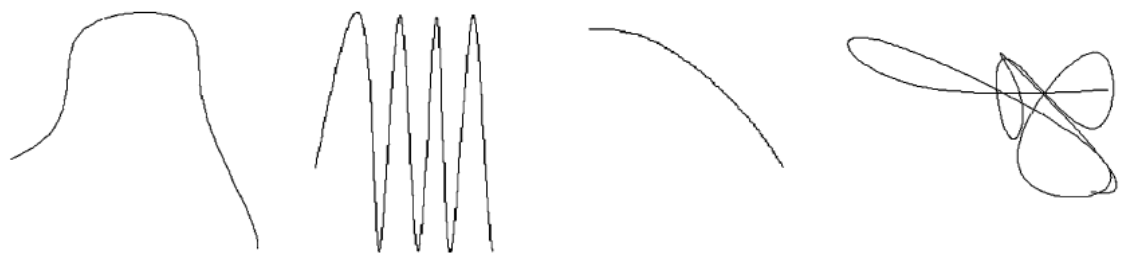


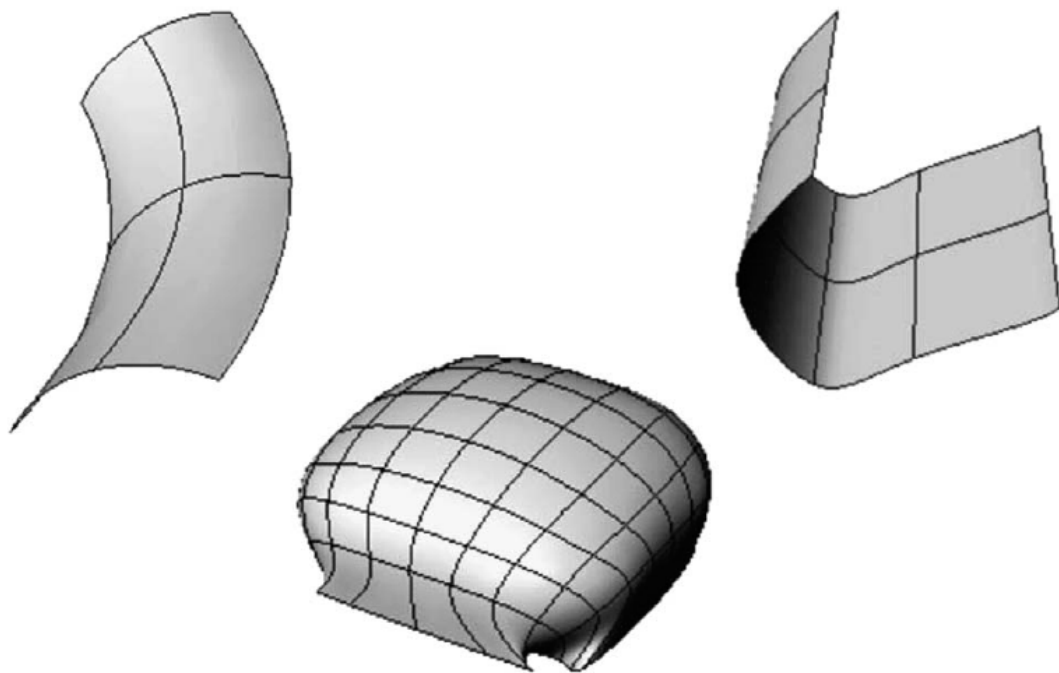
**Fig. 1.1** Concepts of non-uniform (top) and uniform (bottom) subdivisions of an interval.

NURBS became the standard for CAD software and are still widely used in the CAD industry for designing free-form curves and surfaces. The reason for this success was because CAD software could use a single internal representation of a wide range of curves and surfaces, from straight lines and flat planes to precise circles and spheres as well as intricate piecewise sculptured surfaces (Rogers, 2001).

Since NURBS are a generalisation of the concept of splines, they include all the other classes of splines, as well as lines and conic sections (curves such as circle, ellipse, parabola and hyperbola obtained by intersecting a circular conical surface with a plane) as particular cases. More details on how to obtain conics from NURBS can be found in Farin (1992). Examples of NURBS curves and surfaces are shown in Fig. 1.2.



(a)



(b)

**Fig. 1.2** Examples of NURBS curves (a) and surfaces (b) (Selimovic 2006).

A complete and detailed description of NURBS can be found in Piegl and Tiller (1997), while a review of the 3D geometric modelling techniques based on NURBS can be found in Dimas and Briassoulis (1999).

### 1.1.1 Solid Modelling

In 1963 a new version of Sutherland's software, SKETCHPAD III was developed at MIT by Timothy Johnson (Johnson, 1963). This version implemented the traditional three orthogonal views as well as perspective views of parts in the Euclidean space. The perspective views were made by using wire-frame entities such as lines and arcs, representing the edges of the part. An example is shown in Fig. 1.3.

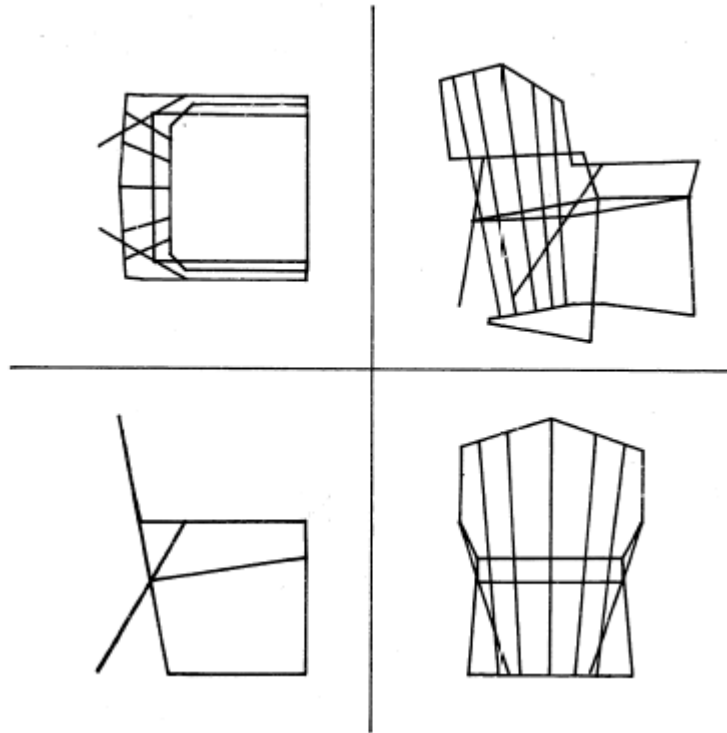


**Fig. 1.3** Example of wire-frame perspective design in SKETCHPAD III (Johnson, 1963).

A major limitation of 3D wire-frame representations is that they cannot provide an unambiguous description of the object and therefore they are not suitable to represent complex real parts (Ault, 1999).

Much of the early pioneering research in 3D solid modelling was done by Charles Lang's group at Cambridge University and by Herb Voelcker and his team at the University of Rochester at the end of 1960s and throughout the 1970s. The approaches followed by these two groups were fundamentally different, resulting in two different solid representations that are still widely used in current CAD software.

Voelcker's group developed a solid representation named Constructive Solid Geometry (CSG), in which a model is constructed starting from simple solid primitives (such as cylinders, spheres, prisms, cones, etc) combined by using Boolean operations. The first CAD solid modeller based on CSG was released in 1978 with the name of 'Part and Assembly Description Language' (PADL). More details on the CSG representation are provided in section 1.1.1.1.

Lang's team focused on Boundary-representation (B-rep) data structures, in which a solid is described through its boundaries (as a collection of connected surfaces and edges). Ian Braid (one of Lang's team) in 1978 developed the first B-rep solid modeller, named BUILD, which was the basis for other research and commercial B-rep solid modelling systems, such as ROMULUS, PARASOLID and ACIS. Much of today's CAD software adopts either PARASOLID or ACIS as a kernel for solid modelling (a kernel is a collection of software items grouped together to serve some distinct purpose). More details on the B-rep data structures are provided in section 1.1.1.2.

In the 1980s steadily increasing computer performance led to a greater usage of CAD solid modellers, most of which were based on either CSG or B-Rep. In 1987 Parametric Technology Corporation (Needham, Massachusetts) released the first version of Pro-Engineer (Pro-E), a CAD modeller based on the concept of parametric feature design. Pro-E contained two important innovations for CAD systems, feature based design and parametric design. In the feature-based approach, the design is carried out by using primitives that also have a well defined engineering meaning, such as pockets, holes, slots, chamfers, etc, as shown in Fig. 1.4. Form features allowed design with different level of abstraction, by capturing higher level of intents from the designer, thus improving the integration between CAD, CAM (Computer Aided Manufacturing) and other steps of product development. The pure description of a geometry does not provide additional information on manufacturing, dimensions, tolerances, etc and thus constitutes a low level of information. By using form features other relevant information can be included in the design process. More details on feature-based design can be found Sheu and Lin (1993), Salomons et al. (1993), Hoffmann and Arinyo (1998) and Roller (1989).



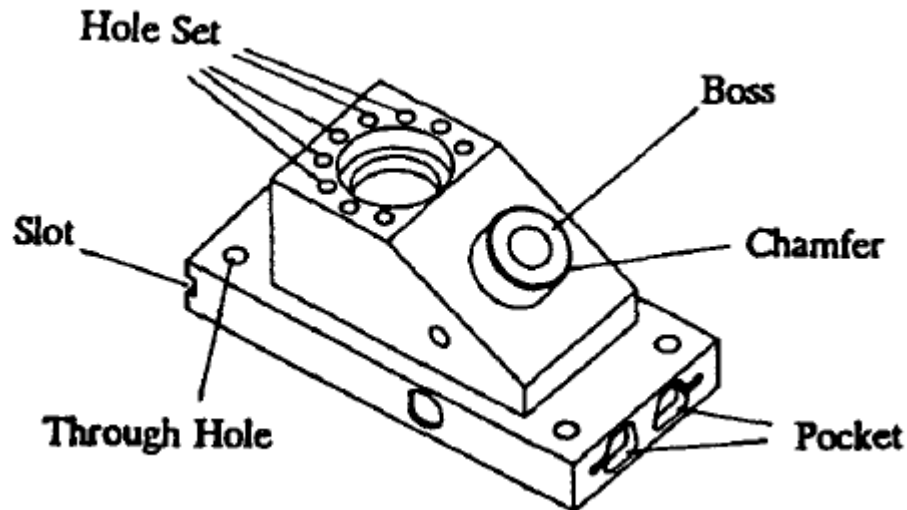


**Fig. 1.4** Example of feature-based design approach (Roller 1989).

Parametric design refers to the introduction of dimensional parameters (such as sizes, distances, angles, etc) and geometrical constraints (like symmetry, tangency, perpendicularity, parallelism, coincidence, colinearity, etc) in the solid geometry, in order to improve the editing process. Parametric design is usually combined with form features. Since changes in feature parameters propagate to the whole solid geometry, history trees recording the sequential geometry generation are required. By using history trees, the geometry can be edited at any step of the design process, and automatically recalculated and adjusted to preserve the established relationships. More details on parametric design can be found in Anderl and Mendgen (1996), Wang and Ozsoy (1991) and Monedero (2000), Roller (1991) and Hoffmann and Arinyo (2002).

CAD software based on parametric form features like Pro-E are the current standard of CAD technology. Parametric features have been implemented on both CSG (Rosen *et al.*, 1991; Van Emmerik and Jansen, 1989) and B-Rep (Pratt, 1988; Cutkosky *et al.*, 1988), although most current CAD software use hybrid models of CSG and B-Rep (Gomes and Teixeira, 1991; Shah and Rogers, 1988; Wang and Ozsoy, 1991), to exploit the advantages of each individual representation.

### 1.1.1.1 Constructive Solid Geometry

In CSG representation complex models are generated by sets of standard solid primitives which are combined through Boolean operations. The operations used are union, intersection and difference, as illustrated in Fig. 1.5 (a), (b) and (c) respectively.

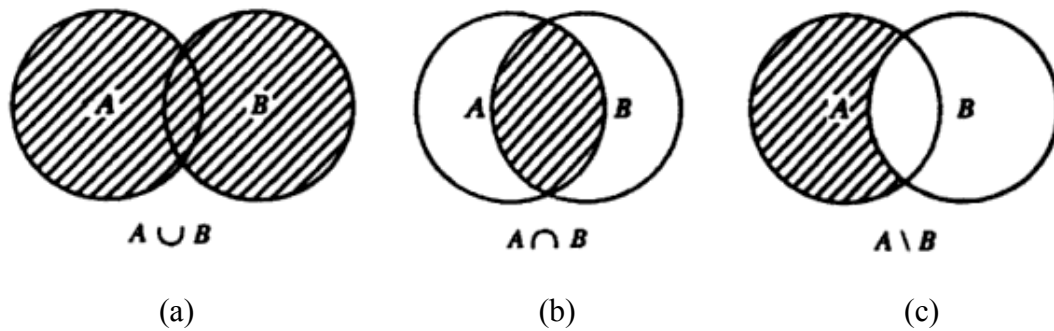


**Fig. 1.5** Boolean operations: (a) union, (b) intersection, (c) difference  
(Savchenko and Pasko, 2002).

CSG models are represented by binary trees whose branches are the primitives, and whose nodes are the Boolean operations. This ordered structure provides a natural template for the history trees required by parametric design, where the primitives are defined by variables whose values can be edited by the user at any point during the design process. The model is subsequently recalculated and updated. CSG models require less storage space than B-rep models, but require more computational time. This is because CSG models are unevaluated, which means that the geometry is defined implicitly during construction. Boundary elements such as curves and surfaces are not directly defined and stored in the model, but have to be computed every time they are required. An example of a CSG model and relative binary tree is shown in Fig. 1.6.

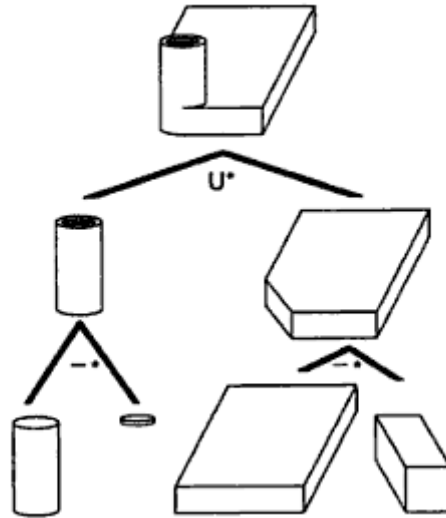


**Fig. 1.6** Example of CSG representation and relative binary tree (Foley *et al.*, 1997).

An advantage of CSG is that the objects produced are guaranteed to be always solid, as they are made by combinations of primitive volumes, while B-rep models have to be checked in order to verify that either gaps or overlaps do not exist among the boundaries. For this purpose, Boolean operations in CSG are also modified in order to produce only regular solids and avoid the generation of dangling edges, such as the one depicted in Fig. 1.7.

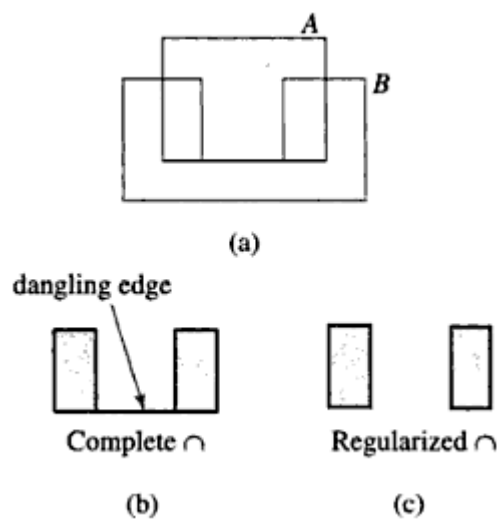


**Fig. 1.7** Example of dangling edge generated by Boolean operations: (a) operands, (b) standard intersection, (c) regularised intersection (Mortenson, 1999).

Primitive solids can also be defined by using basic surfaces called half-spaces, which separate the space in two regions, one above the surface and one below it, schematising the solid and the void side (Pratt, 2001). Combinations of half-spaces further divide the space in more regions, generating closed volumes which represent the primitive solids.

### 1.1.1.2 Boundary representation

The data structure used in B-rep solid description consists of two parts, one containing geometric data and the other one containing topological information. The latter describes the interconnections among the different boundary elements, which are faces, vertices and edges, while the geometrical part stores all the information about the surfaces, curves and points that constitute the solid's boundary. Faces, edges and vertices are the topology counterpart of surfaces, curves and points respectively.

The topological data is arranged in a top-down sequence, in which each face is described as a set of loops (closed group of edges surrounding a face), each loop as a set of edges and each edge as a group of vertices. An example of a B-rep topological structure is shown in Fig. 1.8.

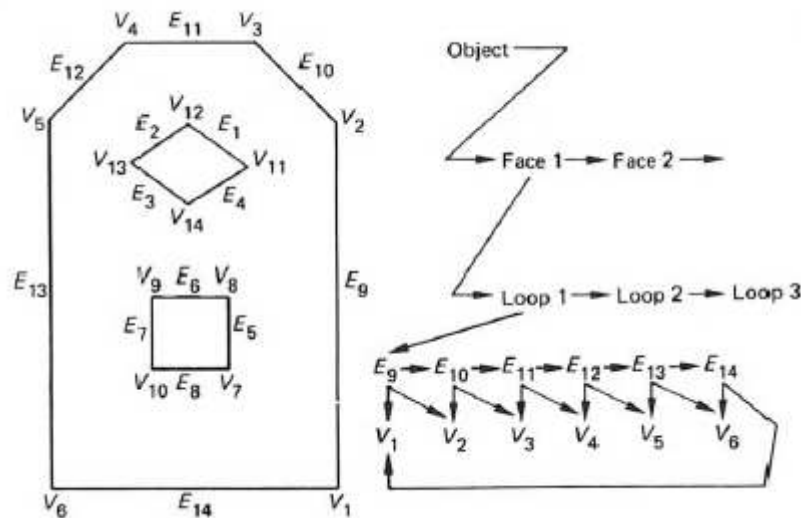


**Fig. 1.8** Example of topological connections in boundary representation  
(Rooney and Steadman, 1993).

All B-rep solids belong to an important class of solids, named as ‘manifold’ solids. In manifold solids, each edge connects only two faces, as in real solids. Examples of non manifold geometries are shown in Fig. 1.9. In the first case (a) the edges highlighted in red connect only one face, while in the other cases (b and c), there is one edge shared by four faces. Boundary representation can also be extended to allow special non-manifold models, as described in Sang and Kunwoo (2001).

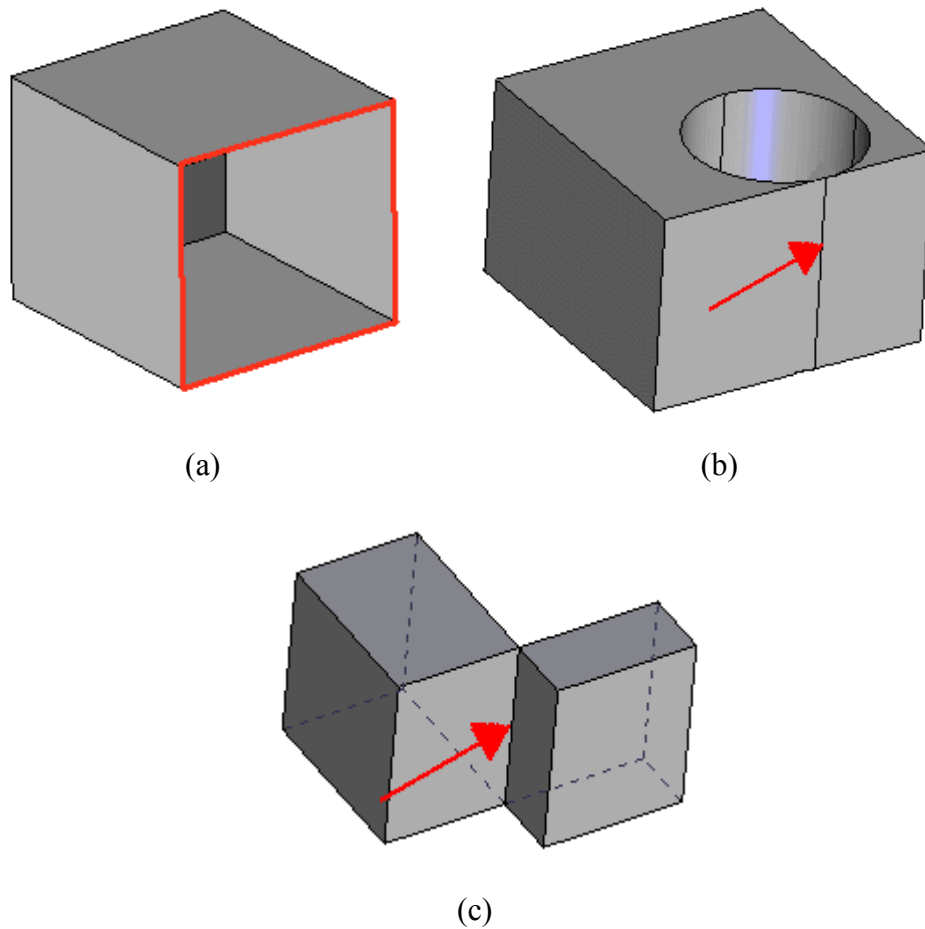


**Fig. 1.9** Examples of non-manifold solids.

B-rep is particularly suitable for CAD systems as it supports a wide set of operations, such as Boolean, sweeping, chamfering, filleting, drafting, shelling, etc.

Boolean operations on B-rep solids are similar to those used in CSG, but are much more computationally intensive as potential overlaps between boundaries have to be identified by pairwise comparison of each face of one object with each face of the other (Rooney and

Steadman, 1993). Intersection geometries between the boundaries have to be computed at each comparison, increasing the computational time, particularly when complex solids presenting a large number of faces are involved.

An important operation, particularly for sketch based features (a sketch is a set of planar elements), is sweeping, in which a closed 2D curve is swept along either a linear direction or a 3D curve, as shown in Fig. 1.10 (a) and (b) respectively. When the sweeping is made through several sketches, it generates a multi-sections solid.

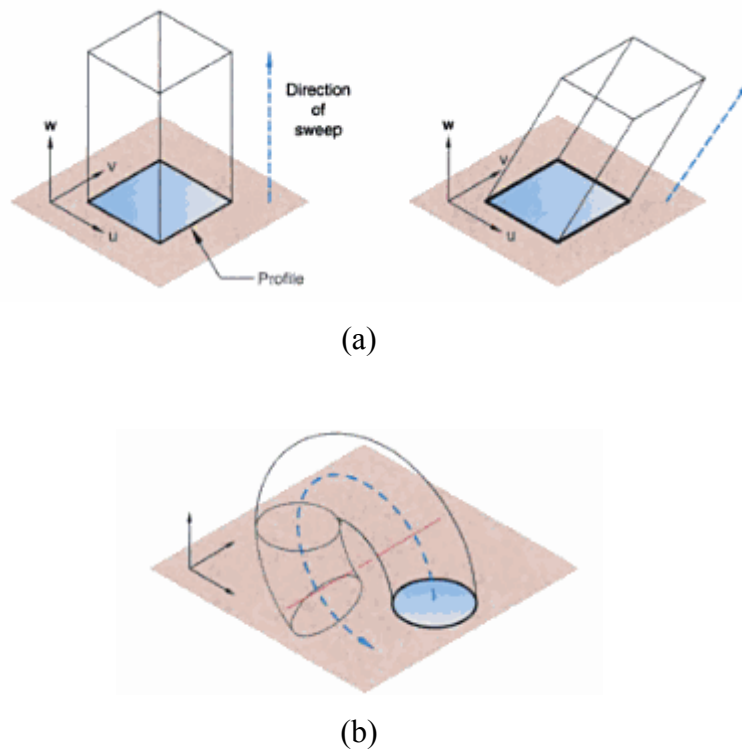


**Fig. 1.10** Example of solid modelling by sweeping a 2D profile (Bertoline and Wiebe, 2002).

## 1.2 Principles of the Additive Manufacturing Processes

In this section, a general description of Additive Manufacturing (AM) processes is provided. The literature on this topic is extensive and only a few references are provided, as AM does not constitute a major part of this work rather a significant application of the resulting design methods. More detailed descriptions of the AM processes can be found in Chua *et al.* (2003) and Gebhardt (2003) for example.

The term AM is adopted throughout this work to indicate those automated processes which are able to form solid objects by adding layers of material derived from a computerised

description (e.g. CAD). These techniques allow the "rapid" realization of physical parts, like prototypes for evaluation and assessment, and have been historically classified as Rapid Prototyping (RP) methodologies.

According to Kruth (1991) AM processes can be classified according to the state of the bulk material, which can be liquid, in powder form, or in solid sheets. Techniques belonging to the first group involve the solidification of a liquid monomer or a molten material. The second group includes the fusing of particles by laser or their joining by a binder, while the third group involves the bonding of solid sheets by light or adhesives. Table 1.1 illustrates this classification. The most prevalent AM techniques will be discussed in greater detail in the following sections.

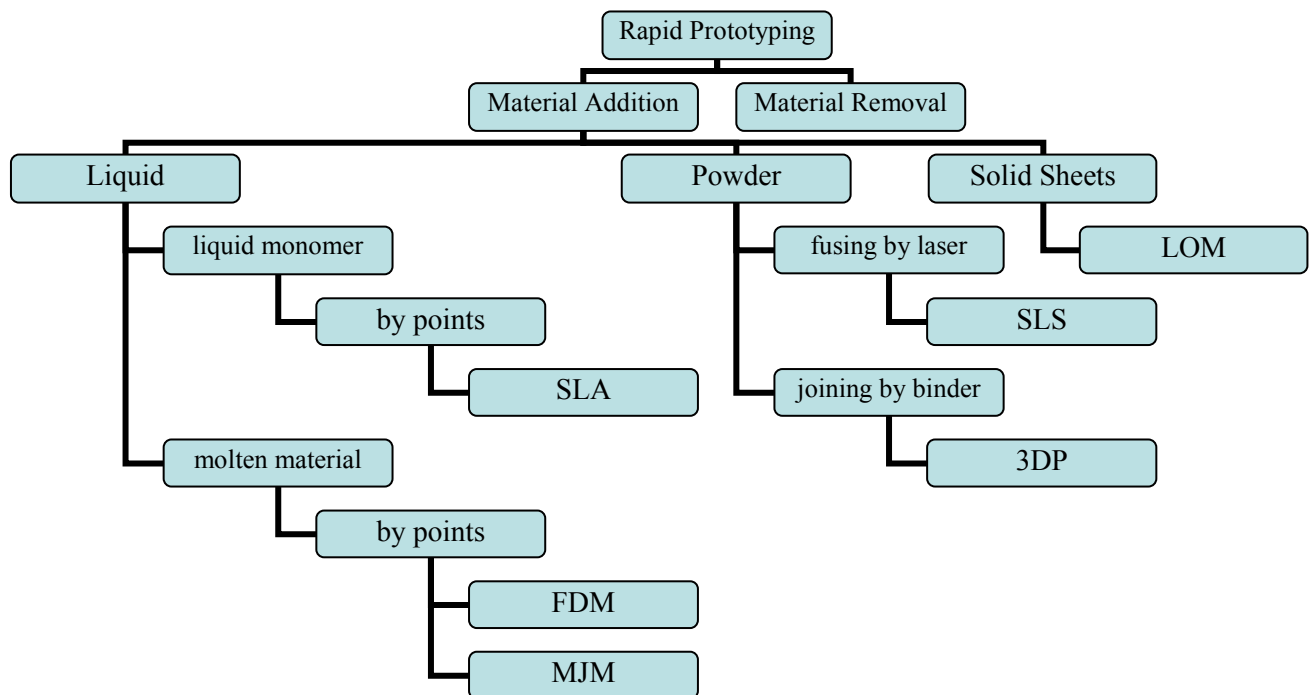


**Table 1.1** Classification of additive manufacturing processes.

All AM techniques require some common stages of pre-processing. Common steps are summarised as follows:

- Generation of a three dimensional solid geometry by means of CAD software or via reverse engineering.
- File conversion into a standard format for AM, such as STL (Stereolithography file format). This format is the de facto standard accepted by all AM machines.

- Selection of the build orientation.
- Generation of support structures (where required).
- Positioning of the parts into the build volume.
- Slicing.

After a solid 3D geometry is designed, the native CAD file is converted into the STL format. During this process, all the faces (external and internal) of the part are approximated by a tessellation of triangles, which form a mesh around the model. An example of triangular mesh is shown in Fig. 1.11.

The number and size of triangles constitute an index of accuracy because a greater number of triangles of a smaller size better approximate complex surfaces.

All the triangles must be connected to one another so as to form closed surfaces with the absence of gaps and overlaps between them.

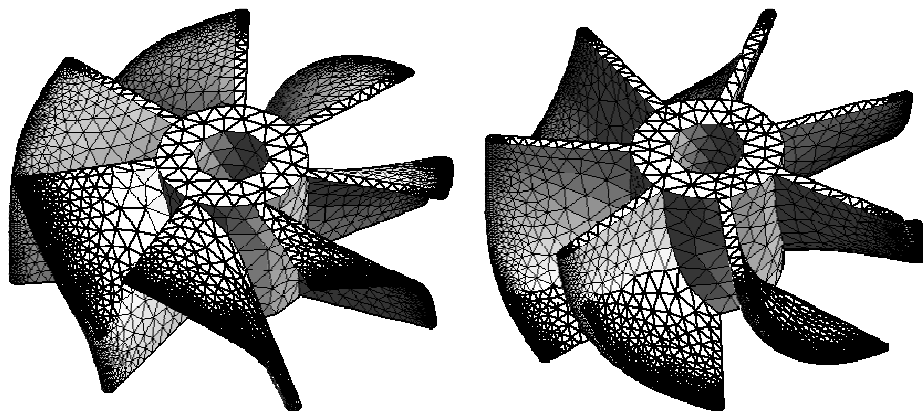


**Fig. 1.11** Example of triangular mesh

A closed mesh is necessary because the cross-sections obtained from the slicing process must be formed by closed loops (curves), in order to define the boundaries of the part. The STL generation is normally performed in the same CAD program so as to avoid additional conversions that could generate further losses of accuracy. Specific software is also available to repair and modify the mesh when required.

Depending on the particular process adopted, the build orientation can affect parameters such as build time, support structures, cost, accuracy, stair-stepping effect and surface finish.



Therefore there are no general rules to define it, as it will differ from part to part even for the same AM process.

Some AM technologies require the incorporation of support structures to hold up overhangs and undercuts of the part. Those supports are usually in the form of thin, column-like structures, which can be made using either the same material as the part or a different one.

Specific tools for designing these structures are generally included within the proprietary control software for the different AM processes. The generation is automatic, although the user can usually modify manually if required. The removal of these support structures varies from process to process, and can be either manual or semi-automated.

The last two steps involve the positioning of the part in the build volume and the slicing. The positioning is usually determined by considering factors such as build time, the amount of support structures required and their removal. The slicing process consists of dividing the meshed geometry by planes, which are orthogonal to the build orientation. As a result, the cross-section outlines of the part for each layer are generated.

The thickness of the layers can be constant or adapted to the curvature of the surface. It may typically range from 0.02 to 0.25 mm. After the slicing, the physical construction of the model may be initiated.

### **1.2.1 Liquid Monomer Based Processes**

Liquid monomer based processes (or photolithography) build parts using ultraviolet (UV) light to selectively solidify a photo curable resin, layer by layer. When exposed to the UV light, the monomer polymerizes and solidifies either by points or by layer, depending on the process. Commercially, the most widespread process is Stereolithography (SLA). The first SLA apparatus was developed in 1986 by Charles Hull at 3D Systems Inc. (Valencia, California, USA). Later, other companies in Europe and Japan developed similar commercialised technologies.

#### ***1.2.1.1 Stereolithography***

This process is depicted in Fig. 1.12. A platform is initially positioned just below the surface of a vat filled with a photosensitive monomer liquid, which, when exposed to the UV light, polymerizes and solidifies. The exposure and absorption of the UV light produces parabolically cylindrical, three-dimensional pixels called voxels (Fuh *et al.*, 1999).

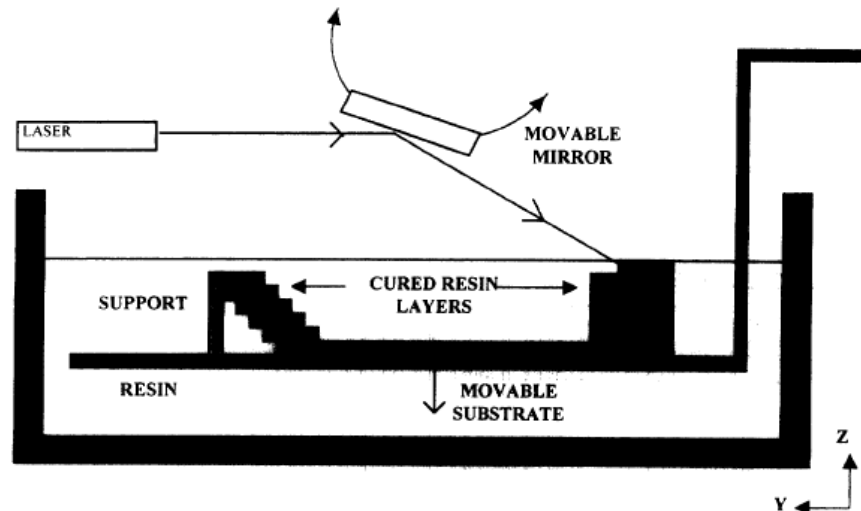


**Fig. 1.12** Stereolithography process (Pham and Gault, 1998).

The UV beam is moved over the surface of the liquid photopolymer to trace the geometry of the cross-section of the part. Several build styles are possible, depending on the particular scan pattern adopted. Detailed descriptions of different build styles can be found in Fuh *et al.* (1999), Venuvinod and Ma (2004) and Hague *et al.* (2001).

After a cross-section is produced, the table is lowered into the vat at a distance equal to the layer thickness. However, because photopolymers are quite viscous, simply lowering the elevator of a layer thickness down into the vat does not permit the liquid to uniformly recoat the upper surface of the part in a short time. Several recoating mechanisms have therefore been developed to facilitate this process. One example is “deep dipping” recoating, in which the elevator is first lowered by a greater layer thicknesses, so that the liquid completely flows over the upper surface of the part. It is then moved up to the required position, where a blade traverses the surface so as to level and remove the excess viscous material.

After completion, the object is elevated from the vat and the support structures are removed from the part. Afterwards, the model is cleaned of excess resin and a final cure is often provided by bathing it in a UV environment.

Materials used in SLA are thermosets such as acrylates, epoxies, epoxy/acrylic blends and filled resins. Acrylics are now rarely used since they present a high shrinkage rate which results in less accurate parts. Epoxies are used most frequently because they have high

accuracy and a low shrinkage rate. Filled resins are adopted primarily for functional uses, since they are reinforced with ceramics or metals.

SLA can be used for several applications such as concept, functional and medical models, for aerodynamic testing, investment casting and rapid tooling.

### 1.2.2 Molten Material Based

Molten material-based processes build parts by the deposition of a molten or semi-molten material through one or more heated nozzles. The nozzles move along the build platform to produce each cross-section of the part. Some processes have a dedicated nozzle for the deposition of the support material. Commercially, the most widespread processes are Fused Deposition Modelling (FDM), and Multi-Jet Modelling (MJM). FDM was invented by Scott and Lisa Crump in 1988 and patented four years later by Stratasys Inc. (Eden Prairie, Minnesota, USA). MJM has been developed and commercialised by 3D Systems.

#### 1.2.2.1 Fused Deposition Modelling

The process is depicted in Fig. 1.13.

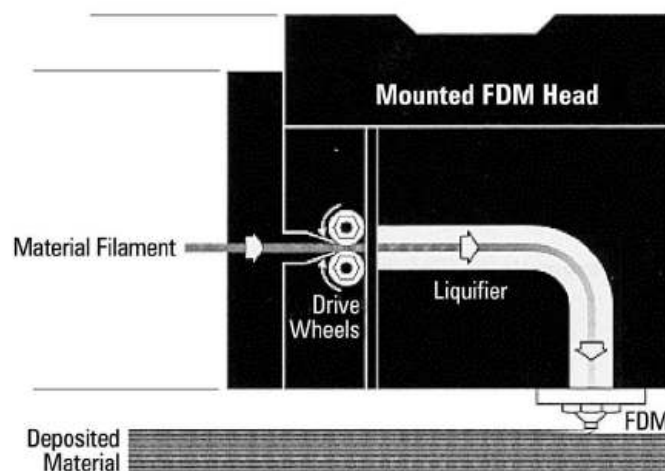


**Fig. 1.13** Fused deposition modelling process (Ahn *et al.*, 2002).

A thermoplastic filament, approximately 1/16 inch in diameter, is unwound from a coil to supply material to an extrusion nozzle, which heats the filament through a resistant heater to just above its softening point. The softened material is continuously extruded and solidifies after deposition. The flow of molten material is controlled through drive wheels, while the nozzle is moved in the *X* and *Y* axis to deposit the cross-sections of the parts. After a layer is

produced, the extrusion head moves up by the given layer thickness and the process is repeated.

FDM requires the building of explicit thin walled support structures for overhangs and undercuts. FDM systems commonly incorporate two nozzles, one for the build material and one for the support material, which is removed after completion. The support removal can be either manual or semi-automatic, in which case they are dissolved into a water-based solution.

FDM has a reasonable range of modelling materials, most of which are thermoplastics. It includes acrylonitrile butadiene styrene (ABS), polycarbonate (PC) and polyphenylsulphone (PPSU).

FDM can be used for the production of concept, functional and medical models, and for investment casting patterns.

#### ***1.2.2.2 Multi Jet Modelling***

The MJM process is depicted in Fig. 1.14.

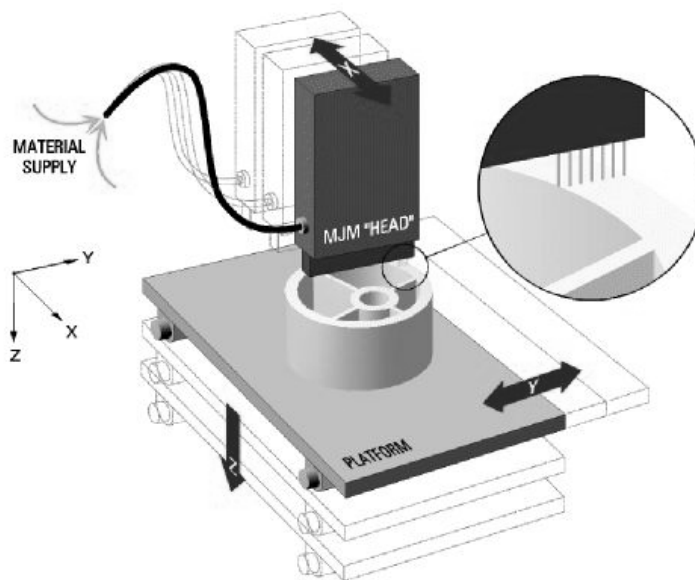


**Fig. 1.14** Multi jet modelling (Cooper, 2001).

MJM uses a print head formed by a number of jets oriented in a linear array, each of which can be electrically activated in order to release thin droplets of a molten material, typically a thermoplastic or a wax. The material is kept in a dedicated reservoir which feeds each individual jetting head. The temperature of the reservoir is slightly higher than the melting point of the thermoplastic/wax, so that after deposition, the droplets can harden almost immediately, creating a bond with the previous layer. In order to produce the cross-sections of the part, the print head is moved in the  $X$  axis while the platform is moved along the  $Y$  axis. The build platform moves vertically by one layer thickness after each cross-section is completed.

Supports are required and are in the form of thin, column-like structures, which can be made using either the build material or another material. These supports are then removed manually or dissolved in solvents after completion.

The process is fast (1 to 2 vertical inches per hour, depending on the layer density), as the print head simultaneously deposits the build material from hundreds of jets.

Materials commercially available for MJM are thermoplastic polymers containing paraffin, hydrocarbon waxes and polymers/hydrocarbons blends. Natural and synthetic waxes, generally soluble at 50-70° C, are utilized for the support structures.

Applications of MJM include the production of concept models and patterns for investment casting.

### **1.2.3 Powder Based**

Powder based processes build parts by selectively fusing or joining discrete particles of a powder material. In the first case, each layer of the part is scanned by a laser beam on to a powder bed, causing the particles to fuse only in those areas exposed to the laser. In the second case, a nozzle deposits thin droplets of a binder on to a powder bed, causing the particles to stick together.

#### ***1.2.3.1 Selective Laser Sintering***

Selective Laser Sintering (SLS) was developed by Carl Deckard and Joseph Beaman at the University of Texas in 1987. It was commercialised by 3D Systems and EOS GmbH (Munich, Germany). The process is depicted in Fig. 1.15.

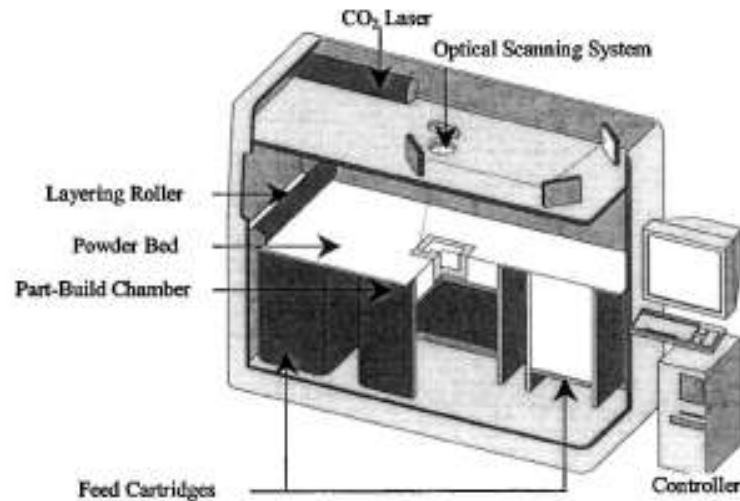


**Fig. 1.15** Selective laser sintering (Pham and Dimov, 2003).

A layer of material is spread out on to a powder bed and levelled by a roller or a blade from a powder-feed cartridge. The powder bed is preheated to a temperature just below its melting point (for crystalline materials), or just below the glass transition temperature (for amorphous materials, like PC). This is conducted in order to reduce the part distortion, facilitate fusion between the layers and reduce the thermal energy which needs to be supplied by the laser. Through a set of moveable mirrors controlled by a computer, a laser beam scans the top of the powder bed, tracing a cross-section of the part. The particles exposed to the laser can be fused together in varying degrees depending on process parameters.

Powder not exposed to the laser remains in place, and acts as a support for the next layer. At completion, the unfused powder is brushed off and recycled in varying ratios.

After a cross-section is produced, the powder bed descends the given layer thickness, the powder-feed cartridge is elevated correspondingly and a new layer of powder is deposited. The process is then repeated until the part is completed. Before removal, the part must be allowed to cool down and stabilise for several hours in order to prevent warping, shrinkage and residual stresses. A nitrogen atmosphere is maintained during fabrication to reduce oxidation and prevent explosion.

Commercial materials available for SLS include various form of amorphous polymers such as polycarbonate and polystyrene (PS), as well as semi-crystalline polymers such as

polyamides (PA, nylon). Metal powders like bronze, steel, polymer/steel, bronze/steel and copper/steel blends are also available.

SLS polymers are used in many areas for both concept and functional models, as well as for the production of patterns for investment casting. Metal powders have been used for rapid tooling and for the manufacture of functional metal parts.

### 1.2.3.2 Three Dimensional Printing

Three Dimensional Printing (3DP), depicted in Fig. 1.16, was developed and patented at the MIT, which licences the technology out to several companies for different applications. Z-Corporation (Burlington, Massachusset, USA) commercialises the technology to produce machines for plaster and starch parts, while ProMetal Inc. (Troy, Minnesota, USA), Soligen Inc. (Santa Ana, California, USA) and Therics (Akron, Ohio, USA) commercialise the process respectively for metal, investment casting and pharmacology applications.

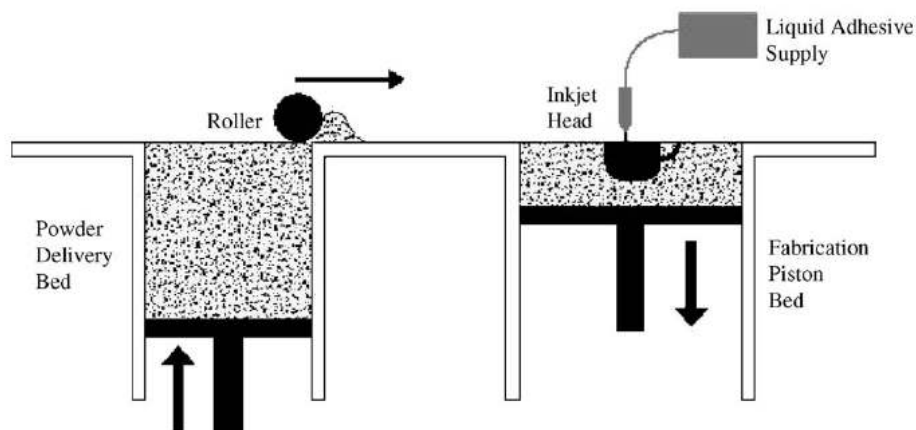


**Fig. 1.16** Three Dimensional Printing (Ryan *et al.*, 2006).

A layer of powder is first spread by a roller from a feed box on to the top of a powder bed. Either continuously or on demand, an inkjet print head deposits thin droplets of binder material (typically a polymer-based adhesive) on to the powder bed, adhering particles only where required. The print head is moved along the *XY* plane to produce a cross-section. After one layer is selectively adhered, the powder bed is lowered in the *Z* direction by one layer thickness using a piston, while the feed box is moved up correspondingly. The roller then spreads a new layer of powder and the process is repeated until completion. The unbound

powder acts as support for overhangs and undercuts during fabrication, and is removed and recycled when printing is finished. Metal powders require a high-temperature firing treatment prior to post-process infiltration, both to sinter the part and to remove the binder. Green parts are porous and always require an infiltration process to improve the density and mechanical properties. Infiltration can be performed using low melting point metals for metal powders, while epoxy resins, glues or water may be used for plaster and starch materials.

Several materials can be used in 3DP including starch, cellulose, plaster and their blends, as well as steel/bronze powders and ceramic/polymer blends. The use of the inkjet technology also allows for printing in different colours. Plaster based materials are used to produce concept, medical and architectural models, whereas starch and cellulose for investment casting patterns. Metal powders are mainly used for tooling applications.

#### **1.2.4 Laminate Based Processes**

Laminate based processes build parts from paper, plastic, metal or composite foils. These processes build parts by stacking and binding together foils of the same material, each containing a cross-section of the part. The sections are drawn by either using a cutting knife or a laser beam. The process was initially commercialised by Helisys Inc. (Torrance, California, USA; no longer in service) with the name of Laminate Object Manufacturing (LOM).

##### ***1.2.4.1 Laminate Object Manufacturing***

The process is depicted in Fig. 1.17.



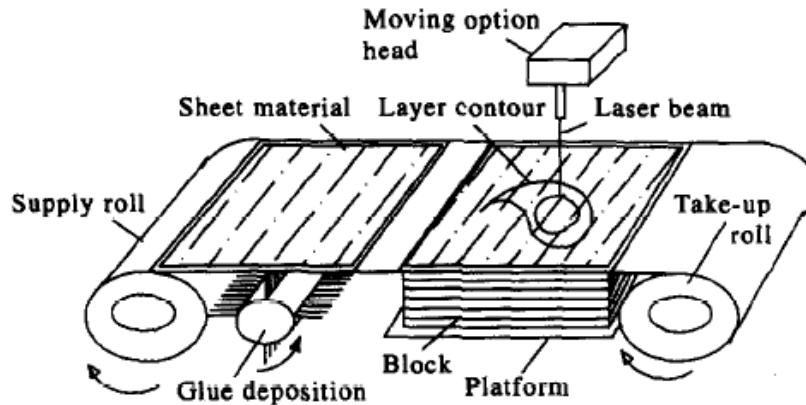


**Fig. 1.17** Laminated object manufacturing process (Yan and Gu, 1996).

The build material consists of foils with an adhesive coating on one side, which can be thermally activated. One sheet is unwound from a roll, positioned over the sheet stack and bound to the previous layer by a heated roller. The cross-section outline is then drawn by a CO<sub>2</sub> laser, which is carefully modulated to penetrate to the exact depth of one layer. After a cross-section is traced, the remaining material is trimmed into rectangles by the laser, to facilitate its removal after completion. It remains in place during fabrication in order to act as a support for overhangs and undercuts. Afterwards, the stack is lowered by one layer thickness through a moveable platform, and a new foil of material is positioned. The whole process is then repeated. Since laser cutting generates considerable fumes, an extraction system is required, along with fire protection.

Removing the part from the stack after completion can be a time-consuming process, particularly with large models. Nevertheless, the fabrication process is quick, as only the contours of the cross-sections have to be drawn. Complex geometries with internal cavities cannot be made by LOM, due to the difficulties of removing the internal material, and that therefore limits the applications of this process.

In order to prevent distortion of the parts due to water absorption, a sealing process with a urethane, silicone or epoxy spray is often required.

LOM can process a wide range of materials, including papers, metals and plastic foils. The main applications of this technology are for producing architectural, sculptural and concept models.

### 1.3 Tissue Engineering

Tissue Engineering (TE) is "an interdisciplinary field that applies the principles of engineering and the life sciences toward the development of biological substitutes that restore, maintain or improve tissue function" (Langer and Vacanti, 1993).

The main goal of this discipline is to "restore function through the delivery of living elements which become integrated into the patient" (Vacanti and Langer, 1999).

Broadly, two approaches may be followed in TE. The first is termed "direct organ printing", and consists of the direct manufacture of tissues using the principles of AM, modified for processing biological materials, cells and living tissues (Mironov *et al.*, 2003). However, it is likely to be many years before the direct printing of complete living tissues becomes possible.

The second approach consists of using cell seeded scaffolds with controlled micro architecture, in order to promote the natural regeneration of tissues *in vitro*, i.e. a simulated body environment (Sharma and Elkinsseff, 2004). The newly grown tissue should then be implanted *in vivo* (in living organisms) to restore the biological functions. Alternatively, the cell seeded scaffold can be implanted directly *in vivo*, to serve as guidance for cell and tissue growth in a real body environment (Capito and Spector, 2003).

The main functions of TE scaffolds are to promote cell attachment, proliferation, migration and differentiation, as well as providing a spatial arrangement for cells. However, highly porous scaffolds alone, even if seeded with appropriate types of cells, do not entirely facilitate the characteristics required. The interaction between cells and the scaffold surface, and the micro-environment surrounding individual cells, have a great effect on their ability to attach, proliferate, migrate and differentiate (Bhatia and Chen, 1999). For instance, a low pH in the microenvironment surrounding a scaffold is not ideal for tissue regeneration, as it could elicit an inflammatory response (Kohn *et al.*, 2002).

Similarly, most tissues require an extensive vascularisation network for the transport of oxygen and nutrients, with the exception of cartilage where cells can survive in conditions of very low oxygen (Rajpurohit *et al.*, 1996).

*In vitro* tests show that the lack of oxygen and nutrients governs the penetration depth of the new tissue into the scaffold geometry (Rose *et al.*, 2004).

Scaffolds with complex architectures can be manufactured using processes that do not allow a full control over the internal geometry, resulting in foam structures with uncontrolled

porosity, pore size and interconnectivity. In this work, those manufacturing techniques are classified as ‘conventional’, to distinguish them from AM technologies, which instead allow a high degree of control over the scaffold's internal architecture. The use of conventional manufacturing and AM for TE is described in sections 1.3.1 and 1.3.2 respectively.

Ishaug-Riley *et al.* (1997) found that the maximum depth of penetration of new tissue in the foam structures was less than 500  $\mu\text{m}$  - a consequence of scarce pore interconnectivity. In addition, cells colonising the periphery of the scaffold tend to act as a barrier to the further diffusion of oxygen and nutrients, preventing new cells from deeper migration (Sachlos and Czernuszca, 2003). This phenomenon is illustrated in Fig. 1.18.

According to Colton (1995), no cells except for chondrocytes (which constitute cartilage) exist further than 25-100  $\mu\text{m}$  from the blood supply (i.e. oxygen). That is why only cartilage tissue has been successfully grown *in vitro* using conventional scaffold fabrication techniques, as well as skin, which is largely a 2D tissue. As a result, scaffold architectures and materials play an essential role in tissue regeneration.

Details on TE scaffold requirements are provided in section 1.3.3.

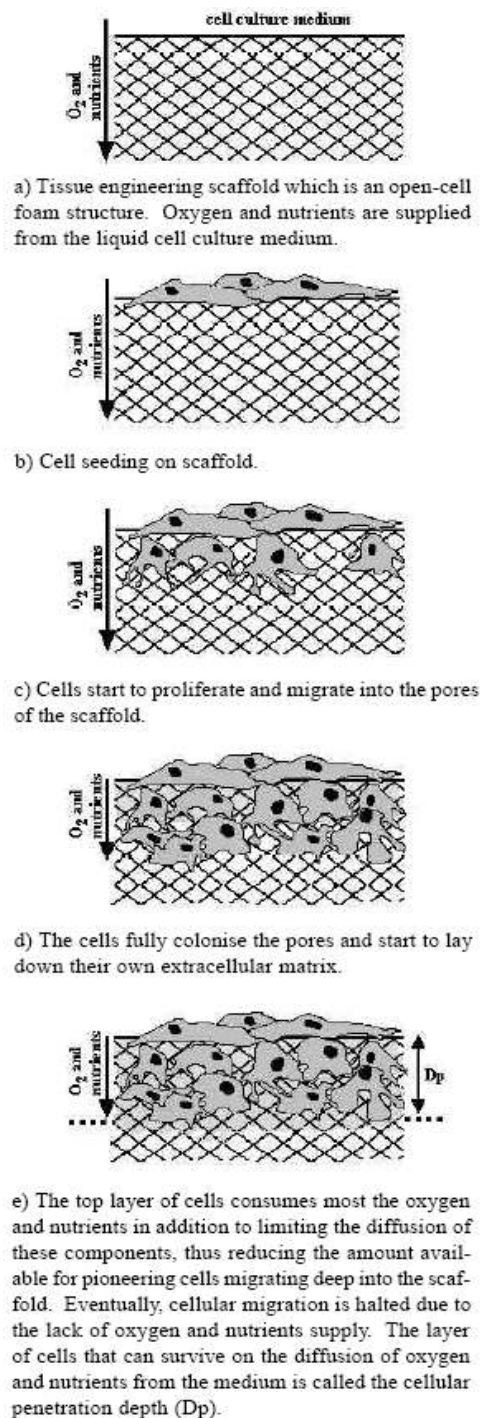


**Fig 1.18** Cells colonising the periphery of the scaffold tend to act as a barrier to the further diffusion of oxygen, preventing new cells from deeper migration (Sachlos and Czernuszca, 2003).

### 1.3.1 Conventional Manufacturing and Tissue Engineering Scaffolds

Conventional manufacturing processes typically attempt to control the micro-architecture of TE scaffolds by varying the process parameters (Taboas *et al.*, 2003). Such techniques are limited in terms of resolution and reproducibility, and can generate a wide distribution of pore sizes, with scarce control over interconnection, geometry and spatial distribution, resulting in random foam structures (Bartolo *et al.*, 2009; Manjubala *et al.*, 2005). As explained in section 1.3, these parameters greatly affect the flow of oxygen and nutrients inside the scaffold, which are essential to tissue regeneration (Naing *et al.*, 2005).

Ishaug-Riley *et al.*, (1997) found that the average penetration depth of regenerated tissue in foam structures ranged from 190 +/- 50  $\mu\text{m}$  for foams with 500-710  $\mu\text{m}$  pores, to 370 +/- 160  $\mu\text{m}$  for foams with 150-300  $\mu\text{m}$  pores, after 49 days *in vivo*.

Mooney *et al.*, (1996) estimated that only 10-30% of pores are interconnected in foam structures produced by a conventional process named as gas foaming.

Furthermore, most of those techniques use organic solvents to dissolve synthetic polymers, and the presence of residual solvents may cause toxicity to cells. A full review of these manufacturing techniques can be found in Tsang and Bhatia (2004).

### 1.3.2 Additive Manufacturing and Tissue Engineering Scaffolds

The main advantage of combining AM and TE scaffolds is the possibility of designing and manufacturing scaffolds with a reproducible internal structure and controlled porosity, pore size, interconnectivity and shape (Roy *et al.*, 2003). These conditions are essential to facilitate and control the flow of oxygen inside the scaffold. In addition, CAD designs can be used in conjunction with Computed Tomography (CT) or Magnetic Resonance Imaging (MRI) data to produce customised scaffolds with anatomical shapes. In such cases, two design steps take place, one for the global implant geometry and one for the scaffold element. The two geometries are then combined to produce the final architecture.

The final architecture can be produced either directly using an AM process, or indirectly, typically by producing a sacrificial mould into which a biomaterial is cast. The latter case offers the possibility of using biomaterials that cannot be processed directly via AM. Examples of moulds fabricated by SLA and FDM can be found in Chu *et al.* (2001) and in Bose *et al.* (2002).

The current drawbacks of using AM for TE scaffolds include the limited amount of directly processable bio-materials, the minimum feature resolution, sometimes limited mechanical properties, support removal (process dependant), and the low symmetry of small pores as shown in Fig. 1.19 (Buckley and O'Kelly, 2004). Support removal can be critical for some AM processes, as any material trapped inside pores and channels will affect the porosity, pore size and shape.

SLS has more limitations in terms of minimum feature resolution compared with other AM processes. That is mainly due to the laser spot diameter and average particle size, which for commercial SLS apparatus, are typically 100-200  $\mu\text{m}$  and 20-100  $\mu\text{m}$  respectively.

Sriram *et al.* (2003) investigated the minimum hole diameter achievable by SLS using two different materials. It was found that with polyamide, the minimum hole diameter was  $0.52 \pm 0.02$  mm, for an intended hole diameter of 1.0 mm, with a shrinkage of 48%. Using an alumina-polyamide blend, the minimum hole diameter was  $1.02 \pm 0.02$  mm, for an intended hole diameter of 1.0 mm. As a result, the feature resolution is also dependant on the material used. Chua *et al.* (2003a) also investigated the minimum pore size achievable by different AM processes (3DP, FDM, SLA and SLS). The results are summarised in Table 1.2.

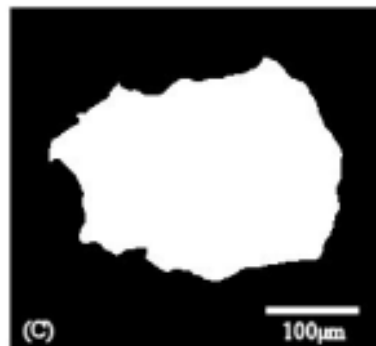


**Fig. 1.19** Example of low symmetry in small pores by SLS (Buckley and O'Kelly, 2004).

Process	Materials	Achievable pore size ( $\mu\text{m}$ )	Advantages	Disadvantage
3D-P	Polymers, ceramics, starch, metals	45–100	100% interconnected porous structure; no heating of powders necessary; wide material choice	Trapped materials in the interior may be difficult to remove
FDM	Thermoplastic polymers, ceramics	50–1000	100% interconnected porous structure; no trapped material problem	Requires support structures; anisotropic mechanical properties; high heat effect on raw materials
SL	Polymers, ceramics	$\geq 70$	100% interconnected porous structure; no trapped material problem; capable of producing very fine features	Requires support structure; limited material choice
SLS	Polymers, ceramics, metals	$\geq 500$	100% interconnected porous structure; wide material choice	Trapped materials in the interior may be difficult to remove

**Table 1.2** Minimum pore size achievable by some AM processes (Chua *et al.*, 2003a).

### 1.3.3 TE Scaffold Requirements

Several requirements for TE scaffolds have been identified. According to Hutmacher *et al.* (2001), scaffolds should possess the following characteristics:

- High porosity and interconnecting pores of appropriate size and shape. The optimum architecture should mimic the properties of the natural tissue.
- External shape to fit anatomical sites.
- Fully controllable and reproducible internal structures.
- Made of bio-materials with controlled degradation and resorbability rates.
- Suitable mechanical properties for load-bearing applications.

The mechanical properties of scaffolds should match those of the natural tissue, or a percentage of it (Lin *et al.*, 2004).

According to Hollister *et al.* (2005), scaffolds for bones and craniofacial cartilage tissue should possess an elastic modulus ranging from 100 to 30000 MPa, and from 0.9 to 60 MPa respectively.

An elastic modulus for human trabecular bone should range from 52 to 67 MPa, with a compressive yield strength ranging from 2 to 3.2 MPa (Williams *et al.*, 2005). According to Yang *et al.* (2001), the compressive yield strength of human trabecular bone should range from 4 to 12 MPa, while that of the elastic modulus from 20 to 500 MPa. For cartilage tissue, an elastic modulus between 0.7 and 15.3 MPa, and tensile yield strength between 3.7 and 10.5 MPa were suggested (Parsons 1998).



Mechanical properties for other tissues can be found in Woo and Levine (1998) and Yang *et al.* (2001).

In terms of pore size, Hulbert *et al.* (1970) suggested a minimum pore size of 100  $\mu\text{m}$  for *in vivo* bone regeneration. This value was also proposed as a boundary to distinguish between macro and micro pores. However, Itala *et al.* (2001) showed that no statistical differences in bone regeneration occurred by testing *in vivo* titanium plates with four different pore sizes (50, 75, 100 and 125  $\mu\text{m}$ ) under no load condition, thus suggesting that 100  $\mu\text{m}$  may not be the minimum pore size when non-load bearing is required.

Kuboki *et al.*, (2001) compared blocks of hydroxyapatite (up to 70% of bone is comprised of this inorganic mineral) with different pore sizes *in vivo*. New bone formation was higher for 300-400  $\mu\text{m}$  pores than for smaller sizes, and that was also the critical size above which capillaries (small blood vessels) were observed.

Chang *et al.* (2000) observed more *in vivo* bone regeneration in hydroxyapatite implants with 200-400  $\mu\text{m}$  interconnected pores than for other sizes, also suggesting that pore interconnectivity rather than pore size has a greater influence on osteogenesis (bone regeneration).

Jin *et al.*, (2000) and Kuboki *et al.* (2002) tested *in vivo* hydroxyapatite scaffolds with different pore sizes. Osteogenesis and vascularisation (blood vessel regeneration) resulted in 350  $\mu\text{m}$  pores, while pores of 90–120  $\mu\text{m}$  size showed more chondrogenesis (cartilage regeneration).

Kruyt *et al.* (2003) compared hydroxyapatite scaffolds with different pore sizes and porosities (800  $\mu\text{m}$  of average pore size and 70% porosity, versus 400  $\mu\text{m}$  of average pore size and 60% porosity) *in vivo*. More bone formation was observed in the scaffold with higher pore size and porosity, confirming that higher pore size and porosity enhance the flow and exchange of nutrients.

In summation, these studies show that pores bigger than 300  $\mu\text{m}$  have an increased osteogenesis *in vivo*.

Pores with appropriate diameters alone are not sufficient to regenerate a connected tissue. Bruder *et al.* (1998) found that scaffolds with uncontrolled pore architecture, produced a large amount of new bone *in vivo*, although it had poor mechanical properties. That is because the regenerated tissue tends to follow the geometry of the scaffold while it degrades over time. Chu *et al.* (2002) developed cylindrical scaffolds with two different internal



channel geometries, orthogonal and radial. After 9 weeks of implantation *in vivo*, the shape of the new bone was found to be significantly different, as it tended to follow the geometry of the pores.

Porosity is defined as follows:

$$P(\%) = \frac{V_{voids}}{V_{voids} + V_{solid}} 100$$

Where:

$P(\%)$  is the porosity in percentage.

$V_{voids}$  is the volume of voids.

$V_{solid}$  is the volume of solid material.

High porosity *in vivo* improves the degree of osteogenesis, as it allows a better flow of nutrients and oxygen (Karageorgiou and Kaplan, 2005). There is no clear quantitative requirement for porosity, though most authors cited in this section suggest values in the range of 70-90%. In principle, the porosity should be as high as possible so as to achieve a good diffusion of nutrients. An upper limit to porosity is established by the mechanical properties of the scaffold, which are crucial in load-bearing applications. Das and Hollister (2003) proposed a technique to design scaffolds with the desired mechanical properties, maintaining a target value of porosity.

The studies show that, as with the mechanical properties, the quantification of geometrical requirements for TE scaffolds is not well defined at this time. The data reported give only a general indication of bone scaffold requisites, more precise data are not currently available. The lack of more precise data is currently a major limitation for specific TE scaffold design. Furthermore, mechanical and geometrical requirements strongly depend on the type of tissue to be regenerated, making their prediction even more difficult.

#### 1.4 Trabecular Bone Architecture

The literature describing bones from a biological and mechanical point of view is vast, and beyond the remit of this work. The purpose of this section is to illustrate the irregular

structures of trabecular bone, through 3D computerised geometric reconstructions. Such 3D representations are typically used for bone morphology assessment, mechanical properties evaluation by Finite Element Analysis (FEA) and for AM purposes.

Classically bone structure comprises of trabecular bone, which presents a porosity that varies from 50% to 90%, surrounded by cortical bone, which possesses a highly dense structure (Sommerfeldt and Rubin, 2001). The differences in mechanical properties between cortical and cancellous bone are due to the different geometries, as the materials and composition are the same (Rho *et al.*, 1998).

Micro-Computed Tomography ( $\mu$ CT) is a technology that allows the non-destructive assessment and analysis of 3D trabecular bone structures (Nazarian *et al.*, 2008; Ritman, 2004). This is due to its high resolution, capable of acquiring images with a resolution of up to  $2\mu\text{m}$  on a cubic sample of 50 mm wide (www.skyscan.be). Details on 3D geometrical reconstructions (in form of STL triangular meshes) from  $\mu$ CT scan data can be found in Jaecques *et al.* (2004), Tellis *et al.* (2008) and Sisiyas *et al.* (2002).

According to Uchiyama *et al.* (1999), trabecular bone is formed by three major microstructures: (1) plates; (2) rods; and (3) a combination of these. These structures can be detected by using high-resolution 3D reconstruction from  $\mu$ CT scan data. An example of a trabecular plate-like structure is illustrated in Fig. 1.20.



**Fig. 1.20** 3D reconstruction of a trabecular plate-like structure (Uchiyama *et al.*, 1999).

Marks and Hermey (1996) used  $\mu$ CT scan data to evaluate the effects of osteoporosis in a clinical case. Osteoporosis is a condition of microarchitectural loss of bone tissue leading to

decreased density and bone fragility (Downey and Siegel, 2006). A 3D reconstruction of trabecular bone morphology before (top) and after (bottom) osteoporosis is shown in Fig. 1.21.

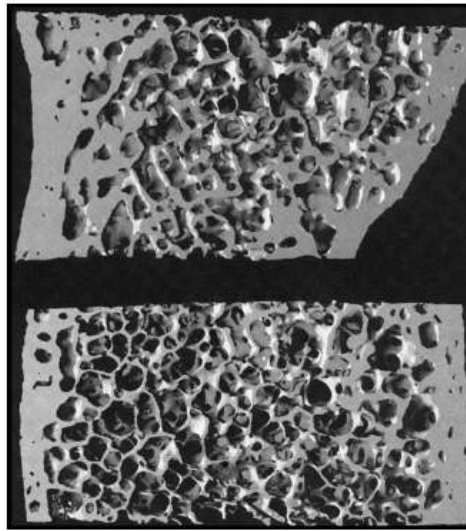


**Fig. 1.21** 3D reconstructions of trabecular bone morphology from  $\mu$ CT scan data (Marks and Hermey, 1996).

Parfitt *et al.* (1983) developed a method for examining the changes in trabecular bone structures due to osteoporosis, suggesting that in normal subjects the decreased density is caused by a reduction of the number of trabeculae, with no significant decrease in rod/plate thickness. Subjects with previous fractures also presented significant reduction in rod/plate thicknesses.

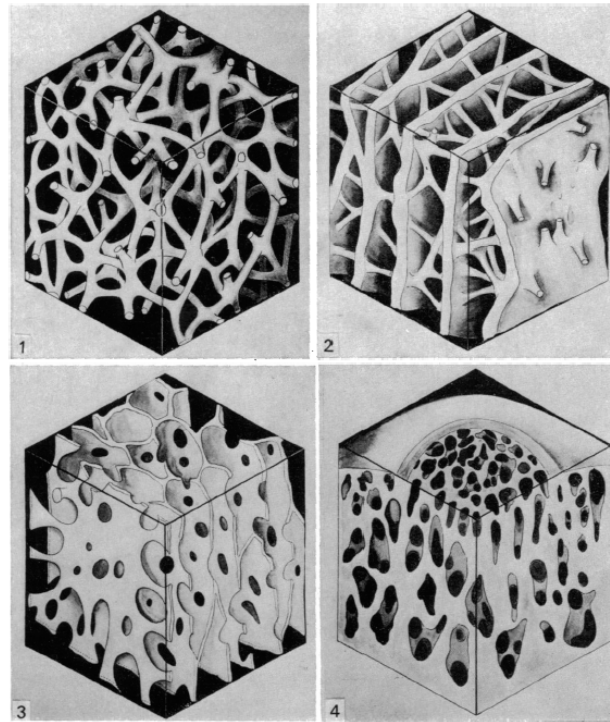
According to Wakamatsu and Sissons (1969) trabecular thicknesses are difficult to measure and define due to the irregular arrangement of the bony structures. Several techniques have been developed to define and measure the mean trabecular thickness (Wakamatsu and Sissons, 1969; Parfitt *et al.*, 1983; Garrahan *et al.*, 1987). However, all these models are based on traditional histomorphometry, which analyse 2D sections of tissue by using microscopes and often include assumptions on bone morphology that are difficult to verify. In addition, the large variation in trabecular architecture presents difficulties for such idealised models to produce data that are valid in general, and researchers should be very careful to verify the assumptions before interpreting results (Odgaard, 1997). The advent of computerised 3D descriptions of trabecular geometries allows the direct study of such

architectures, with no restrictive assumptions. In 3D representations any parameter pertaining to the architecture can be quantified, the real problem is defining what should be measured, as rigorous definitions are nontrivial for such irregular structures (Odgaard, 1997).

Singh (1978) proposed a classification of trabecular bone structures in three types:

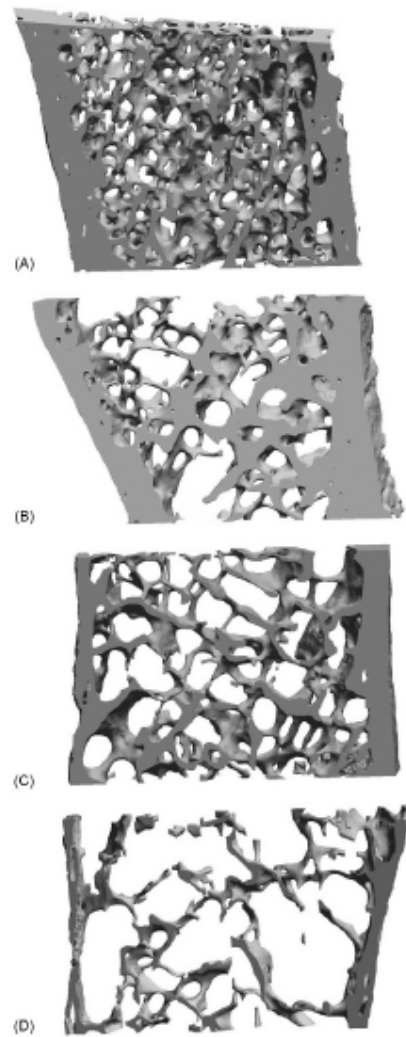
- Type I is made up of fine straight or curved rods 0.08-0.14 mm in diameter and about 1 mm in length. The rods interconnect with each other to form a three-dimensional network and do not appear to have any preferential orientation.
- Type II is made up of both rods and plates, and can be further divided into three categories:
  1. Subtype IIa is composed of a network of interconnected rods (similar to those of Type I) and plates. These plates are 0.1-0.2 mm thick and approximately 1 mm long and have variable shapes.
  2. Subtype IIb is similar to Subtype IIa, but the plates are much more extensive, up to several millimetres long. These plates show a well defined orientation and present numerous fenestrations.
  3. Subtype IIc consists mainly of parallel plates, which are typically 0.16-0.3 mm thick. These plates are separated from each other by intervals of 0.4-0.8 mm, and are cross linked by networks of rods of the Type I.
- Type III consists of plates of varying size and shape that intersect to form a network. The plates present numerous fenestrations that interconnect the spaces of the network. This type can be further divided into three categories:
  1. Subtype IIIa consists of networks of plates 0.1-0.2 mm thick and about 1 mm long. These plates may present a tendency to a particular orientation.
  2. Subtype IIIb is composed by parallel plates, with no rods connecting them. The plates present irregular shapes with numerous fenestrations and interconnect by forming large longitudinally orientated spaces between them. The plates are only 0.12-0.24 mm thick, while the tubular spaces can have a diameter of 0.7-2 mm.
  3. Subtype IIIc is composed by solid mass of bone fenestrated by numerous interconnecting spaces. The plates are 0.2-0.4 mm thick, while the spaces are typically 0.4-0.6 mm.

Fig. 1.22 shows an example of Type I, Type IIc, Type IIIb and Type IIIc structures.



**Fig. 1.22** Examples of trabecular bone structures. (1) Type I, (2) Type IIc, (3) Type IIIb and (4) Type IIIc (Singh, 1978).

Chappard *et al.* (2008) investigated the alterations of human trabecular micro-architecture during ageing, both in male and female subjects. In the young, the trabecular network is thick and dense, as shown in Fig. 1.23 A, but during ageing bone trabeculae becomes thinner, due to a progressive conversion of the plates into rods. In females, the alteration is characterised by an increased number of trabecular perforations and loss of connectivity, as shown in Fig. 1.23 B, which disorganise the 3D micro-architecture. In males, the alteration is characterised by a conversion of plates into rods, but the connectivity is preserved, even if the trabeculae are thinner, as shown if Fig. 1.23 C. However, the loss of connectivity can happen in those subjects with multiple risk factors (i.e. other diseases), as illustrated in Fig. 1.23 D.



**Fig. 1.23** Alterations of trabecular bone structures during ageing. (A) In the young, (B) alteration in females, (C) alteration in males, (D) alterations in males with other diseases (Chappard *et al.*, 2008).

Jinnai *et al.* (2002) proposed a method for measuring surface curvatures on trabecular bone samples, classified as “plate-like,” “rod-like,” and a mixture of the two, as often trabeculae present curved shapes. The effect of the curvature on mechanical properties of trabeculae has been investigated by Miller and Fuchs (2005).

Stauber and Müller (2006) proposed a methodology for the volumetric decomposition of trabecular bone samples into its basic elements (rods and plates). 3D volumetric representations of bone samples were generated from  $\mu$ CT scan data and processed by using



a decomposition algorithm. Fig. 1.24 shows the decomposition of a group of trabecular elements, while Fig. 1.25 illustrates the whole decomposition of a  $\mu$ CT cubic sample. This technique allows further investigations to assess and quantify individual rods and plates geometries, in terms of size and shape. It may also improve the understanding of the site-specific role of bone micro-architecture.

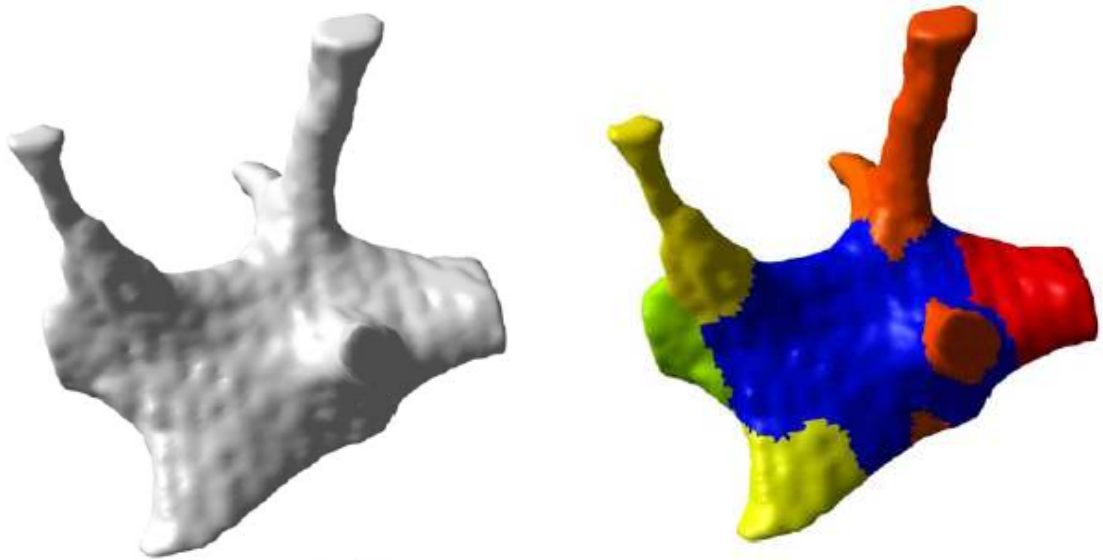


**Fig. 1.24** Example of volumetric decomposition of a group of trabeculae (left) into basic rods and plates elements (right) (Stauber and Müller, 2006).

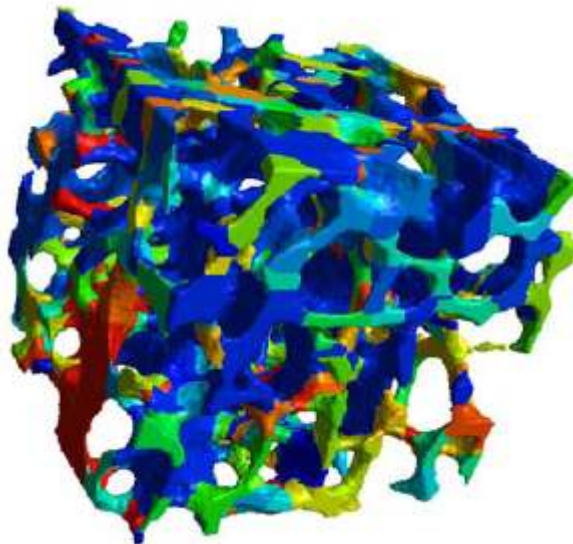


**Fig. 1.25** Example of volumetric decomposition of a whole  $\mu$ CT cubic sample into basic rods and plates elements (Stauber and Müller, 2006).

High resolution 3D reconstructions have been utilised to generate meshed models for Finite Element Analysis (FEA). Examples of this application can be found in Van Rietbergen *et al.* (1998), Van Cleynenbreugel (2006) and Ulrich *et al.* (1998). Ulrich's study aimed to generate and evaluate different types of meshes, as shown in Fig. 1.26.

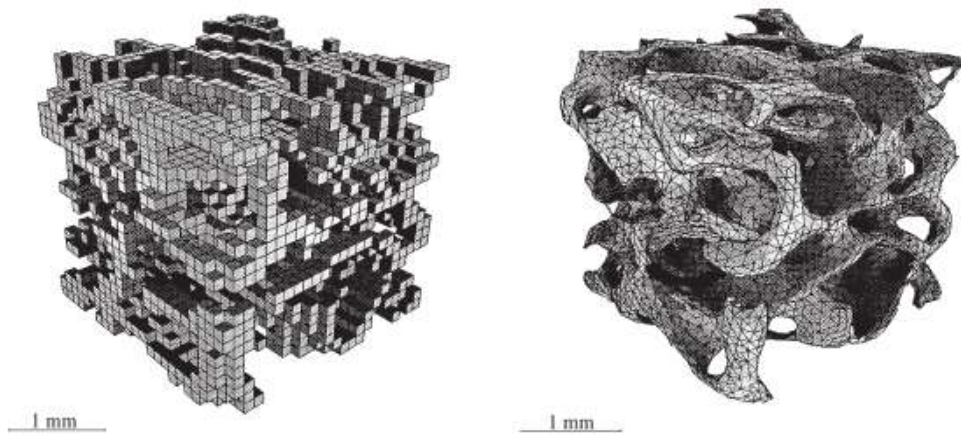


**Fig. 1.26** Examples of trabecular bone meshes for FEA. Left: brick elements mesh. Right: tetrahedron elements mesh (Ulrich *et al.*, 1998).

Das *et al.* (2002) used  $\mu$ CT-derived architectures of human trabecular bone for SLS fabrication. Due to the high resolution of the  $\mu$ CT data, the part was scaled-up four times for fabrication. Fig. 1.27 shows the 3D reconstruction of the  $\mu$ CT data (a), and a portion of the model fabricated by SLS (b).



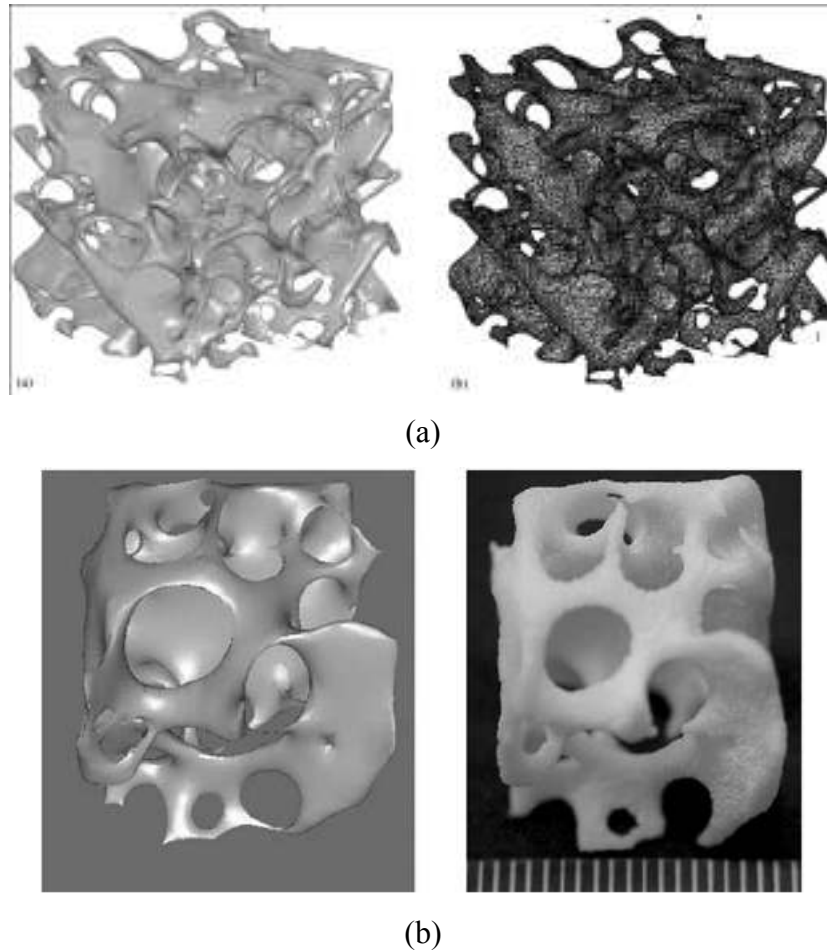


**Fig. 1.27** 3D reconstruction of human trabecular bone sample from  $\mu$ CT data (a). Detail of the 3D model and corresponding SLS replica scaled up four times (b) (Das *et al.*, 2002).

Dobson *et al.* (2006) investigated the manufacture of human trabecular bone structures using SLA, starting with Micro-Computed Tomography ( $\mu$ CT) data from trabecular bone samples taken from different sites. Fig. 1.28 depicts those SLA models. SLA models were also investigated by Bibb and Sias (2002).

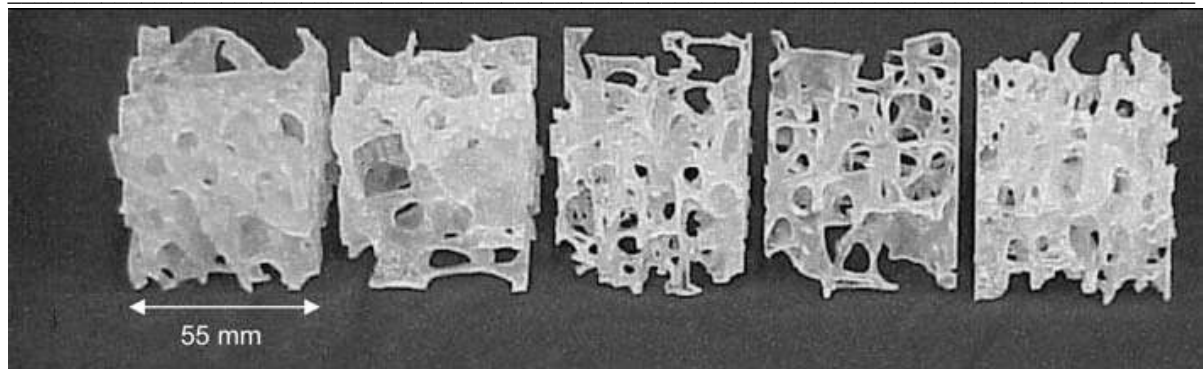


**Fig. 1.28** SLA models of human trabecular bone structures from  $\mu$ CT scan data  
(Dobson *et al.*, 2006).

### 1.5 TE Scaffolds and Computer Aided Design

The most widely investigated approach for CAD design of TE scaffolds consists of selecting a unit cell with a predefined internal geometry from a dedicated library of unit cells. Each cell possesses a particular internal structure, which defines its pore size, shape, interconnectivity, porosity and mechanical properties. These parameters can be modified by setting different values for the design variables, in order to match particular requirements. When the scaffold geometry needs to be adapted to an anatomical shape, the selected unit cell is repeated in 3D to form a prism with the same dimensions of the anatomical volume. The two geometries are subsequently merged to produce a scaffold with the external shape of the implantation site and a predefined internal structure. This approach, illustrated in Fig. 1.29, has been proposed by Starly *et al.* (2006) and several other authors.

Anatomical volumes are designed starting from CT or MRI scan data, by using specific software such as MIMICS (by Materialise Inc., Leuven, Belgium), which can reconstruct 3D geometries from 2D slices, and export them in different file formats, including STL, IGES (Initial Graphics Exchange Specification) and STEP (Standard for the Exchange of Product Data). Examples of 3D reconstructed geometries from CT scans can be found in Viceconti *et al.* (1999), Hutmacher *et al.* (2004), Sekou *et al.* (2004), Malleprey and Bergers (2009), Truscott *et al.* (2007) and Hieu *et al.* (2003). Other methods to reconstruct anatomical volumes in CAD can be found in Eggbeer *et al.* (2005), Eggbeer *et al.* (2006) and Bibb *et al.* (2006).

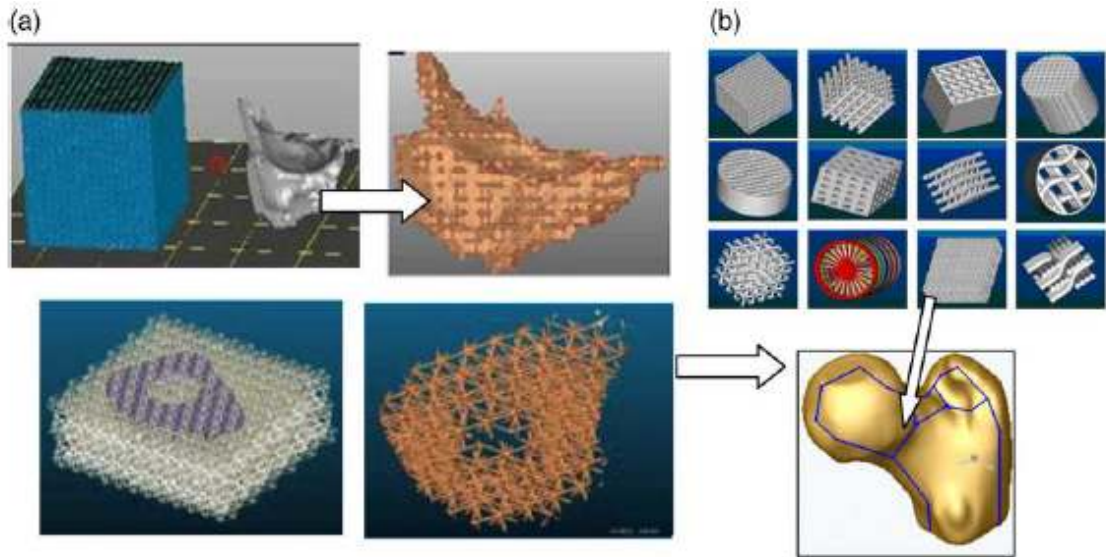


**Fig. 1.29** Example of femoral TE scaffold design (a), using a library of predefined unit cells (b) (Starly *et al.*, 2006).

Tan *et al.* (2005) used a polyhedral unit cell (i.e. bound by polygons) to design circular scaffolds of different sizes, which are then fabricated by SLS. The struts diameter was 600  $\mu\text{m}$ , with a length of 1.5 mm, while the scaffold diameter was 16 mm with a variable height between 1 mm and 2.5 mm. Fig. 1.30 illustrates the design process.

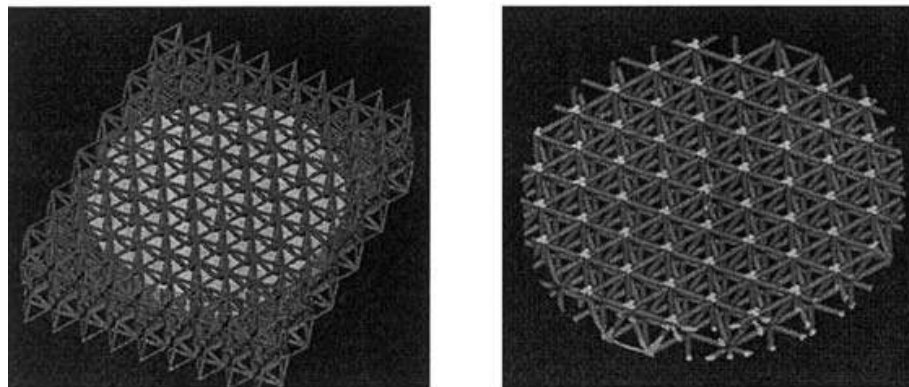


**Fig. 1.30** Example of a design of a circular scaffold by polyhedral unit cell (Tan *et al.* 2005).

Chua *et al.* (2003a) developed an algorithm to automatically assemble unit cells - or their combinations - to match anatomical shapes (using Boolean operations), while Chua *et al.* (2003b) also developed a library of polyhedral unit cells, some of which are depicted in Fig.

1.31. By changing the strut parameters, different combinations of pore size, porosity and mechanical properties could be achieved.

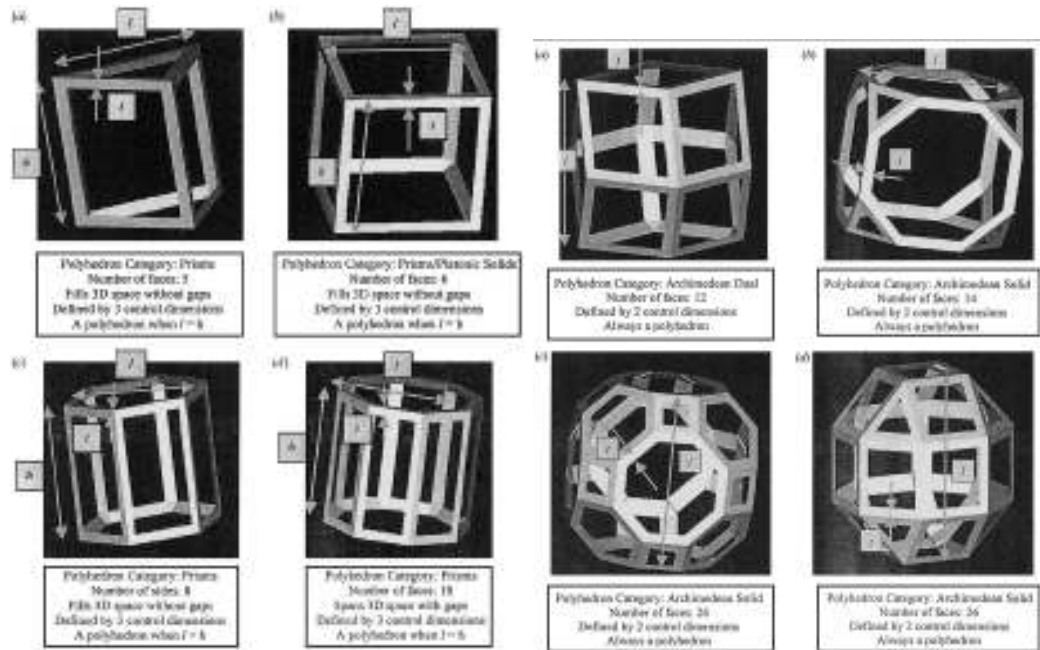


**Fig. 1.31** Examples of polyhedral unit cells (Chua *et al.*, 2003b).

The prismatic cells were defined by three parameters: the length of the prism  $l$ , the height  $h$  and the strut thickness  $t$ . All other unit cells were defined by only two variables - the perpendicular distance between two opposite parallel faces  $l$ , and the strut thickness  $t$ . The cross-section of the struts was defined by an isosceles triangle.

Williams *et al.* (2005) designed several radial and orthogonal porous architectures in cylindrical scaffolds (12.7 mm diameter, 25.4 mm height), each with a different pore diameter, ranging from 1.75 to 2.5 mm. An example is shown in Fig. 1.32.

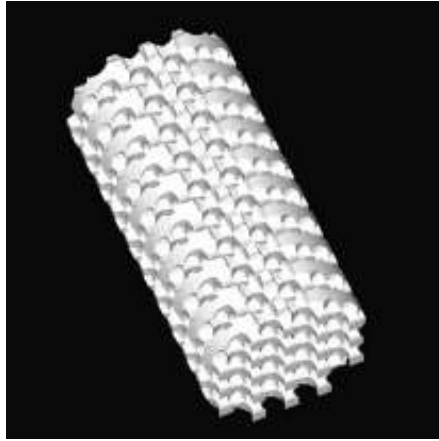


**Fig. 1.32** Example of a cylindrical scaffold with 1.75 mm orthogonal pores  
(Williams *et al.*, 2005).

Hollister *et al.* (2002) developed a technique to design scaffolds with predefined mechanical properties and porosity, by using a unit cell made from three orthogonal pores, each with a different diameter, as shown in Fig. 1.33. Hollister *et al.* (2005) developed a mini pig mandibular condyle (the part of the mandible that articulates with the skull) scaffold, by using a design approach based on the repetition of unit cells. The resultant scaffold is depicted in Fig. 1.34.

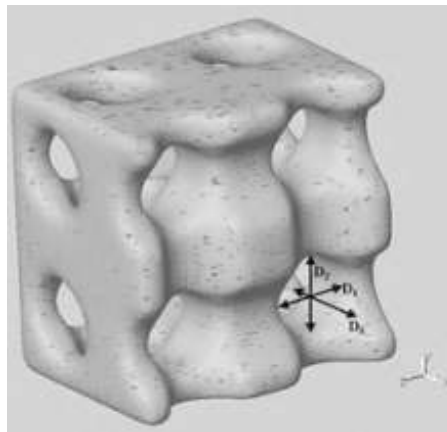


**Fig. 1.33** Unit cell made from three orthogonal cylinders of different diameter.  
(Hollister *et al.*, 2002)



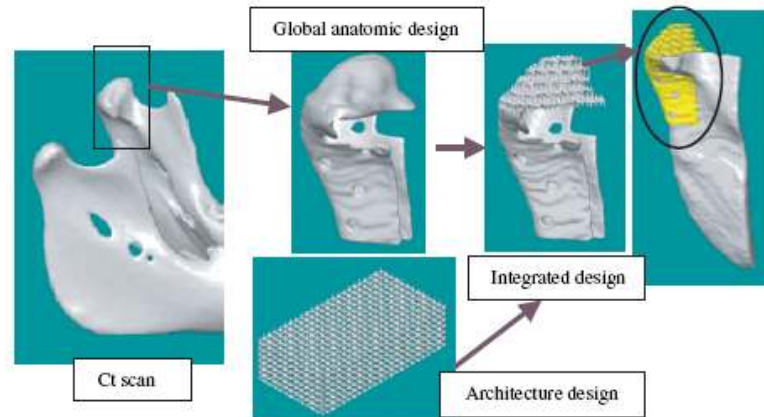


**Fig. 1.34** Design of a minipig mandibular scaffold (Hollister *et al.*, 2005).

Das *et al.* (2003) designed 8 mm cubic and 8 mm diameter cylindrical scaffolds, made from 800  $\mu\text{m}$  orthogonal channels and 1200  $\mu\text{m}$  pillars, as shown in Fig. 1.35. These scaffolds were fabricated by SLS for *in vivo* implantation and histology assessment.

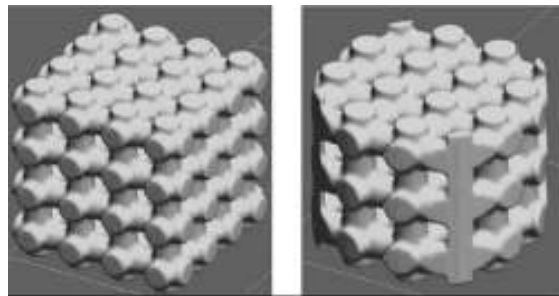


**Fig. 1.35** Example of cubic and cylindrical scaffolds with 800  $\mu\text{m}$  orthogonal channels and 1200  $\mu\text{m}$  pillars (Das *et al.*, 2003).

Woesz *et al.* (2005) developed a 10 mm (height and diameter) cylindrical scaffold with orthogonal interconnected channels and struts, both of 450  $\mu\text{m}$ . The CAD model is shown at Fig. 1.36.

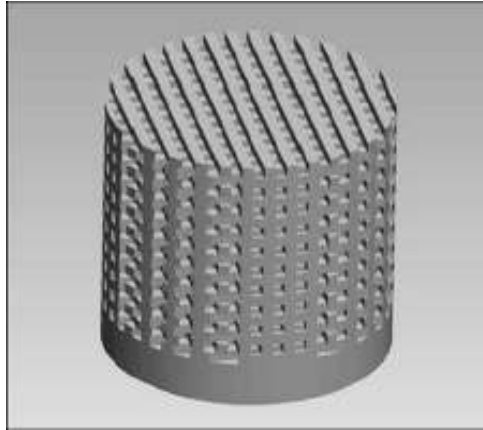


**Fig. 1.36** CAD model of a 10 mm cylindrical scaffold with strut and pore size of 450  $\mu\text{m}$  (Woesz *et al.*, 2005).

Xiang *et al.* (2005) fabricated a calcium phosphate scaffold through indirect AM using a SLA mould. The scaffold and the mould are depicted in Fig. 1.37 (a) and (b) respectively. The designed scaffold was an annular cylinder with a height of 22.6 mm, with an external diameter of 14.5 mm and an internal diameter of 4.5 mm. The cylinder had square channels of 300  $\mu\text{m}$  extending in the radial direction, circular channels of 500  $\mu\text{m}$  extending in the vertical direction and annular channels of 300  $\mu\text{m}$  in height and 500  $\mu\text{m}$  in width, which connected the square and the circular pores. The resultant porosity was 54.45%, with an average compressive yield strength of  $5.8 \pm 0.8$  MPa.

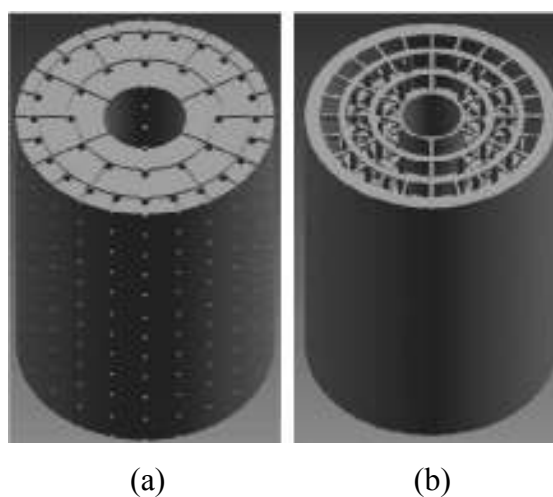


**Fig. 1.37** Example of annular scaffold with controlled architecture (a), and relative mould (b) (Xiang *et al.*, 2005).

Charriere *et al.* (2003) designed the negative macro porosity of a cylindrical scaffold, composed of orthogonal and circular struts of 1 mm diameter, as shown in Fig. 1.38. This geometry represents the theoretical shape of the regenerated tissue, assuming that it will fill all the pores in the scaffold, with voids remaining in the space formerly occupied by scaffold material (Hollister *et al.*, 2002).

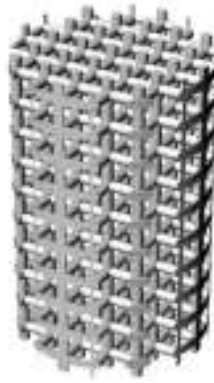


**Fig. 1.38** Negative macro porosity in a cylindrical scaffold made of interconnecting orthogonal struts (Charriere *et al.*, 2002).

Lal and Sun (2004) developed a technique to design scaffolds made of micro spheres. Three different packing models in a cylindrical area were illustrated - the minimum density, the maximum density and the statistical packing. A basic packed pattern was assumed, in which the spheres formed an equilateral triangle with a side equal to  $aR_s$ , where  $a$  was a spacing parameter dependant on the packing model, and  $R_s$  the radius of the micro sphere. It was also assumed that the basic pattern started at the centre of the cylindrical area, where the radius is  $R_c$ , as shown in Fig. 1.39.



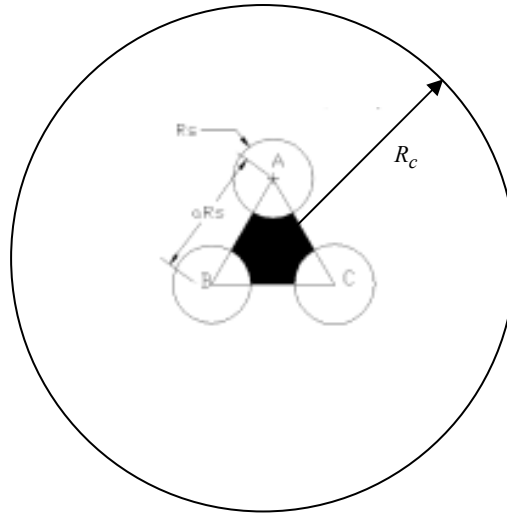


**Fig. 1.39** Assumed basic pattern for micro sphere packing models (Lal and Sun, 2003).

In the maximum density packing model (minimum porosity, unconnected pores),  $a=2$ , while in the minimum density packing model (maximum porosity)  $a=3$ . Since trabecular bone structure is a combination of both open (connected pores) and closed (unconnected pores) porosity, a statistical packing model was proposed as a combination of the previous two. According to this model,  $a=2.36$  for values of  $R_c = 2500\mu m$  and  $R_s = 300\mu m$ .

Zhongzhong *et al.* (2004) proposed a design technique for bone TE scaffolds. This consisted of the generation of a microtubule structure (spatial distributions of segments) using reverse engineering software that was able to generate data from histological analysis (tissue microstructure) and micrographs (photographs taken through microscopes). The CAD model of the proposed scaffold is shown in Fig. 1.40.

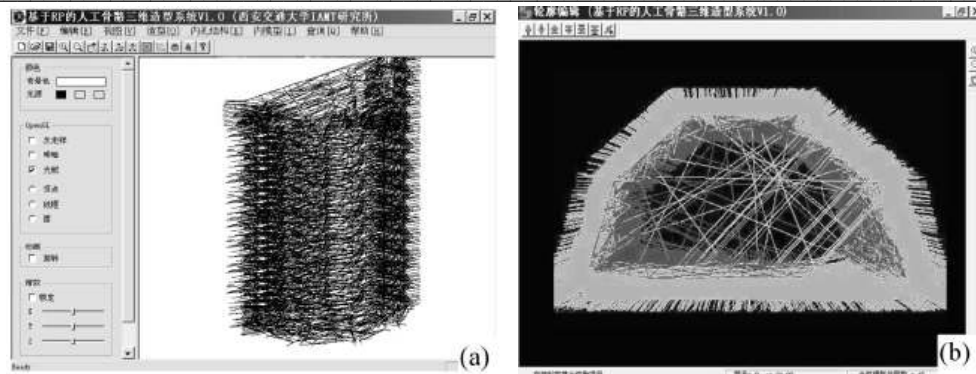


**Fig. 1.40** Example of bone TE scaffold made from a microtubule structure: (a) perspective view, (b) frontal view (Zhongzhong *et al.*, 2004).

## 1.6 Hypothesis

Several parties are investigating the use of AM to produce articles with complex internal geometrical structure. These works are demonstrating great potential to realise newfound functionality along with rapid one-off manufacture. However, the currently available techniques for the necessary design of such geometries using CAD, would require hundreds of hours of manual design for each individual product or in the case of current automated techniques, cannot reproduce the necessary complexity.

These restrictions of the pre-requisite CAD ultimately negate the viability of these applications.

Initial quantified data concerning the ideal bone TE scaffold geometry has been produced by several parties, although this work is ongoing and should be considered indefinite at this time. There is a consensus that ideal geometry is evident in biological trabecular structures. In their most basic topological form, these structures consist of the non-linear distribution of irregular interconnecting rods and plates of different size. The size of those rods and plates ranges between approximately 50 and 300  $\mu\text{m}$  (Rho *et al.*, 1998).

*Therefore, the hypothesis of this work is to investigate an automated design methodology that allows complete variability within the specified size limits, through the formulation of novel algorithms and sub-programmes to produce bio-mimetic trabecular geometrical structures in CAD in accordance with given input parameters derived from existing data on TE requirements and biological trabecular structures.*

### 1.7 Research Novelty

Several shortcomings regarding the design of bone TE scaffolds by CAD can be identified from this literature review. As explained in section 1.5, the most investigated approach consists of using repeated unit cells that are eventually combined with anatomical implants designed from CT or MRI data. A unit cell of appropriate pore size, porosity and mechanical properties is selected from a library of pre-designed elements.

A drawback of this approach is due to the limited gradients of porosity, pore size and achievable interconnectivity, because only one unit cell, with a pre-defined geometry, is used to form the internal structure of the scaffold. Furthermore, the unit cells are regular and made of basic geometrical elements, with no variation of shape or size.

The simplicity and regularity of these geometries are fundamentally unable to mimic human trabecular structures, which are highly complex and irregular. The CAD modelling of highly complex and irregular geometries would be extremely time-consuming when performed manually.

Another shortcoming regards the amount of data that are currently available on the optimum geometry for bone TE scaffolds, as there is a considerable lack of knowledge about the quantification of their geometrical requirements (Tomlins *et al.*, 2006; Willows *et al.*, 2006). While natural tissue morphologies have been identified as representing ideal target geometry, more data on their full geometrical definition is required.

The purpose of this work is to develop viable solutions to overcome these major shortcomings. The novel aspects of the research are listed below:

- Automation in the CAD process, so as to allow the generation of complex and irregular anatomical scaffolds with controlled architecture within minutes, instead of the days or even weeks that would be required by manual design.
- The introduction of a new analysis technique for complex and irregular structures, such as those found in biological trabecular bone structure, in order to better understand and characterise their morphology and to produce new quantitative data on their geometries.
- The realisation of a novel design technique that utilises the newly produced quantitative data in combination with currently known TE design requirements, in order to design bio-mimetic structures.

- 
- Adaptability of the design methodology to readily incorporate future design requirements as these emerge.

The challenge and boundaries of this research is focussed on the computerised design derived from bio-mimetic and informed design cues.

Elements out of scope include:

- Manufacturing considerations
- Mechanical evaluation
- Biological analysis

## **CHAPTER 2**

### **- METHODOLOGY-**

#### **2.1 Need for an Automated, Efficient and Flexible Design Method**

The automated CAD of complex, irregular geometrical structures with given input parameters through formulation algorithms involves several requirements.

A CAD program must be able to model complex and parametric 2D and 3D curves and surfaces, together with the possibility of accessing the same commands by external, independent sub-programmes. Two approaches to automation are used in this research: 1) an emulation of manual design that utilises the native modelling capabilities of CAD software, and 2) new modelling capabilities developed and added to existing CAD applications. Chapters 3 and 4 propose automated design methodologies based on the first approach, while chapters 5 and 6 are based on the second approach.

The main advantage of automation is the possibility of performing those operations that an operator would normally do manually in many hours or weeks, within minutes. In addition, since the greater the geometrical complexity, the greater the time saved, automation is particularly useful when complex and irregular geometries are required.

Complex structures in CAD are usually constructed by hundreds or thousands of geometrical elements, each with different sets of input parameters that consequently produce different shapes. Ideally, once the inputs (type of geometrical elements, boundary volume and values/ranges for the variables) are specified, the design process should enable the construction of the selected elements within the boundary volume. Each element should be repeated a number of times, each time in a different location and with different values for the parameters. In this research the entire process should be carried out efficiently in order to minimise the computational time, the memory requirements and the file size. Ideally, the algorithms controlling the automated design should be flexible to allow for easy modification or adaptation should new quantitative requirements emerge.

Since a large variety of geometrical elements can be inserted into a specified volume, the user should be able to select those that are suitable for each particular case. For this purpose, a library of geometries can be developed, each defined by its constituent parameters. The user should also be able to specify either a value for each parameter, or a range of variability. In the latter case, a function to define the manner in which the input parameter changes should also be specified. This can be performed by introducing either a mathematical function or a random variation.

## 2.2 Aim

The purpose of this chapter is to establish an appropriate methodology in order to pursue an automated, efficient and flexible design methodology that uses commercially available CAD software and computerised facilities. Conventional apparatus has been used in this work to avoid the need for high performance computers and software, which would ultimately restrict the applicability, flexibility and further developments of the methodology

The computer adopted to develop and test the proposed methodology consisted of a standard Intel® Pentium® M (Intel Inc., USA) processor 1.60 GHz, with 752 MB of RAM and an Intel® Extreme® graphic card, with 64 MB of dedicated memory. The operating system was Windows XP® Professional Service Pack 2 (Microsoft Inc., USA), and the CAD software was selected from those commercially available, based on specific requirements. The justification of CAD programme selection is provided in section 2.5.

The methodology explained in this chapter aims to automatically design combinations of a particular 3D geometrical element into a given volume, and control the relative parameters. The volume can be regular or irregular (anatomical), and generally it will be represented by a solid geometry or a group of closed surfaces (i.e. surrounding a volume), as shown in Fig. 2.1 (a) and (b) respectively. Therefore, meshed models (such as STL) need to be converted into closed surfaces or solids in order to be utilised by this methodology.

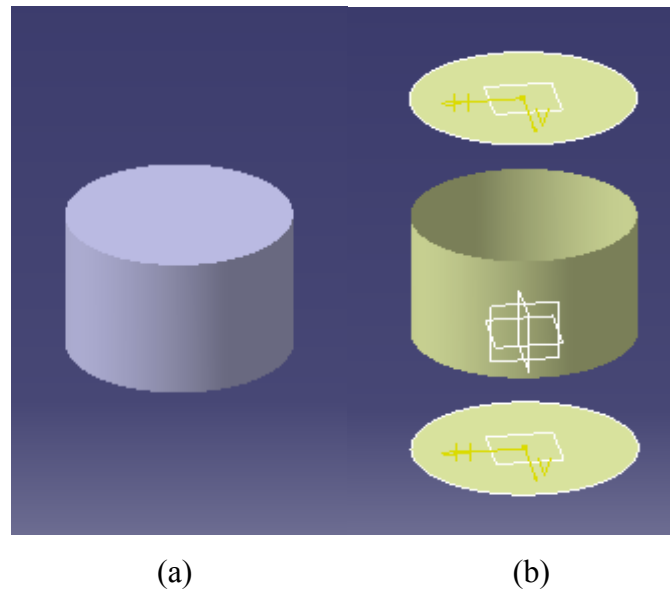


**Fig. 2.1** Example of solid volume (a) and boundary surfaces enclosing it (b).

### 2.3 Overview of the Methodology

The definition of the methodology encompasses four elements:

- Selection of tissue
- Definition of the 3D geometrical element
- Efficiency of the methodology
- Flexibility of the methodology

The following sections describe each element in more detail.

#### 2.3.1 Selection of Tissue

The kind of tissue to be modelled defines the geometrical requirements of the relative scaffolds. This work focuses on bone TE scaffolds, and according to the literature review carried out in sections 1.3 and 1.3.3, the geometrical requirements can be summarised as followed:

- Pore size range: 200  $\mu\text{m}$  to 800  $\mu\text{m}$
- Porosity: 50% to 90%

Other geometrical requirements concern the shape of the tissue. According to the trabecular bone classification proposed by Singh (1978) and shown in section 1.4, this work focuses on Type I and Type IIa of bone, although the other types could also be represented. The reasons

for this choice are that these types of bones are widespread and most TE scaffold research efforts are oriented toward representations of rod networks. Since rod networks may intersect in ways to form small plates, Type IIa of trabecular bone has also been included.

The rod networks proposed in this work present variability in size, shape, orientation and curvature. The geometrical details are explained in the next section.

### **2.3.2 Definition of the 3D Geometrical Element**

In this work, the attention focused on one particular type of geometrical element to be designed into the given volume. This is not a limitation of the design technique, the same approach could have to be used for any other three-dimensional element.

The selected geometrical element is a multi-sections solid, defined by a number of cross-sections and by a 3D curve representing its curvature. This element was chosen because it offers a good representation of a curved rod with an irregular size and shape, such as that featured in trabecular architectures. The resulting geometries will therefore be composed of a network of irregular and interconnected rods, designed into a given volume.

Either one or two cross-sections were used at this stage - although any other number could have been chosen - and they were drawn into planes that were tangential to the boundary surfaces of the volume at specified points. The path of each rod was defined either by a line segment or a 3D curve. An example of a curved multi-section solid made from two sections is found in Fig. 2.2. This figure also shows the terminology used in the work to refer to the different parts of the multi-section solid in different contexts (i.e. solid or void).

More details on the geometrical parameters defining this feature are explained in section 2.4.

A multi-section solid can also be represented in reverse, thus forming a channel (void) inside the reference volume. Negatives correspond to the scaffold structure. Positive representations are used throughout this work for the theoretical shape of the regenerated tissue, assuming that the channels of a resultant scaffold act as an ingrowth template for the regeneration of new tissue, while the rest of the scaffold progressively degrades.

Throughout this work, the methodology was used first to produce the rod structures, which were subsequently converted into the corresponding channels. The reason for that was because rod structures provided a better visualisation of the internal networks. If the methodology were fully developed, it would be used to generate channels directly and would therefore be even more efficient.



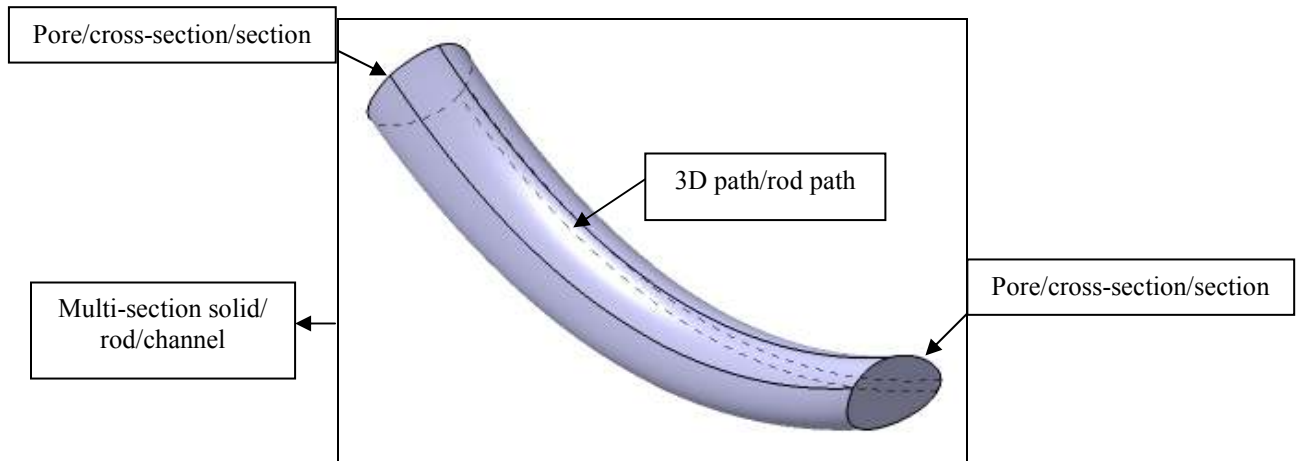


**Fig. 2.2** Example of a multi-section solid representing an irregular rod, and terminology adopted throughout this work.

### 2.3.3 Efficiency of the Methodology

A quantification of the efficiency of the proposed methodology was performed by measuring design time. For automated design the computational time is measured in the design routines, and then compared with the estimated time required by manual design. The fastest manual design into regular (cubic) volumes for comparative purposes, using the above equipment, has been approximated as follows:

- 30 seconds for a one-section linear rod
- 45 seconds for a two-section linear rod
- 1 minute for a one-section curved rod
- 1 minute and 15 seconds for a two-section curved rod

These estimated figures for manual design were assumed by considering the following design steps for the creation of each CAD multi-section solid:

1. Computation and creation of the central points: 5 s/cross-section
2. Plane selection and design of the four control points curve: 5 s/cross-section.
3. Setting random values for the four tangents: 5 s/cross-section.
4. Design of a linear 3D path and random selection of the 1<sup>st</sup> and 3<sup>rd</sup> points: 10 s
5. Design of a linear multi-section solid/ channel: 5 s

6. Computation and design of 3D curved paths, including random selection of the 1<sup>st</sup> and 3<sup>rd</sup> points: 35 s
7. Design of a curved multi-section solid/ channel: 10 s

The fastest manual design into irregular (anatomical) volumes largely depends on the complexity of the volume and would be substantially higher than the previous figures. In such cases, the operator would need to design points on different surfaces and the relative tangential planes before drawing the sections.

Curved rods might not be geometrically feasible for some combinations of the constituent parameters, particularly for anatomical volumes. That situation is commonly encountered with the random generation of parameters. Although automated design algorithms may be instructed on how to deal with such cases (by generating a large number of other random combinations) in a few seconds, the manual design would take much longer because the random values would have to be selected by the operator. This also assumes that any combination found by the operator will be acceptable. In addition, the estimated time for manual design assumes that a human operator is capable of performing an uninterrupted design over many consecutive hours, which is another unrealistic scenario.

As described in section 1.5, Boolean operations have been proposed by several researchers as the way to subtract a designed scaffold architecture from a designed anatomical volume. This subtraction process can often generate non-manifold topologies, particularly when the two geometries are complex. Non-manifold geometries generate run-time errors in CAD applications, and the user must modify (manually) the two geometries in order to produce a valid volume. Such operation can be extremely time consuming, also because the design of the two geometries must be completed before using the Boolean subtraction.

The proposed methodology overcomes this problem by performing the design of the internal architecture directly into the final volume (either cubic or anatomical), thus avoiding the use of Boolean operations. In addition, the design is performed progressively and evaluated at each step (i.e. after the design of each rod/channel), so that run time errors are managed by specific routines, which automatically modify the geometry of the freshly introduced rod/channel. An example of such routines is explained in section 3.3.5.

Performing the design of the internal architecture directly into anatomical volumes also has another advantage. The use of Boolean subtraction between two volumes can lead to poor control over the final geometry, as shown in Fig. 2.3. In this figure, the two highlighted

cross-sections represent the one designed in the reference volume (with controlled parameters), and the actual section after the subtraction operation. The loss of control on the actual section will result in uncontrolled pore size and shape in the scaffold geometry.

Computational time is further reduced by avoiding all those operations related to manual design such as feature selection, input windows, rotation, zoom, etc, which become unnecessary when automation is introduced.

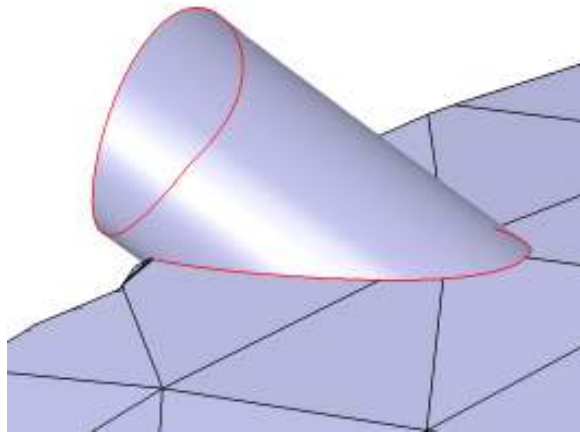


**Fig. 2.3** Example of loss of control over the actual geometry due to Boolean operations.

#### 2.3.4 Flexibility of the Methodology

A flexible methodology has been pursued to allow easy future modification or adaptation when new geometrical requirements emerge. The methodology explained in this chapter achieves that goal by using parametric geometrical elements, which allow the modification of all constituent parameters related to features. Newly emerged optimum values for pore size range, pore shape, orientation and curvature can be introduced in this methodology by modifying the relative parameters. In addition, new shapes can be parametrically defined and introduced, in order to model other types of trabecular bone, not considered in this work. These include Type IIb, Type IIc, Type IIIa, Type IIIb and Type IIIc trabecular structures (as defined in section 1.4), as well as newfound types.

## 2.4 Design Variables

Since this methodology aims to design complex trabecular structures, parameters such as pore size, shape, interconnectivity and porosity play a significant role in defining geometry. The approach described in this chapter allows the direct control of pore size, shape, number and orientation, while pore interconnectivity and porosity are considered as output variables of the design process. The design variables can be classified into four different groups:

- Geometrical variables, necessary for describing a particular 2D or 3D feature. This category includes the variables that define pore size, location and shape, as well as rod paths.
- Coupling variables, which are used internally by the algorithm to couple two cross-sections, located on different surfaces.
- Volumetric variables, which are used to describe the volume.
- Output variables, which are used to assess both the methodology and the resultant geometry.

The following sections describe each variable in detail.

### 2.4.1 Pore size

The size and shape of pores are controlled by planar curves that are defined by a number of control points. When the first and the last of those points coincide, the curve becomes closed. In this work, 5 control points are used to define a pore section, although any other number could have been used, with the first and the fifth vertex coincident. In addition, each control point is positioned as a vertex of an ideal square and, in the first approximation, all pore sizes are an estimation based on the size of that square. Naturally, the value of the actual pore size will be slightly greater, and can be computed more precisely by knowing the mathematical formulation used in the CAD. However, in this work, the pore size will be estimated, given that a more precise computation does not affect the design methodology. Fig. 2.4 shows an example of a planar, five control point curve, together with an explanation of the algorithm used to draw it. The approximated pore area is defined by the highlighted square, and the actual area is enclosed by the curve.

It is of course possible to define any other design layout - by using a different number of control points whose co-ordinates do not necessarily form the vertexes of a square, for example - without affecting the methodology.

For the algorithms, because of the square layout adopted for the control points, only one variable is required to define the pore size, and the range of variability has to be specified by the user.

#### DESIGN OF A PLANAR 5 CONTROL POINTS CURVE:

- Definition of pore size range (example 0.2 to 0.8 mm)
- Generation of a random number within this range (0.3 mm in this example)
- Design of 5 control points (1st and 5th coincident and equal tangent) positioned as vertices of an ideal square
- To obtain different shapes, the tangents are modified

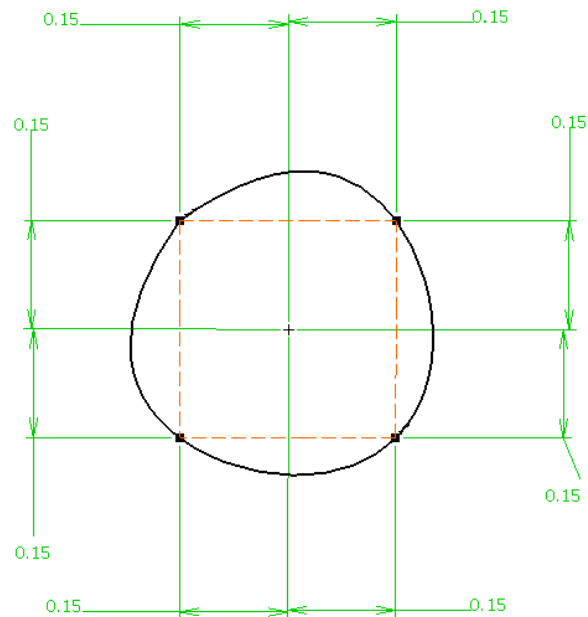


**Fig. 2.4** Steps to generate different pore sizes and shapes.

#### 2.4.2 Pore shape

The shape of each pore is controlled by the values of the tangents at the five control points. These values constitute four independent input variables, because the tangents at the first and fifth control points are set to have the same value so as to avoid cusps.

Since the curves are planar, the unit vector defining each tangent has 2 components, with values ranging from 0 to 1. Only one component has to be set for a planar unit vector. The range of variability for these variables is therefore defined by geometrical considerations, and does not have to be specified by the user.

The highlighted vectors in Fig. 2.5 illustrate the tangents at the five control points.

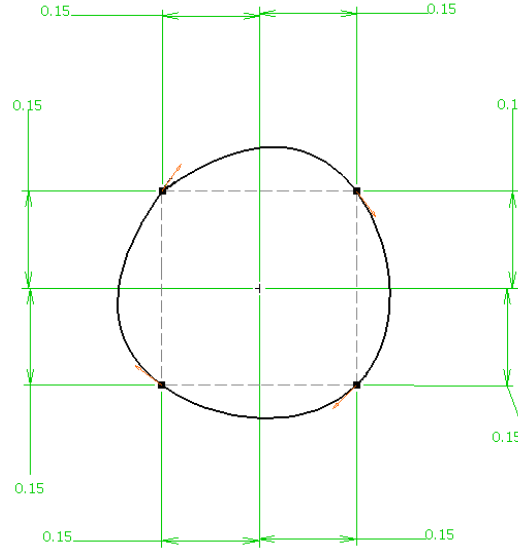


**Fig. 2.5** The highlighted vectors represent the tangents at the five control points, defining the shape of the pore.

### 2.4.3 Pore location

In this work, two types of volumes have been considered: cubic and anatomical. Cubic volumes have been used to test the design algorithms, while anatomical volumes represent an application of the methodology. The pore location has been defined in two different ways, depending of the type of volume used.

For cubic volumes, pore location is defined by the absolute co-ordinates of the centre of the enclosed square on the main planes. These co-ordinates have been expressed as follows:

$$\begin{cases}
 X_i = a_x + \frac{l-2a_x}{n_x-1}(i-1) & i = 1, \dots, n_x \\
 Y_j = a_y + \frac{w-2a_y}{n_y-1}(j-1) & j = 1, \dots, n_y \\
 Z_k = a_z + \frac{h-2a_z}{n_z-1}(k-1) & k = 1, \dots, n_z
 \end{cases}
 \quad (2.1)$$

$$\begin{cases}
 X_i = a_x + \frac{l-2a_x}{n_x-1}(i-1) & i = 1, \dots, n_x \\
 Z_k = a_z + \frac{h-2a_z}{n_z-1}(k-1) & k = 1, \dots, n_z
 \end{cases}$$

where:

$a_x$  = minimum distance from the  $X$  border.

$a_y$  = minimum distance from the  $Y$  border.

$a_z$  = minimum distance from the  $Z$  border.

$n_x$  = number of rods along  $X$ .

$n_y$  = number of rods along  $Y$ .

$n_z$  = number of rods along  $Z$ .

$l$  = length of the prism.

$w$  = width of the prism.

$h$  = height of the prism .

Naturally,  $l=w=h$  in cubic volumes. Fig. 2.6 illustrates some variables used for pore location in prismatic or cubic volumes, along with the absolute axis system.

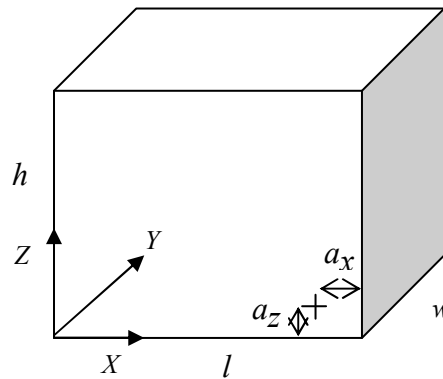


**Fig. 2.6** Definition of pore location in either prismatic or cubic volumes.

As a result, the pore location in cubic volumes is defined by the 6 variables  $a_x, a_y, a_z, n_x, n_y, n_z$ . The variables  $l, w, h$  are classified as volumetric variables.

This allocation model produces regular distributions of pores into the faces of the cube. Other non-linear models would have produced irregular pore distributions, which generate more intricate and complex geometries, but in the initial experiments, attention was focused on regular distributions to pursue the development of the automated design algorithms. This

limitation applies only to cubic volumes, because the pore allocation model adopted for anatomical implants produces irregular pore distributions.

For anatomical volumes, the pore location is still defined by the centre of the enclosed square, but because of the irregular surfaces, the co-ordinates of this point are computed differently. The input variables consist of three co-ordinates of a reference point on the surface (defining the 'zero' of the curvilinear co-ordinate), three co-ordinates of a vector specifying a curved co-ordinate line, and a value that expresses the curvilinear co-ordinate. The total number of variables in such cases is therefore seven. In Fig. 2.7, the reference point on the surface is 'P' and the direction specified by the vector, 'D'. The projection of this direction onto the surface forms a 3D curved co-ordinate line 'C'. The curvilinear co-ordinate is measured on this curve, starting from the reference point. It should be noted that the system of co-ordinates used to specify the direction 'D' is the same as the absolute system used for the volume, except that the origin has been translated into point 'P'.

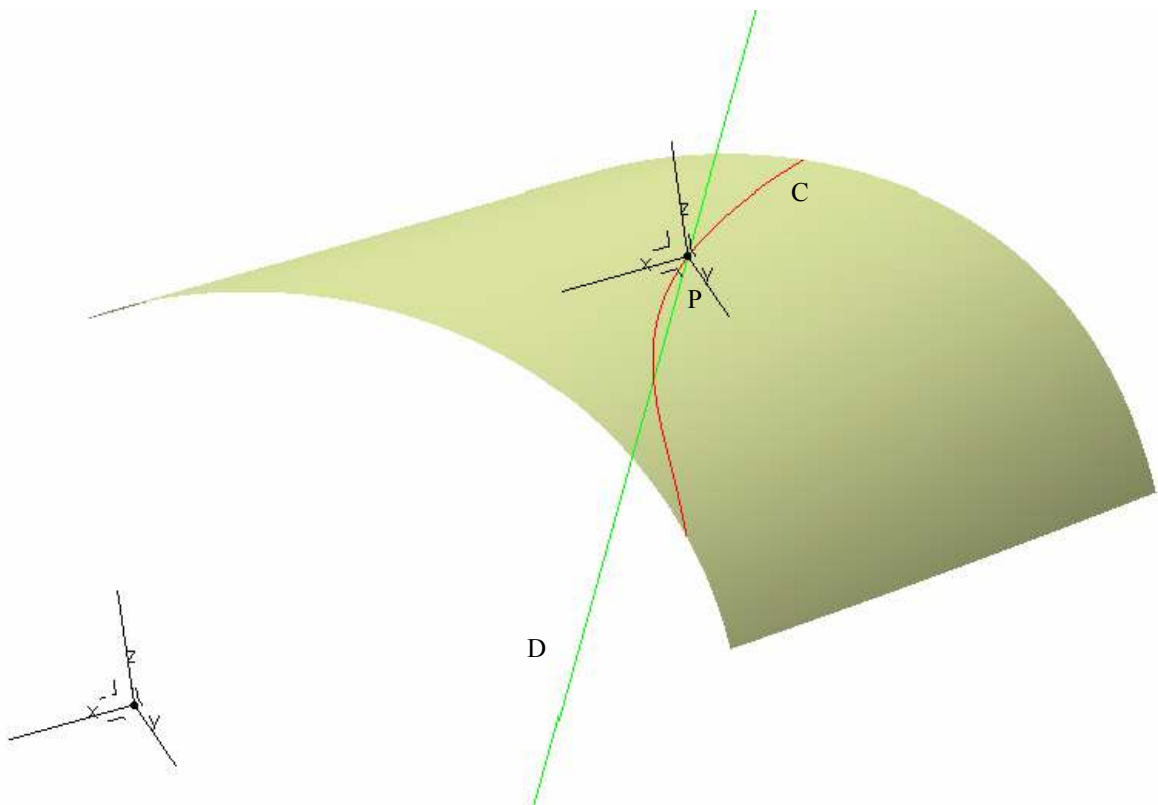


**Fig. 2.7** Definition of pore location on a generic surface.



#### 2.4.4 Rod paths

The path followed by a multi-section solid can be either linear or curved. If it is linear, a straight line connecting the central points of two cross-sections is traced, even when the rod is made from only one cross-section. In such cases, the central points on the other surface are still drawn. As a result, no additional variables to define linear paths are required. Similarly, when the linear path is orthogonal to the cross-sections, the result is automatically defined.

Curved paths are defined by using a 3D open curve composed of three control points, the first and the third of which are coincident with the first control points of the two cross-sections. To find the definition of the second control point, two approaches were followed. In the first approach, the point is made coincident with the geometrical centre of the volume, as is common for all the rods. In this case, the variables were the three co-ordinates of the geometrical centre of the volume.

In the second approach, the second control point can be any point within the volume and is therefore still defined by three variables. The user can specify a range for each co-ordinate, restricting the volumetric domain.

An alternative definition of curved paths that has been used in this work (on anatomical volumes) uses a 3D two control points curve, with controlled tension in two tangential directions. In this case, the number of variables is eight, since each vector has three components, and each tension requires one variable.

An example of a linear path is given in Fig. 2.8 (a), while (b) and (c) show curved paths through the centre and a random point respectively.

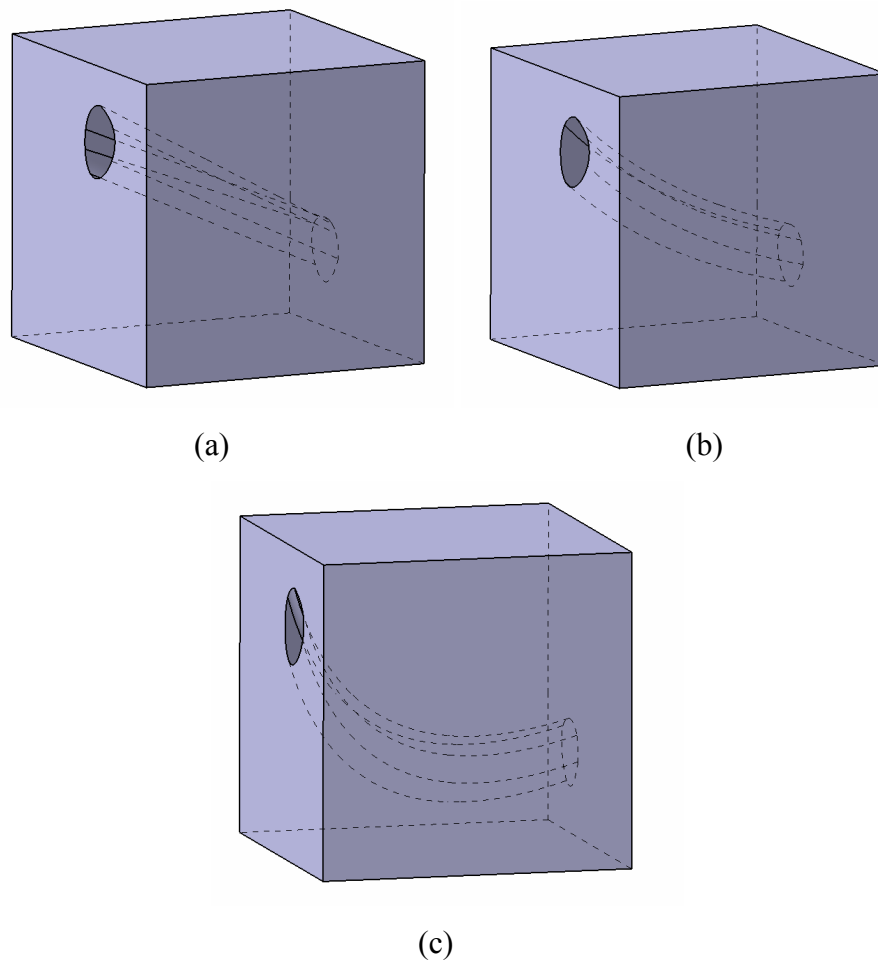


**Fig. 2.8** Examples of linear path (a), curved path through the centre (b) and curved path through a random point (c).

#### 2.4.5 Coupling variables

These variables combine the surfaces or the faces of a solid to be connected by a rod, as well as the cross-sections. For this purpose, each surface and cross-section has been identified by a variable. The total number of variables is therefore equal to the number of surfaces plus the number of cross-sections, for both cubic and anatomical volumes.

Since there are many ways of coupling surfaces and cross-sections, each volume has to be considered individually.

Due to pore interconnectivity, all surfaces - even those not directly connected - should result as interconnected by the end of the design process.

### 2.4.6 Volumetric Variables

For anatomical volumes, the variables refer to the orientation of the surfaces surrounding the volume. The orientation defines the inner side of the volume, and two values are possible -1 for clockwise and 1 for anticlockwise. Since each surface possesses an orientation, the number of variables required is equal to the number of surfaces. Values are specific to the anatomical implant used, and therefore they have to be set only once for a given volume.

On prismatic (or cubic) volumes, these variables are represented by the lengths  $l$ ,  $w$ ,  $h$  as seen on Fig. 2.6.

### 2.4.7 Output Variables

These variables are used to assess both the designed geometry and the efficiency of the methodology. Porosity is the variable used to evaluate the scaffold structure, while computational time and CAD/STL file sizes are indexes of efficiency. The total number of variables is therefore three.

For scaffold geometries, porosity is defined as:

$$P(\%) = \frac{V_{voids}}{V_{implant}} 100 \quad (2.2)$$

Where:

$P(\%)$  is the porosity in percentage

$V_{voids}$  is the volume of voids (equal to the volume of the complementary rods,  $V_{rods}$ )

$V_{implant}$  is the volume of the implant (without any internal void)

The volumes are measured in the CAD application used for the design.

The file sizes are obtained from the operative system, while the computational time is automatically measured by introducing a specific function (such as the 'Time' function in Visual Basic, which returns the system time when it is called) in the design algorithms. This function stores the instants at which the design starts and finishes.

### 2.4.8 Concept of random variation

All the parameters explained so far can be set as either constant or variable during run time. Variability implies the definition of a range of acceptable values, as well as a model of variation. Such parameters can be changed either randomly or according to a mathematical

expression. In order to generate random values, specific functions exist in programming languages. For example, Visual Basic (VB, by Microsoft Inc., USA) possesses a function called 'Rnd' that generates random real numbers between 0 and 1.

These numbers are not truly random, but pseudo-random, since the function accesses a very long list of values and returns them in the same order, but it does not always start at the same place in the list. In fact, the function 'Randomize' redefines a new starting point in the sequence, and thus the 'Rnd' function appears to produce different values at every call. If the 'Randomize' function is not used before 'Rnd', the same sequence is always generated.

To produce random integers within a specified range, the following expression has been used:

$$\text{Int}((A - B + 1) \text{Rnd} + B) \quad (2.3)$$

$A$  and  $B$  are the maximum and minimum values on the range, and 'Int' is a function that returns the integer portion of a real number.

To generate random real numbers smaller than  $A$  but greater than  $B$ , another formula has been used:

$$(A - B) \text{Rnd} + B \quad (2.4)$$

## 2.5 CAD Requirements

The following CAD modelling capabilities are required by this methodology:

- A command to generate a point on a surface. The positioning of a point on a surface can be set in different ways, although the proposed method is particularly useful for generating point clouds on anatomical volumes. This point defines the centre of the square enclosed by the pore.
- A command to design a plane that is tangential to a surface on a specified point. The plane defines the location where the cross-section is drawn.
- A command to design a planar 5 control point closed curve on a specified plane, representing the pore size and shape. Control points are defined by their co-ordinates (which can be computed by knowing the size of the square and the position of the centre), and tangents by one component of the unit vector, at each control point.

- A command to design either a non-planar three control point curve, or a non-planar two control point curve with controlled tension in two tangential directions, or a line that defines the path of a rod.
- A command to design a multi-section solid/channel by specifying one or more sections and a 3D curve. Channel representations are necessary for scaffold structures.

The methodology explained in this chapter requires these capabilities to be accessible by sub-programmes, in order to automate the design process. Other capabilities may also be accessible in CAD software, such as different 3D and 2D elements, and those constitute an index of flexibility of this methodology.

Another essential requirement for the CAD is the ability to import and export standard CAD formats (such as IGES and STEP) and meshed formats (such as STL), as anatomical volumes are usually derived from CT or MRI data by software other than CAD.

The final requisite - although not absolutely necessary - is the use of parametric CAD software that allows the constituent parameters of a feature to be modified once it has been generated. Non-parametric software does not allow any changes, and a designed geometry has to be deleted first and subsequently redrawn with the new values. Parametric CAD programmes are therefore more efficient in terms of both computational time and requirements.

### **2.5.1 Programming language requirements**

The programming language used for the sub-programmes should possess the following functions:

- Functions to detect and manage run time errors, in order to allow the algorithm to invoke an action when an error occurs during the execution of the program. These actions are predefined by the user and generally include modifications of the geometry (for parametric CAD), since most run time errors are due to impossible geometrical situations. Visual Basic, for example, offers the statement 'On Error' to identify run time errors and continue the execution at a specified point in the code.
- Functions for generating random numbers over given intervals, as explained in section 2.4.8.

---

### 2.5.2 Application Programming Interface

In order to use the libraries of CAD software (which contain all the functions, routines and classes), they have to be written as an Application Programming Interface (API), which defines the interfaces between the CAD application and an external program. It specifies the syntax and calling conventions for each function or class contained in a library. By following these conventions, an external program can communicate and interact with the CAD software.

The methodology explained in this chapter requires that the libraries of a CAD application are written as API, in particular those libraries containing the functions necessary to perform the commands listed in section 2.5. The evaluation of different CAD software was conducted considering all those requirements.

### 2.5.3 CAD Evaluation

Three CAD softwares were evaluated in this work, Unigraphics® NX 3 (by EDS Inc., USA), Rhino® 3.0 (by Robert McNeel & Associates, USA) and Catia® V5R16 (by Dassault Systemes, France). Many other CAD applications are commercially available, these packages were initially selected as they include a number of libraries written as API. In addition, the use of other CAD software - provided they are suitable - does not affect the methodology itself. It should be noted that the evaluation was conducted in 2007 and features may change over time.

Unigraphics NX3 is a parametric CAD program with advanced modelling commands for designing both solid geometries and surfaces. It allows the full manual modelling of the features required, although the API libraries are mainly for 2D elements.

Rhino 3.0 is a low-cost CAD software with all libraries written as API, thus allowing the whole design process to be automated. However, it does not possess all the modelling capabilities specified in section 2.5, and it is not parametric.

Catia V5R16 is a parametric CAD software that offers advanced modelling capabilities and is fully accessible through API interfaces. It possesses all the requisites specified in section 2.5, and supports a standard programming language such as Visual Basic for Applications (VBA, by Microsoft Inc., USA), which satisfies the requirement listed in section 2.5.1. For those reasons, Catia V5R16 was the CAD software utilised to implement this methodology, and VBA the programming language used to write the automated design algorithms.

Newer versions of both Unigraphics NX 3 and Rhino 3.0 may also satisfy all the requisites but, as previously noted, the use of other suitable CAD software does not affect the methodology itself.

A summary of a comparison between these three CAD software, as of 2007, is shown in Table 2.1.

Characteristics (M=manual, A=API):	Unigraphics NX3	Rhino 3.0	Catia V5R16
Point on a surface	Yes, M/A	No, M/A	Yes, M/A
Plane tangent to a surface at a specified point	Yes, M	No, M/A	Yes, M/A
2D control points curves, with specified tangents	Yes, M/A	Yes, M/A	Yes, M/A
3D control points curves, with specified tangents and tensions	Yes, M	Yes, M/A	Yes, M/A
Multi-sections solids/channels	Yes, M	Yes, M/A	Yes, M/A
Flexibility	Low	High	High

**Table 2.1** Summary of the comparison between different CAD software.

#### 2.5.4 Routines to convert rods into channels

Routines to convert a network of rods into the corresponding network of channels are required when designing TE scaffolds. The use of Boolean operations is not recommended, as they considerably increase computational time and may lead to non manifold geometries, particularly for complex architectures. In this work, several routines have been developed for either cubic or anatomical volumes. These routines identify all the multi-sections solids in a body (in CAD terms, a body includes wireframe geometries and a solid) and delete them, keeping all the primitives (which contain the geometrical data). The volume of the implant (or cube) is then copied into another body, in which the channels are designed using the data stored in the previous body. Fig. 2.8 shows an example of a rod and channel obtained from the same wireframe elements.

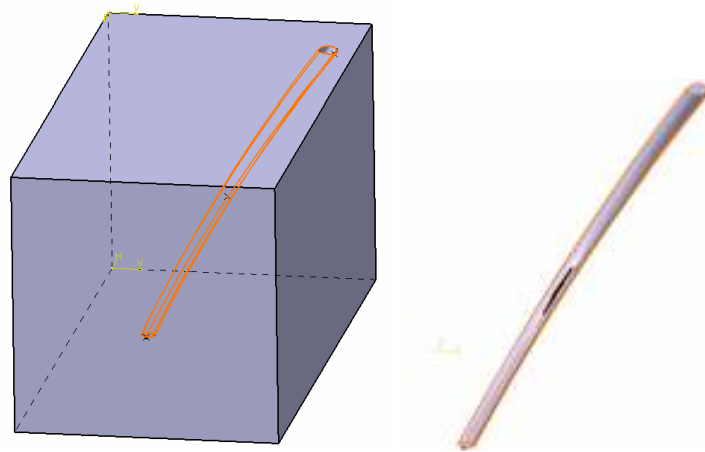


**Fig. 2.8** Example of a rod and channel obtained from the same wireframe elements.

## 2.6 Stages of Experiments

This methodology has been tested, developed and evaluated in four different stages of experiments, as follows:

- Stage 1 corresponds to chapter 3 of this work, which contains the initial experiments on cubic volumes. The purpose of these experiments was to test and assess the design methodology, and therefore attention was focused on the design variables and algorithms.
- Stage 2 corresponds to chapter 4 of this work, which contains more advanced experiments on anatomical volumes. The purpose of these experiments was to test and assess the applied version of the methodology.
- Stage 3 corresponds to chapter 5 of this work, in which an advanced technique of analysis of the automated designed geometries has been developed. The purposes of the chapter were to assess such geometries and to propose a general technique of analysis for trabecular bone structures, which may overcome the lack of knowledge about their geometrical characteristics.
- Based on the results of the third stage, a new bio-mimetic design technique has been developed and tested in chapter 6.

A schematic chart of the different stages of experiments is shown in Fig. 2.9.



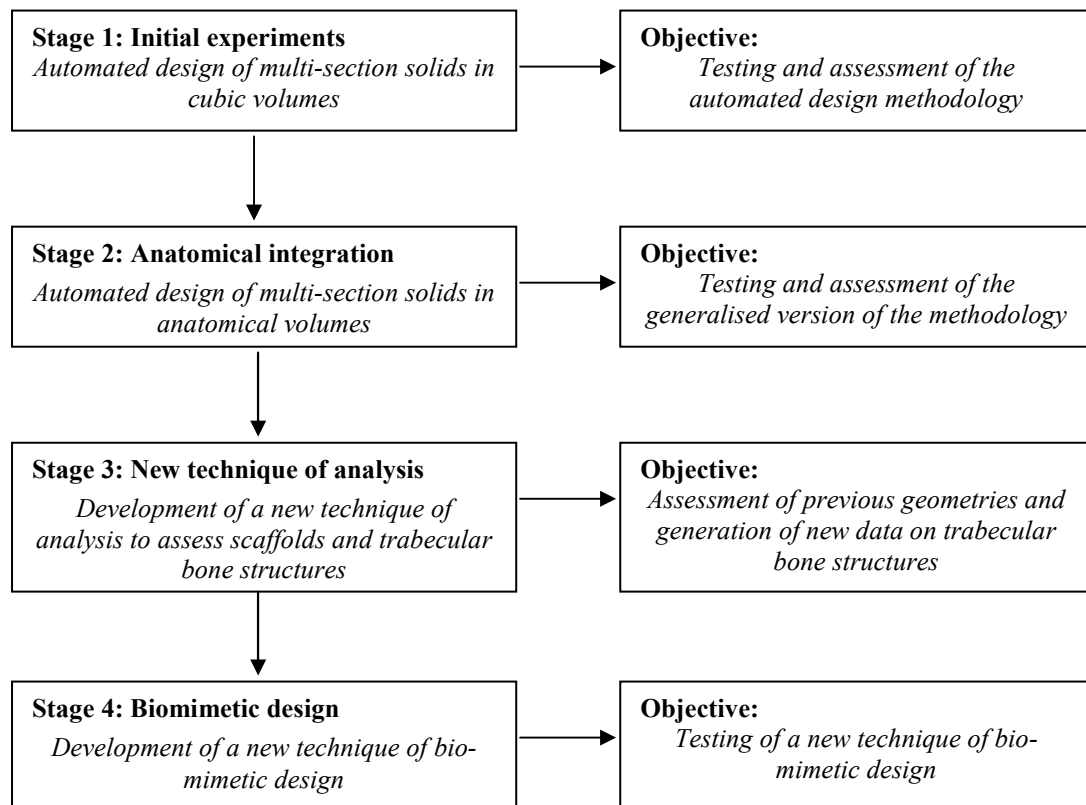


**Fig. 2.9** Schematic chart of the different stages of experiments.

## **CHAPTER 3**

### **- AUTOMATED DESIGN IN CUBIC VOLUMES -**

#### **3.1 Introduction**

In this chapter, initial experiments consisting of six different case studies were performed to test and assess the automated design methodology explained in chapter 2. These geometries exhibited a progressive increase in geometric variables, and a subsequent complexity that related to an increasing number of design functions and routines, in accordance with the input data set by the user. Such routines were assessed by output data of computational time and file size, while the scaffold geometry was assessed by the porosity.

The tests consisted of six small cubic scaffolds (10 mm) comprising of differently oriented channels of various shapes and sizes. There was no particular requirement to use a cubic shape - any other reference geometry could have been used - but this provided a regular volume to assess the effect of the variable parameters, aside from the location of each channel.

#### **3.2 Application of the Methodology**

The methodology explained in chapter 2 and the variables listed in section 2.4 for cubic volumes have been used in this chapter.

##### **3.2.1 Pore Size and Shape**

The pore size range was set between 0.2 and 0.8 mm for all six cases, as this range has been identified suitable for bone regeneration in the literature available to date.

Random variations of pore size and shape were achieved by using the VBA functions 'Randomize' and 'Rnd', as explained in section 2.4.8. Since 'Rnd' returns real values between 0 and 1, it was used directly for both pore shape and size. Any value outside this range was discarded and the function repeated, until an acceptable value was generated. The cross-sections were drawn on each face of the cube and the co-ordinates of the four control points

that defined each pore were traced in a local axis system parallel to the absolute co-ordinates. The origin of this local axis system coincided with the location of each pore.

### 3.2.2 Pore Location

The pore location on each face of the cube was defined by using the expressions (2.1) in section 2.4.3. According to those expressions, the co-ordinates at the centres of squares, are functions of both the minimum border distances and the number of rods in the three directions. In all six cases, the minimum border distance was selected to be the same on each face of the cube, and was equal to 1 mm:

$$a_x = a_y = a_z = 1 \text{ mm}$$

The number of rods in each direction and face of the cube were also selected to be the same. However, in cases 1 and 2 that number was set as 5, while in cases 3 to 6 it was increased to 7. Therefore:

$$n_x = n_y = n_z = 5 \text{ (for cases 1 and 2)}$$

$$n_x = n_y = n_z = 7 \text{ (for cases 3 to 6)}$$

Fig. 3.1 shows an example of pore location.

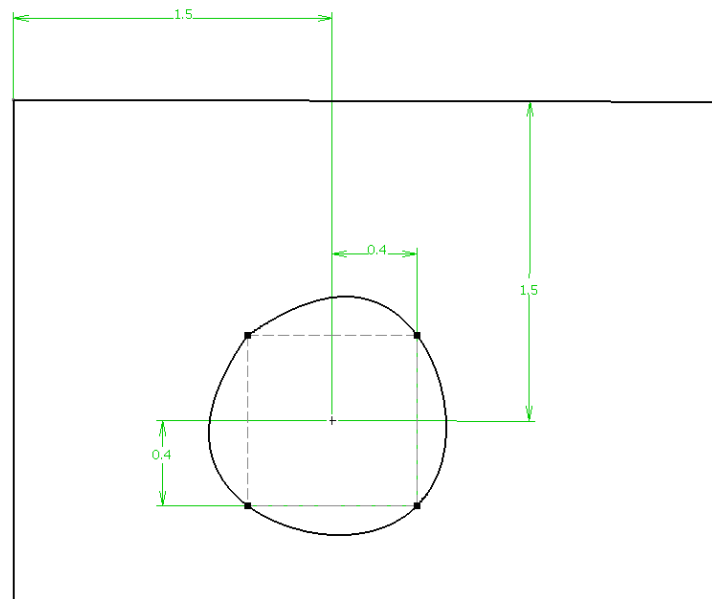


**Fig. 3.1** Example of pore location on a cubic face.

### 3.2.3 Coupling Variables

In these six case studies, only cross-sections on opposite faces of the cube were coupled in the same multi-section solid. In addition, since each face presented the same number of pores, all the cross-sections on a face were connected with another section on the opposite face.

In curved or linear non-orthogonal rods (cases 3 to 6), the association between the two sections was made randomly by using the 'Randomize' and 'Rnd' functions. Each section was identified by its location because regular distributions of pores can always be associated with matrices. Since the number of pores on a face resulted as  $n \times n$  ( $n_x = n_y = n_z = n$ ), the 'Rnd' function returned two integer values between 1 and  $n$ , as each pore was identified as an element of a matrix. By repeating the same procedure on the opposite face, the functions could randomly associate two cross-sections.

Linear and orthogonal rods (cases 1 and 2) did not require any association.

### 3.2.4 Rods Paths

Linear paths, orthogonal to the cross-sections, were used in cases 1 and 2, while linear and non-orthogonal paths were used in cases 3 and 4. In the latter cases, the lines were drawn by connecting the central points of associated pores, as explained in section 2.4.4. When only one cross-section was required, as in case 3, the central points on the opposite face were still designed, which allowed the tracing of linear paths.

In curved paths, two cross-sections on opposite faces were randomly associated, defining the first and third control points of a 3D curve, as explained in section 2.4.4. In case 5, the second control point was set as the centre of the cube, while in case 6 it was randomly selected within a given volume. The coordinates of such point  $X_s, Y_s, Z_s$  were computed using the expression (2.4):

$$\begin{aligned}
 X_s &= \Delta x Rnd + X_c - \frac{\Delta x}{2} \\
 Y_s &= \Delta y Rnd + Y_c - \frac{\Delta y}{2} \\
 Z_s &= \Delta z Rnd + Z_c - \frac{\Delta z}{2}
 \end{aligned} \tag{3.1}$$

Where  $\Delta x$ ,  $\Delta y$  and  $\Delta z$  describe a prism whose centre coincides with the centre of the cube  $X_c, Y_c, Z_c$ .

The expressions (3.1) define the co-ordinates of a random point within this ideal prism. In case 6, the same value of 2 mm was used for  $\Delta x = \Delta y = \Delta z$ .

### 3.2.5 Volumetric Variables

For cubic volumes, the only variable is the size of the cube, which was fixed at 10 mm for all six cases.

### 3.2.6 Output Variables

The porosity for the scaffold geometries was evaluated using expression (2.2) in section 2.4.7, while file (CAD and STL) size data were obtained from the operative system. The computational time of the automated design was compared with the estimated figures for manual design, as explained in section 2.3.3. Both design time and file size referred to the generation of the rods structure.

## 3.3 Results

In each case study, two structures were shown - the scaffold and its complementary geometry. The first consisted of a group of open channels, while the latter was depicted as a group of interconnected rods representing the voids in the channels. The latter solid feature provides a better visualisation of the entire network.

### 3.3.1 Case 1

This case presents a regular distribution of straight and orthogonal channels of different diameters, ranging from 0.2 to 0.8 mm. The computation of the pore size is exact, since each cross-section is defined by a circle. The scaffold is illustrated in Fig. 3.2 (a), while (b) shows its negative geometry. The details of this case are summarised in Table 3.1.

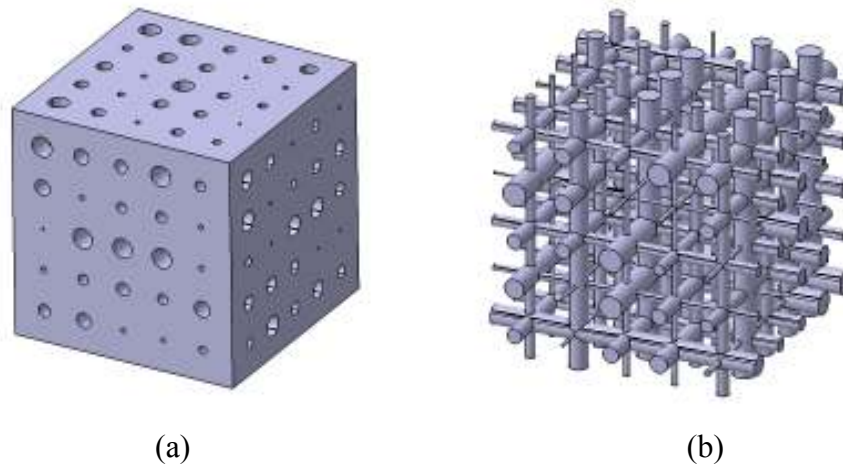


**Fig. 3.2** Case 1: (a) scaffold and (b) negative geometry.

Group of variables	Description	Value
Pore size	0.2 to 0.8 mm range	Random diameter
Pore location	Min. border distance $ax=ay=az$	1 mm
	Number of rods on each direction ( $nx=ny=nz$ )	5
Pore shape	Circular	-
Volume variables	Cube size	10 mm
Coupling variables	Surface coupling	opposite faces of the cube
	Sections coupling	-
3D path	Orthogonal to cross sections	-
Multi-section solid	1 cross section	-
Output variables	Computational time	10 mins
	Average computational time/rod	8 sec/rod
	Estimated time manual design/rod	30 sec/rod
	Catia File size	5.47 MB
	STL file size (ASCII)	12 MB
	Porosity %	16.66%

**Table 3.1** Case 1: input and output data.

### 3.3.2 Case 2

This case presents a regular distribution of straight and orthogonal channels of different shapes, obtained by randomly changing the tangent values at the four control points. The pore size was estimated by considering the square area enclosed by the cross-sections. The scaffold is illustrated in Fig. 3.3 (a), and its negative geometry in (b). The details of this case are summarised in Table 3.2.

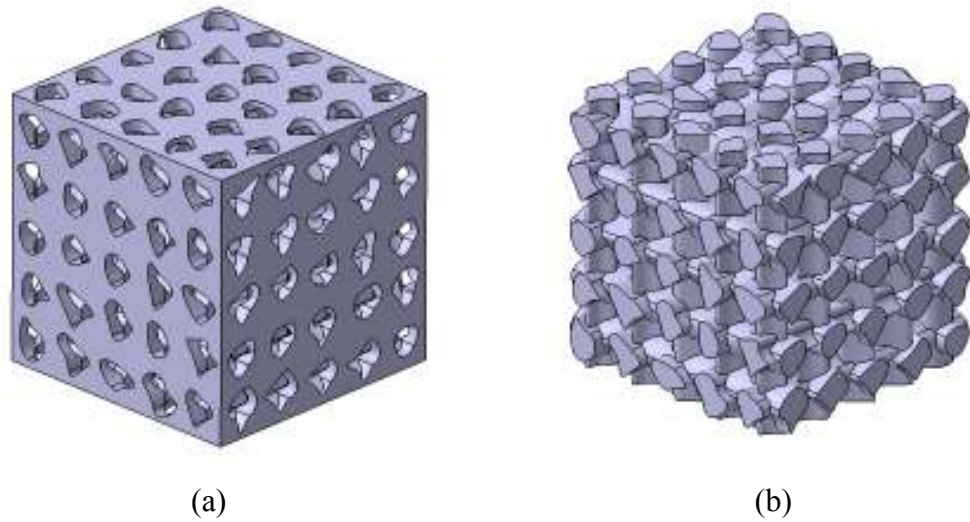


**Fig. 3.3** Case 2: (a) scaffold and (b) negative geometry.

Group of variables	Description	Value
Pore size	0.2 to 0.8 mm range	Random
Pore location	Min. border distance $ax=ay=az$	1 mm
	Number of rods on each direction ( $nx=ny=nz$ )	5
Pore shape	Tangents at four control points	Random
Volume variables	Cube size	10 mm
Coupling variables	Surface coupling	Opposite faces of the cube
	Sections coupling	-
3D path	Orthogonal to cross sections	-
Multi-section solid	1 cross section	-
Output variables	Computational time	13 min
	Average computational time/rod	10.4 sec/rod
	Estimated time manual design/rod	30 sec/rod
	Catia File size	10.7 MB
	STL file size (ASCII)	9.95 MB
	Porosity %	55.27%

**Table 3.2** Case 2: input and output data.

### 3.3.3 Case 3

This case consists of a regular distribution of straight and non-orthogonal channels of different shapes, with constant cross-sections. For each channel, the linear path was defined by randomly connecting two different central points, located on opposite faces. The number of channels was almost doubled in respect to the previous cases (from 25 to 49 per face), showing little difference in both computational time and file size.



The scaffold and its negative shape are illustrated in Fig. 3.4 (a) and (b) respectively. Fig. 3.5 depicts some linear and non-orthogonal rods in more details, while Table 3.3 summarises the input and output data.

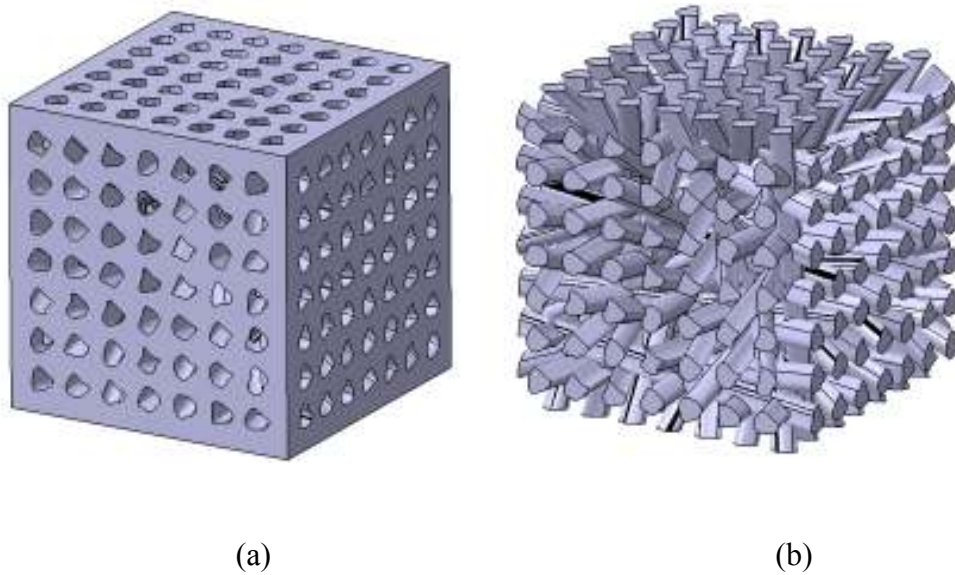


**Fig. 3.4** Case 3: (a) scaffold and (b) negative geometry.

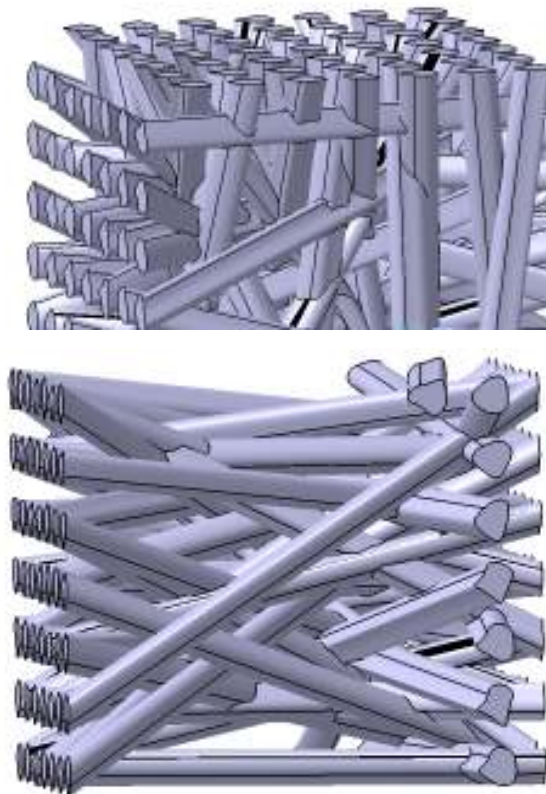


**Fig. 3.5** Case 3: details of some linear and non-orthogonal rods.



Group of variables	Description	Value
Pore size	0.2 to 0.8 mm range	Random
Pore location	Min. border distance $ax=ay=az$	1 mm
	Number of rods on each direction ( $nx=ny=nz$ )	7
Pore shape	Tangents at four control points	Random
Volume variables	Cube size	10 mm
Coupling variables	Surface coupling	Opposite faces of the cube
	Sections coupling	Random: 1 section to 1 central point
3D path	Linear non-orthogonal	-
Multi-section solid	1 cross section	-
Output variables	Computational time	18 mins
	Average computational time/rod	7.35 sec/rod
	Estimated time manual design/rod	30 sec/rod
	Catia File size	26.8 MB
	STL file size (ASCII)	9.97 MB
	Porosity %	44.49%

**Table 3.3** Case 3: input and output data.

### 3.3.4 Case 4

This case is similar to case 3, with the difference that each channel is now defined by two cross-sections. The scaffold and its negative shape are illustrated in Fig. 3.6 (a) and (b) respectively. Fig. 3.7 illustrates some linear and non-orthogonal rods in more detail, showing the changes in the cross-sections. Table 3.4 summarises the input and output data for this case.

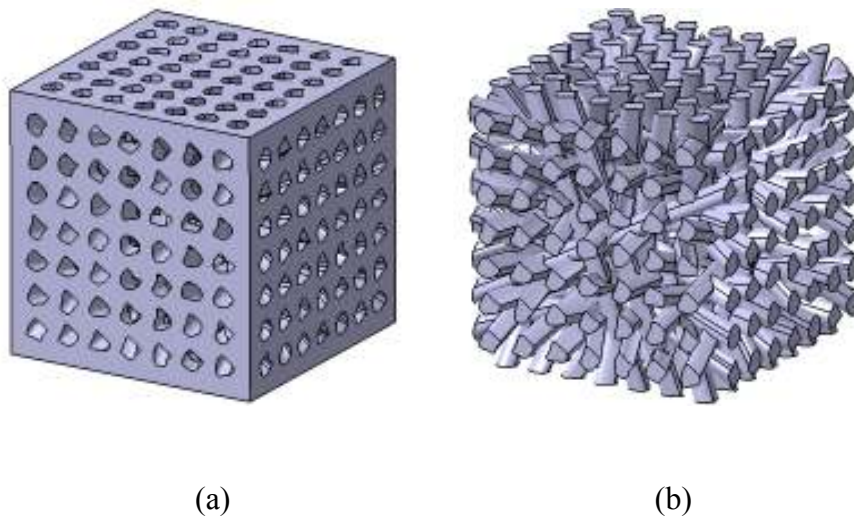


**Fig. 3.6** Case 4: (a) scaffold and (b) negative geometry.

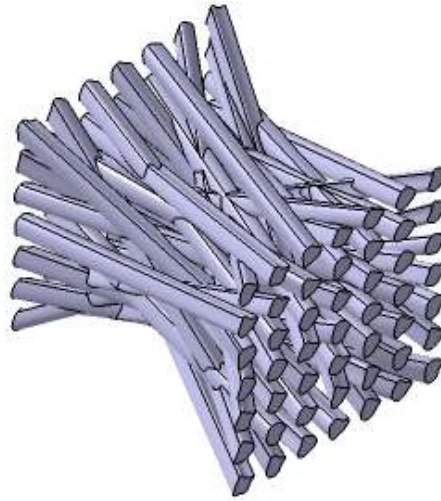


**Fig. 3.7** Case 4: details of some linear and non-orthogonal rods with different cross-sections.

Group of variables	Description	Value
Pore size	0.2 to 0.8 mm range	Random
Pore location	Min. border distance $ax=ay=az$	1 mm
	Number of rods on each direction ( $nx=ny=nz$ )	7
Pore shape	Tangents at four control points	Random x 2 sections
Volume variables	Cube size	10 mm
Coupling variables	Surface coupling	Opposite faces of the cube
	Sections coupling	Random
3D path	Linear non-orthogonal	-
Multi-section solid	2 cross sections	-
Output variables	Computational time	20 mins
	Average computational time/rod	8.16 sec/rod
	Estimated time manual design/rod	45 sec/rod
	Catia File size	35.7 MB
	STL file size (ASCII)	17.4 MB
	Porosity %	44.16%

**Table 3.4** Case 4: input and output data.

### 3.3.5 Case 5

This case presents a regular distribution of curved channels with two cross-sections of different shape, converging on the centre of the volume. This arrangement sought to illustrate that a higher porosity and pore interconnectivity could be directed on a given convergence, utilizing the centre as an example. Convergence could be situated at any given location at single or multiple sites. In this case, all the channels were forced to pass through the centre of the cubic volume in order to increase the porosity at the centre of the scaffold.

This may promote tissue regeneration deeper into thick section geometries, overcoming the limit of 500  $\mu\text{m}$  indicated by Ishaug-Riley et al. (1997).

The curved path of each channel was defined by a curve with three control points, where the second point was made coincident to the centre of the cube. It is possible that with curved channels, particular combinations of parameters would lead to run time errors, due to impossible geometrical situations. Subsequently, it was necessary to design routines specifically to detect those errors and correct the geometry. VBA provides the 'On Error' statement to manage run time errors, so that necessary actions to resume the execution of the program can be taken. Since Catia V5R16 is parametric software, geometrical features can be modified after their generation, with no need to redefine the whole set of variables. In this chapter, the design algorithms have been programmed to randomly change the values of the tangents at the four control points, in case of run time errors. The process can be repeated for a number of times, until a combination of compatible values is found.

These procedures increase the computational time, as they need to calculate many different combinations of parameters in order to find one suitable. Their advantage is that they allow the automated design of more complex multi-section solids, involving a curvature. The scaffold and its negative shape are illustrated in Fig. 3.8 (a) and (b) respectively. Fig. 3.9 shows some curved paths and their convergence on the centre of the cube in more detail. Table 3.5 summarises the input and output data for this case.

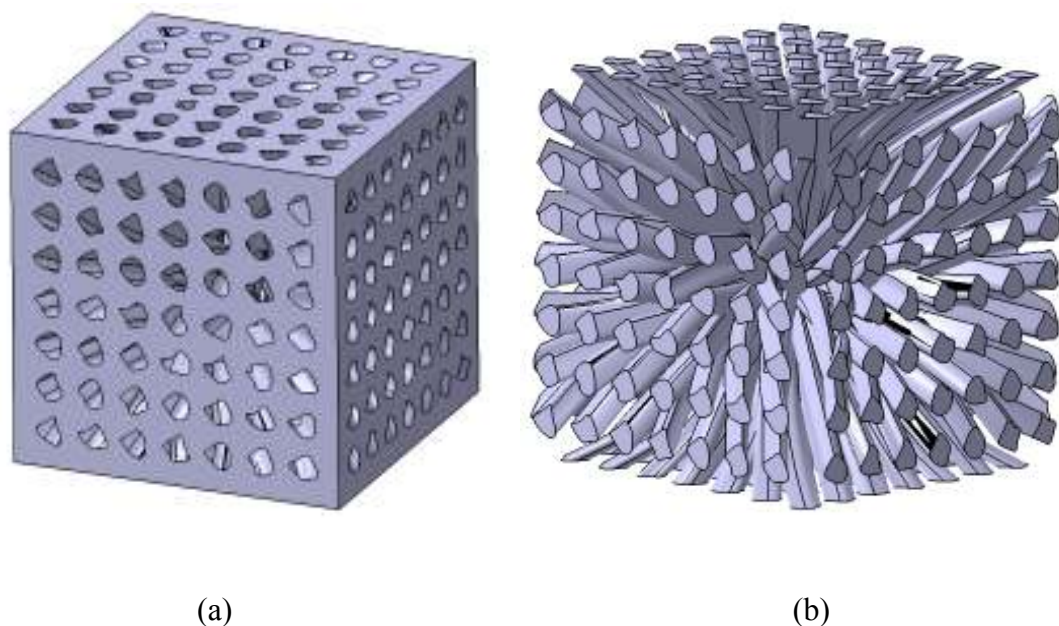


**Fig. 3.8** Case 5: (a) scaffold and (b) negative geometry.

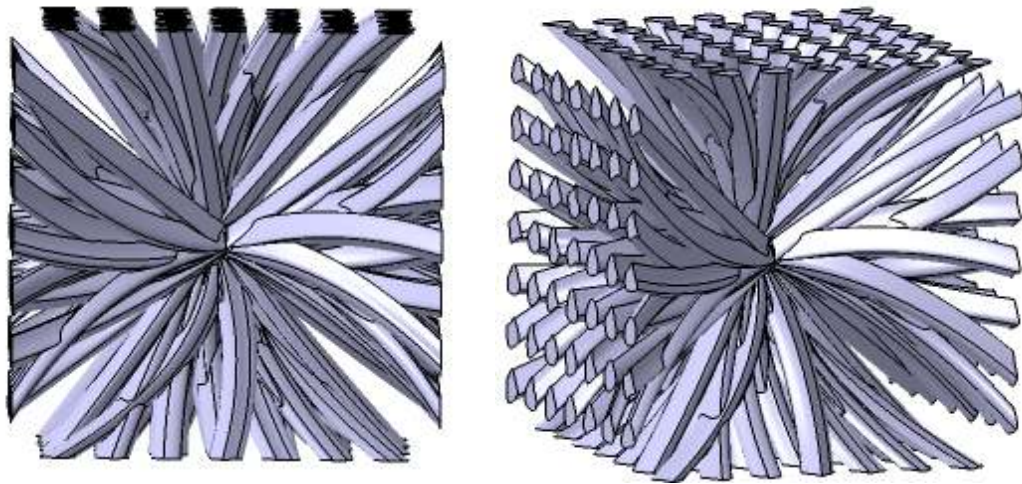


**Fig. 3.9** Case 5: details of some curved paths and their convergence to the centre of the cube.

Group of variables	Description	Value
Pore size	0.2 to 0.8 mm range	Random
Pore location	Min. border distance $ax=ay=az$	1 mm
	Number of rods on each direction ( $nx=ny=nz$ )	7
Pore shape	Tangents at four control points	Random x 2 sections
Volume variables	Cube size	10 mm
Coupling variables	Surface coupling	Opposite faces of the cube
	Sections coupling	Random
3D path	3 control points curve	centre of the cube
Multi-section solid	2 cross sections	-
Output variables	Computational time	20 mins
	Average computational time/rod	8.16 sec/rod
	Estimated time manual design/rod	1 min:15 sec/rod
	Catia File size	20.6 MB
	STL file size (ASCII)	13.6 MB
	Porosity %	33.56%

**Table 3.5** Case 5: input and output data.

### 3.3.6 Case 6

This case relates to case 5, although the network is arranged differently. The channels no longer converge on the centre and instead, their path is randomly set. That was achieved by randomly changing the co-ordinates of the second control point of the 3D curve within a specified range. This domain can be either the whole cube or a portion of it.



In this example, a range of  $\pm 20$  per cent the length of the cube was chosen, meaning  $\pm 2$ mm in each direction from the centre of the cube. Naturally, any other value or location could have been used. In this case, all the channels were forced to pass through a central region of the cubic volumes in order to increase the porosity around the centre of the scaffold. As with the previous case, this may promote deeper penetration of new tissue into thick section geometries, overcoming the limit of  $500\text{ }\mu\text{m}$  indicated by Ishaug-Riley et al. (1997).

A routine to detect and automatically correct run-time errors was also required. The parameters modified by this routine were the tangents at the four control points, for each cross-section. As in the previous case, the tangents were modified a number of times, until a suitable combination was found.

The scaffold and its negative shape are illustrated in Fig. 3.10 (a) and (b) respectively, while Fig. 3.11 shows some curved paths and their random interconnections in more details. Table 3.6 summarises the input and output data for this case.

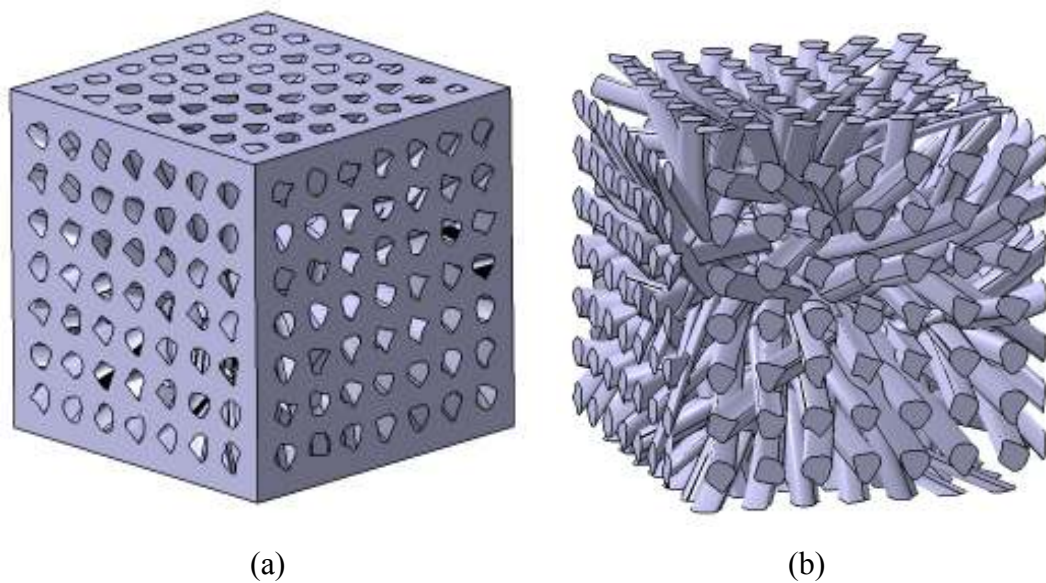


**Fig. 3.10** Case 6: (a) scaffold and (b) negative geometry.

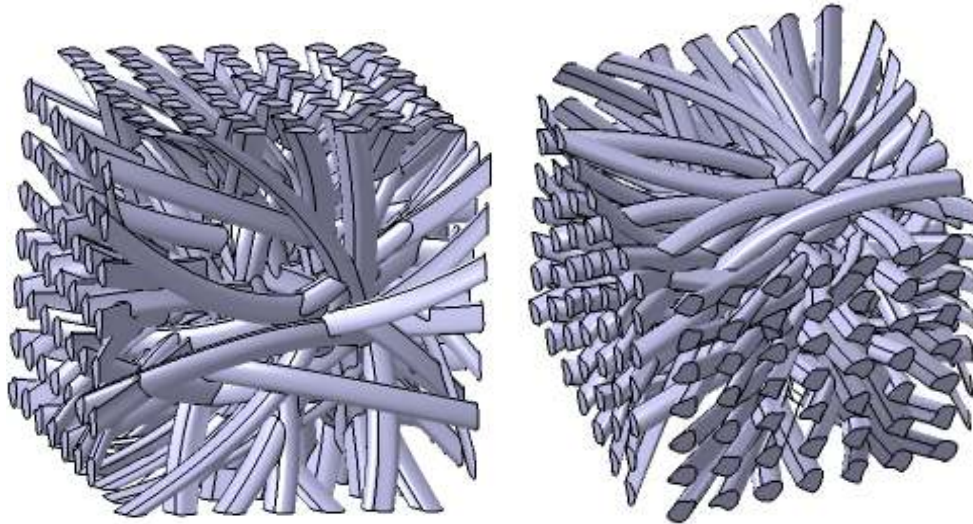


**Fig. 3.11** Case 6: details of some curved paths and their random interconnections

Group of variables	Description	Value
Pore size	0.2 to 0.8 mm range	Random
Pore location	Min. border distance $ax=ay=az$	1 mm
	Number of rods on each direction ( $nx=ny=nz$ )	7
Pore shape	Tangents at four control points	Random x 2 sections
Volume variables	Cube size	10 mm
Coupling variables	Surface coupling	Opposite faces of the cube
	Sections coupling	Random
3D path	3 control points curve	Random 2nd control point around $\pm 2$ mm the centre of the cube ( $\Delta x=\Delta y=\Delta z=4\text{mm}$ )
Multi-section solid	2 cross sections	-
Output variables	Computational time	22 mins
	Average computational time/rod	9 sec/rod
	Estimated time manual design/rod	1 min:15 sec/rod
	Catia File size	35.5 MB
	STL file size (ASCII)	24 MB
	Porosity %	36.77%

**Table 3.6** Case 6: input and output data.

### 3.4 Review

The cases investigated in this chapter show that the automated design of complex networks of interconnected rods/channels can be achieved in conventional CAD. The time saving is considerable when the size of the reference volume becomes larger, as in the prism shown in Fig. 3.12. The size of this prism was 51 x 40.6 x 8.55 mm, and the structure was made of

420 - case 5 - rods, connecting the lateral faces. The design time required by the - case 5 - routine for such structures was 15 minutes, with an average of 2.14 s/rod, against an estimated 1min:15 sec/rod for the manual design. The Catia file size was 78.8 MB. In the cases presented in this chapter, the slowest automated design time was 10.4 sec/rod (for case 2), against an estimated 30 sec/rod for the manual design.

The assessment of the geometries was performed by determining the resultant scaffold porosity, since this is the primary quantifiable characteristic sought in current TE scaffold research. From current literature, the porosity requirements are rather vague, as wide ranges (from 50% to more than 90%) are usually suggested. According to those figures, the designed geometries do not present enough porosity, except in case 2 where the porosity is slightly higher than the lower limit of the range (55.27%). In all the other cases, such values range from 16.66% in case 1 to 44.49% in case 3. As the pore size range was set according to the figures suggested as suitable for bone regeneration, higher porosity could be achieved either by increasing the number of rods in each direction or by decreasing the minimum border distance.

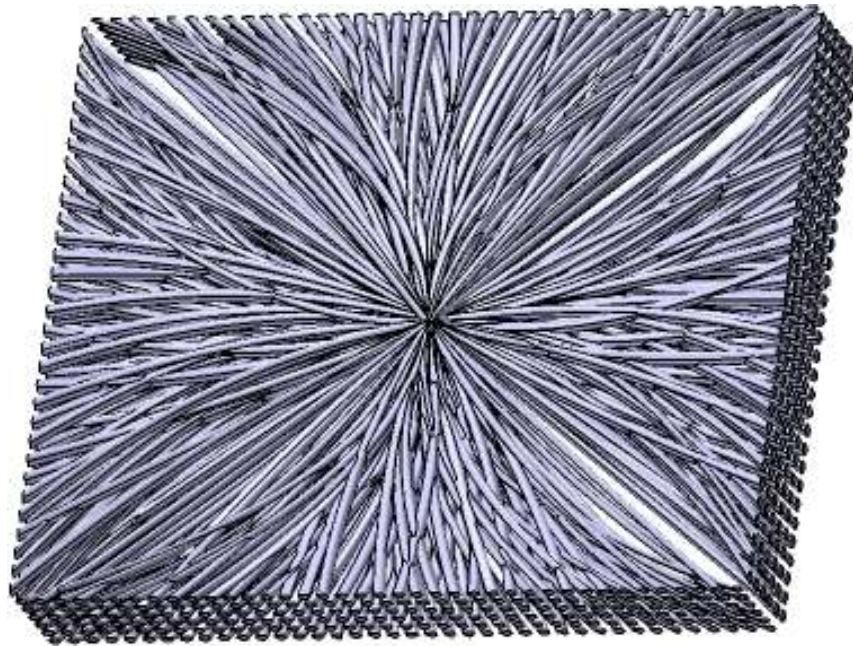


**Fig. 3.12** Example of a large network of multi-section solids on a prismatic volume (51 x 40.6 x 8.55 mm).

STL files generated in CATIA V5R16 were in ASCII format, as that was the default setting used in the software. CATIA V5R16 software does not allow the user either to select the STL format, or to alter the parameters used to generate STL geometries, and therefore standard settings had to be used (CATIA has a dedicated module for advanced STL manipulation, which was not available for this project).

Although ASCII STL format requires more space to store the same data than the binary format (in some cases up to 50% more), it was used in this work because the file sizes involved did not present any processing delays or storage difficulties for a standard specification computer (for example, a typical CAD file size for a cylinder head is about 60 MB). On the contrary, STL files generated from  $\mu$ CT scans were used throughout this work in binary format, since high resolution scans usually produce a large amount of data, which would be impractical for a standard specification computer to handle. In such cases, the binary format can significantly reduce the file size, compared with the ASCII format. Another reason for using STL binary format for the  $\mu$ CT samples was that they were supplied externally and therefore there was no opportunity either to alter the quality parameters or to change the STL format.

Although these cases were used for testing and assessing the automated design methodology explained in chapter 2, at this stage they were limited to cubic/prismatic volumes because they are unsuitable for performing the same designs in a complex anatomical volume, such as the one shown in Fig. 3.13. This anatomical volume refers to a theoretical clinical case study of craniofacial injury at Queens Medical Centre (QMC) in Nottingham, UK, and is investigated in the next chapter.

The use of Boolean operations to merge the two structures in Fig. 3.14 led to an error (because of non-manifold geometries) in the CAD software (Catia V5R16). In addition, two hours of computational time and hundreds of megabytes of RAM memory were required before this error occurred, confirming the inefficiency of Boolean operations for complex geometries. As a result, this automated design methodology required further development in order to be used efficiently on anatomical volumes.



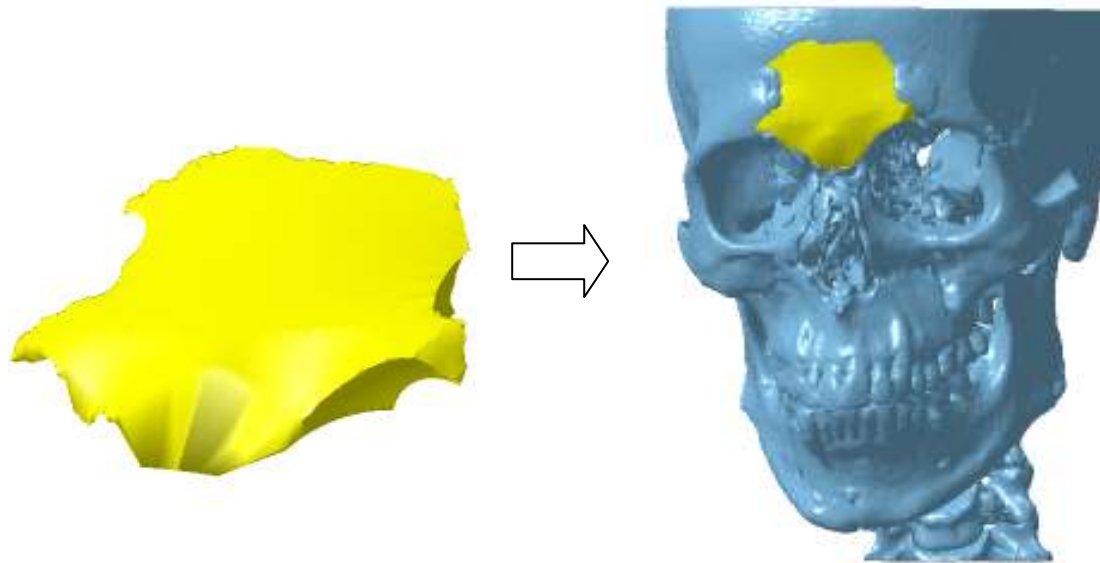


**Fig. 3.13** Example of anatomical volume reconstructed from a CT scan, from a clinical case study of craniofacial injury at Queens Medical Centre in Nottingham, UK.

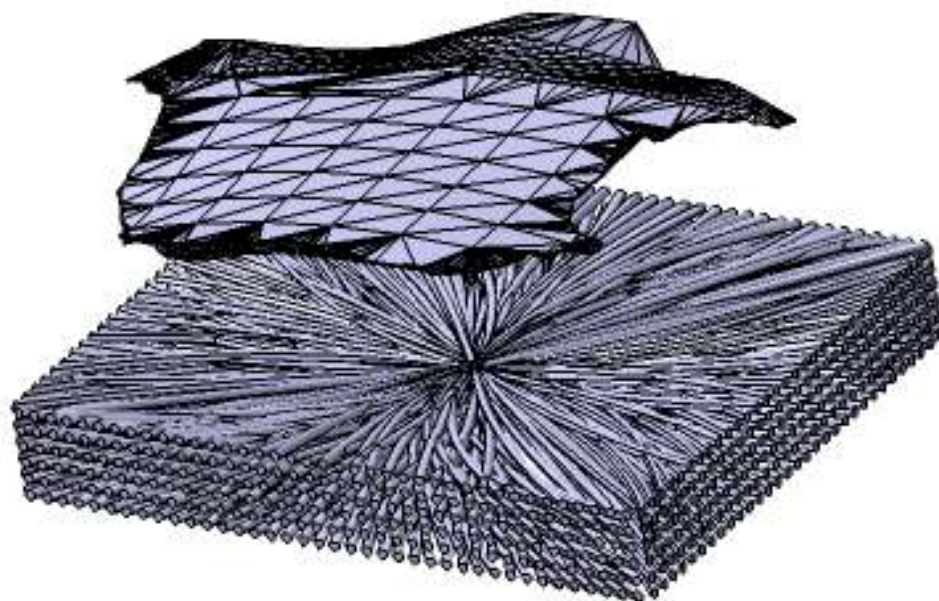


**Fig. 3.14** Example of an anatomical volume and prismatic network of multi-section solids.

## **CHAPTER 4**

### **- AUTOMATED DESIGN INTEGRATION IN ANATOMICAL VOLUMES -**

#### **4.1 Introduction**

In this chapter, experiments consisting of two different anatomical case studies were performed to test and assess a revised version of the automated design methodology explained in chapter 2. In these case studies, it is intended to integrate the networks of curved rods produced by the work of chapter 3 efficiently into two anatomical volumes, avoiding the use of Boolean operations. This would enable the proposed automated design methodology to overcome the limitations dictated by the target shape and the need for Boolean operations. This version of the methodology has been termed Automated Design Integration (ADI).

Although any network shown in chapter 3 could have been assessed with anatomical volumes, curved networks were preferred as they generate more complex and irregular geometries than linear ones. Design routines were again assessed by output data of computational time and file size, while the scaffold geometry was assessed by the porosity.

The proposed anatomical volumes were chosen according to the project needs. The first sample referred to a theoretical clinical case study of a craniofacial implant, and the CAD model was provided by the QMC in Nottingham, UK. The second sample referred to a mouse humerus theoretical implant, and the CAD model was supplied by SkyScan Inc., Belgium.

The craniofacial implant was limited in size because it was a segment of a larger bone, and that resulted in a smaller number of rods and a less complex internal structure.

The mouse humerus implant was particularly important for the project for two reasons. First, it represented an entire bone structure and not just a portion of one. As such, the size of the

sample was much bigger than in the previous case, resulting in a larger number of rods and a more complex architecture. For the same reason, the results obtained for this case were not dependant on location, orientation, size or origin of the sample.

Secondly, it allowed a deeper characterisation and assessment of the ADI methodology through the comparison with the target geometry, whose internal structure could be scanned via  $\mu$ CT. The ADI mouse humerus geometry also presented random variations in all the key geometrical parameters for bone TE scaffolds, pore size, shape and interconnectivity. The mouse humerus geometry was selected due to the limited number of samples available.

## 4.2 Application of the Methodology

The methodology explained in chapter 2 and the variables listed in section 2.4 for anatomical volumes have been used in this chapter. All the following illustrations from Fig. 4.1 to Fig. 4.7 refer to the clinical case study of a craniofacial implant at QMC, introduced in section 3.4 and shown in Fig. 3.13. This case study is entirely theoretical, and has not been used in any clinical context. Its geometrical design was derived in conjunction with clinical staff at QMC.

### 4.2.1 Pore Size and Shape

The pore size ranges were set from 0.2 to 0.8 mm and from 0.2 to 0.4 mm for the first and second case study respectively. Random variations of pore size and shape were achieved by using the VBA functions 'Randomize' and 'Rnd', as explained in section 2.4.8. Since 'Rnd' returns real values between 0 and 1, it was directly used for both pore shape and size. In this last case, a value outside the range was discarded and the function repeated until the generation of an acceptable value. Each cross-section was drawn on a plane that ran tangential to a given surface at a given location. The co-ordinates of the four control points that defined each pore were traced in a local right-handed axis system that was obtained by the projection of direction  $d_1$  (defined in the following section) on the plane, and the outer-pointing normal to the plane (the third axis is then determined by the right-hand rule). The origin of this axis system coincides with the location of each pore.

### 4.2.2 Pore Location

The pore location adopted for anatomical volumes has been explained in section 2.4.3. For each surface, one origin point  $P$  and two directions,  $d_1$  and  $d_2$ , were specified, defining the two curved co-ordinate lines  $u$  and  $v$ , from which each pore was located, as shown in Fig. 4.1. The origin point was set at the centre of each surface, whose co-ordinates were computed by CatiaV5R16, while the directions of the two vectors were defined differently on each surface. This origin point could have been set at any location, and centre was only chosen to assess the ADI methodology.

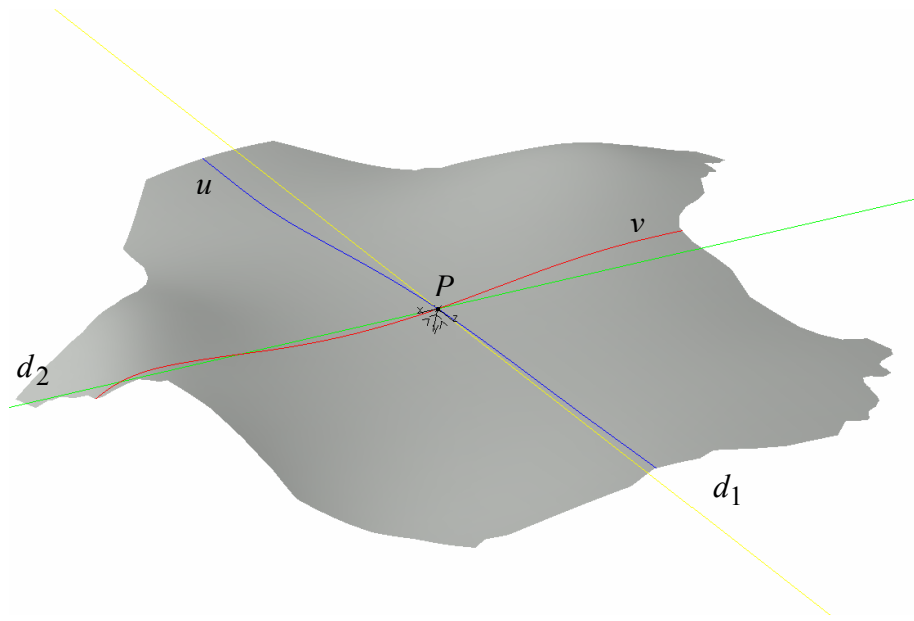


**Fig. 4.1** Example of curved co-ordinate lines ( $u$ ,  $v$ ) on an irregular surface.

On the first co-ordinate line  $u$ , several points were traced in both directions as multiples of a specified distance  $c_u$ , also termed spatial resolution. Therefore, the curvilinear co-ordinate  $u_i$  of a generic point  $i$  on  $u$ , is given by:

$$u_i = c_u i; \quad i = n_u^-, \dots, -1, 0, 1, \dots, n_u^+$$

$$n_u^- = \text{Int} \left( \frac{l_u^- - b_u}{c_u} \right)$$

$$n_u^+ = \text{Int} \left( \frac{l_u^+ - b_u}{c_u} \right)$$

Where:

$c_u$  = spatial resolution on  $u$

$n_u^+$  = number of points in the positive side of  $u$

$n_u^-$  = number of points in the negative side of  $u$

$l_u^-$  = length of the negative part of  $u$

$l_u^+$  = length of the positive part of  $u$

$Int$  = VBA function that returns the integer portion of a number

$b_u$  = minimum distance along  $u$  from the border

Fig. 4.2 shows the lengths  $l_u^+$  and  $l_u^-$  for the co-ordinate  $u$ , while Fig. 4.3 illustrates the distances  $c_u$  and  $b_u$ , along with some points on both the positive and negative co-ordinates of  $u$ .

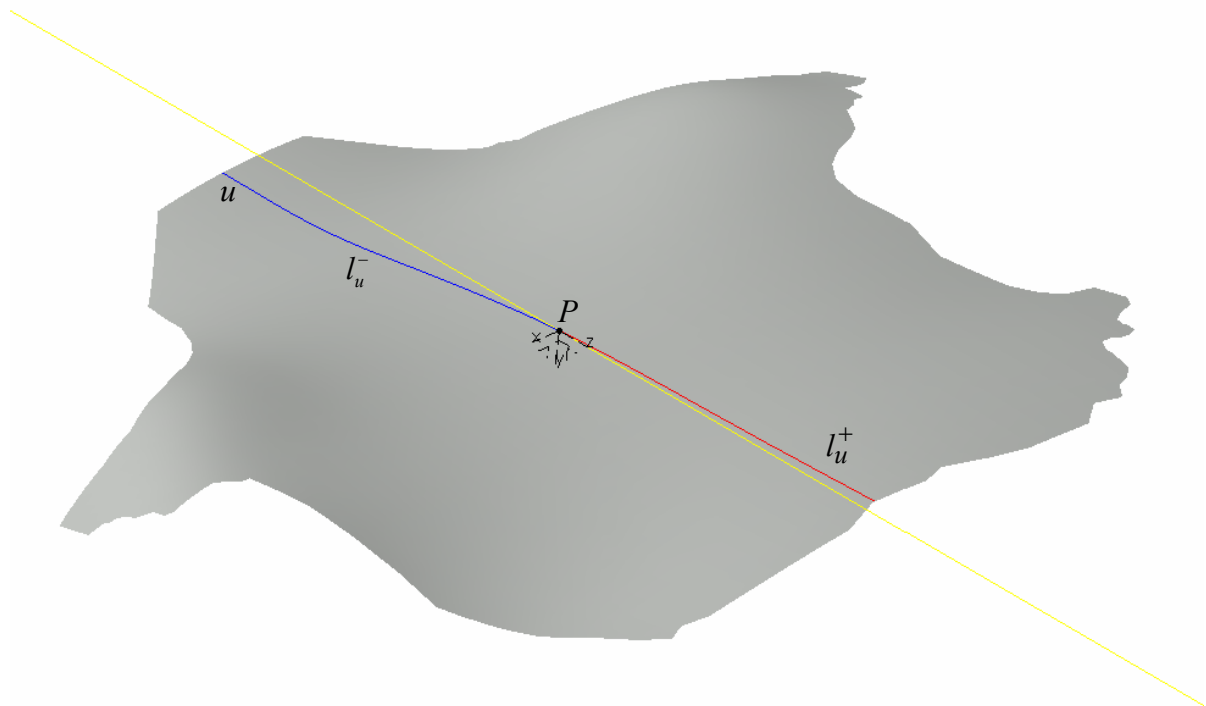


**Fig. 4.2** Positive and negative parts of the co-ordinate line  $u$ .

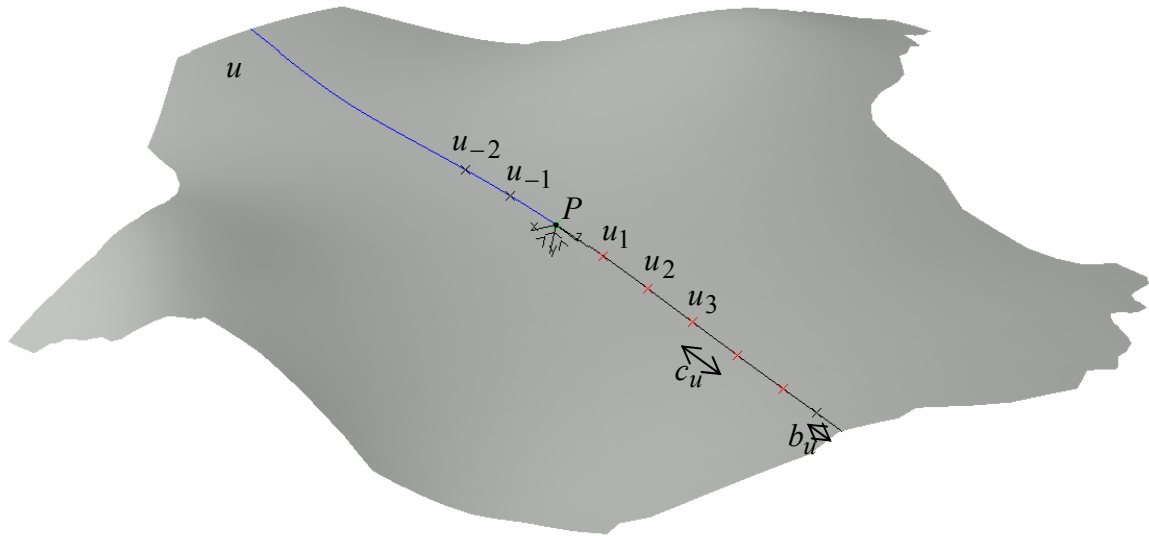


**Fig. 4.3** Spatial resolution and minimum border distance along the co-ordinate line  $u$ .

After the required number of points has been generated along  $u$ , the algorithm designs another point along  $v$ , which defines the origin  $P_1$  of a new curved co-ordinate line  $u'$ , obtained by projecting the direction  $d_1$  on to the surface. An example of new origin  $P_1$  and new co-ordinate line  $u'$  is shown in Fig. 4.4. The points along  $u'$  are then traced as with the previous line, and the process is repeated until all the points on all ' $u$ ' co-ordinates have been designed.

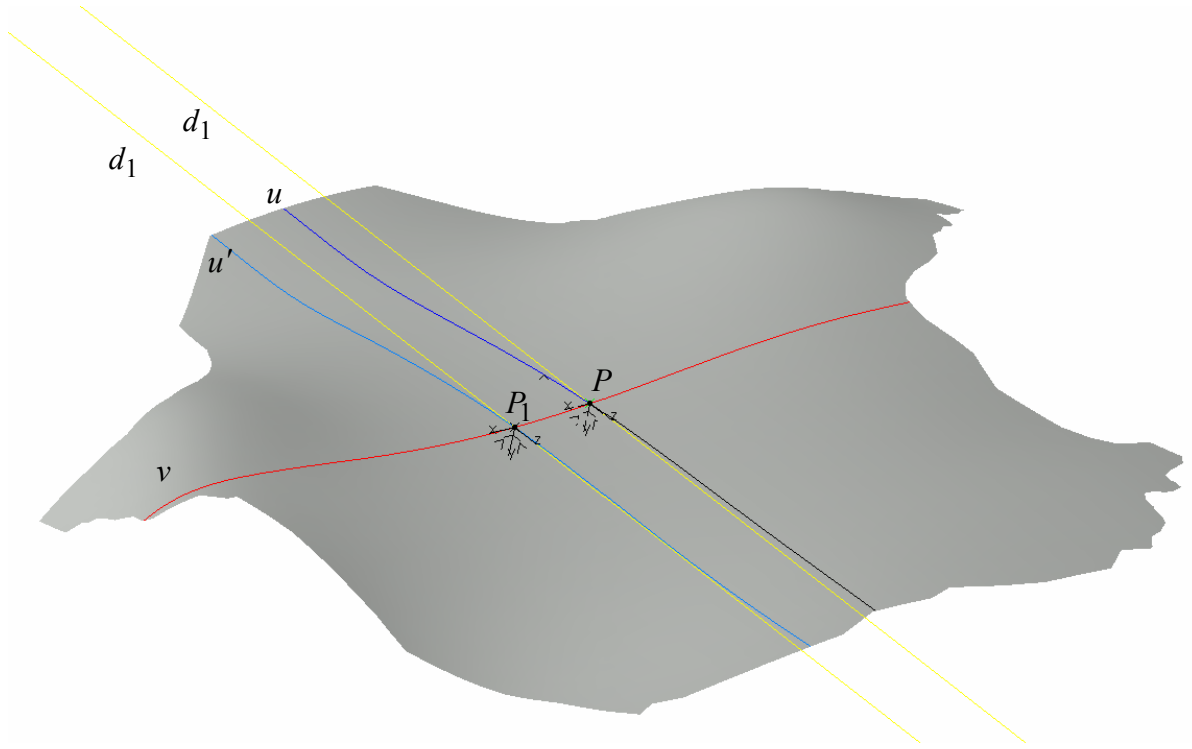


**Fig. 4.4** Definition of a new co-ordinate line  $u'$  with origin in the point  $P_1$

The curvilinear co-ordinate  $v_i$  of a generic point  $i$  on  $v$ , is given by:

$$v_i = c_v i; \quad i = n_v^-, \dots, -1, 0, 1, \dots, n_v^+$$

$$n_v^- = \text{Int} \left( \frac{l_v^- - b_v}{c_v} \right)$$

$$n_v^+ = \text{Int} \left( \frac{l_v^+ - b_v}{c_v} \right)$$

Where:

$c_v$  = spatial resolution on  $v$

$n_v^+$  = number of points in the positive side of  $v$

$n_v^-$  = number of points in the negative side of  $v$

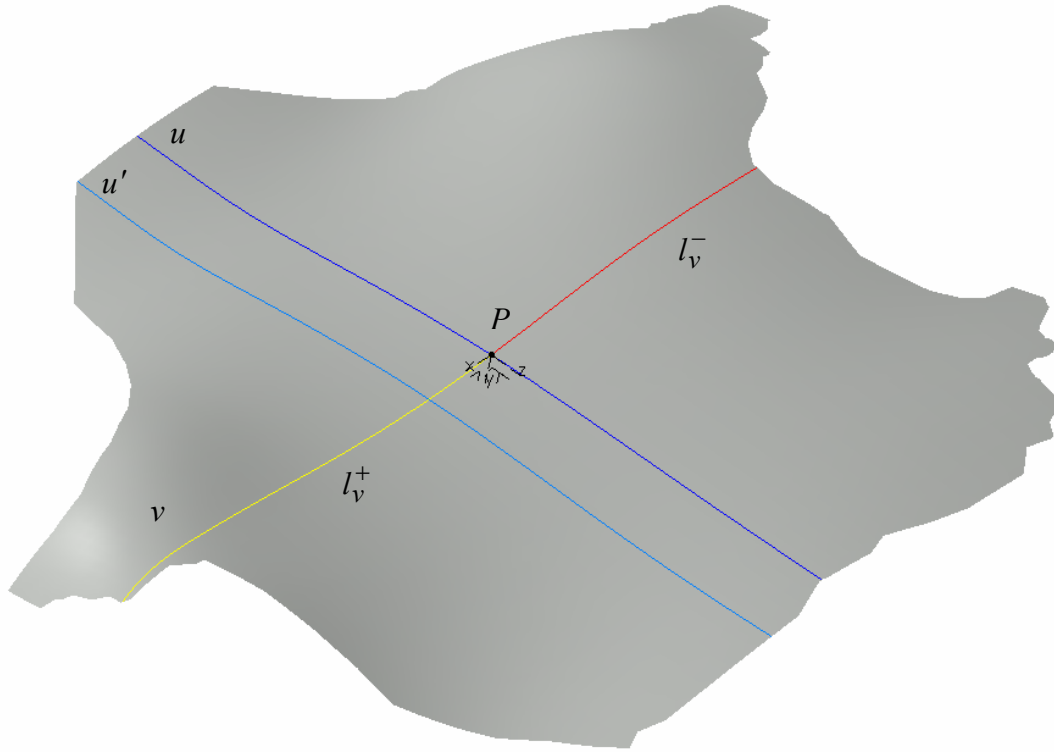
$l_v^-$  = length of the negative part of  $v$

$l_v^+$  = length of the positive part of  $v$

$Int$  = VBA function that returns the integer portion of a number

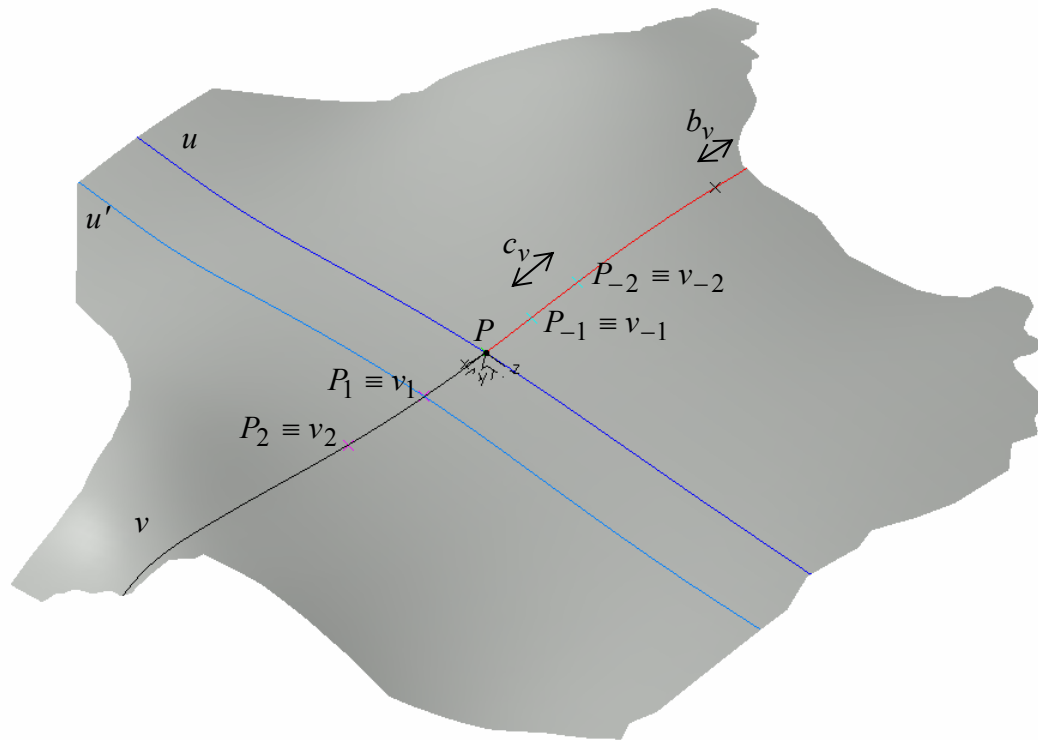
$b_v$  = minimum distance along  $v$  from the border

Fig. 4.5 shows the lengths  $l_v^+$  and  $l_v^-$  for the co-ordinate  $v$ , while Fig. 4.6 illustrates the distances  $c_v$  and  $b_v$ , along with some points on both the positive and negative co-ordinates of  $v$ .



**Fig. 4.5** Positive and negative parts of the co-ordinate line  $v$ .





**Fig. 4.6** Spatial resolution and minimum border distance along the co-ordinate line  $v$ .

The pore locations obtained by this method are irregular, since the ' $u$ ' curves differ from one another. This is a consequence of irregularities in the surfaces of anatomical volumes.

### 4.2.3 Coupling Variables

The connections between the surfaces surrounding the implant are still dictated by the user, but the main difference compared with the previous chapter is that now one surface can be directly connected to more than one surface. Since each surface possesses a different number of pores, only the one with fewer pores will be fully connected. On the other surface, a number of pores will still be available for other connections.

Since the surface couplings differ from case to case, they will be explained for both case studies.

Once the surfaces to be connected have been set, the algorithm randomly selects a pore location on each surface to be included in the same multi-section solid. Since the location of pores is irregular, they are identified by a string variable containing the name of the surface

followed by a progressive number. This variable also includes information on the status of the point - whether it is connected or not. An example of such a string variable is as follows:

$$\underbrace{\text{Surface\_1.}}_{\text{SurfaceID}} \underbrace{\overset{\text{PointID}}{138}}_{\text{status}} \underbrace{.connected /.non\_connected}_{\text{status}}$$

If  $N_1$  and  $N_2$  are the numbers of non-connected points on each surface, two random numbers from 1 to  $N_1$  and  $N_2$  respectively are generated by using the expression (2.3). Both  $N_1$  and  $N_2$  are automatically computed and updated by the design routines after each connection. By using such variables, the algorithm can identify and randomly associate two non-connected sections to be included in a multi-section solid.

#### 4.2.4 Rods Paths

In the first case study, each path was defined by a three control point curve, the first and the third of which coincided with the first points of the cross-sections. The second control point was set constantly as the centre of the implant, meaning that all the rods converged on it, as shown in chapter 3 - case 5.

In the other case study, the second control point of the curve was randomly varied within a volume around the centre of the implant. As in chapter 3, case 6, the volume was defined as a cube of 4 mm size, concentric to the implant.

Because of the irregularities of anatomical volumes, run-time errors are more likely to occur than on cubic volumes. In such cases, it is essential to properly manage run-time errors in order to reduce the computational time and the number of random parameters to be generated. The modification of the tangent values on the two cross-sections is often not sufficient to solve geometrical errors with anatomical volumes, even after a large number of attempts.

In both case studies, the rod path was modified after a run-time error, as this was the most effective way to solve impossible geometrical situations incurred. The modification involved the removal of the second control point of the 3D curve, and the introduction of two tangential directions and two tensions. The two directions specified a tangency constraint on the endpoints, while the two tensions represented the magnitude of the tangential vectors.

In both cases, the tangential directions were defined as the inner-pointing normals to the two planes containing the cross-sections. An example is shown in Fig. 4.7.

Initially, the magnitudes were set at a low value (0.1 mm), and were increased by 0.1 mm for each further step required to solve the error. Although the change of rod path alone solved most run-time errors, in some cases a more 'guided' path was required, hence the necessity of modifying the magnitude of the tangential vectors.

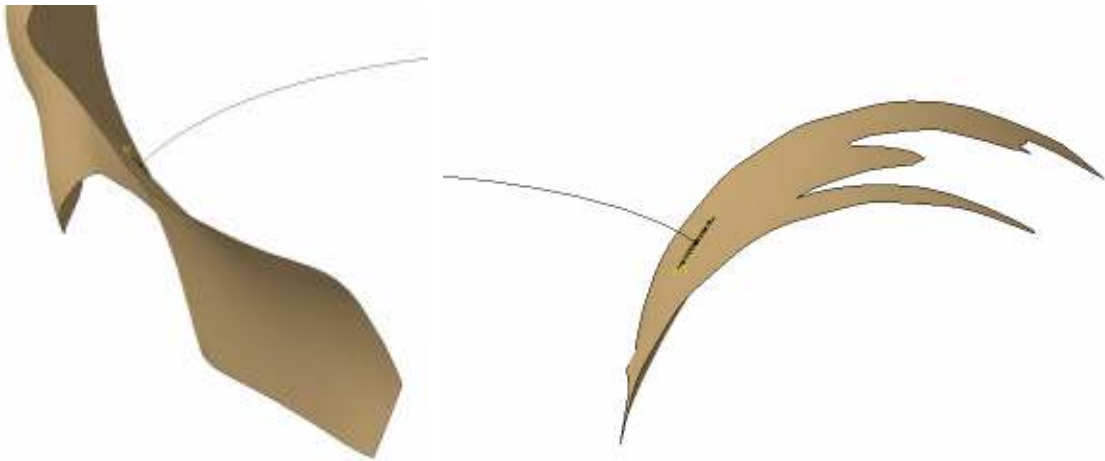


**Fig. 4.7** Example of the tangential directions defined as inner-pointing normals to the two planes containing the cross-sections.

#### 4.2.5 Volumetric Variables

Anatomical volumes are described by the surfaces surrounding them. In the two case studies presented in this chapter, each surface was identified by a name and an orientation, defining the inner side of the volume. The latter parameter was used in the correction due to run-time errors, so as to define the correct sense of the tangential vectors at the end points of the 3D curve.

For this methodology, either STEP or IGES formats are required, as the geometrical entities have to be recognised and used by CAD software.

The two anatomical models used in this chapter were provided externally in STEP format, the first from the QMC, relative to the clinical case study shown in Fig. 3.13, and the second from a company specialised in the development and manufacturing of micro-tomography equipment (SkyScan Inc, Belgium). Fig. 4.8 shows the mouse humerus volume used in the

second case study. For both geometries, the main surfaces were extracted from the manifold solids, and imported in CatiaV5R16.

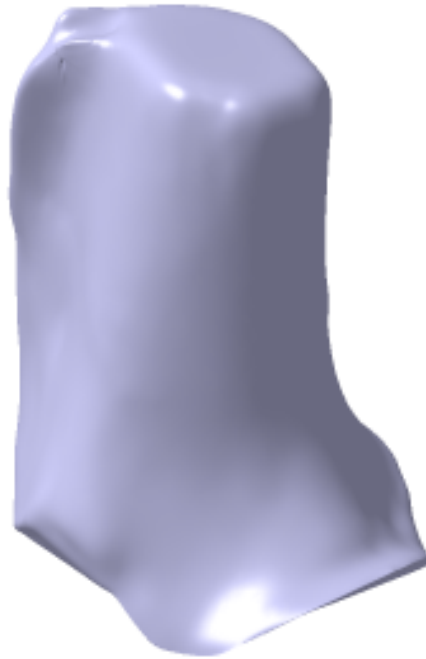


**Fig. 4.8** Anatomical volume of a mouse humerus, reconstructed from a  $\mu$ CT scan.

#### **4.2.6 Output Variables**

The scaffold geometry was evaluated in accordance to its porosity as determined using expression (2.2) in section 2.4.7, while the methodology was assessed by file size and design time. File sizes were specified for both rod network and scaffold geometry, whereas computational time referred only to the rod network. This last parameter was computed by adding the time required to design all the pore locations and rods, and compared with the estimated time for manual design. The computational time for the scaffold structures was also reported, although it was less significant as it did not require any random number generation.

#### **4.3 Results**

In each case study, two structures are provided - the rod network and the scaffold geometry. The automated design was programmed to generate the rod networks, which was subsequently converted to the scaffold structure by using a dedicated routine, as explained in section 2.5.4. Chapter 3 - case 5 and case 6 rod networks were applied to the first and second

anatomical volume respectively. There was no need to associate a particular network design with a particular form of anatomy, as the purpose of these case studies was to test the two curved networks on representative anatomical volumes.

#### 4.3.1 Case Study 1: Craniofacial Implant

The anatomical geometry for a theoretical bone replacement implant used in this case study is shown in Fig. 3.13, while Fig. 4.9 shows the notation used to identify the main surfaces surrounding the volume.

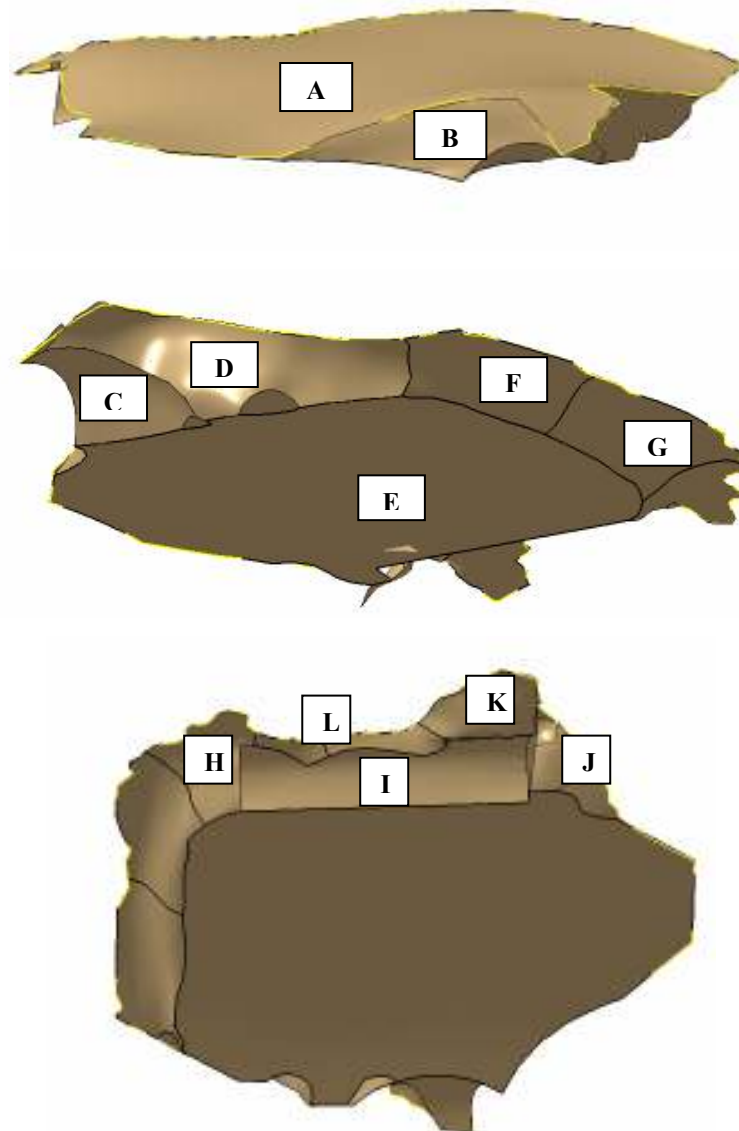


**Fig. 4.9** Main surfaces surrounding the craniofacial implant and relative notation.

Fig. 4.10 shows the pore locations on each surface, while Table 4.1 shows the input and output data used to define them. The  $X$ ,  $Y$  and  $Z$  abbreviations on Table 4.1 refer to the unit vectors of the absolute system of co-ordinates adopted for the implant.

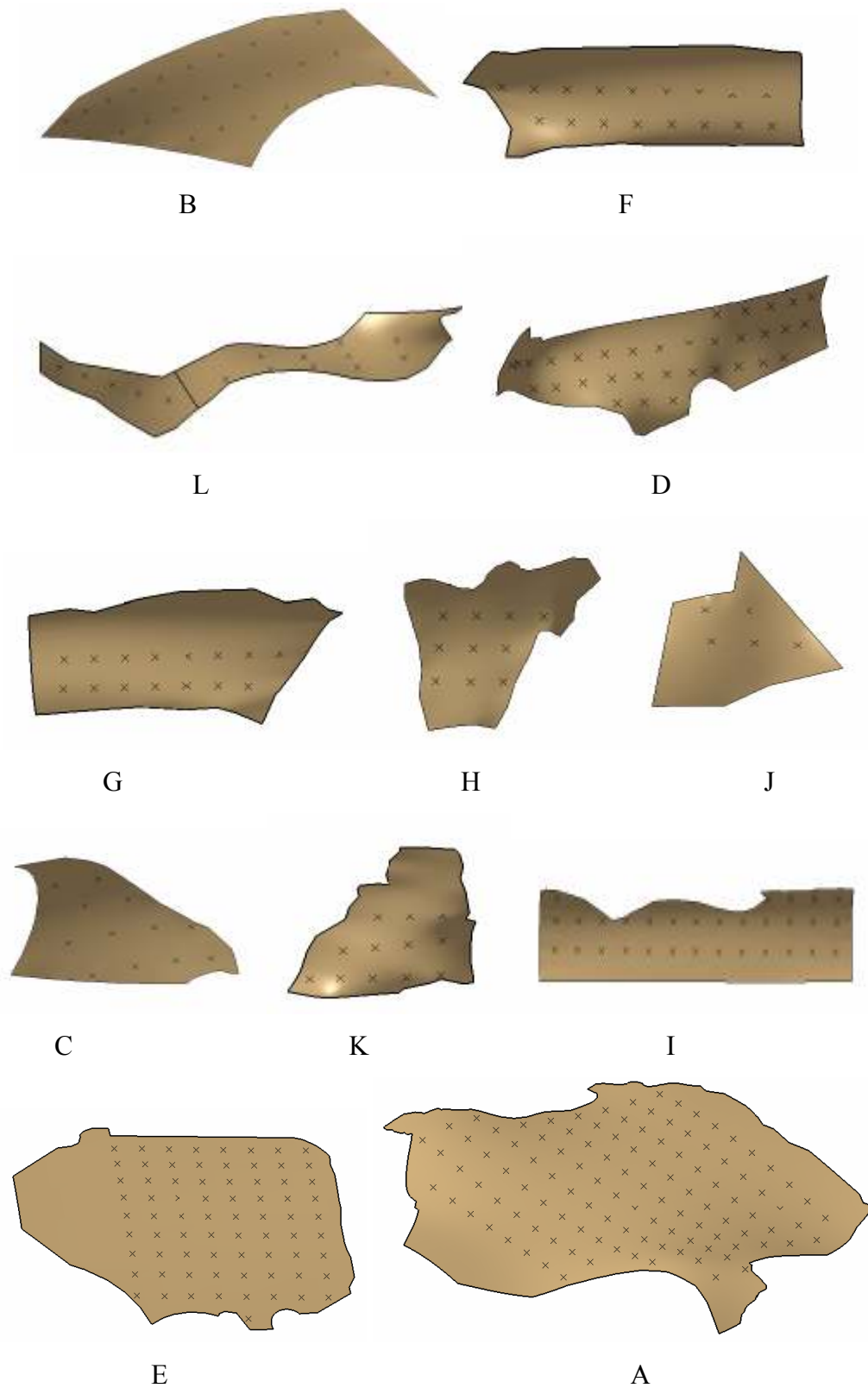


**Fig. 4.10** Pore locations on the main surfaces surrounding the craniofacial implant.

Surface	Unit Vector 1 - d1 - (X,Y,Z)	Unit Vector 2 - d2 - (X,Y,Z)	Spatial Resolution d1 (mm)	Spatial Resolution d2 (mm)	Border Distance d1 (mm)	Border Distance d2 (mm)	Number of points	Computational Time (s)
A	Z	X	3.0	3.0	3.5	1.5	111	70
B	0.923, -0.218, 0.317	-0.322, -0.906, -0.275	1.5	1.5	0.5	0.5	25	20
C	-0.743, 0.524, 0.415	-0.146, 0.183, -0.972	2.0	2.0	0.5	0.5	12	5
D	0.5064, -0.203, -0.838	-0.046, 0.953, -0.298	1.5	1.5	0.3	0.3	33	27
E	Z	X	3.0	3.0	1.5	1	73	55
F	0.993, 0.114, -0.028	-0.211, 0.810, -0.546	1.5	1.5	1.0	1.0	17	10
G	0.995, 0.046, 0.081	-0.1, -0.54, 0.836	1.5	1.5	1.0	1.0	15	8
H	0.729, 0.577, -0.368	-0.565, 0.078, -0.82	1.5	1.5	0.5	0.5	10	5
I	Z	Y	1.5	1.5	0.5	0.5	31	25
J	Y	Z	1.0	1.0	0.5	0.5	5	2
K	X	Z	1.5	1.5	0.5	0.5	12	5
L	-0.43, 0.097, 0.898	0.823, 0.413, 0.39	1	0.5	0.5	0.5	15	8
-	-	-	-	-	-	-	-	Total: 240 s

**Table 4.1** Input and output data used to define the pore locations on the craniofacial implant.

The connections established among the different surfaces are summarised in Table 4.2. As explained in section 4.2.3, some surfaces present more than one connection, while others possess unconnected pores. The connecting surface pairs were arbitrarily selected by the user to be approximately opposite.

Surface 1	Surface 2	Initial Points Available on Surface 1	Initial Points Available on Surface 2	Number of Rods (Channels)	Final Points Available on Surface 1	Final Points Available on Surface 2	Computational Time (s)
L	C	15	12	12	3	0	45
F	I	17	31	17	0	14	55
K	D	12	33	12	0	21	46
D	I	21	14	14	7	0	50
H	D	10	7	7	3	0	35
G	B	15	25	15	0	10	52
B	L	10	3	3	7	0	20
J	B	5	7	5	0	2	25
H	B	3	2	2	1	0	10
A	E	111	73	73	38	0	209
-	-	-	-	Total: 160	-	-	Total: 547 s

**Table 4.2** Surface couplings used to design a network of rods in the craniofacial implant.

One point on surface H and thirty eight points on surface A resulted as unconnected, because no points on their opposite surfaces were available. The time required by this methodology to design the entire rod network was 240 seconds for the pore locations, plus 547 seconds for the multi-section solids. Since the overall geometry was composed of 160 interconnected rods, the average design time was 4.9 s/rod.

Fig. 4.11 shows the individual groups of connections explained in Table 4.2. Since craniofacial implants are essentially flat, most connections (from 1 to 9) were in the main plane, while connection 10 was between the two top surfaces of the volume (A and E). A perspective view of this last local network is shown in Fig. 4.12.



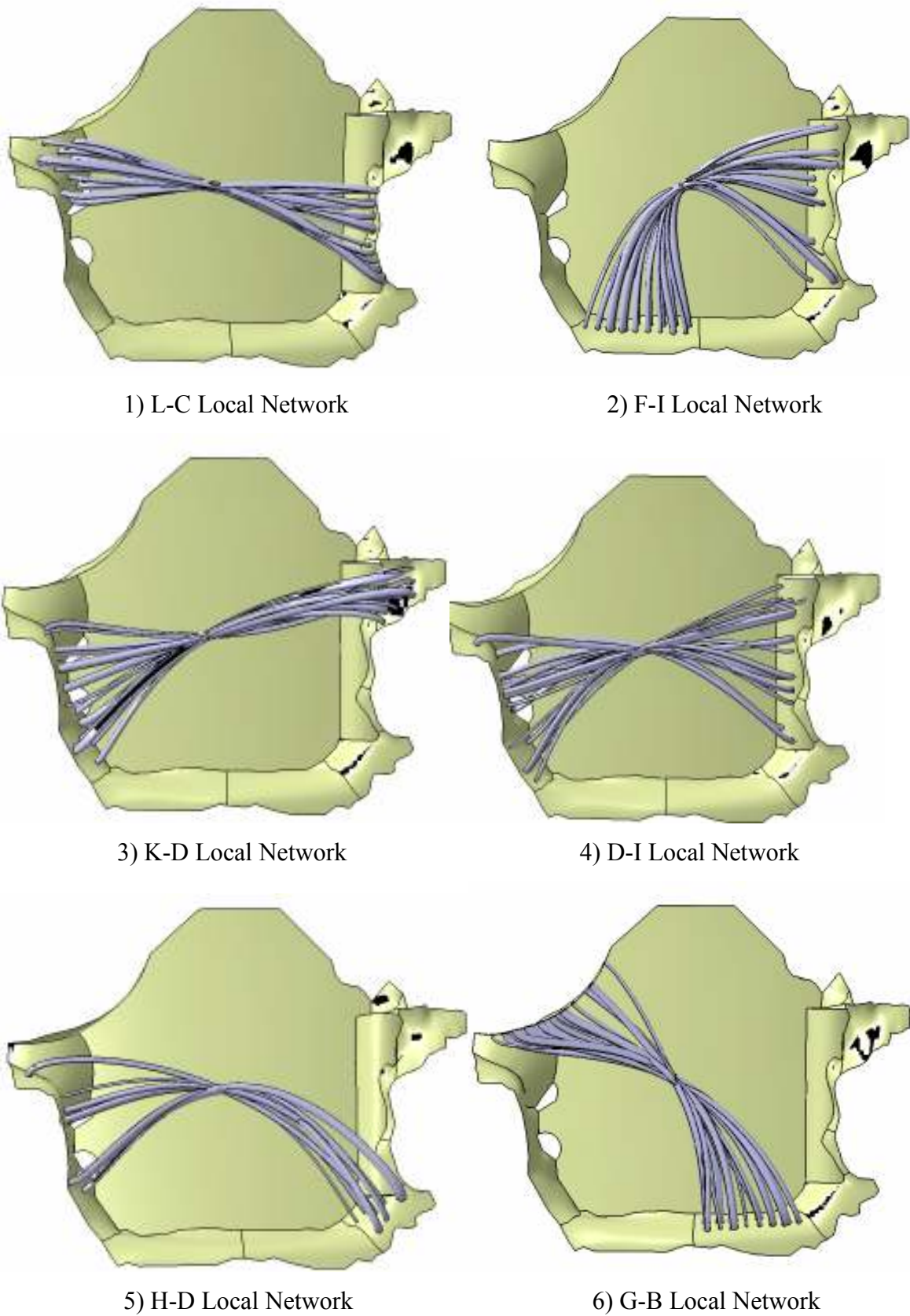


*Fig. 4.11 (continued)*

Fig. 4.11 (continued)

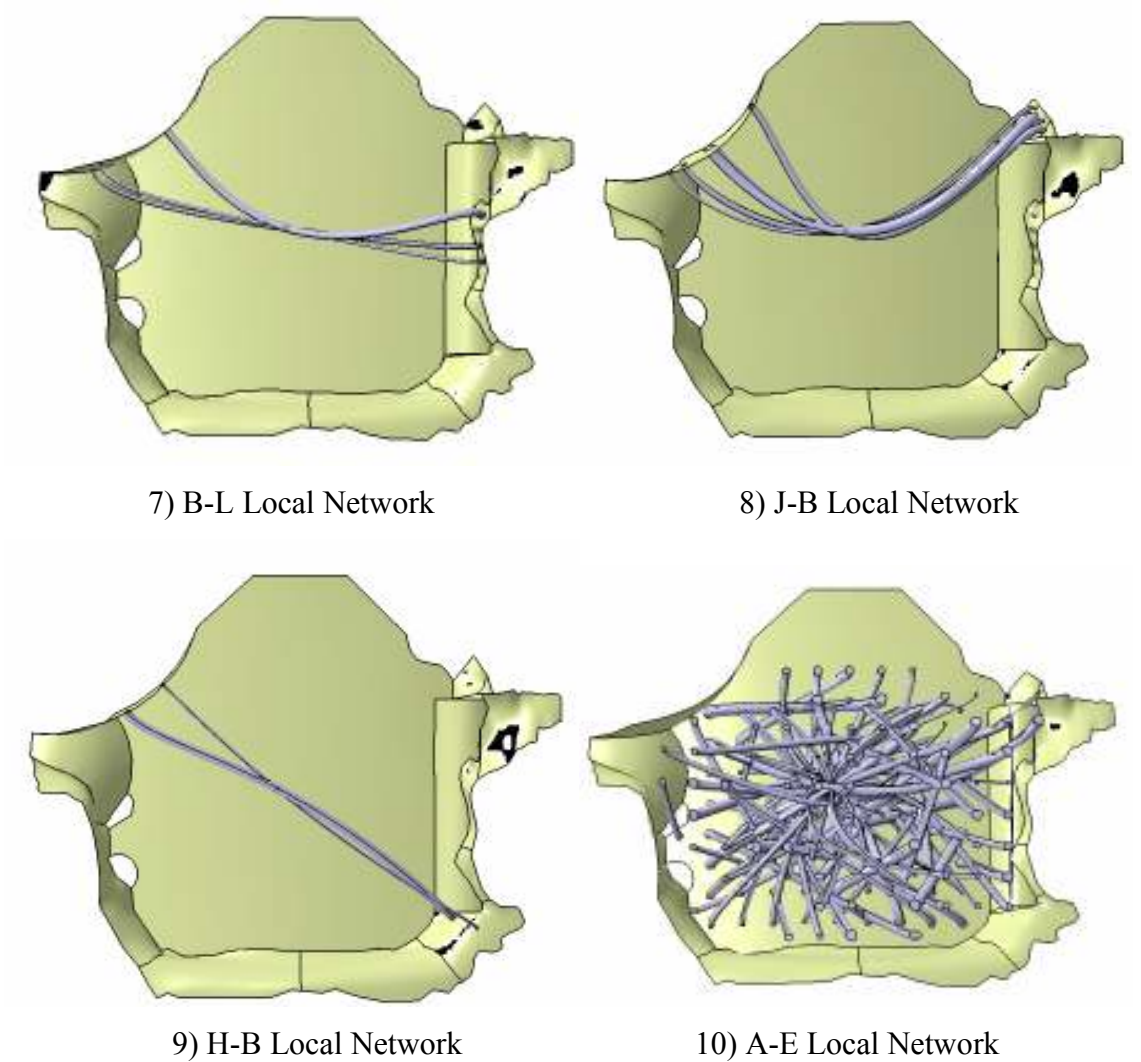


Fig. 4.11 Singular groups of connections, as explained in Table 4.2.

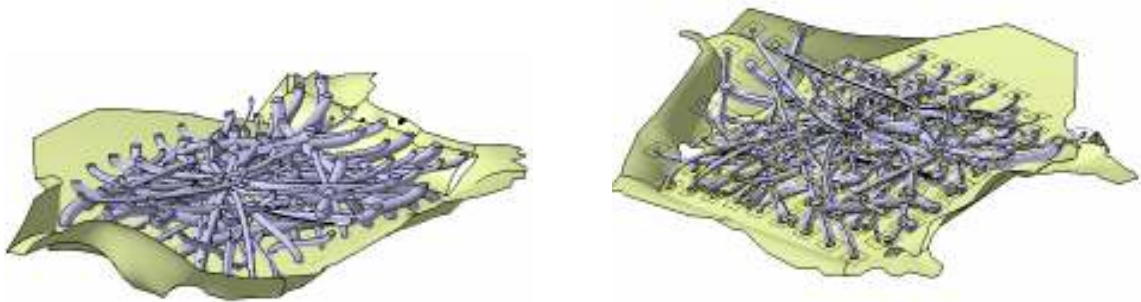
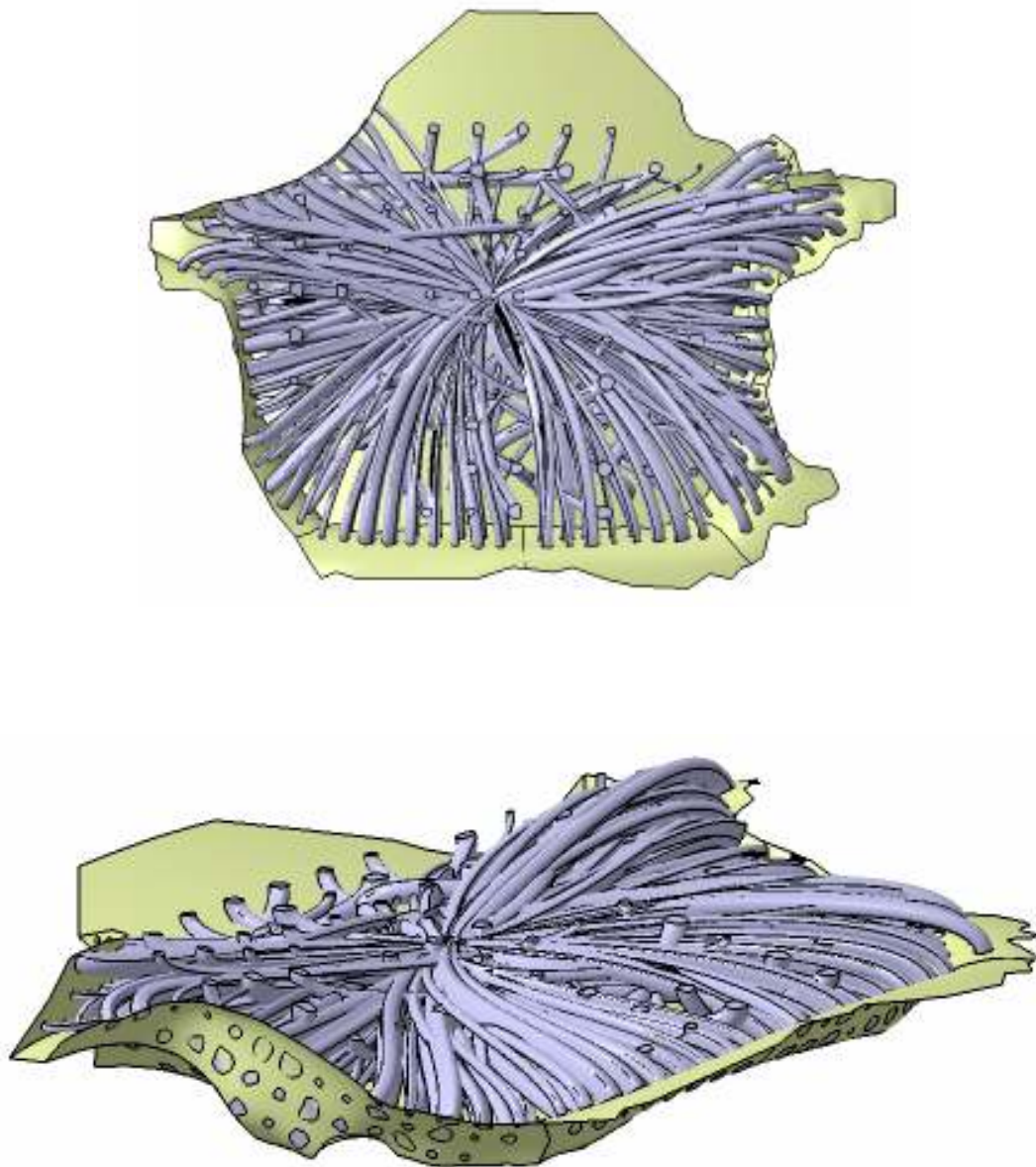


Fig. 4.12 Perspective view of the A-E transversal network

Fig. 4.13 shows the whole network of rods enclosed by the external surfaces of the anatomical volume.



**Fig. 4.13** Global network of rods enclosed by the surfaces surrounding the craniofacial implant.

For craniofacial implants, which are essentially flat bones (Ono *et al.*, 1992, Schaaf *et al.*, 2008), the two top surfaces of the volume can be extruded by a given thickness to mimic the compact bone layers surrounding the trabecular bone. Fig. 4.14 shows the structure obtained by setting a thickness of 1mm on each respective surface. The addition of the 1mm thickness



at the top and bottom surfaces was made after the creation of the channels, with the purpose of evaluating the feasibility of such features, since in this sample they would close off the channels passing between the two largest surfaces. For that reason, if the methodology were used properly, these surfaces would not be used to produce channels.

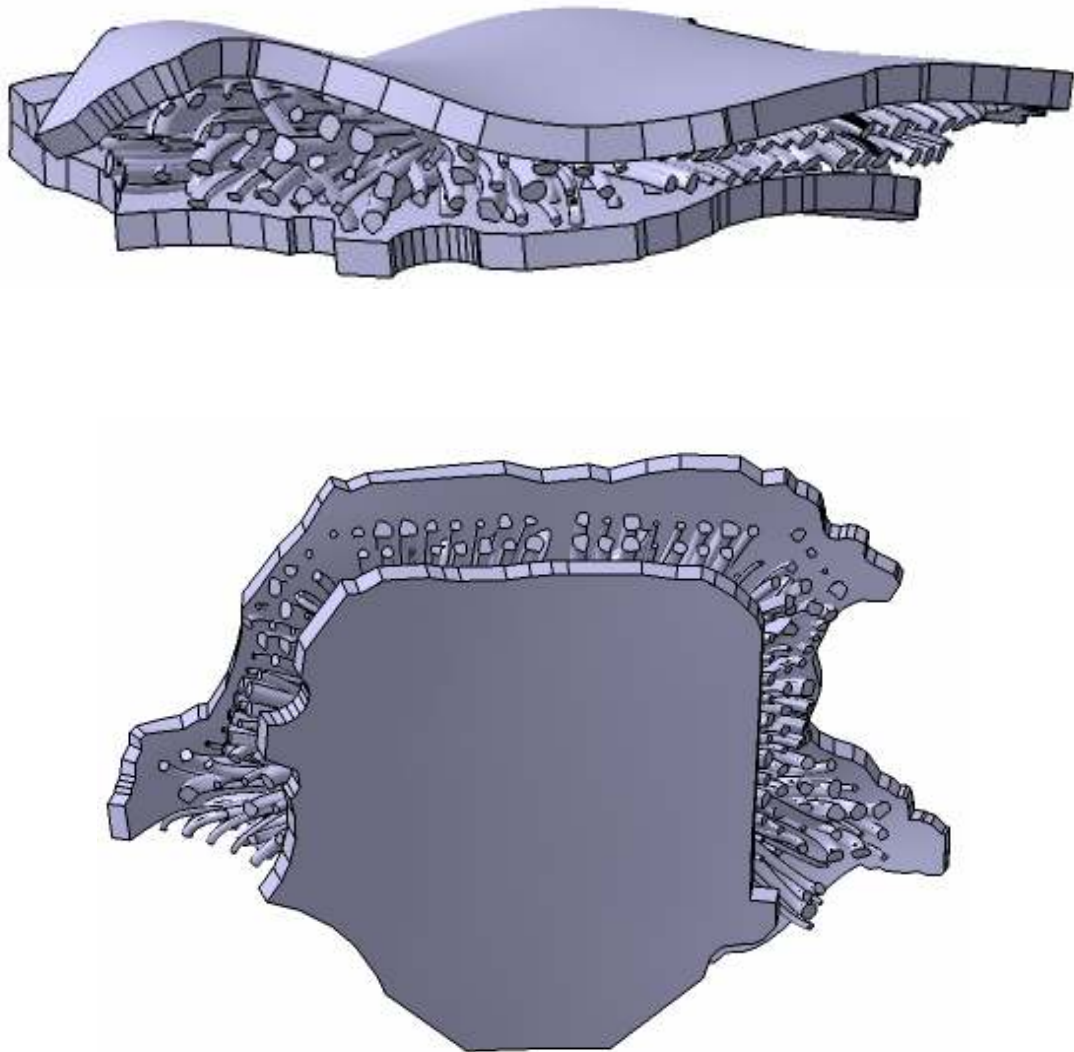


**Fig. 4.14** Simulated trabecular and compact bone structures.

The complementary scaffold has been automatically designed from the rod network, and is shown in Fig. 4.15. The design time for the scaffold, including the time required to delete the solid rods, was 356 seconds.

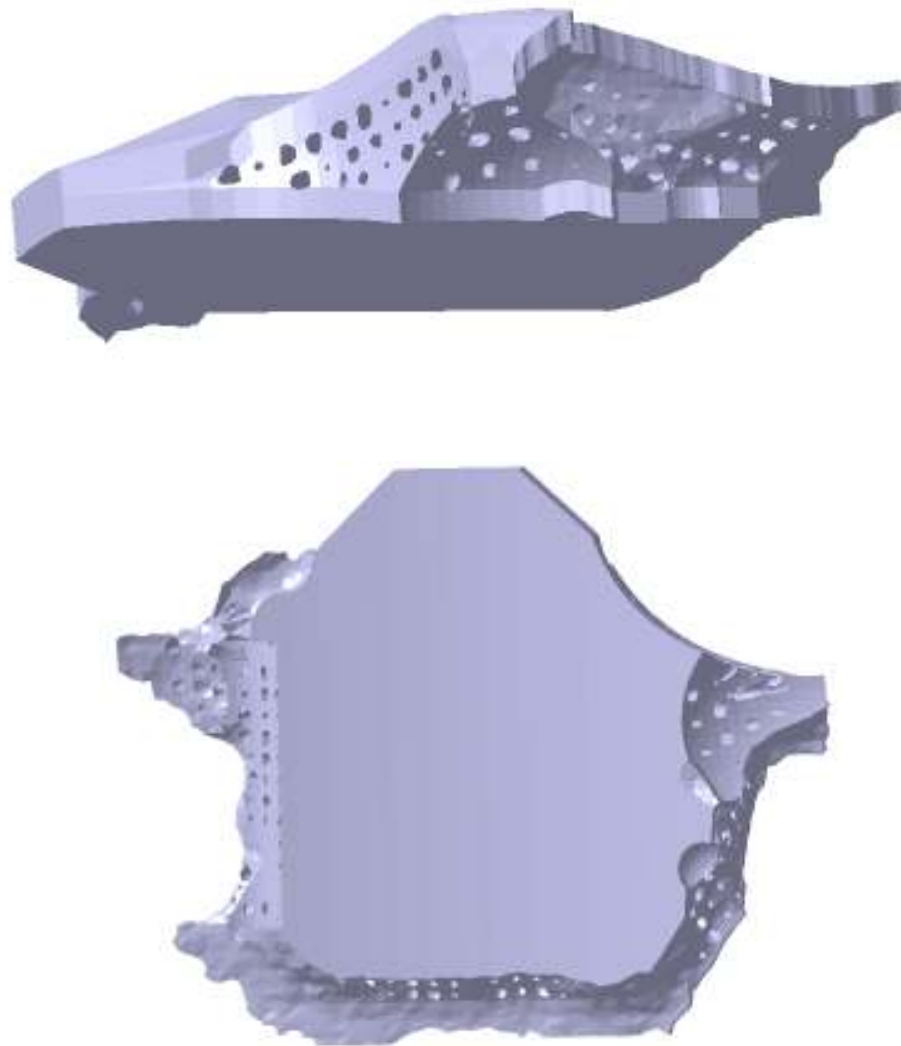


**Fig. 4.15** Scaffold geometry for the craniofacial implant analysed.

Table 4.3 summarises the output data for both rod network and scaffold geometry.

<b>Implant</b>	STEP file size	15 MB
<b>Rod network</b>	Computational time	787 s
	Average computational time/rod	4.9 s/rod
	Estimated time manual design/rod	75 s/rod
	Catia file size	43.4 MB
	STL file size (ASCII)	48 MB
<b>Scaffold</b>	Catia file size	98 MB
	STL file size (ASCII)	41.4 MB
	Porosity %	53.4%
	Computational time	356 s

**Table 4.3** Output data for rod network and scaffold geometry

#### 4.3.2 Case Study 2: Mouse Humerus

The anatomical geometry for a theoretical bone replacement implant used in this case study is shown in Fig. 4.8, while Fig. 4.16 shows the notations used to identify the main surfaces surrounding the volume.

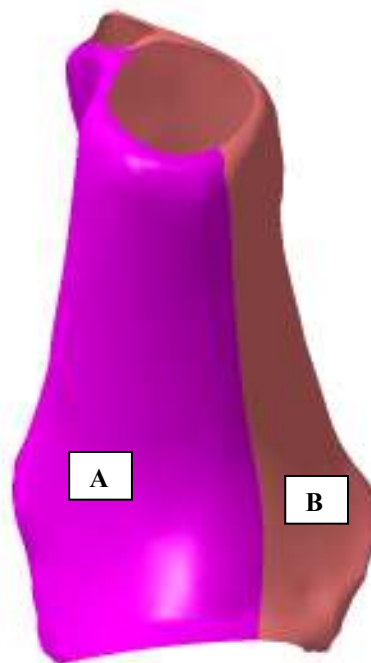
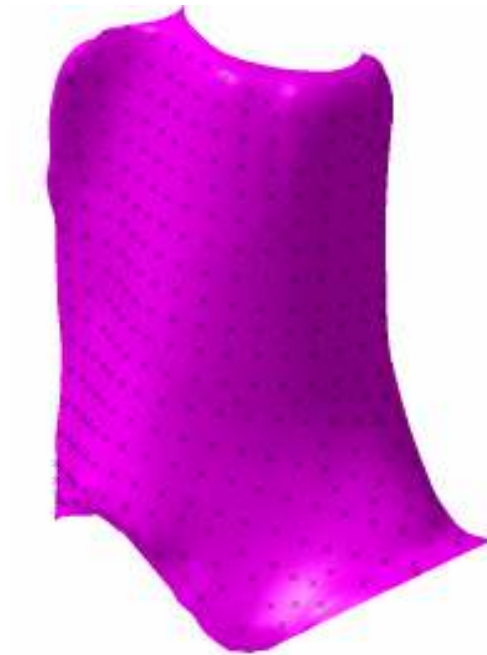
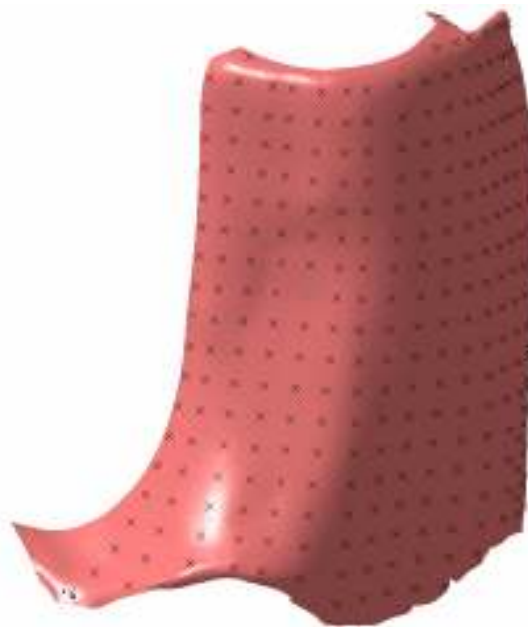


**Fig. 4.16** Main surfaces surrounding the mouse humerus implant.

Fig. 4.17 shows the pore locations on each surface, while Table 4.4 shows the input and output data used to define them.



A



B

**Fig. 4.17** Pore locations on the main surfaces surrounding the mouse humerus implant.

Surface	Unit Vector 1 - d1 - (X,Y,Z)	Unit Vector 2 - d2 - (X,Y,Z)	Spatial Resolution d1 (mm)	Spatial Resolution d2 (mm)	Border Distance d1 (mm)	Border Distance d2 (mm)	Number of points	Computational Time (s)
A	-0.869, 0.325, -0.373	-0.372, -0.927, -0.041	1.25	1.25	0.25	0.25	297	289
B	0.748, -0.365, 0.554	0.175, 0.93, 0.307	1.25	1.25	0.25	0.25	284	250
-	-	-	-	-	-	-	-	Total: 539 s

**Table 4.4** Input and output data defining the pore locations on the mouse humerus implant.



Since only two main surfaces were present in this case study, one surface coupling was required, as shown in Table 4.5.

Surface 1	Surface 2	Initial Points Available on Surface 1	Initial Points Available on Surface 2	Number of Rods (Channels)	Final Points Available on Surface 1	Final Points Available on Surface 2	Computational Time (s)
A	B	297	284	284	13	0	2385
-	-	-	-	Total: 284	-	-	Total: 2385 s

**Table 4.5** Surface coupling used to design a network of rods in the mouse humerus implant.

Thirteen points on the surface A resulted as unconnected, because no other points on the opposite surface were available. The time required by this methodology to design the entire rod network was 539 seconds for the pore locations, plus 2385 seconds for the multi-section solids. Since the overall geometry was composed of 284 interconnected rods, the average design time was 10.29 s/rod.

Fig. 4.18 shows the whole network of rods for this case study, while Fig. 4.19 illustrates the scaffold geometry. The design time for this scaffold, including the time required to delete the solid rods, was 1800 seconds.

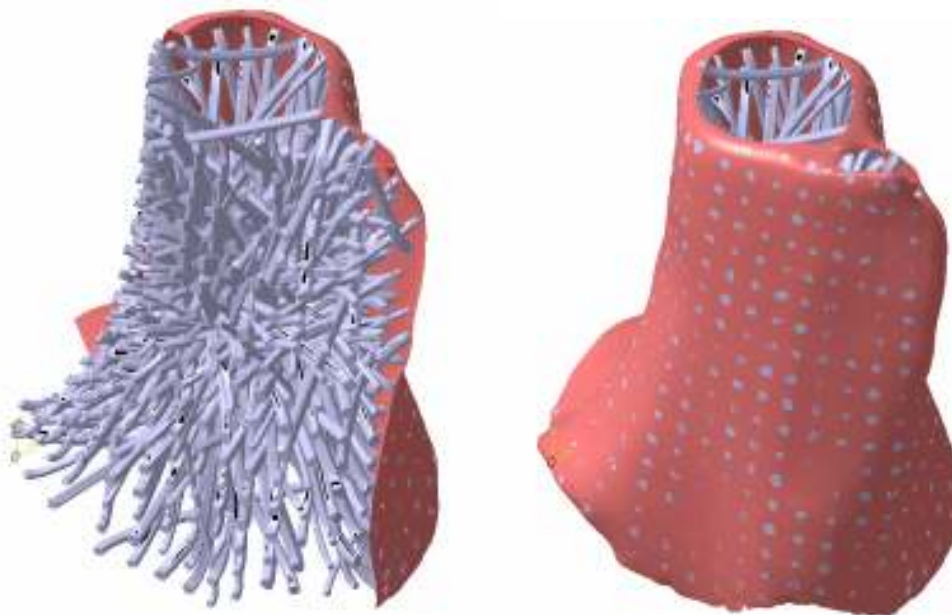


**Fig. 4.18** Global network of rods enclosed by the surfaces surrounding the mouse humerus implant.



**Fig. 4.19** Scaffold geometry for the mouse humerus implant analysed.

The main output data for the two geometries are summarised in Table 4.6.

<b>Implant</b>	STEP file size	6.40 MB
<b>Rod network</b>	Computational time	2924 s
	Average computational time/rod	10.29 s/rod
	Estimated time manual design/rod	75 s/rod
	Catia file size	95 MB
	STL file size (ASCII)	87.8 MB
<b>Scaffold</b>	Catia file size	102 MB
	STL file size (ASCII)	89.1 MB
	Porosity %	30.15%
	Computational time	1800 s

**Table 4.6** Output data for rod network and scaffold geometry

#### 4.4 Review

The integration process explained in this chapter was able to successfully design complex networks of interconnected rods of different pore size and shape into generic anatomical volumes, derived from CT scan data.

The ADI methodology was assessed by computational time and file size. In both case studies, the average computational time per rod (4.9 s/rod for the first case, 10.3 s/rod for the second case) was significantly lower than the estimated time for manual design (75 s/rod). The Catia and STL file sizes for the rod networks did not present processing delays or storage difficulties for a standard specification computer (43.4 MB and 48 MB for the first case, 95 MB and 87.8 MB for the second case). As explained in section 3.4, STL files generated in CATIA V5R16 were in ASCII format, as that was the default setting used in the software. As CATIA V5R16 software does not allow the user either to select the STL format, or to alter the parameters used to generate STL geometries, the standard settings had to be used (CATIA V5R16 has a dedicated module for advanced STL manipulation, which was not available for this project).

The computational time for scaffold geometries was smaller than the respective time required for the rod networks, because of the method used to design them. The use of a dedicated routine to replace the rods with channels requires additional time to delete the rod network, leaving all the wireframe geometries that contain the information about the structure. In addition, no random numbers need to be generated by such routines, and therefore no corrections to the geometry are required. The Catia and STL file sizes for the scaffolds did not present processing delays or storage difficulties for a standard specification computer, although they were bigger than the respective rod networks (98 MB and 41.4 MB for the first case, 102 MB and 89.1 MB for the second case). ASCII STL files were used for the same reasons specified above.

The efficiency of the ADI methodology was related to design time and based on a comparison with estimated manual design time. In this sense, the results presented in this chapter prove the efficiency of the ADI methodology, which also eliminates the need for Boolean operations.

At this stage, the assessment of the produced geometries has been performed by using the scaffold porosity as the only parameter, because little other quantified data about the optimum scaffold topology is available from literature. In addition, the porosity requirements are vague, as wide ranges from 50% to more than 90% are usually quoted.

The scaffold produced in the first case study had a porosity close to the lower limit of this range (53.4%), while the second scaffold was below that value (30.15%), and therefore it fell outside the specifications. That was mainly due to the maximum pore size, which was limited to 0.4 mm. Naturally, the rod networks present the complementary values of porosity.

The ADI methodology used so far only allows for the quantification of the total porosity to characterise a scaffold geometry, while in reality the porosity of a bone varies across its sections. Therefore, if a structure is to be designed to match a given variation in porosity for a given bone or bone location, a method of ascertaining that porosity variation is required.

---

## **CHAPTER 5**

### **- POROSITY AND PORE SIZE ANALYSIS IN TRABECULAR BONE STRUCTURES -**

#### **5.1 Introduction**

The ADI methodology proposed in the previous chapter has the potential to automate the entire design process by controlling a set of predefined parameters. As a result, an internal geometry could be automatically integrated within a global design as dictated by different input variables, thus producing very complex architectures suitable for many different applications. Depending on the application, the appropriate requirements can be fully or partly defined. When this methodology is applied to the design of trabecular bone-like internal structures, such as TE scaffolds, there is a difficulty in assessing the resultant design due to substantial lack of knowledge of the quantified characteristics of the optimum target geometry.

The literature review on this topic (section 1.3.3) has shown that for bone TE there are only vague quantifications about the pore size range considered suitable for regenerating bone, and there is no information regarding pore distribution and shape. There is a consensus that natural tissue geometries should act as a design inspiration (Hutmacher et al., 2001; Starly and Sun, 2002), but even the description of trabecular bone structures is not well defined, as most research efforts have been focused on investigating the global mechanical properties of bones, rather than analysing the geometrical internal trabecular architectures in detail (sections 1.3.3 and 1.4).

Therefore, there is a significant lack of knowledge about the appropriate requirements of all those applications that require bone-like geometries, which can compromise any design effort aimed at replicating the internal trabecular architectures.

To partially overcome the lack of data on such architectures, this chapter presents a novel methodology for the investigation and analysis of bone internal structures, which can lead to a better understanding and characterisation of trabecular bone geometries, with consequent

benefits for their design. In particular, the methodology of analysis proposed in this chapter can be applied to assess a design methodology, by quantifying and comparing specific properties of both target and simulated structures, and by highlighting the differences, strengths and weaknesses of a particular design.

The objective of this chapter was to produce new quantified data for trabecular bone geometries in order to evaluate and assess the automated design methodology presented in chapter 2. This was conducted by comparing the scaffolds' complementary geometries produced in chapters 3 and 4, which will be referred to in this chapter as ADI samples (either on cubic or anatomical volumes), with real trabecular bone samples.

This methodology of analysis was tested on one cubic  $\mu$ CT sample and the mouse humerus  $\mu$ CT sample, as well as on cases 5 and 6 described in chapter 3 and the second case study from chapter 4.

The two cubic ADI samples were compared with the cubic  $\mu$ CT sample, while the mouse humerus ADI sample was compared with the relative  $\mu$ CT sample. The properties analysed were the distributions of trabecular and sliced area, and the number of trabeculae, in three orthogonal directions (further described in section 5.2.3).

Although the results are specific to the samples adopted for the purposes of this research, they also illustrate the potential of this analysis methodology to be used for further investigations, leading to a better quantitative assessment of trabecular bone architectures.

## 5.2 Methodology of Analysis

The approach developed in this chapter consisted of analysing trabecular bone structures through the study of their sequential slice data. This primarily involves a 3D computerised description of the volume object of investigation, which is sliced in three orthogonal directions in order to obtain the mathematical description of the cross-sections. These data are subsequently analysed to produce the quantified description necessary to characterise the geometry. Since the same analysis can be carried out on both target and simulated geometries, it provides a directly comparable approach for assessing different design methodologies.

Triangular meshes in STL format were produced from  $\mu$ CT bone scans and used to provide the target geometries. Those geometries were subsequently sliced and analysed, as explained in the following sections.

In this work, the analysis of trabecular bone geometries was performed starting from STL representations rather than the pixel data from which STL geometries are derived. That was because according to Odgaard (1997), computerised 3D descriptions of trabecular geometries allows the direct study of such architectures with no restrictive assumptions, as well as the direct quantification of any parameter pertaining to the internal architectures. The analysis of pixel data would have required assumptions on bone morphology that could be difficult to verify (Odgaard, 1997).

In addition, STL representations are more suitable to assess a design methodology, as CAD softwares always produce computerised geometrical descriptions. As a result, it would not have been practical to compare pixel data of target structures with STL representations of the proposed CAD geometries, whose slices are mathematically described by polygons rather than pixels. In order to compare the produced designs with the required target structures, the same type of representation should be used. Since the comparison involves the quantification of the two geometries, mathematical representations are required for both structures.

STL files generated from  $\mu$ CT scans were used throughout this work in binary format, since high resolution scans usually produce large amount of data, which would be impractical for a standard specification computer to handle. In such cases, the binary format can significantly reduce the file size compared with the ASCII format. Another reason for using STL binary format for the  $\mu$ CT samples was that they were supplied externally (from Istituti Ortopedici Rizzoli, Italy, and Sky Scan Inc, Belgium) and therefore there was no opportunity either to alter the quality parameters or to change the STL format.

### 5.2.1 Slicing

Starting from the STL representation of the desired structure, specific software (Magics by Materialise, Leuven, Belgium) was used to slice the STL model in different orientations. Fig. 5.1 shows the main slicing parameters accessible in Magics. The default slicing orientation is the Z axis, but the user can rotate the parts in order to select other orientations. These parameters are classified into three separate groups:

- 
1. Fix parameters, which are used to close and adjust all the contours in a cross-section.
    - The 'gap fill' menu is used to close open contours that present a maximum specified gap. The other field can be used to specify a number of iterations, as gaps are evaluated after each iteration. In this work, the first value was set to 0.01 mm, while the second value was set to 5 (default).
    - The contour filter menu automatically removes small contours, meaning that all the open and closed contours smaller than the values specified in the relative fields are removed. In this work, both values were set to 0 mm.
    - The 'smoothing' setting reduces the number of vertices in the polylines defining the contours, thus simplifying their geometry. As a consequence, the size of the slice file is reduced, but small details can be lost. In this work no smoothing was conducted so as to retain all the small details.
  
  2. Slice parameters, which contain explicit slicing variables.
    - Tool compensation is an AM-machine dependent setting, such as the radius of the laser beam or the average particle size. In this work, the setting was kept to 0, as manufacturing aspects were not considered.
    - The layer thickness represents the distance between two consecutive slicing planes. In this work, two values were used, 0.1 mm or 0.2 mm, depending on the case study. The second value was used for the mouse humerus  $\mu$ CT sample, mainly to reduce the computational time in the Z axis, which would have been significantly bigger due to the large number of slices and data obtained with the 0.1 mm setting. In both cases, the resultant data quality was compromised compared with the resolution of the scan data, and if the methodology were used properly, a smaller value would be used. However, the proposed values were suitable for the purpose of testing and assessing the analysis methodology. In addition, the 0.1 mm value used for the cubic  $\mu$ CT sample limited the number of iterations and voxels in the ABDI algorithm proposed in chapter 6, thus reducing significantly the computational time required to design bio-mimetic structures.
  
  3. Slice format, which specifies the format for the slicing file. Magics slicer supports the formats CLI (Common Layer Interface), SLC (StereoLithography Contour) and
-



SSL (Stratasys Slicing Language). The first two are binary formats and need to be decoded, while the third is in ASCII (American Standard Code for Information Interchange) text. In this work, the SSL format was used, in order to preserve accuracy and avoid further numerical conversions. In addition, ASCII code SSL representation was required because the rest of the programming in this project was done by using ASCII code and therefore binary format would need decoding.

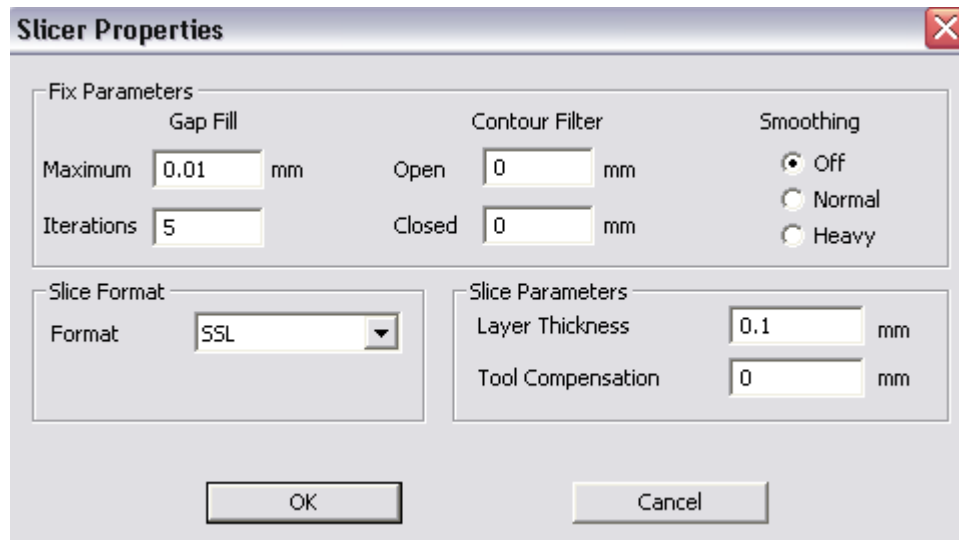


**Fig. 5.1** Dialog window showing the slicing parameters.

### 5.2.2 SSL File Structure

The structure of the SSL file format is illustrated in Fig. 5.2 and shows the data describing the first layer of a 5 mm square box containing a 3 mm square hole. The structure starts with the version of the slicer used (V0), followed by the file name and location, and the units adopted (inches or mm). The geometrical data of the cross-sections are described after the 'Slices ()' statement, starting with the progressive 'Z' co-ordinate followed by the layer thickness (0.1 mm in the example), separated by a blank space.

The co-ordinates of the vertices of each polyline forming a slice are then listed, in the form of 'X' and 'Y' co-ordinates separated by a blank space and followed by an end of line character.

An anti-clockwise orientation of a polyline is used to define the inner side of the section (containing material), while a clockwise orientation defines a void. In the example, the vertices of the first polyline are ordered in an anti-clockwise direction, while those for the second polyline are clockwise. Each polyline is separated by the character 'C'.

After all contours forming a section are listed, the next layer is introduced by the 'Z' character followed by the progressive co-ordinate and layer thickness.

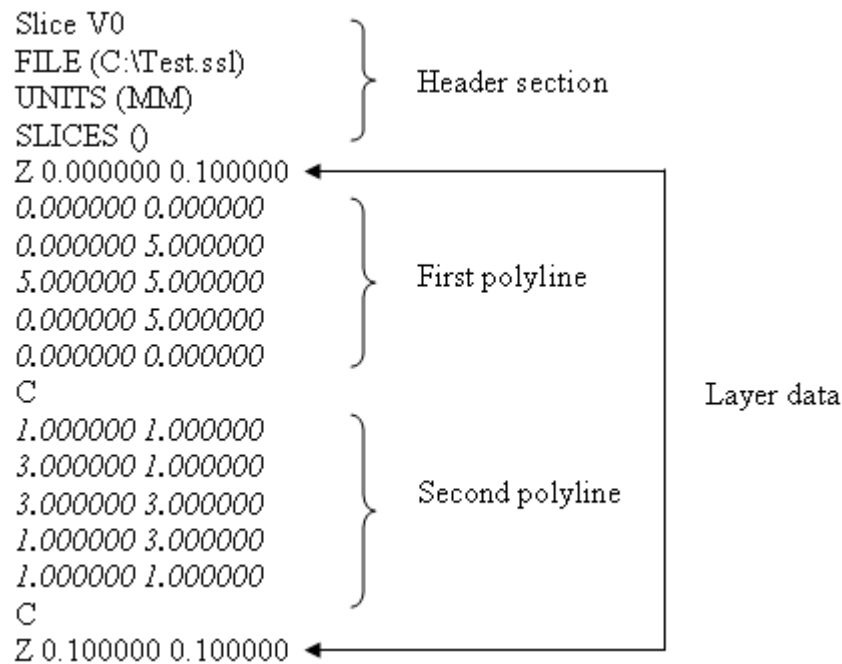


**Fig. 5.2** Structure of an SSL file format.

### 5.2.3 Slice Data Analysis

The slicing process was carried out on the three orthogonal directions defined by a datum co-ordinate system (referred to as  $X$ ,  $Y$ ,  $Z$ , where  $Z$  is normal to the slicing plane), which was different for each case study. Three routines were developed by using the Visual Basic (VB) application included in Excel (both by Microsoft Inc, USA), one to generate a standard template file to store the input and output data, one to read the data contained on each SSL file, and one for analysing the geometry.

#### 5.2.3.1 Template File for Analysis

The first routine generates the template shown in Fig. 5.3 on an Excel spreadsheet, which is used to summarise all the input and output data for the analysis. The template refers to the  $X$  direction, but similar templates are drawn for  $Y$  and  $Z$  on two other spreadsheets.

	A	B	C	D	E	F	G	H
1	X [mm]	Trabecular area [mm2]	X progressive [mm]	Sliced area [mm2]	Number of trabeculae	H bound box [mm2]	V bound box [mm2]	Rod/Plate
2								
3								
4								
5								
6								
7								
8								
9								
10								
11								
12								
13								
14								
15								
16								
17								
18								
19								
20								
21								
22								
23								
24								
25								
26								
27								
28								
29								
30								
31								
32								
33								
34								
35								
36								
37								

**Fig. 5.3** Excel template summarising the all the input and output data for the analysis, in the three directions X, Y, Z.

Each spreadsheet contains the following columns:

- Column A indicates the layer co-ordinate in the slicing direction. This value is repeated for all contours forming the specified layer.
- Column B indicates the area of each individual contour of a cross-section. Together with the previous column, it defines the trabecular area distribution along the slicing direction. If voids are present, the relative area is reported as negative. The computation of the area for each polyline is illustrated in section 5.2.4.
- Column C is similar to the first column except that the co-ordinate is reported once for any given layer.
- Column D is used to compute the total area for a given slice. Together with the previous column, it defines the sliced area distribution along a given direction. This area is computed by adding all the polygonal areas on a given slice.

- Column E indicates the number of closed polylines for the layer specified in the 'C' column.
- Column F indicates the width of the bounding box surrounding the polygon specified in the 'B' column. This value is computed from the minimum and maximum values of the horizontal co-ordinate for each polygon.
- Column G indicates the length of the bounding box surrounding the polygon specified in the 'B' column. This value is computed from the minimum and maximum values of the vertical co-ordinate for each polygon.
- Column H indicates whether the ratio between the area of the polygon specified in the 'B' column, and the area of the bounding box, is above or below a given threshold. In this work, a threshold of 0.6 was proposed. This parameter classifies each polygon as a 'rod' if the ratio is above this limit, or a 'plate' in the opposite case. This threshold is only indicative, and any other value could be set in the routine. Fig. 5.4 shows an example of sliced trabeculae with the ideal bounding box.

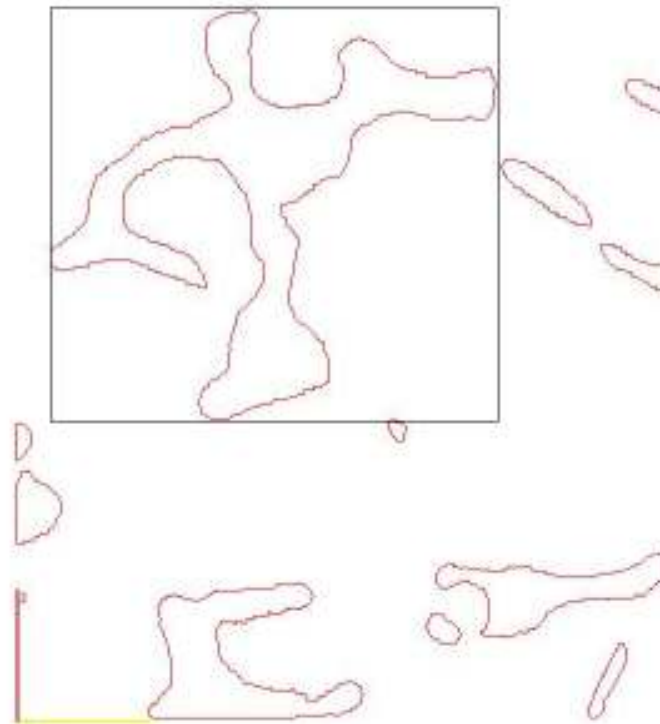


**Fig. 5.4** Example of sliced trabeculae and relative bounding box.

### 5.2.3.2 Input from SSL

The co-ordinates of the vertices of a polyline on a given section are read by using the second routine, which includes the VB set of instructions shown in Fig. 5.5.

```

Open "C:\Test.ssl" For Input As #1
Input #1, a
Data_File = Split(a, "SLICES()")
} Group 1

Slice = Split(Data_File (1), "Z ")
}
For I = 1 To UBound(Slice)
Layer_number= Layer_number + 1
Closed_Curve = Split(Slice(I), "C")
} Group 2

For J = 0 to UBound (Closed_Curve) - 1
Single_line= Split(Closed_Curve(J), vbLf)
}

For K = 1 To UBound(Single_line) - 1
XY_first_point= Split(Single_line (K), " ")
}
If K < UBound (Single_line) - 1 Then
XY_second_point = Split (Single_line (K + 1), " ")
Else
XY_second_point = Split(Single_line (1), " ")
End If
} Group 3

Array_x (K) = CSng(XY_first_point (0))
Array_y (K) = CSng(XY_first_point (1))
Array_x (K + 1) = CSng(XY_second_point(0))
Array_y(K + 1) = CSng(XY_second_point (1))
} Group 4

Next K
Next J
Next I

```

**Fig. 5.5** Set of instructions for input operations on SSL files.

These instructions have been classified into four different groups, as follows:

- The first group specifies the SSL file to be opened and reads all the data contained in the file through the "Input" instruction. The data is stored in the form of a string variable called 'a'. This string is then split after the word "SLICES()", thus separating the header section from the geometrical data, into a two-element array called 'Data\_File'.

- The second group includes three split operations at characters "Z", "C" and "VbLf" (constant used by Visual Basic to indicate the end of line character), which generate three arrays of strings. One array contains all the data on a given layer "I", another contains all the vertexes of a polyline "J" on the layer "I", and the third contains the co-ordinates of the vertex "K" on the polyline "J". Those arrays are called '*Slice*', '*Closed\_Curve*', and '*Single\_line*', respectively.
- The third group is used to extrapolate the individual co-ordinates of a vertex in a string form. The split is performed at the blank character between the co-ordinates, and for two consecutive elements of the array '*Single\_line*', generating two new arrays, named as '*XY\_first\_point*' and '*XY\_second\_point*'. Their elements contain the co-ordinates of two consecutive vertices, named as first and second point. As the polyline is closed, when the former is the last point, the latter must coincide with the starting vertex. This condition is expressed by the "if-then-else" instruction contained in the group.
- In the fourth group of instructions, the co-ordinates are transformed from string form to real numerical values through the use of VB built in function "CSng". The process is then repeated for all vertexes, polylines and layers.

### 5.2.3.3 Output from SSL

After the geometrical information on the slices has been acquired, the third routine computes the area of each polyline by using formula for computing the area of closed non self-intersecting polygons (Zwillinger, 2002):

$$A = \frac{1}{2} \sum_{i=0}^{N-1} (x_i y_{i+1} - x_{i+1} y_i) \quad (5.1)$$

Where:

$N$  = number of vertices.

$x_i$  = horizontal co-ordinate of the generic vertex  $i$ .

$y_i$  = vertical co-ordinate of the generic vertex  $i$ .

As the polygon is assumed to be closed, the last vertex ( $x_N, y_N$ ) coincides with the first. Voids are defined by ordering the vertices in a clockwise direction, thus producing a

negative area. Since valid STL geometries enclose solid volumes, sliced contours are always formed by this type of polygon.

The area of each polyline represents the trabecular area, while the sum of all the trabecular areas on a layer represents the sliced area. The number of polylines on a given section also provides the number of trabeculae.

These output parameters have been investigated as they represent the gradients of pore size and porosity on the complementary geometry (scaffold), as well as the number of pores in each direction. The ratio between the area of a polyline and the area of its bounding box, which provides an estimated indication of the rod/plate topology, has also been analysed.

### 5.3 Results

This method of analysis was conducted on several geometries. The first case study consisted of a human trabecular bone sample taken from a biopsy in the femoral neck region. This sample was scanned by  $\mu$ CT at Istituti Ortopedici Rizzoli, Italy, which provided the STL geometry. As this sample was shaped almost as a 10 mm cube, it was particularly useful for comparing and assessing the cubic ADI samples presented in chapter 3, with particular focus on cases 5 and 6, which present the most intricate geometries.

The second case study was provided by Sky Scan Inc. and referred to the mouse humerus  $\mu$ CT sample from chapter 4. This sample was analysed and compared with the relative ADI sample presented in chapter 4.

This last case is particularly interesting as it involves an entire trabecular bone structure, not only a cubic portion. Therefore, the results obtained are not dependant on the location, orientation, size and origin of the sample.

For all the cases analysed in this chapter, the three orthogonal directions were those defined by the system of co-ordinates in the STL files.

Diagrams relative to trabecular area, sliced area and number of trabeculae are presented for each case study. The computational time required to slice and analyse each sample in three directions is also reported, together with the SSL file sizes.

The computational resources utilised were the same as those specified in section 2.3.2.

### 5.3.1 Analysis of a Cubic $\mu$ CT Trabecular Bone Sample

This sample was obtained from a  $\mu$ CT scan with a pixel size of 19.5  $\mu$ m and a layer thickness of 50  $\mu$ m. The volume was approximately cubic in shape as its size was 10.356x9.45x10.4 mm. The STL file size in binary format was 13.5 MB. Fig. 5.7 shows the STL geometry of the sample, along with an example slice depicting the closed polylines forming the cross-section. The main input and output slicing data for this case are summarised in Table 5.1.

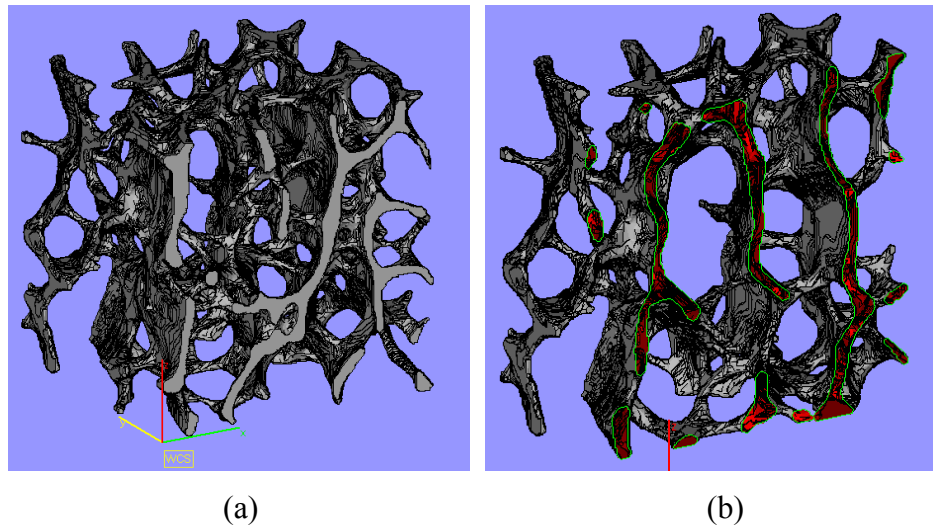


**Fig. 5.7** STL representation of the cubic  $\mu$ CT sample (a), and slice example (b)

<b>STL</b>	Sample size	Boundary Box	10.356 x 9.45 x 10.4 mm
	STL file size	Binary	13.5 MB
<b>SLICING INPUT</b>	Gap Fill	Maximum	0.01 mm
		Iterations	5
	Contour Filter	Open	0 mm
		Closed	0 mm
	Smoothing	Off, Normal, heavy	Off
	Slice Format	Format	SSL
	Slice Parameters	Layer Thickness	0.1 mm
		Tool Compensation	0 mm
<b>OUTPUT</b>	Slicing time	X axis	27 s
		Y axis	30 s
		Z Axis	25 s
	SSL file size	X axis	4.44 MB
		Y axis	2.14 MB
		Z Axis	6.79 MB

**Table 5.1** Main slicing input and output data for the cubic  $\mu$ CT sample.



The inputs specified in Table 5.1 were the same for all three directions so as to achieve more homogenous data with the same resolution (layer thickness) in the diagrams. However, different parameters could have been used for the three directions as required.

Due to the high resolution of the sample, a maximum gap fill of 0.01 mm (10  $\mu$ m) was used, together with the default number of iterations. To preserve the highest level of detail, no contour filters or smoothing was applied. A layer thickness of 1/100 (0.1 mm) the size of the cube was adopted, and no tool compensation was introduced because the purpose of the experiment was to analyse the geometrical characteristics of the sample, and not to study manufacture.

#### ***5.3.1.1 Gradients of Trabecular and Sliced Area***

Fig. 5.8 compares the distributions of the sliced area along the *X*, *Y* and *Z* axes shown in Fig. 5.7(a). From the complementary area on each section, it was possible to draw a similar diagram showing the gradients of porosity (as a percentage, and referred to the cubic area of the slice) on the relative scaffold geometry, as shown in Fig. 5.9.

Finally, Fig. 5.10 to Fig. 5.12 show the trabecular area distributions along the *X*, *Y* and *Z* axes respectively, while Fig. 5.13 to Fig. 5.15 illustrate the relative gradients in the number of trabeculae.

Analysis times, total number of rods and plates (according to specified criteria), ranges of porosity, and the trabecular and sliced areas, are summarised in Table 5.2. A negative value for the lower limit of the trabecular area range meant that voids with that maximum area were present in the geometry.

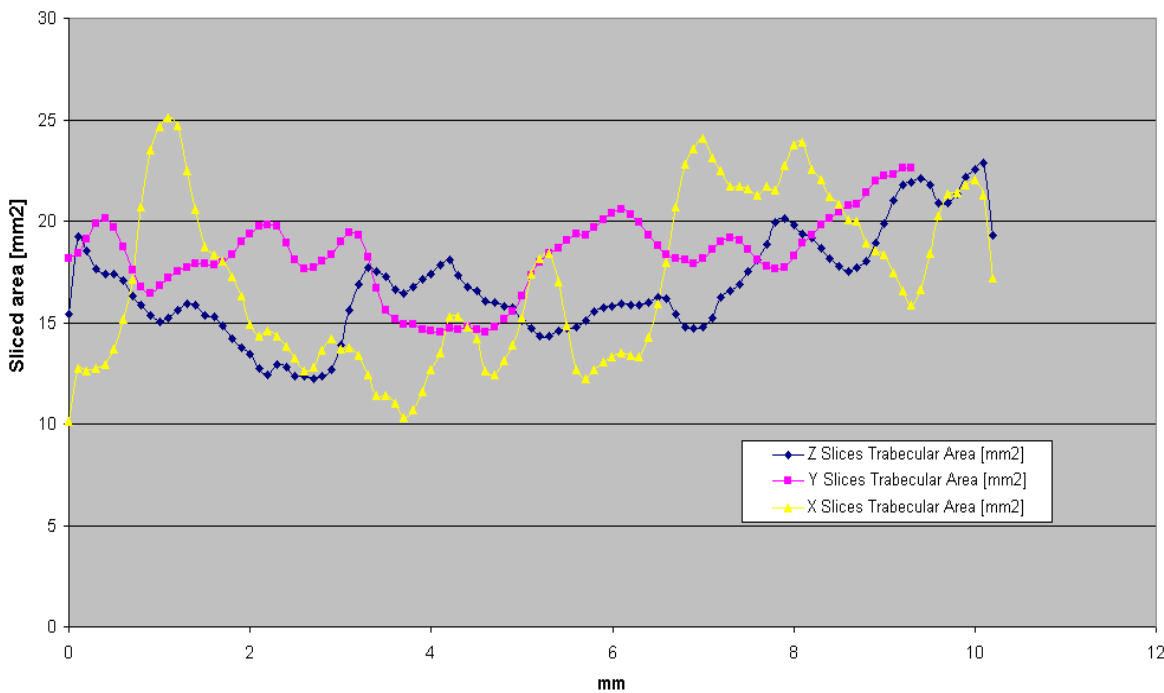


Fig. 5.8 Cubic  $\mu$ CT sample: sliced area distributions along X, Y and Z

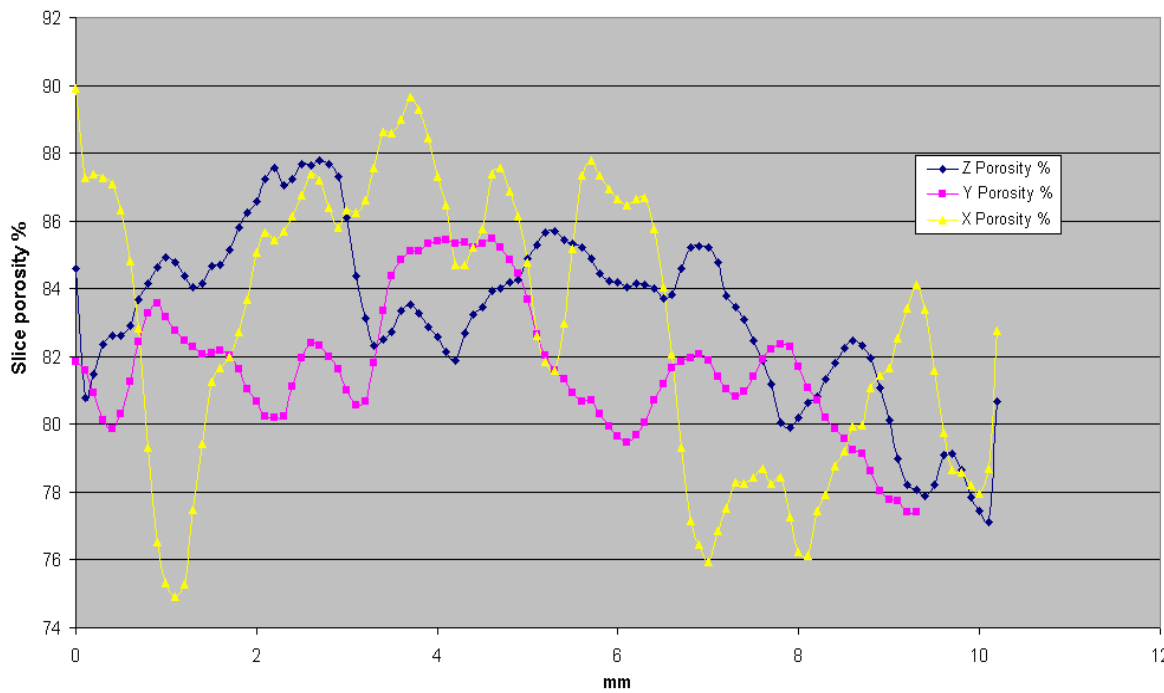


Fig. 5.9 Cubic  $\mu$ CT sample: slice porosity distributions along X, Y and Z

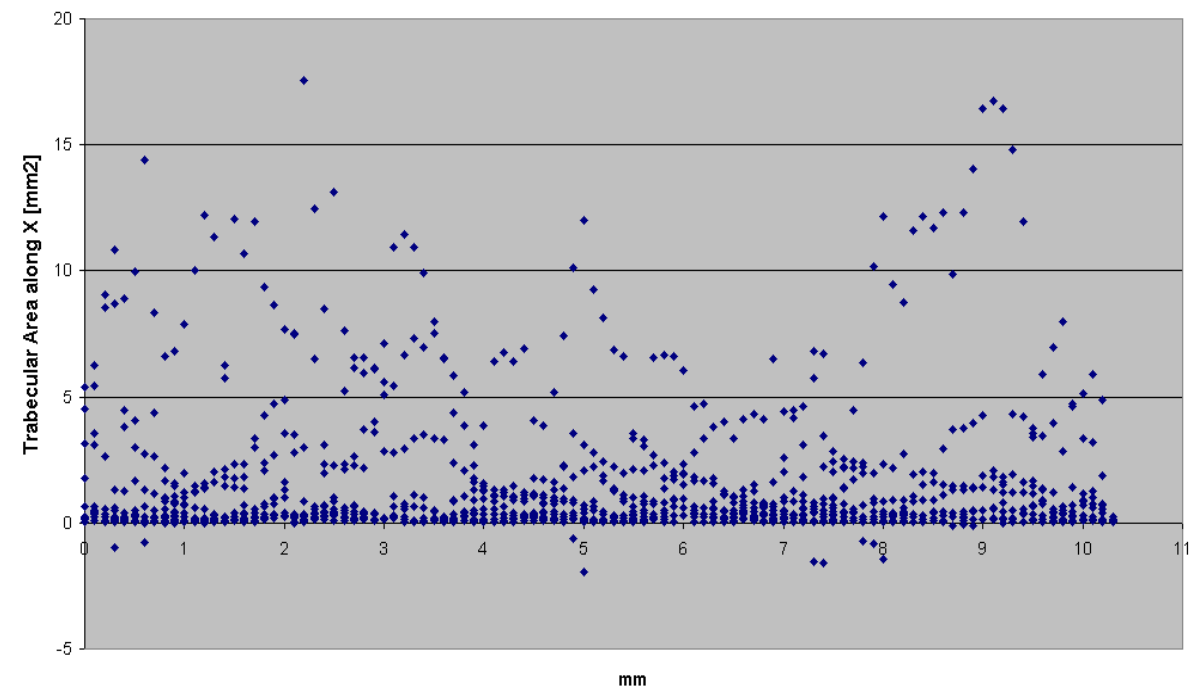


Fig. 5.10 Cubic  $\mu$ CT sample: trabecular area distribution along  $X$

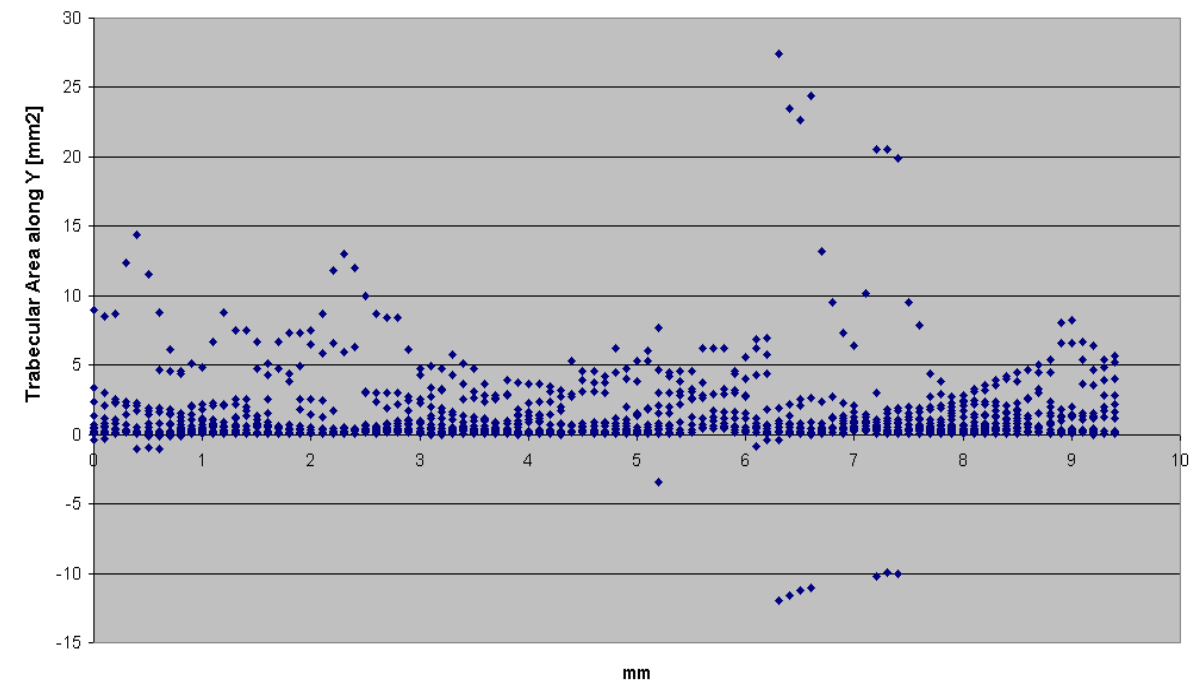


Fig. 5.11 Cubic  $\mu$ CT sample: trabecular area distribution along  $Y$

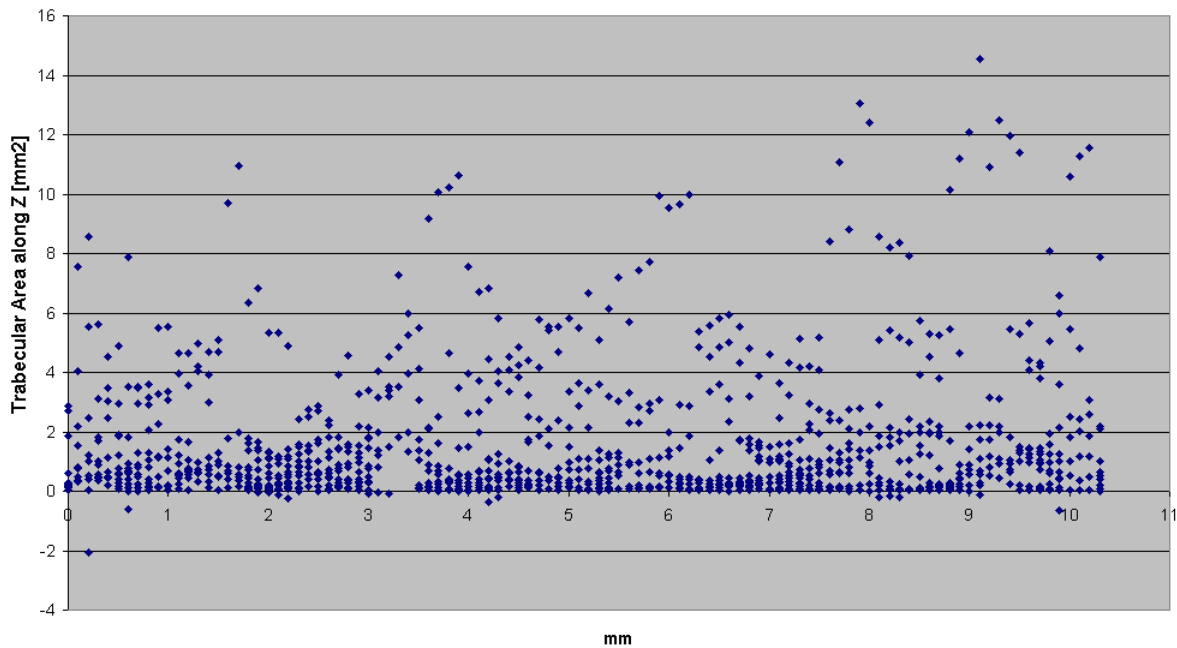


Fig. 5.12 Cubic  $\mu$ CT sample: trabecular area distribution along Z

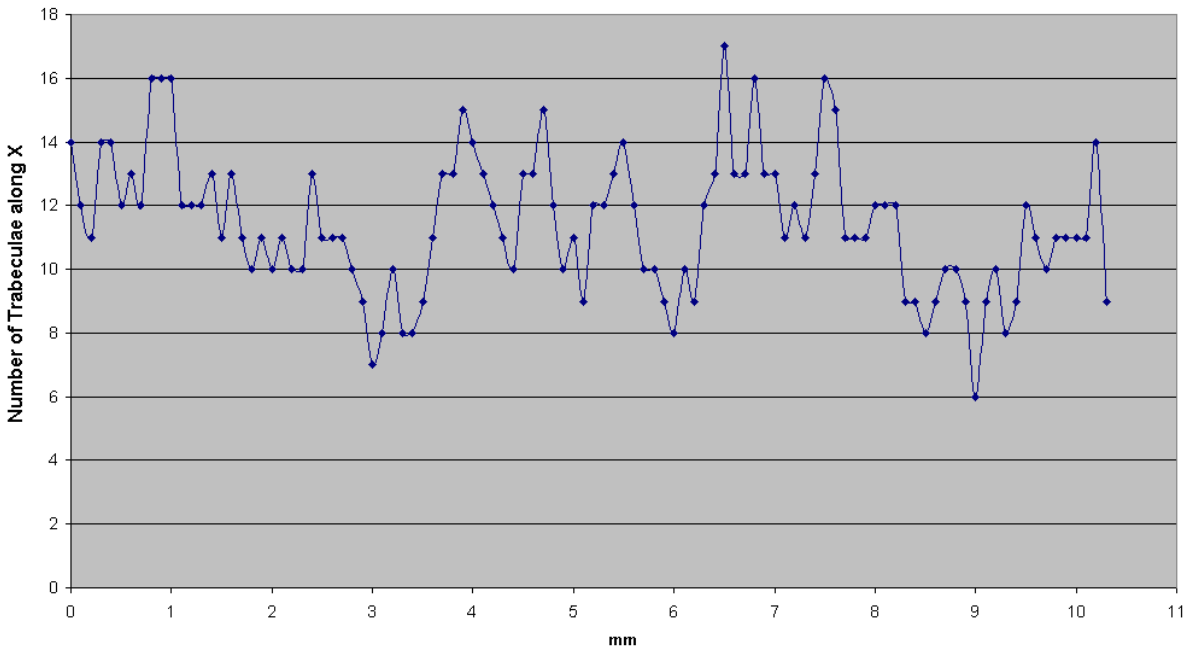


Fig. 5.13 Cubic  $\mu$ CT sample: number of trabeculae along X

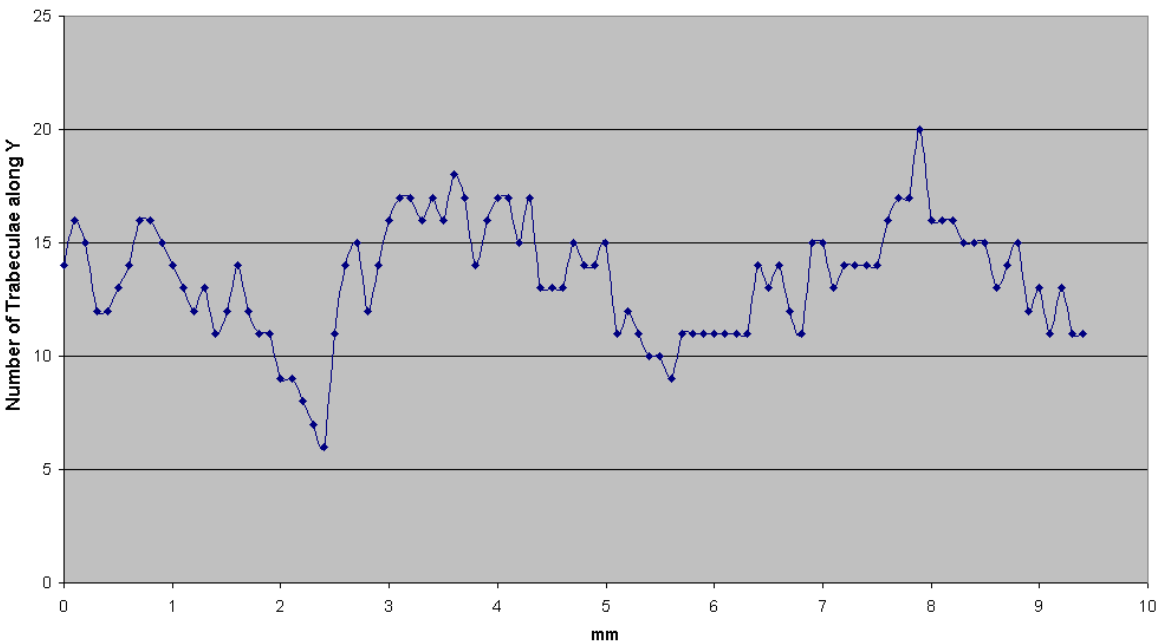


Fig. 5.14 Cubic  $\mu$ CT sample: number of trabeculae along Y

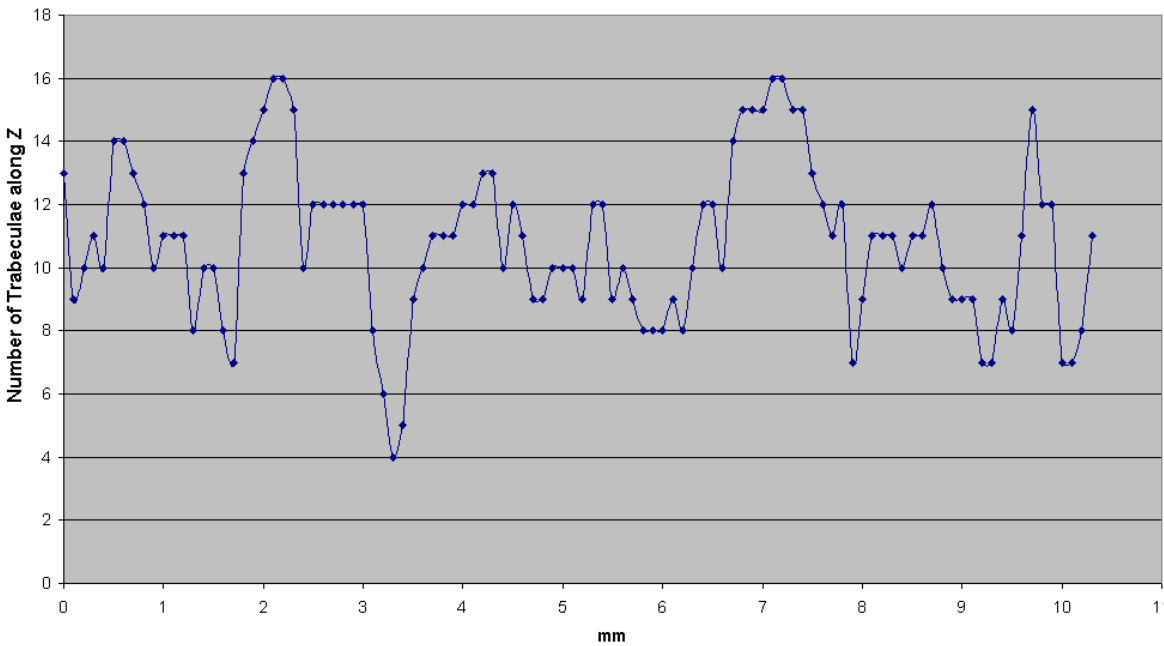


Fig. 5.15 Cubic  $\mu$ CT sample: number of trabeculae along Z

	<b>X</b>	<b>Y</b>	<b>Z</b>
<b>Analysis Time (s)</b>	1323 s	1468 s	1266 s
<b>Total number of rods</b>	504	457	278
<b>Total number of plates</b>	684	820	850
<b>Trabecular Area Range (mm<sup>2</sup>)</b>	-1.967 to 17.56	-11.99 to 27.38	-2.07 to 14.53
<b>Porosity range (%)</b>	74.92 to 89.9	77.41 to 85.47	77.12 to 87.8
<b>Sliced area (mm<sup>2</sup>)</b>	10.1 to 25.08	14.53 to 22.59	12.2 to 22.88

**Table 5.2** Cubic  $\mu$ CT sample: main data from the analysis

### 5.3.2 Analysis of a Mouse Humerus $\mu$ CT Trabecular Bone Sample

This sample was obtained from a  $\mu$ CT scan with a pixel size of 6.8  $\mu$ m and a layer thickness of 25  $\mu$ m. The volume presents an anatomical shape with an envelope size of 21.552x17.589x25.306 mm and an STL file size (in binary format) of 100 MB. Fig. 5.16 shows the STL geometry of the sample, along with an example slice depicting the polylines that form that cross-section. The main input and output slicing data for this case are summarised in Table 5.3. The inputs specified in this table were the same for all three directions, so as to maintain the same precision and layer thickness in the diagrams.

The same slicing parameters used in the previous case were maintained, except for the layer thickness which was set to 0.2 mm in order to reduce both analysis time and SSL file sizes.

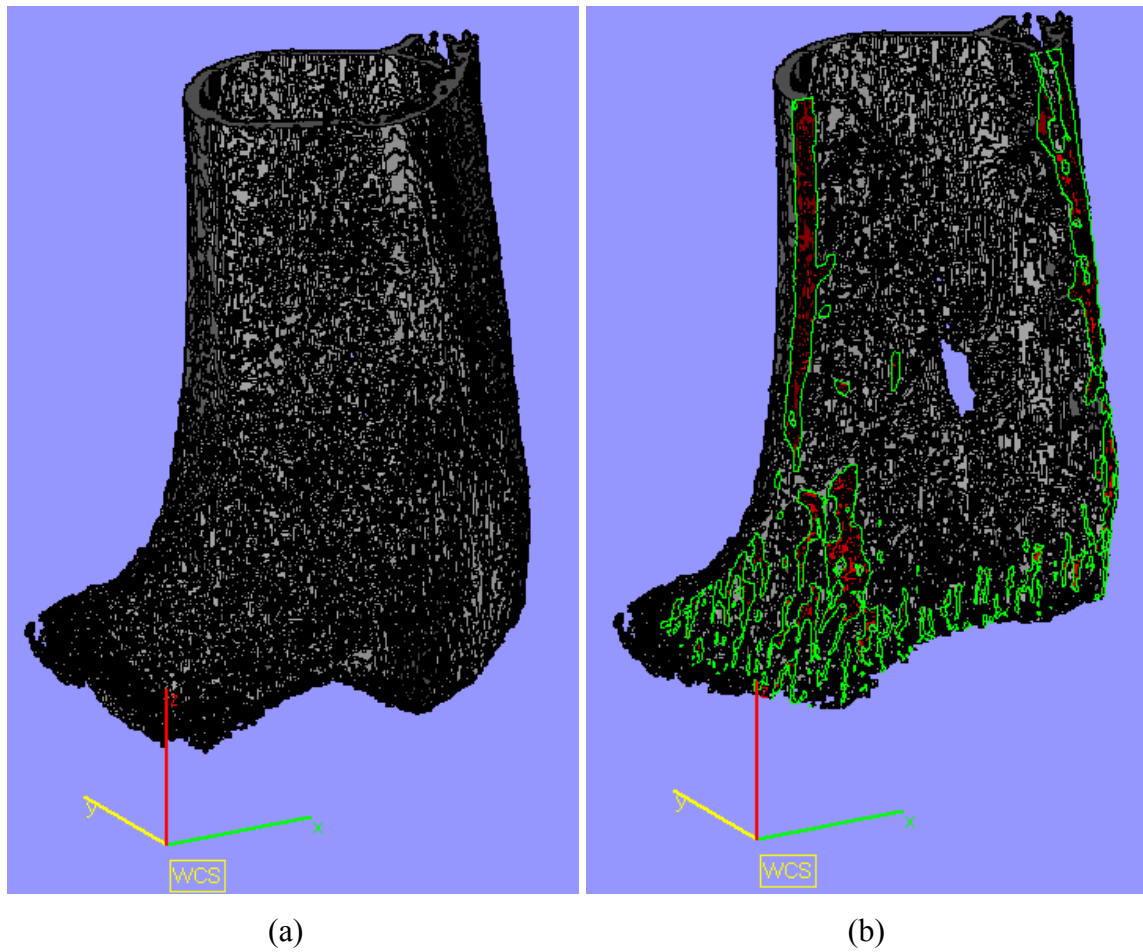


**Fig. 5.16** STL representation of the mouse humerus  $\mu$ CT sample (a), and slice example (b)

<b>STL</b>	Sample size	Boundary Box	21.552x17.589x25.306 mm
	STL file size	Binary	100 MB
<b>SLICING INPUT</b>	Gap Fill	Maximum	0.01 mm
		Iterations	5
	Contour Filter	Open	0 mm
		Closed	0 mm
	Smoothing	Off, Normal, heavy	Off
	Slice Format	Format	SSL
	Slice Parameters	Layer Thickness	0.2 mm
		Tool Compensation	0 mm
<b>OUTPUT</b>	Slicing time	X axis	83 s
		Y axis	72 s
		Z Axis	140 s
	SSL file size	X axis	10.2 MB
		Y axis	10 MB
		Z Axis	12.2 MB

**Table 5.3** Main slicing input and output data for the mouse humerus  $\mu$ CT sample.

### 5.3.2.1 Gradients of Trabecular and Sliced Area

Fig. 5.17 shows the distributions of the sliced area along the  $X$ ,  $Y$  and  $Z$  axes shown in Fig. 5.16 (a). Because the global shape is irregular, the porosity for each slice would need to be referred to a different envelope area, and therefore a diagram showing the porosity distribution as in Fig. 5.9 would not give an idea of the real porosity. The same amount of material on two diverse layers might result in different porosities. Fig. 5.18 to Fig. 5.20 show trabecular area distributions along  $X$ ,  $Y$  and  $Z$ , respectively, while Fig. 5.21 to Fig. 5.23 illustrate the relative gradients in the number of trabeculae.

The analysis data for this sample are summarised in Table 5.4. A negative value for the lower limit of the trabecular area range meant that voids with that maximum area were present in the geometry.

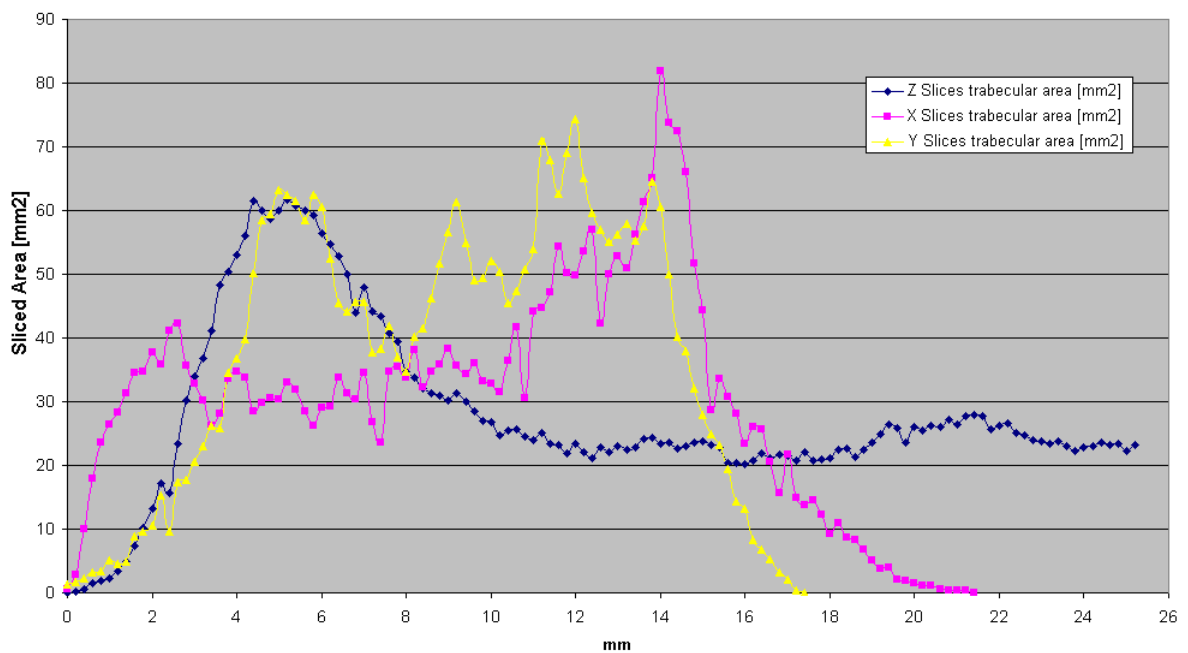


**Fig. 5.17** Mouse humerus  $\mu$ CT sample: sliced area distributions along  $X$ ,  $Y$  and  $Z$



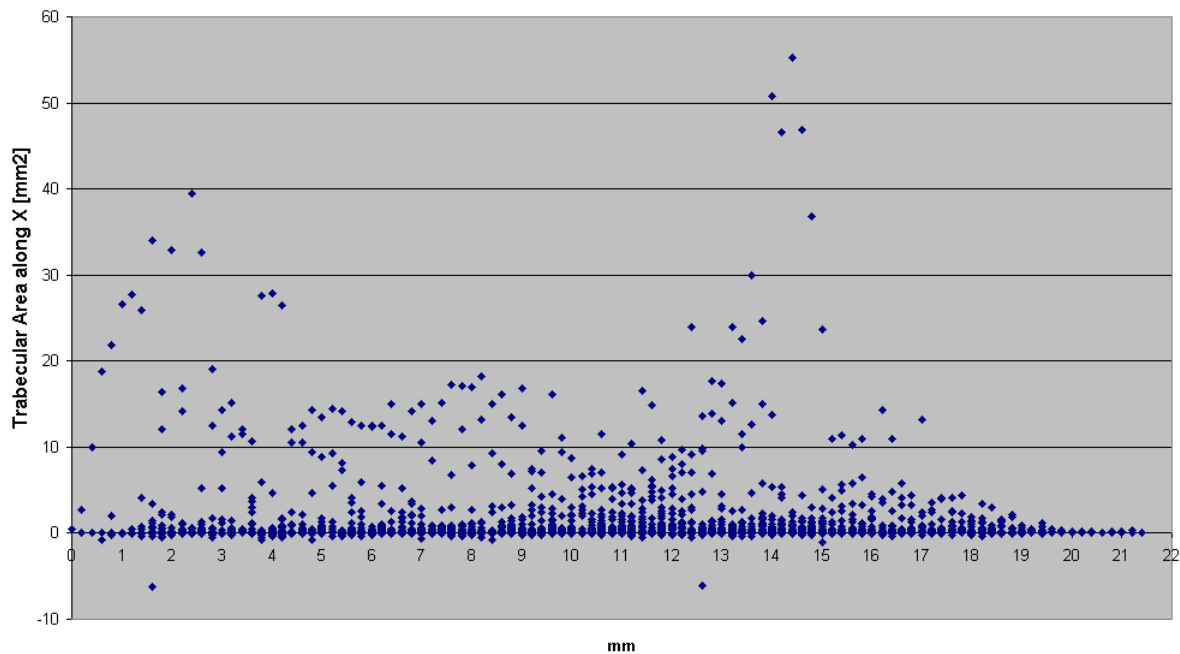


**Fig. 5.18** Mouse humerus μCT sample: trabecular area distribution along *X*

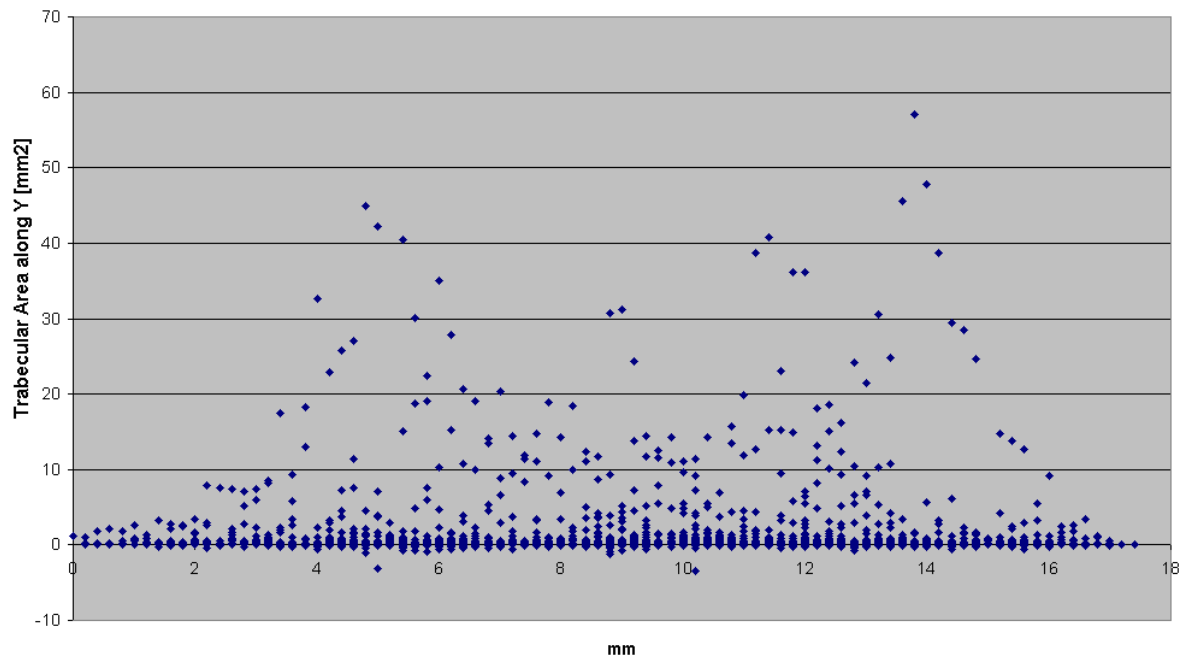


**Fig. 5.19** Mouse humerus μCT sample: trabecular area distribution along *Y*

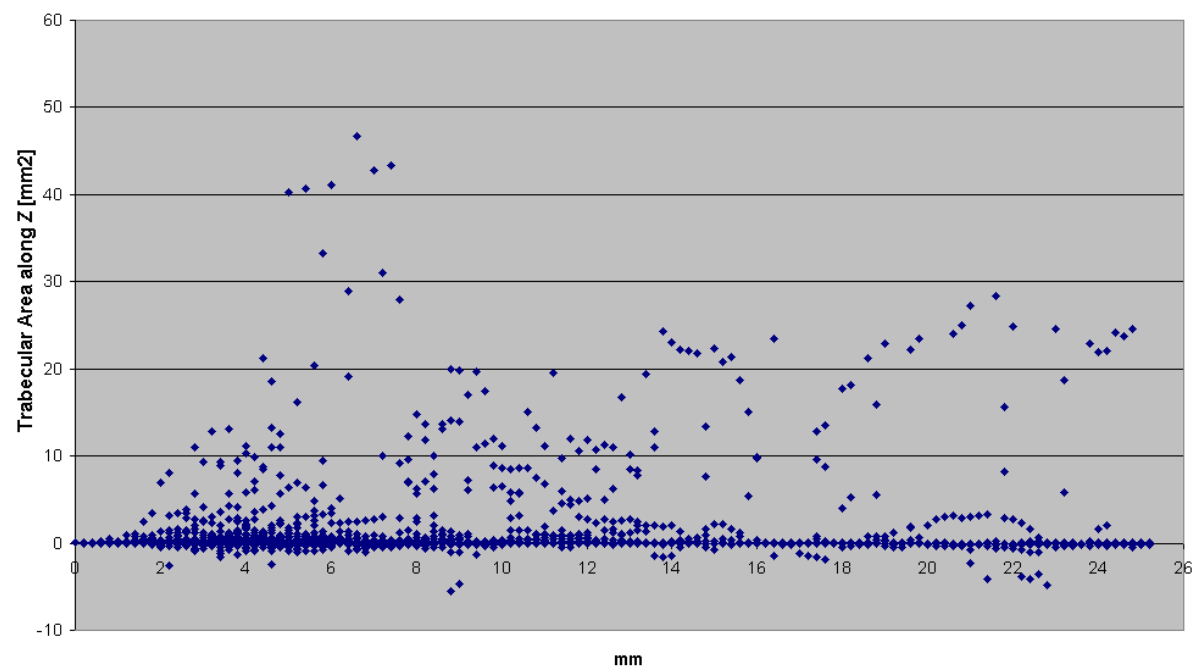


Fig. 5.20 Mouse humerus  $\mu$ CT sample: trabecular area distribution along Z

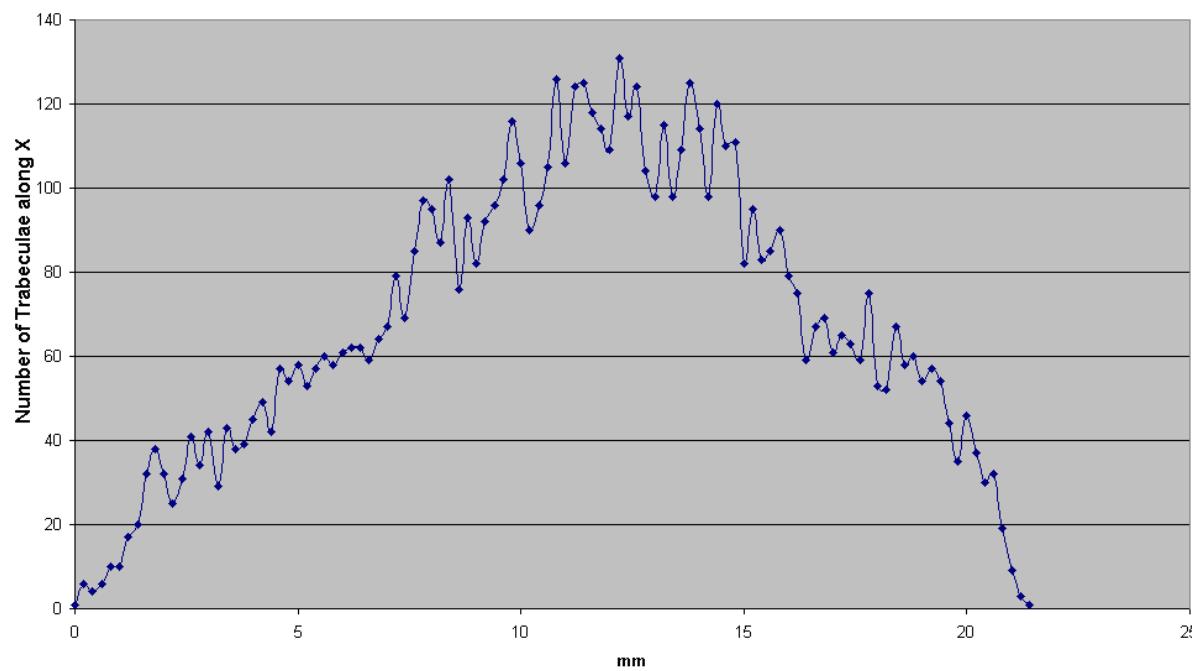


Fig. 5.21 Mouse humerus  $\mu$ CT sample: number of trabeculae along X

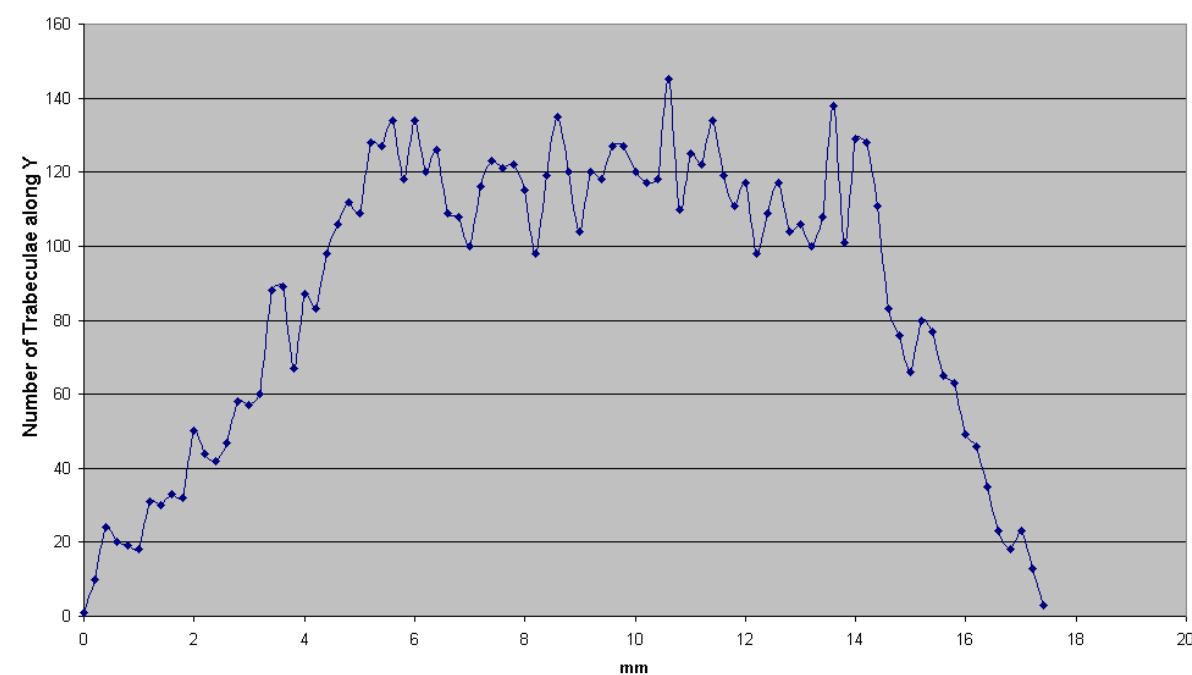


Fig. 5.22 Mouse humerus μCT sample: number of trabeculae along Y

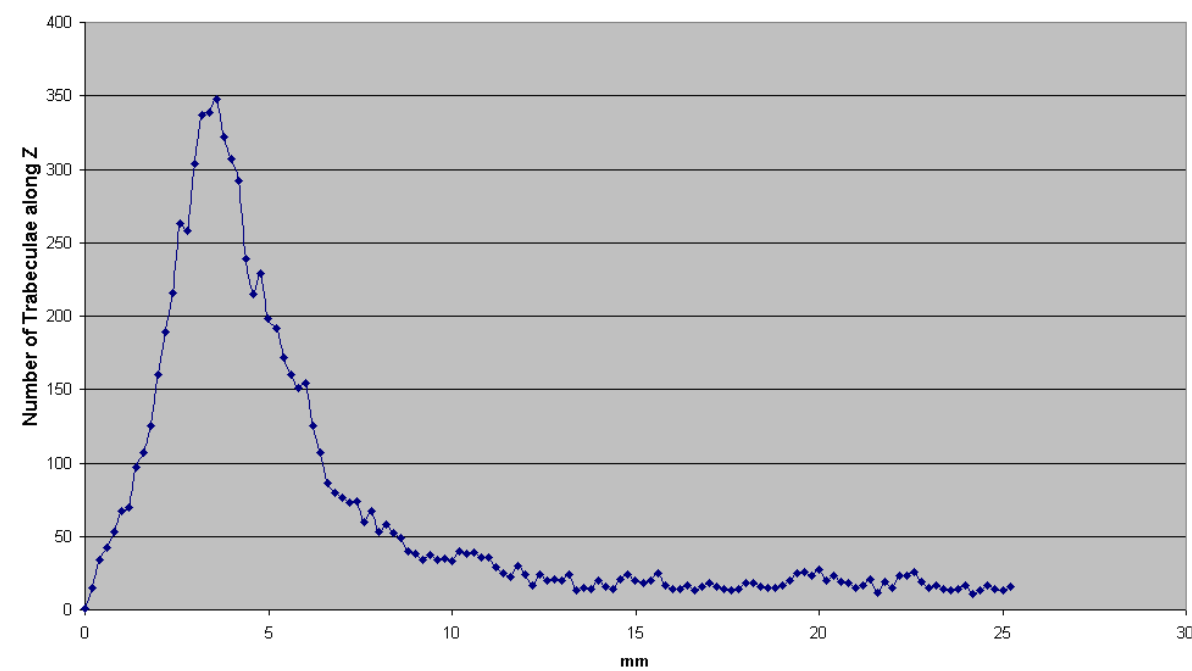


Fig. 5.23 Mouse humerus μCT sample: number of trabeculae along Z

	<b>X</b>	<b>Y</b>	<b>Z</b>
<b>Analysis Time (s)</b>	3360 s	3695 s	4203 s
<b>Total number of rods</b>	2428	2653	1406
<b>Total number of plates</b>	4859	5038	6956
<b>Trabecular Area Range (mm<sup>2</sup>)</b>	-6.24 to 55.25	-3.37 to 56.987	-5.55 to 46.7
<b>Sliced area (mm<sup>2</sup>)</b>	0.069 to 81.837	0.09 to 74.31	0.0125 to 61.765

**Table 5.4** Mouse humerus  $\mu$ CT sample: main data from the analysis

### 5.3.3 Analysis of Cubic ADI Case 5 Sample

The main input and output slicing data for the cubic ADI case 5 sample are summarised in Table 5.5. As in the previous analysis, the slicing parameters specified in this table were the same for all three directions. The layer thickness was set to 0.1 mm, as with the cubic  $\mu$ CT sample.

<b>STL</b>	Sample size	Boundary Box	10x10x10mm
	STL file size	ASCII	13.6 MB
<b>SLICING INPUT</b>	Gap Fill	Maximum	0.01 mm
		Iterations	5
	Contour Filter	Open	0 mm
		Closed	0 mm
	Smoothing	Off, Normal, heavy	Off
	Slice Format	Format	SSL
	Slice Parameters	Layer Thickness	0.1 mm
		Tool Compensation	0 mm
<b>OUTPUT</b>	Slicing time	X axis	46 s
		Y axis	43 s
		Z Axis	52 s
	SSL file size	X axis	4.64 MB
		Y axis	4.3 MB
		Z Axis	4.8 MB

**Table 5.5** Main slicing input and output data for the cubic ADI case 5 sample.

#### 5.3.3.1 Gradients of Trabecular and Sliced Area

Fig. 5.24 shows the distributions of sliced area along the *X*, *Y* and *Z* axes. The same axis system used for the cubic  $\mu$ CT sample was adopted for the cubic ADI samples, in order to compare the two structures. However, several relative orientations of the cubes were possible.

As with the cubic  $\mu$ CT sample, the gradients of porosity are illustrated in Fig. 5.25. Fig. 5.26 to Fig. 5.28 show the trabecular area distributions along  $X$ ,  $Y$  and  $Z$ , respectively, while Fig. 5.29 to Fig. 5.31 depict the relative gradients in the number of trabeculae.

The analysis data for this cubic ADI sample are summarised in Table 5.6.

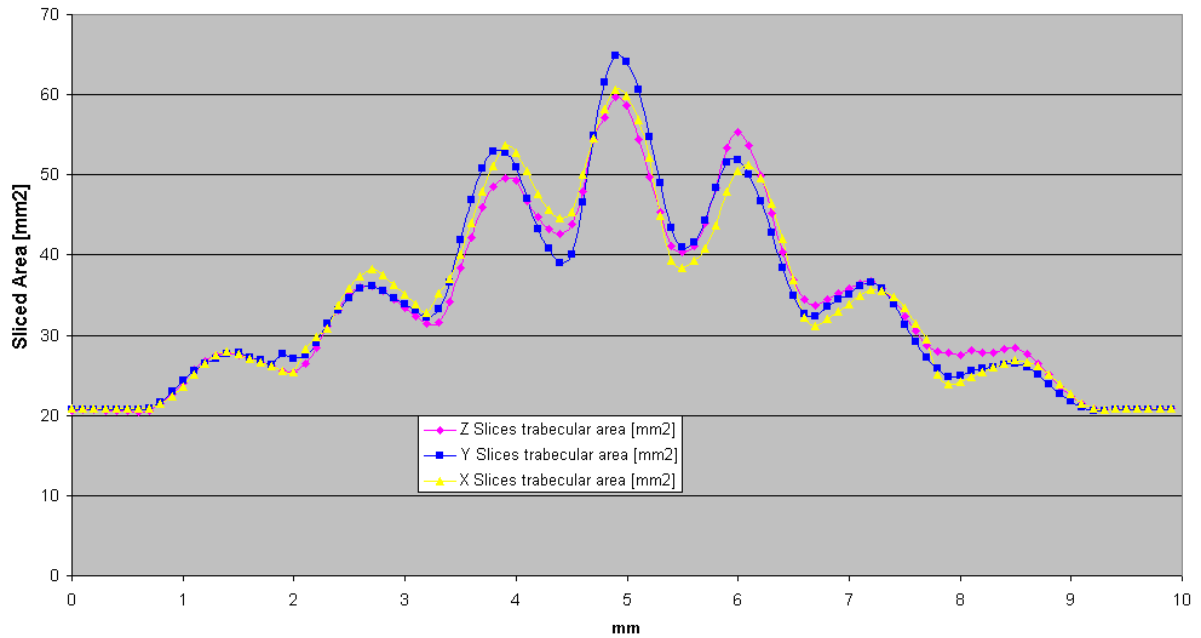


**Fig. 5.24** Cubic ADI case 5 sample: sliced area distributions along  $X$ ,  $Y$  and  $Z$

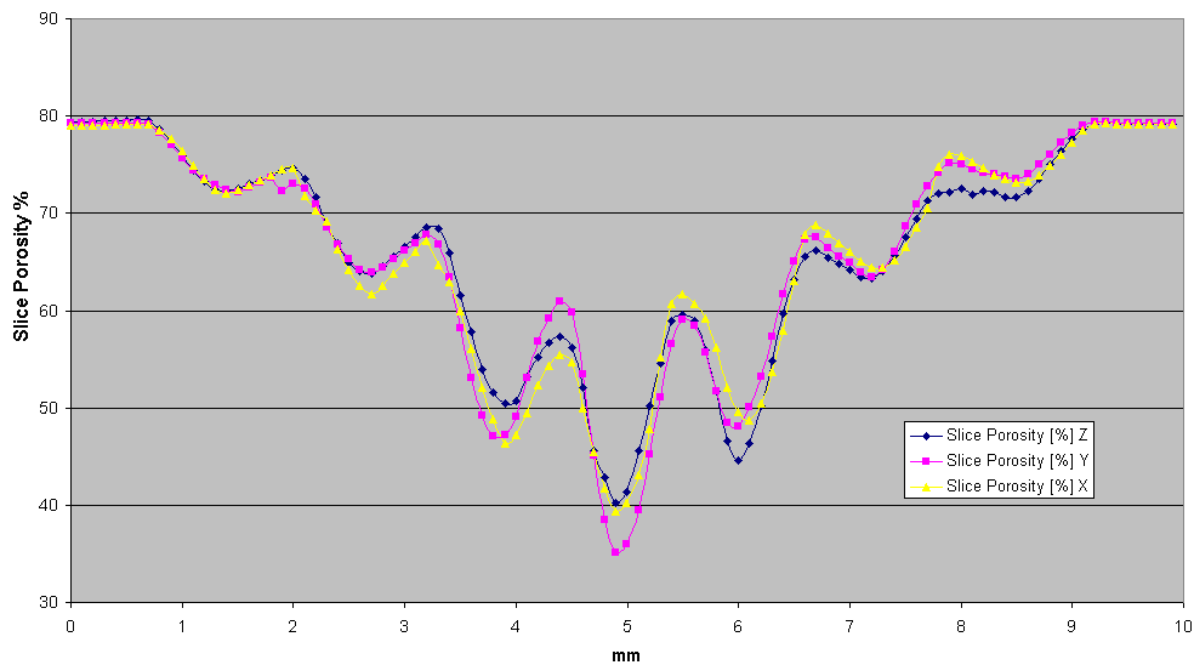


**Fig. 5.25** Cubic ADI case 5 sample: porosity distributions along  $X$ ,  $Y$  and  $Z$

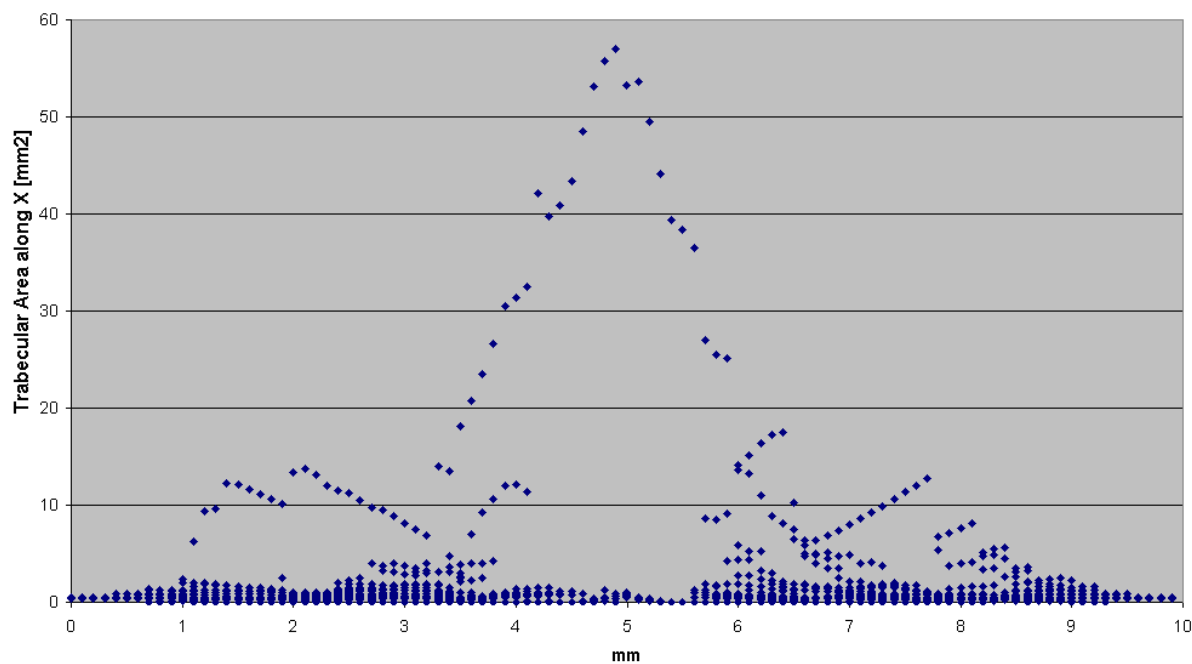


Fig. 5.26 Cubic ADI case 5 sample: trabecular area distribution along  $X$

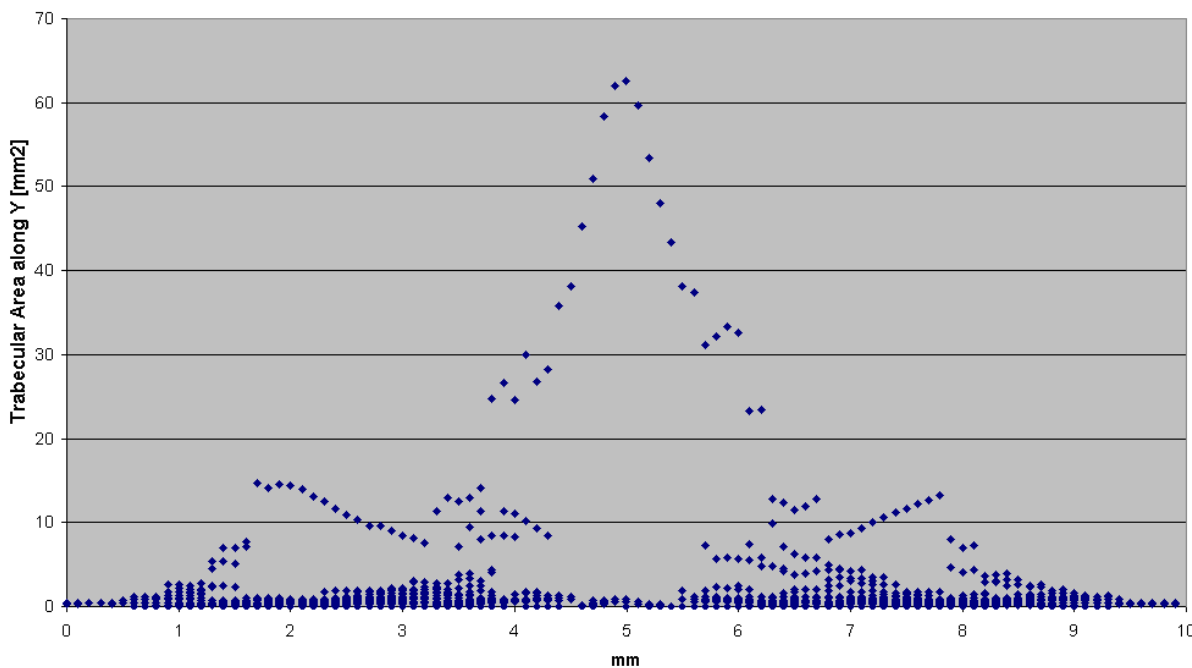


Fig. 5.27 Cubic ADI case 5 sample: trabecular area distribution along  $Y$

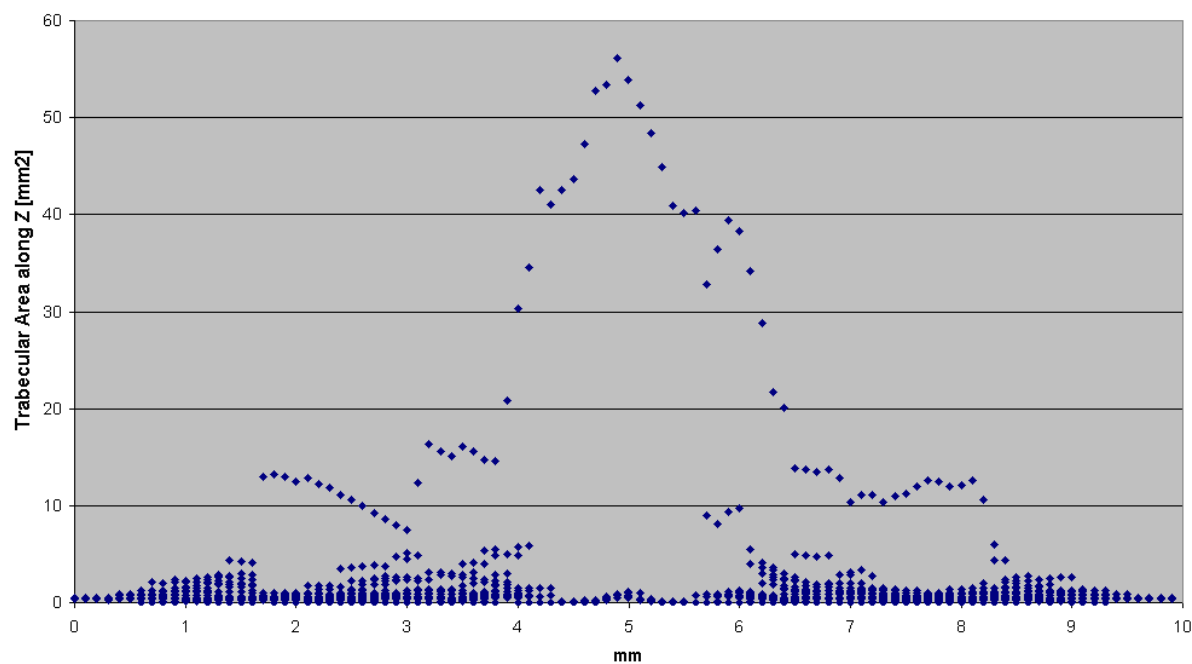


Fig. 5.28 Cubic ADI case 5 sample: trabecular area distribution along Z

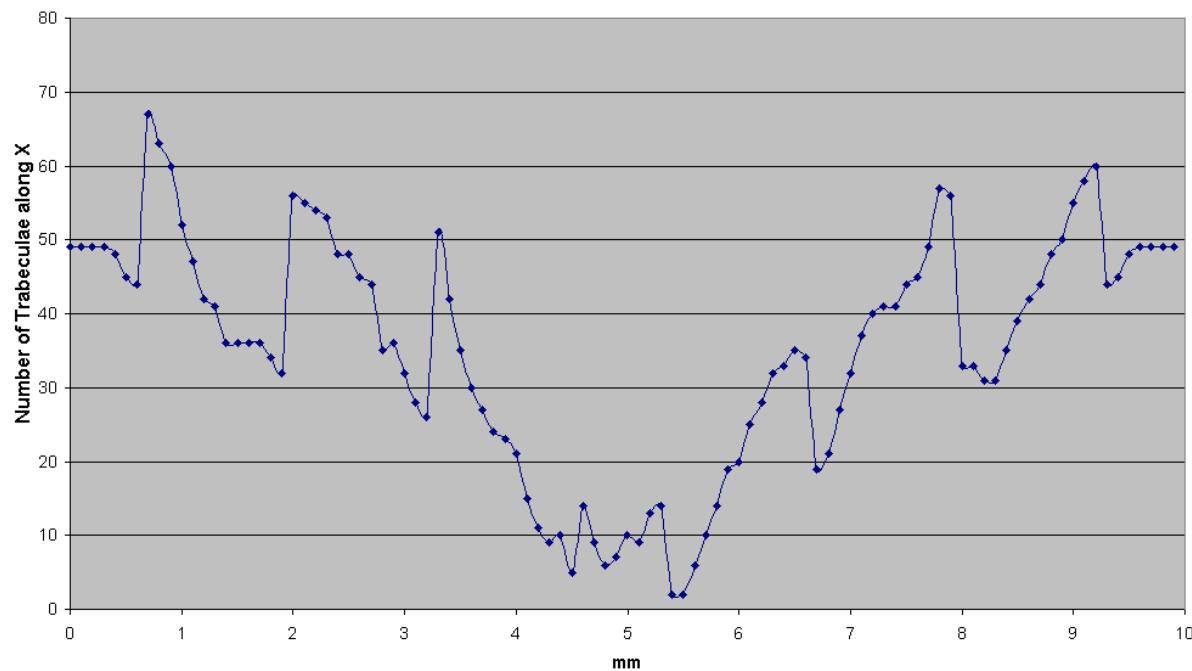
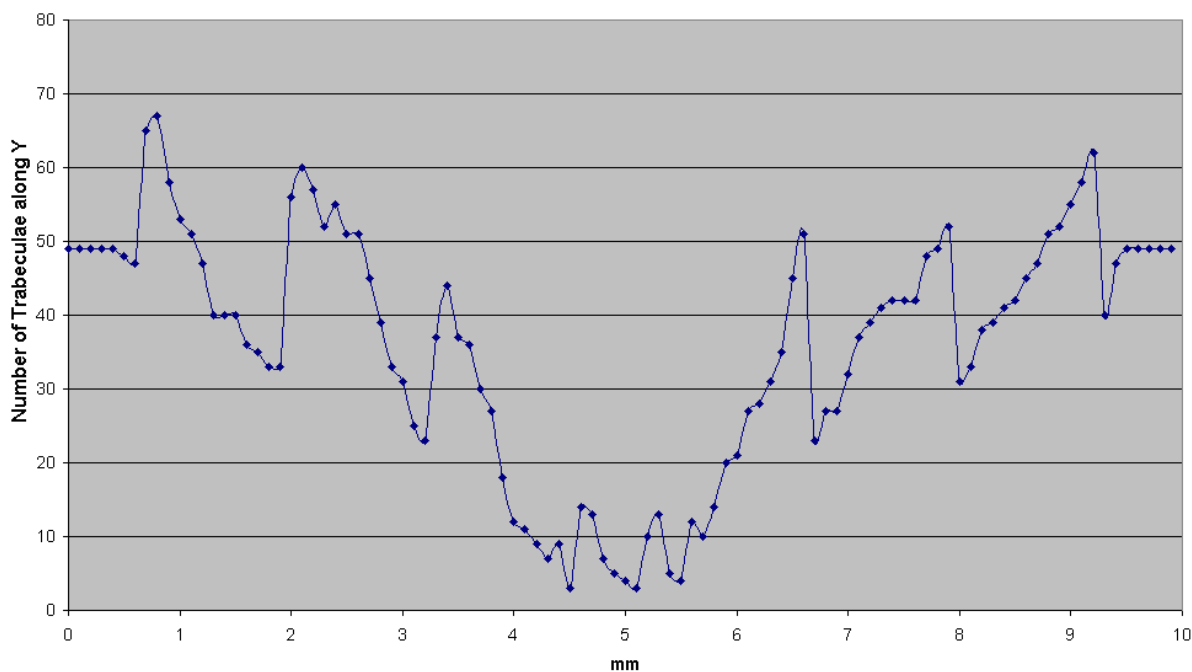
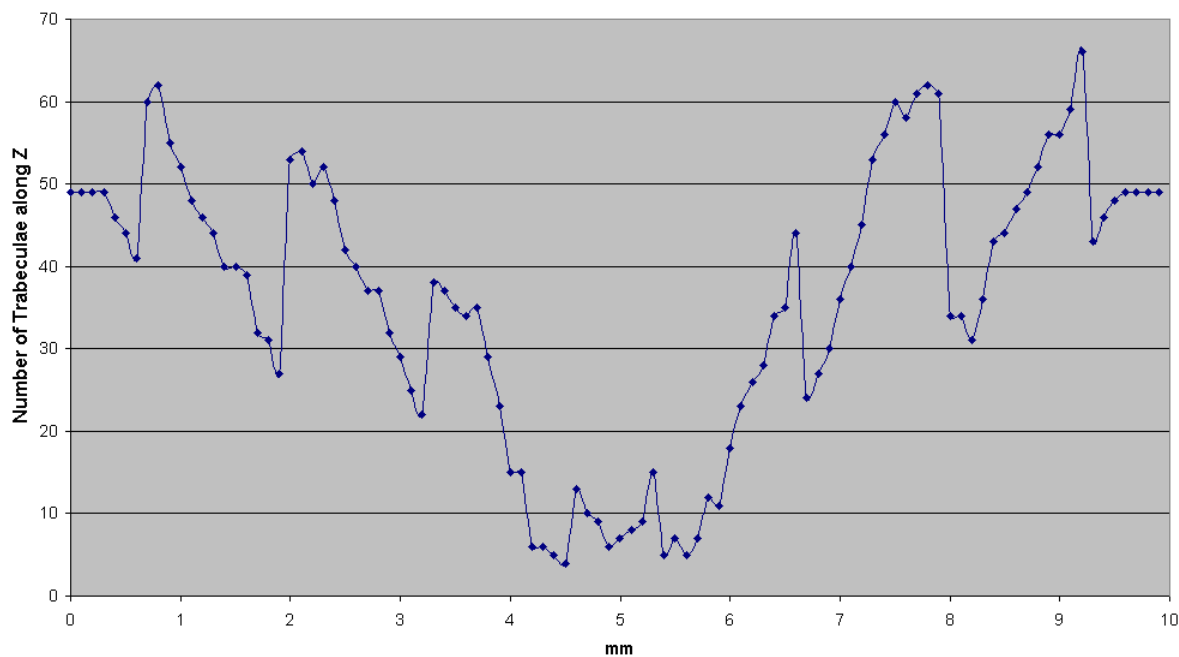


Fig. 5.29 Cubic ADI case 5 sample: number of trabeculae along X



**Fig. 5.30** Cubic ADI case 5 sample: number of trabeculae along Y



**Fig. 5.31** Cubic ADI case 5 sample: number of trabeculae along Z



	<b>X</b>	<b>Y</b>	<b>Z</b>
<b>Analysis Time (s)</b>	2002 s	1965 s	1866 s
<b>Total number of rods</b>	1739	1830	1818
<b>Total number of plates</b>	1782	1765	1773
<b>Trabecular Area Range (mm<sup>2</sup>)</b>	0.00018 to 56.96	0.00011 to 62.58	0.0002 to 56.12
<b>Porosity range (%)</b>	39.41 to 79.11	35.1 to 79.28	40.26 to 79.6
<b>Sliced area (mm<sup>2</sup>)</b>	20.81 to 60.589	20.71 to 64.89	20.407 to 59.74

**Table 5.6** Cubic ADI case 5 sample: main data from the analysis

### 5.3.4 Analysis of Cubic ADI Case 6 Sample

The main input and output slicing data for the cubic ADI case 6 sample are summarised in Table 5.7. The same slicing settings and axis system used for the cubic  $\mu$ CT sample were adopted for this cubic ADI sample.

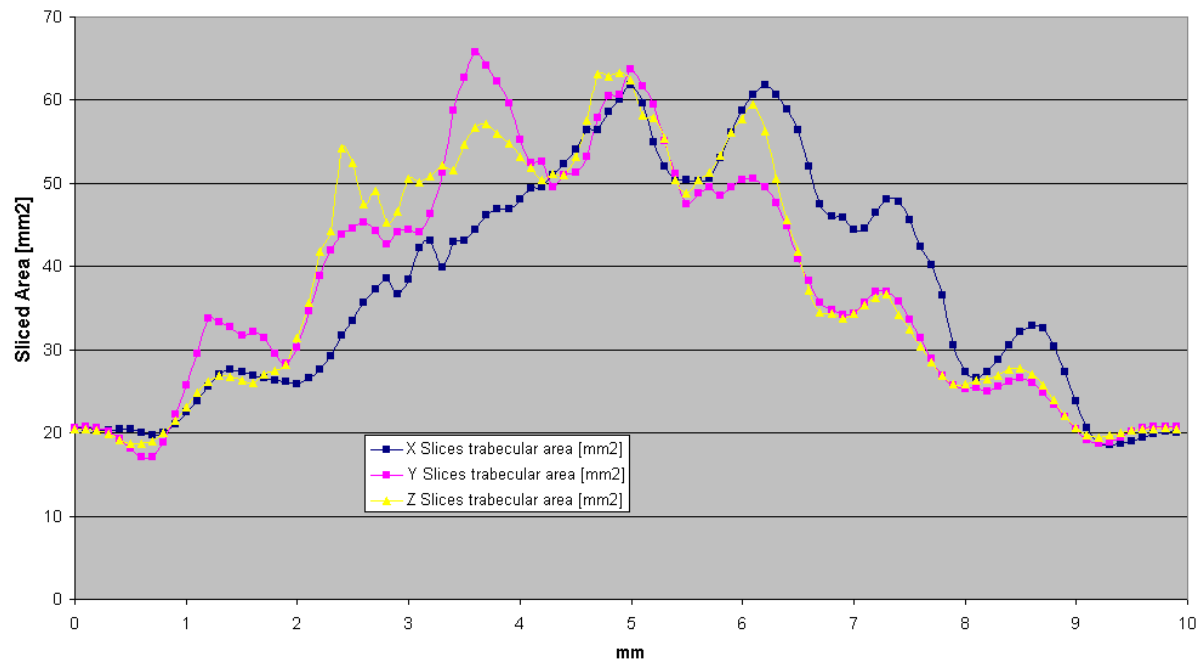
<b>STL</b>	Sample size	Boundary Box	10x10x10mm
	STL file size	ASCII	24 MB
<b>SLICING INPUT</b>	Gap Fill	Maximum	0.01 mm
		Iterations	5
	Contour Filter	Open	0 mm
		Closed	0 mm
	Smoothing	Off, Normal, heavy	Off
	Slice Format	Format	SSL
	Slice Parameters	Layer Thickness	0.1 mm
		Tool Compensation	0 mm
<b>OUTPUT</b>	Slicing time	X axis	50 s
		Y axis	57 s
		Z Axis	53 s
	SSL file size	X axis	4.45 MB
		Y axis	4.91 MB
		Z Axis	4.7 MB

**Table 5.7** Main slicing input and output data for the cubic ADI case 6 sample.

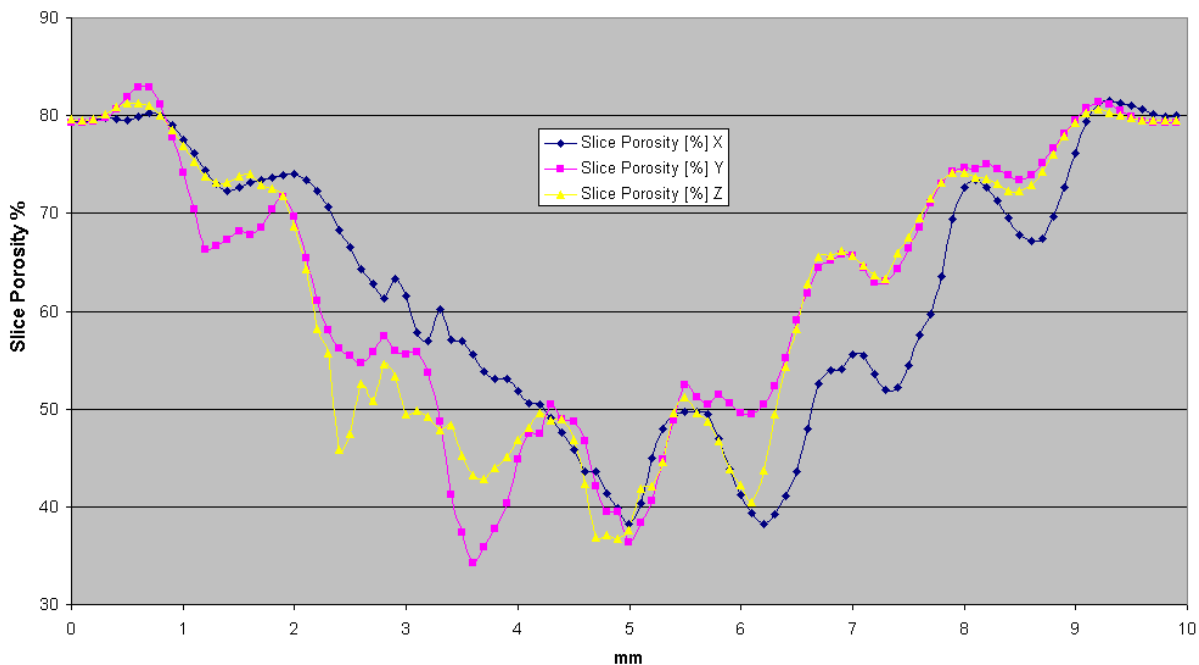
#### 5.3.4.1 Gradients of Trabecular and Sliced Area

Fig. 5.32 shows the distribution of sliced area along the *X*, *Y* and *Z* axes. Fig. 5.33 illustrates the relative gradients of porosity, while Fig. 5.34 to Fig. 5.36 show the trabecular area distributions.

Fig. 5.37 to Fig. 5.39 depict the gradients in the number of trabeculae. The analysis data for this cubic ADI sample are summarised in Table 5.8.



**Fig. 5.32** Cubic ADI case 6 sample: sliced area distributions along *X*, *Y* and *Z*



**Fig. 5.33** Cubic ADI case 6 sample: slice porosity distributions along *X*, *Y* and *Z*

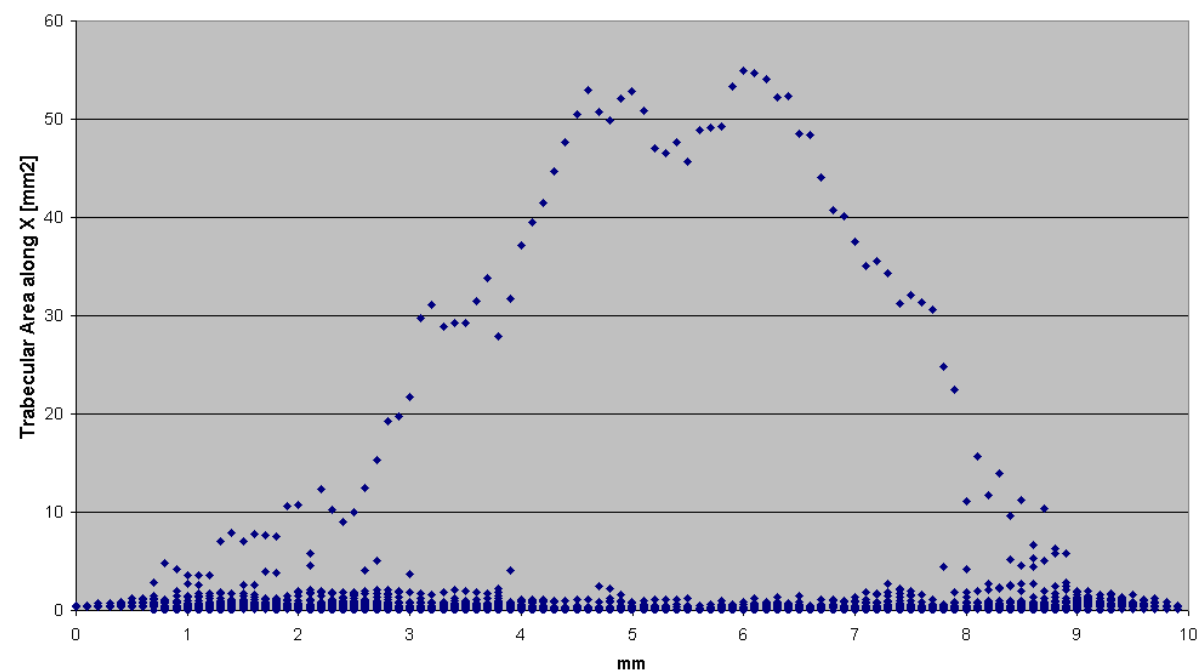


Fig. 5.34 Cubic ADI case 6 sample: trabecular area distribution along  $X$

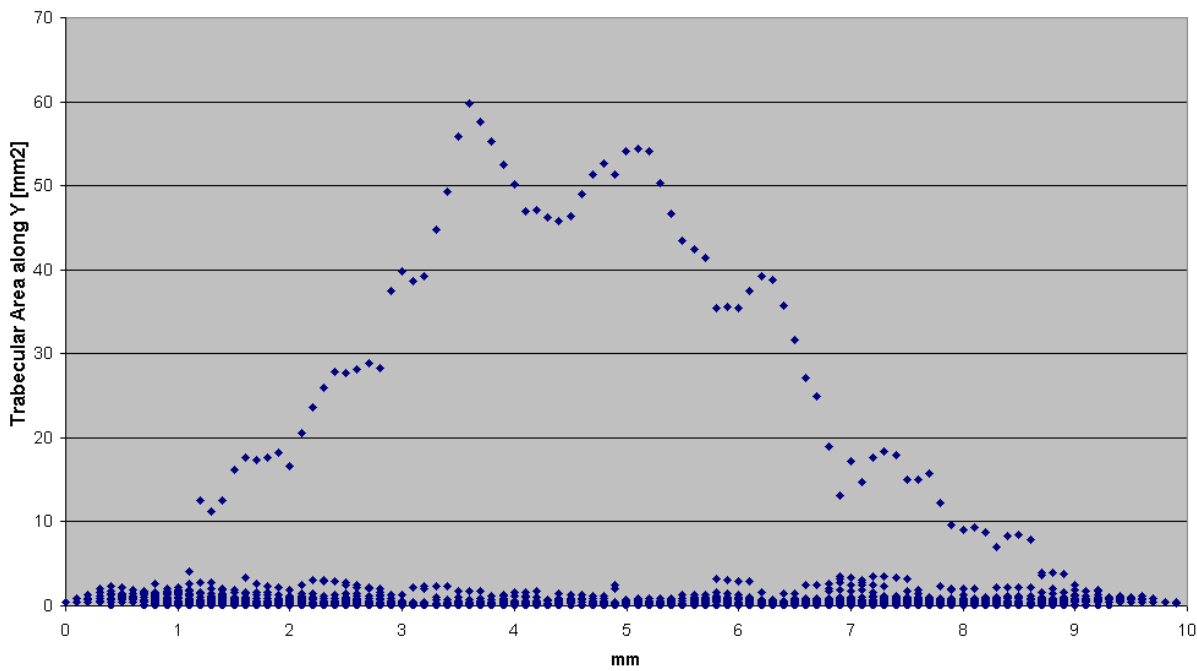


Fig. 5.35 Cubic ADI case 6 sample: trabecular area distribution along  $Y$

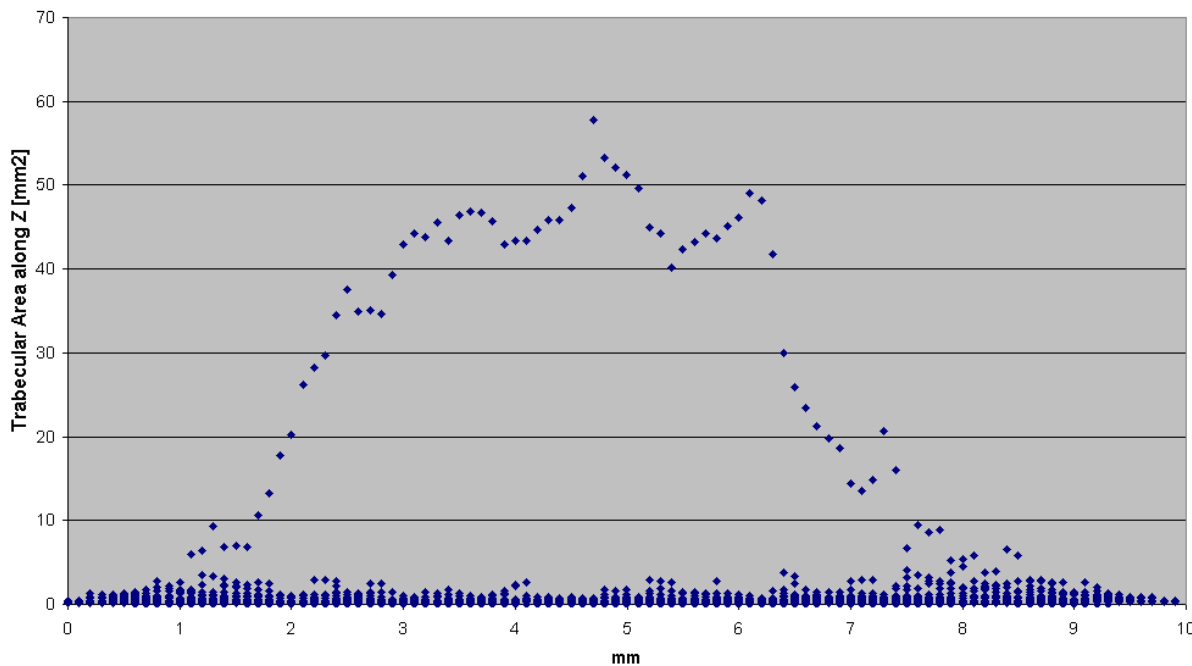


Fig. 5.36 Cubic ADI case 6 sample: trabecular area distribution along Z

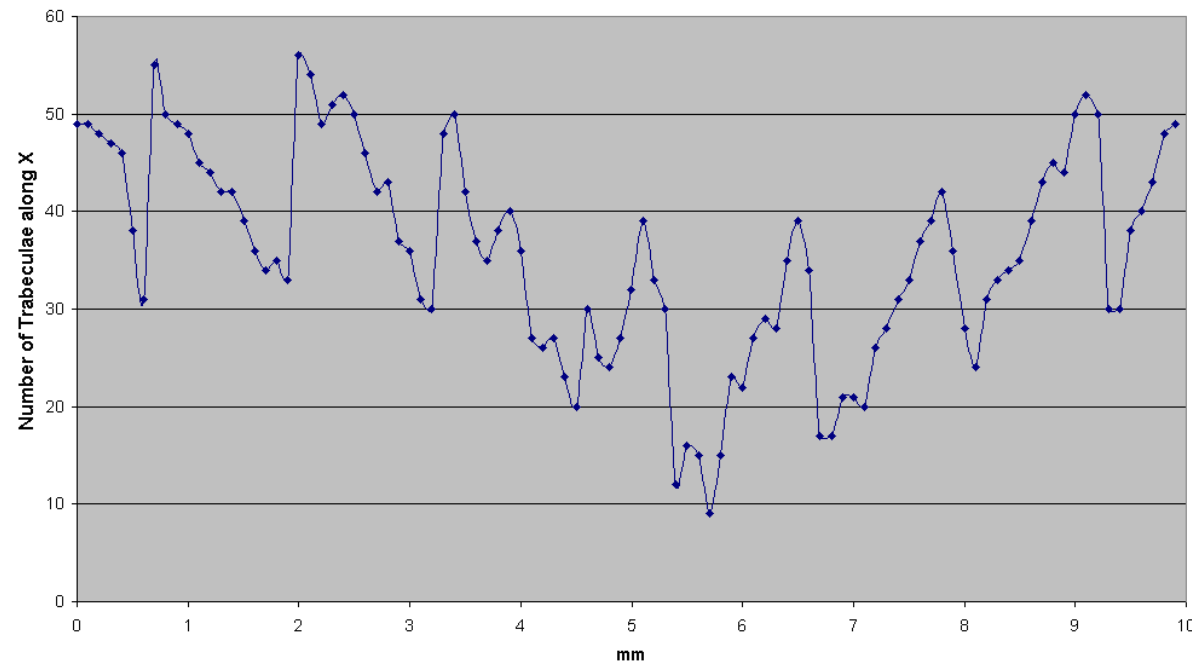


Fig. 5.37 Cubic ADI case 6 sample: number of trabeculae along X

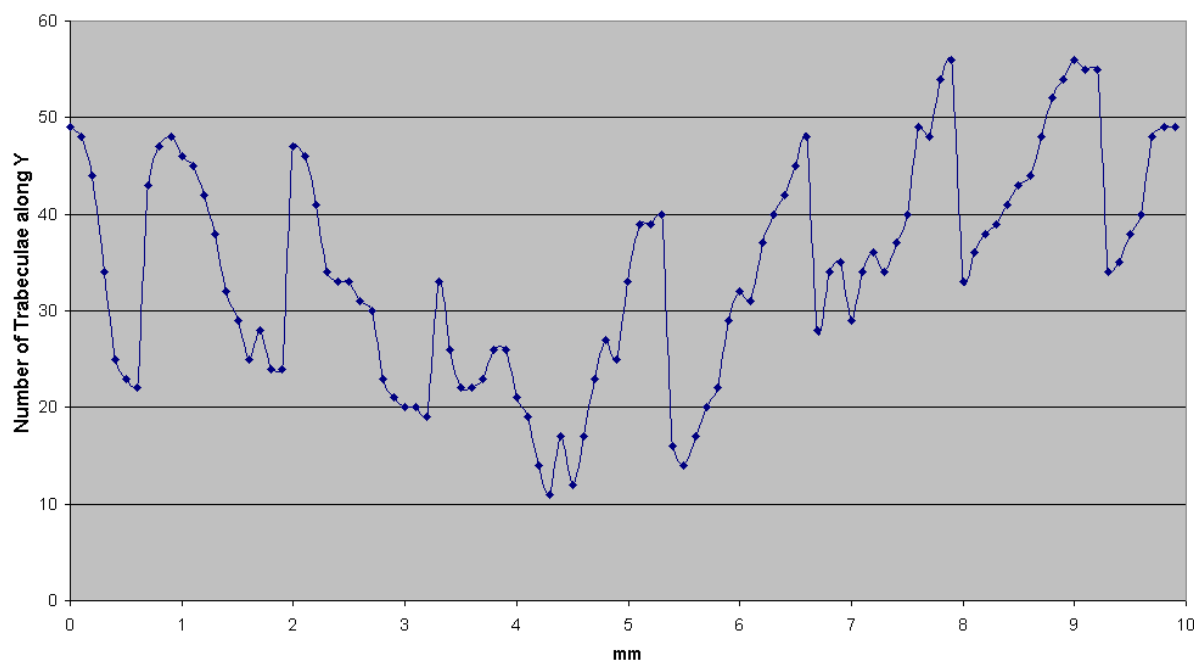


Fig. 5.38 Cubic ADI case 6 sample: number of trabeculae along Y

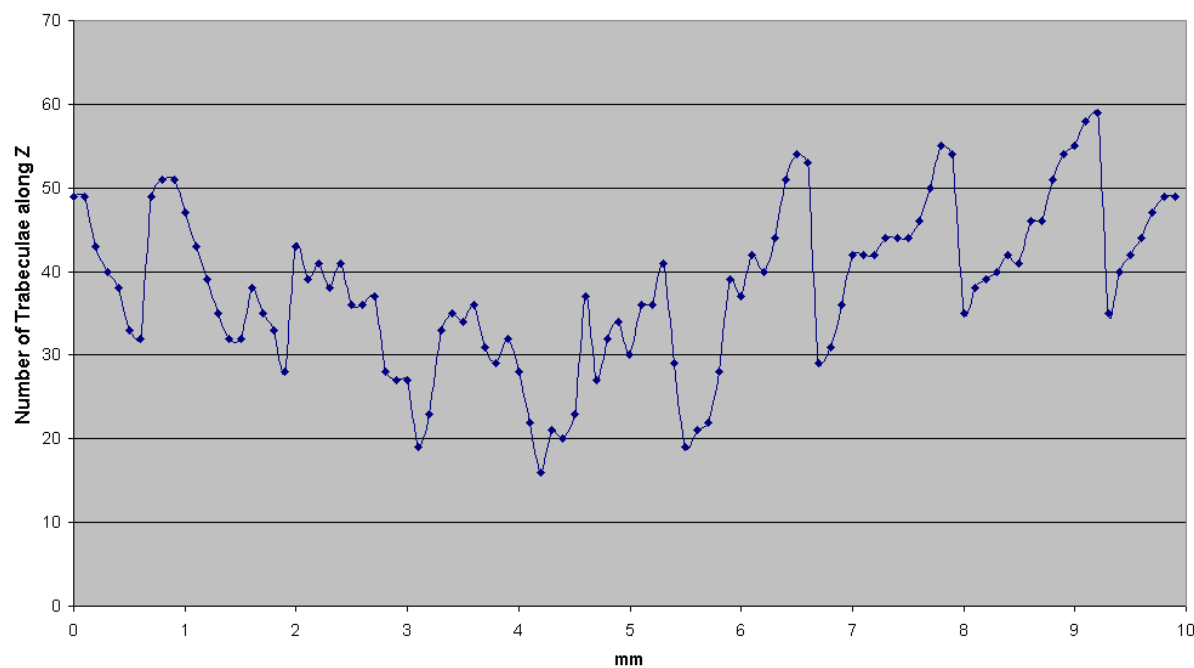


Fig. 5.39 Cubic ADI case 6 sample: number of trabeculae along Z

	<b>X</b>	<b>Y</b>	<b>Z</b>
<b>Analysis Time (s)</b>	2285 s	2066 s	2178 s
<b>Total number of rods</b>	1733	1686	1913
<b>Total number of plates</b>	1851	1737	1900
<b>Trabecular Area Range (mm<sup>2</sup>)</b>	0.00047 to 54.917	0.0003 to 59.77	0.0001 to 57.78
<b>Porosity range (%)</b>	38.18 to 81.51	34.297 to 82.937	36.75 to 81.29
<b>Sliced area (mm<sup>2</sup>)</b>	18.49 to 61.818	17.06 to 65.7	18.705 to 63.245

**Table 5.8** Cubic ADI case 6 sample: main data from the analysis

### 5.3.5 Analysis of ADI Mouse Humerus Sample

The main input and output slicing data for the ADI mouse humerus sample presented in chapter 4 are summarised in Table 5.9. The same slicing settings used for the mouse humerus  $\mu$ CT sample were also used for the this ADI sample, in order to compare the two structures. The ADI mouse humerus sample is illustrated in Fig. 5.40 (a), while (b) depicts a slice example.

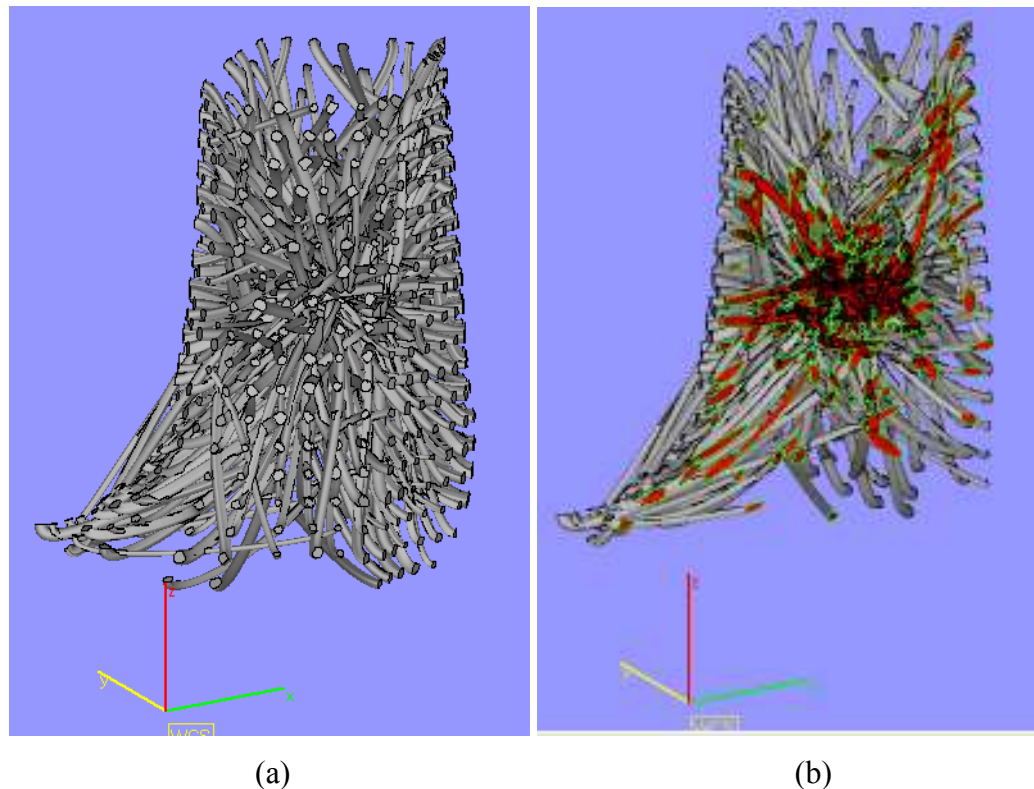


**Fig. 5.40** STL representation of the ADI mouse humerus sample presented in chapter 4 (a), and slice example (b)

STL	Sample size	Boundary Box	20.929x16.476x23.038 mm
	STL file size	ASCII	87.8 MB
SLICING INPUT	Gap Fill	Maximum	0.01 mm
		Iterations	5
	Contour Filter	Open	0 mm
		Closed	0 mm
	Smoothing	Off, Normal, heavy	Off
	Slice Format	Format	SSL
	Slice Parameters	Layer Thickness	0.2 mm
		Tool Compensation	0 mm
OUTPUT	Slicing time	X axis	107 s
		Y axis	99 s
		Z Axis	170 s
	SSL file size	X axis	8.5 MB
		Y axis	8.2 MB
		Z Axis	10.9 MB

**Table 5.9** Main slicing input and output data for the ADI mouse humerus sample presented in chapter 4.

#### 5.3.5.1 Gradients of Trabecular and Sliced Area

Fig. 5.41 shows the distribution of sliced area along the  $X$ ,  $Y$  and  $Z$  axes. The same axis system used for the mouse humerus  $\mu$ CT sample was adopted for the ADI mouse humerus sample, in order to compare the two structures. The porosity distribution diagram has not been drawn for the same reasons explained for the mouse humerus  $\mu$ CT sample.

Fig. 5.42 to Fig. 5.44 depict the trabecular area distributions, while Fig. 5.45 to Fig. 5.47 illustrate the relative gradients in the number of trabeculae.

The analysis data for the ADI mouse humerus sample are summarised in Table 5.10. A negative value for the lower limit of the trabecular area range meant that voids with that maximum area were present in the geometry.

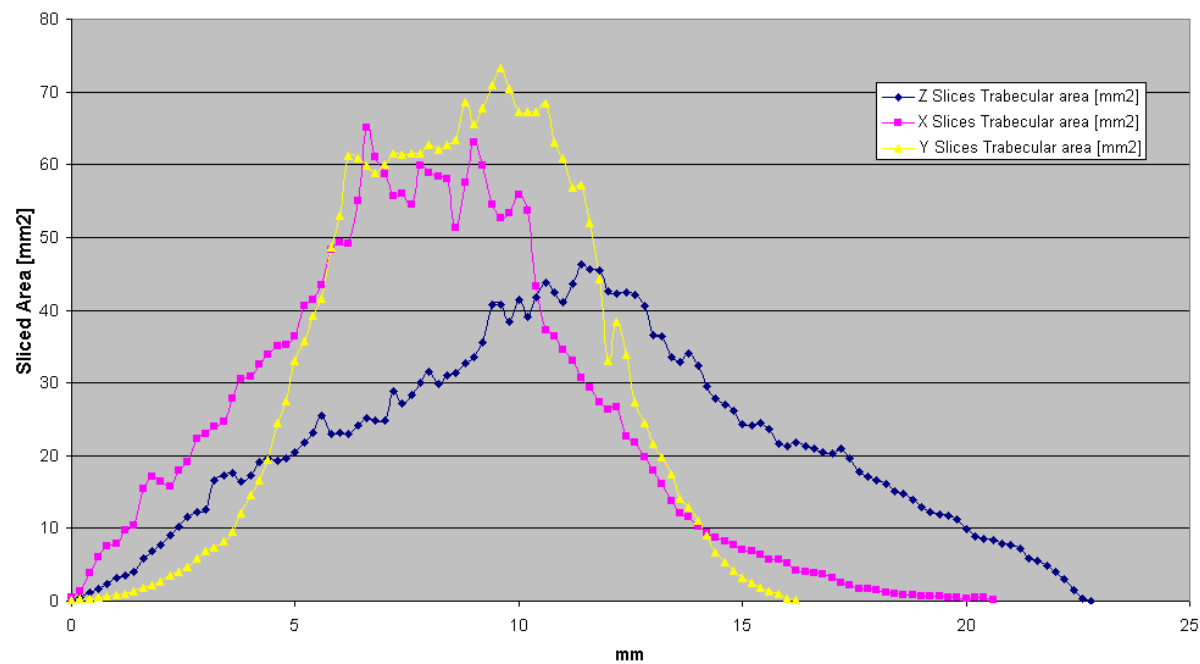


Fig. 5.41 ADI mouse humerus sample: sliced area distributions along *X*, *Y* and *Z*

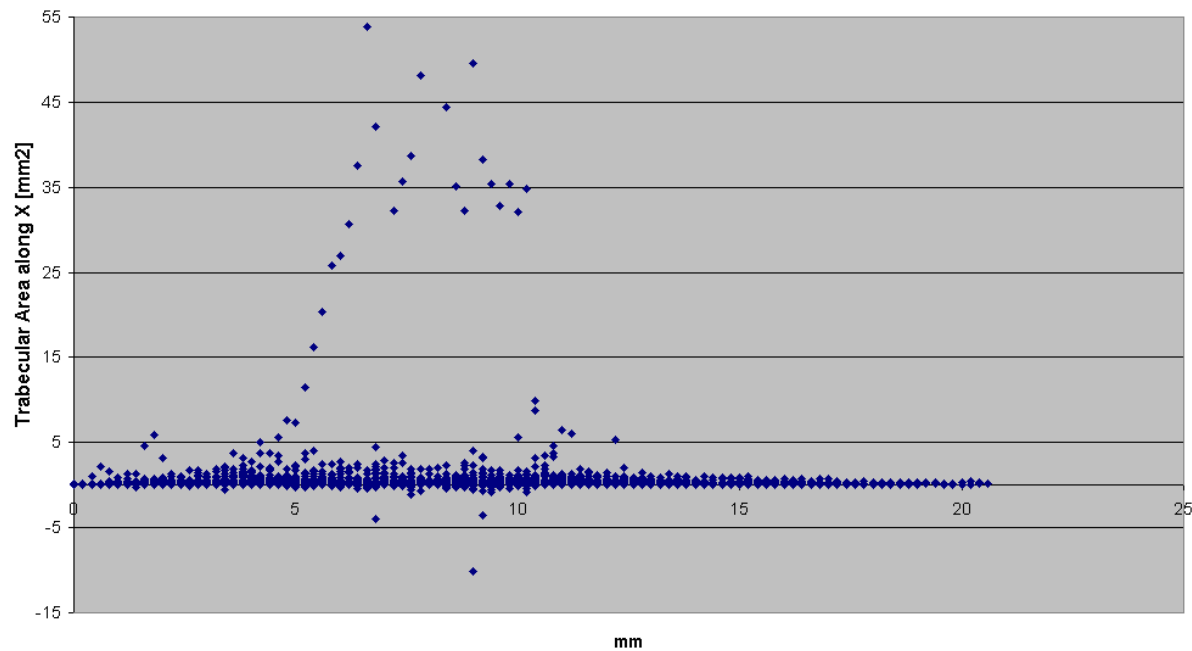


Fig. 5.42 ADI mouse humerus sample: trabecular area distribution along *X*



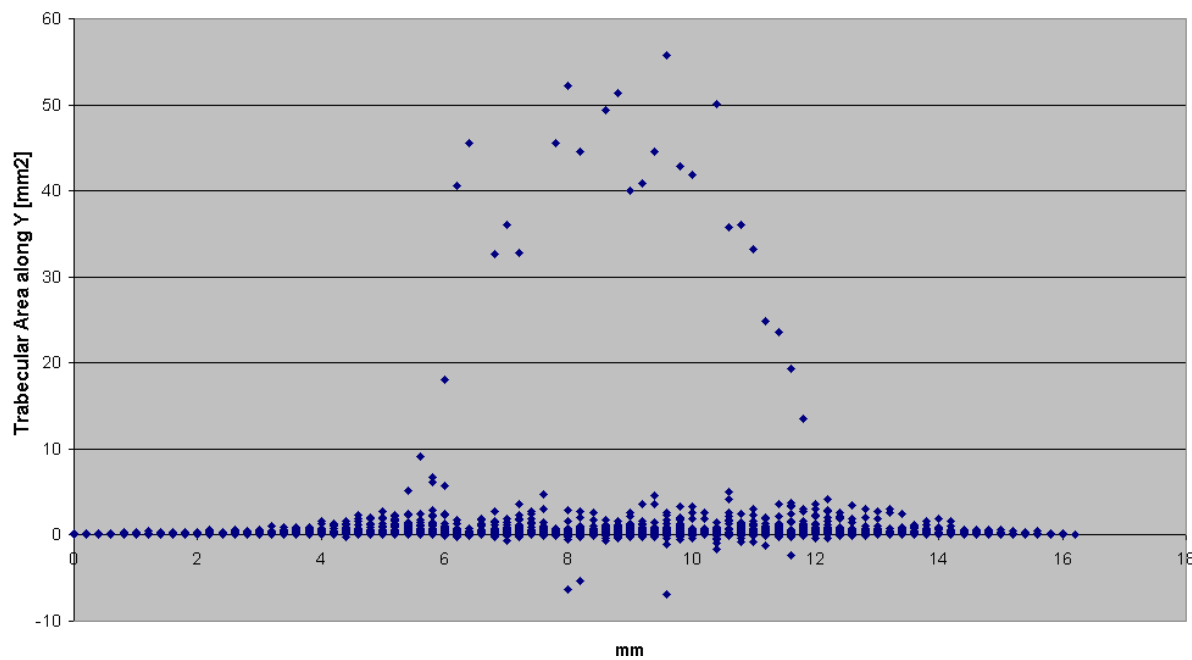


Fig. 5.43 ADI mouse humerus sample: trabecular area distribution along Y

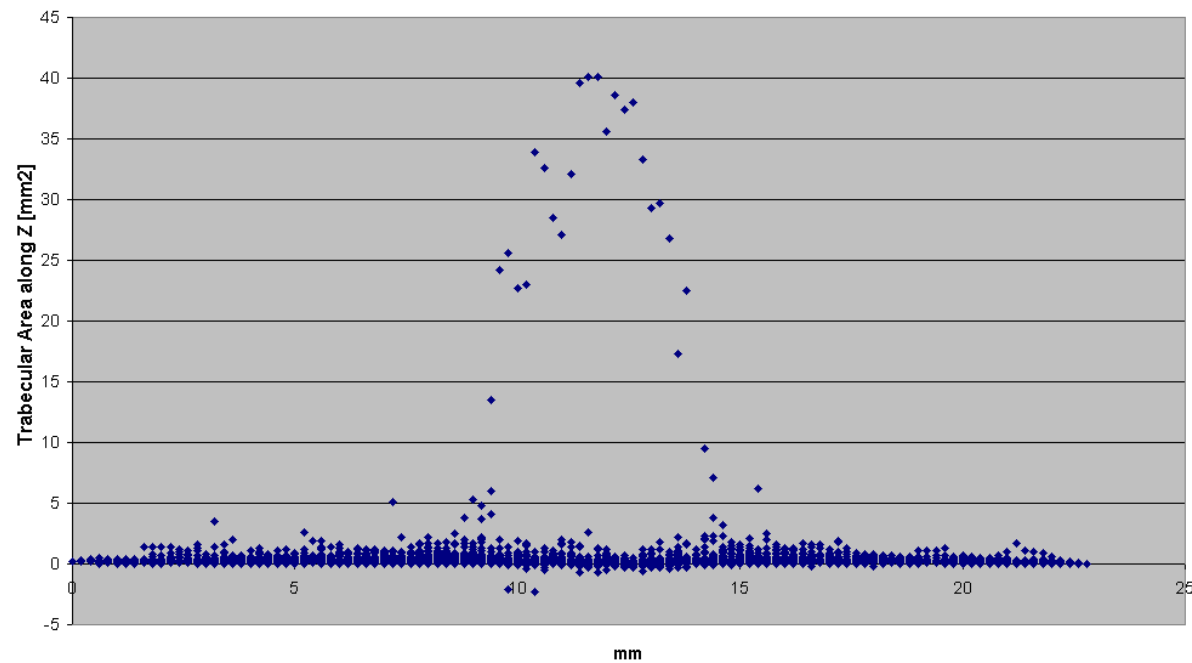


Fig. 5.44 ADI mouse humerus sample: trabecular area distribution along Z

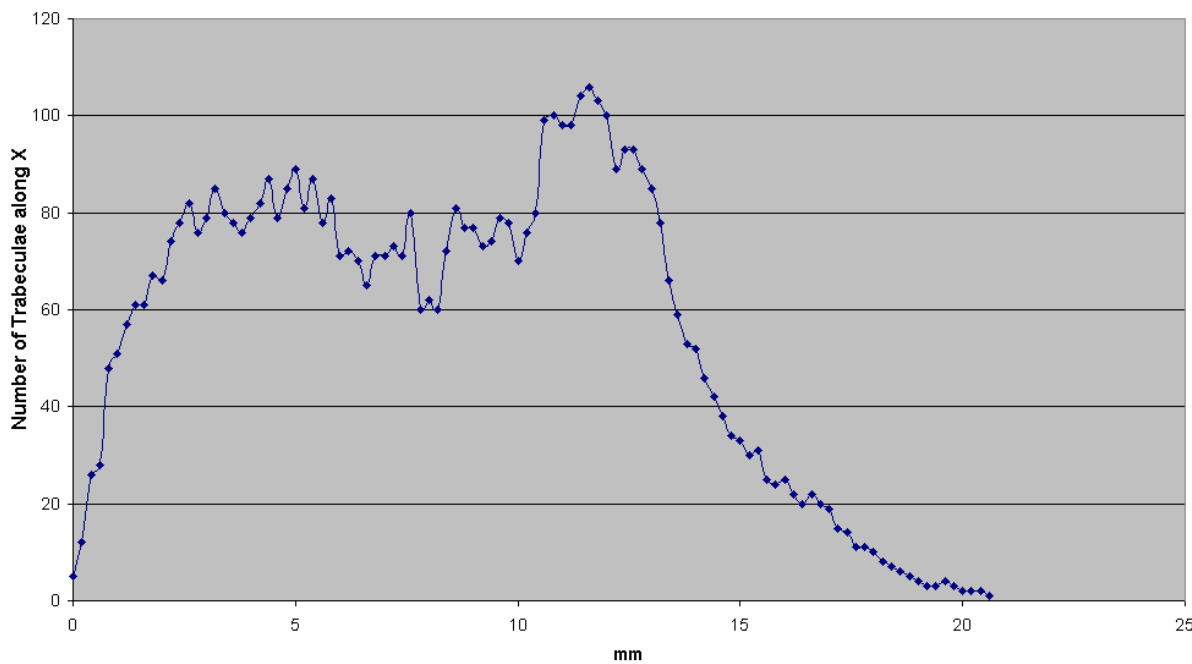


Fig. 5.45 ADI mouse humerus sample: number of trabeculae along *X*

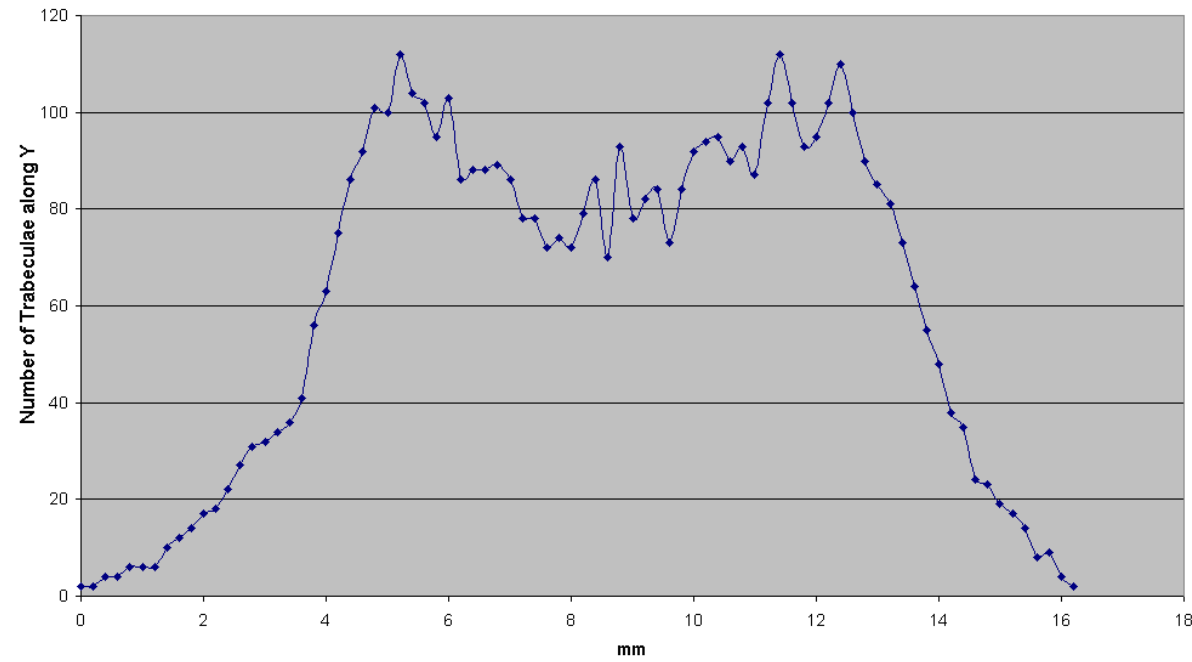
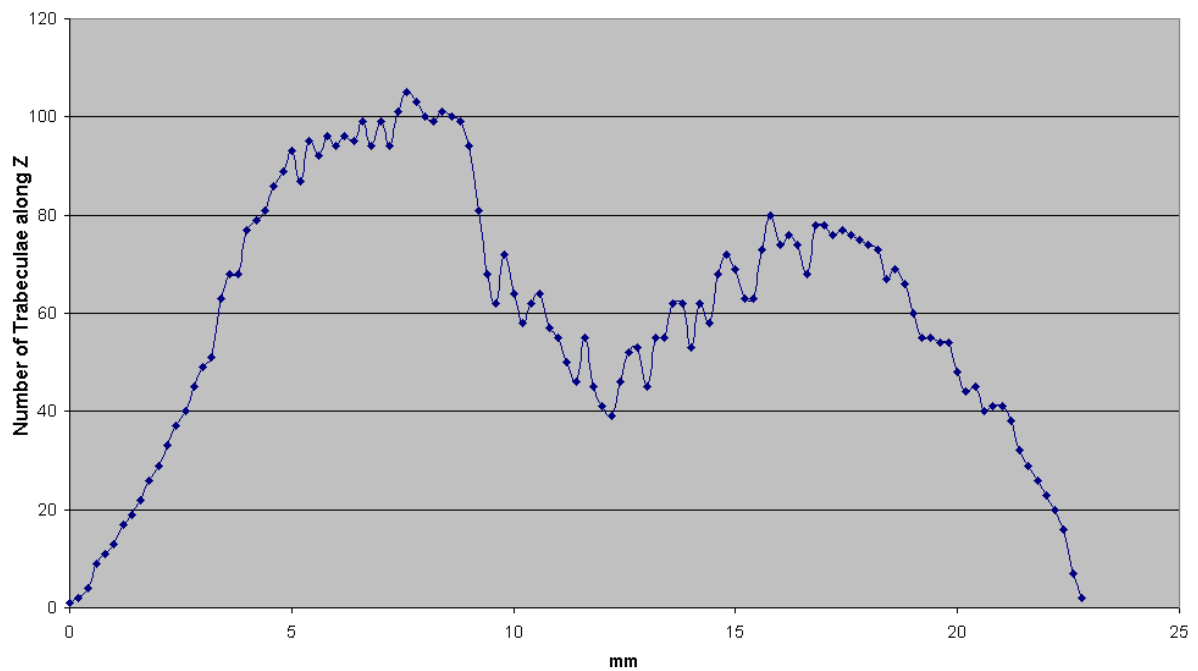


Fig. 5.46 ADI mouse humerus sample: number of trabeculae along *Y*



**Fig. 5.47** ADI mouse humerus sample: number of trabeculae along Z

	<b>X</b>	<b>Y</b>	<b>Z</b>
<b>Analysis Time (s)</b>	3798 s	3909 s	4541 s
<b>Total number of rods</b>	3683	2934	4680
<b>Total number of plates</b>	2107	2075	2216
<b>Trabecular Area Range (mm<sup>2</sup>)</b>	-10.175 to 53.884	-6.93 to 55.79	-2.335 to 40.095
<b>Sliced area (mm<sup>2</sup>)</b>	0.182 to 65.095	0.2165 to 73.295	0.028 to 46.346

**Table 5.10** ADI mouse humerus sample: main data from the analysis

## 5.4 Comparison and Assessment of the Analysed Structures

The comparisons between the cubic  $\mu$ CT sample and the cubic ADI samples, and between the mouse humerus  $\mu$ CT sample and the relative ADI sample, are presented in the following subsections.

### 5.4.1 Comparison between Cubic ADI Case 5 Sample and Cubic $\mu$ CT Sample

The cubic  $\mu$ CT sample presents relatively uniform trends of sliced area, trabecular area and number of trabeculae in the three directions, mainly because it is only a section of a larger bone. In the ADI case 5 sample, however, the shape of the curves is a direct result of the channels being forced through the centre of the volume. As a result, it was expected to have

a maximum value for the sliced and trabecular areas and a minimum number of trabeculae at the centre of the cube. For those reasons, the graphs were never likely to be similar.

The comparisons of sliced areas between the cubic  $\mu$ CT sample and the cubic ADI case 5 sample are depicted in Fig. 5.48 to Fig. 5.50. The level of sliced area at the centre (5mm distance for each axis) is higher in the ADI case 5 sample by  $44.5\text{mm}^2$  along  $Z$ ,  $43\text{mm}^2$  along  $X$  and  $50\text{mm}^2$  along  $Y$ . Ten cross-sections presented the same sliced area on  $X$ , and four on  $Y$  and  $Z$ . The sliced area ranges were also significantly different, with the upper limit of the  $\mu$ CT sample similar to the lower limit of the ADI case 5 sample.

A similar tendency was seen in the trabecular area in the three directions, as shown in Fig. 5.51 to Fig. 5.53. In the middle section, the differences between the two biggest contours were approximately  $45\text{mm}^2$  along  $X$ ,  $55\text{mm}^2$  along  $Y$ , and  $50\text{mm}^2$  along  $Z$ . The trabecular area ranges were also different, with the lower value always negative for the  $\mu$ CT sample and close to zero for the ADI case 5 sample, where no voids were present in the geometry. The upper limits were much higher for the ADI case 5 sample - more than three times on  $X$  and  $Z$ , and twice on  $Y$ .

The number of trabeculae along the three axes is shown in Fig. 5.54 to Fig. 5.56. In the ADI case 5 sample, such values are much higher, except towards the centre of the cube, where they drop to a minimum. This tendency is evidence of a high degree of interconnectivity toward the centre, as a consequence of the design. When the number of trabeculae decreased, the interconnectivity increased, and vice versa. In this comparison, only seven sections had the same number of trabeculae along  $X$  and  $Y$ , and six along  $Z$ .

The number of polylines classified as 'rods' was much higher in the ADI case 5 sample (more than three, four and nine times higher on  $X$ ,  $Y$  and  $Z$  respectively), as well as the number of 'plates' (more than twice on each axis).

The main differences between these two geometries are summarised in Table 5.11.

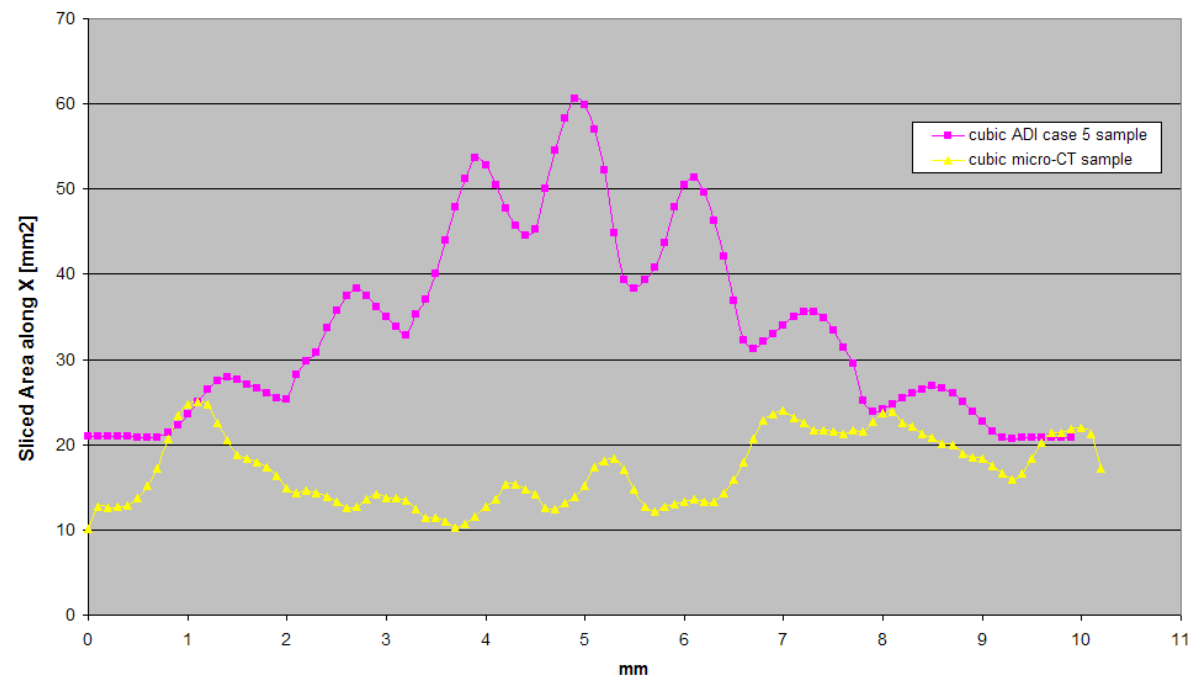


**Fig. 5.48** Comparison of sliced area along *X* between the cubic ADI case 5 sample and cubic  $\mu$ CT sample

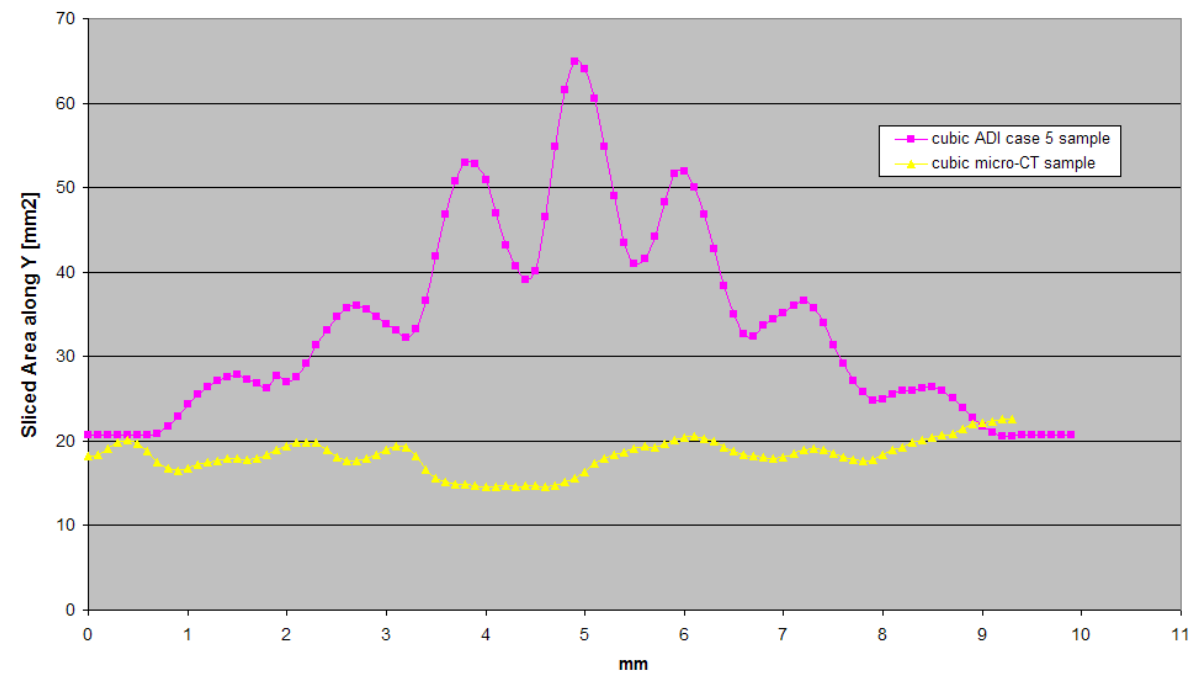


**Fig. 5.49** Comparison of sliced area along *Y* between the cubic ADI case 5 sample and cubic  $\mu$ CT sample

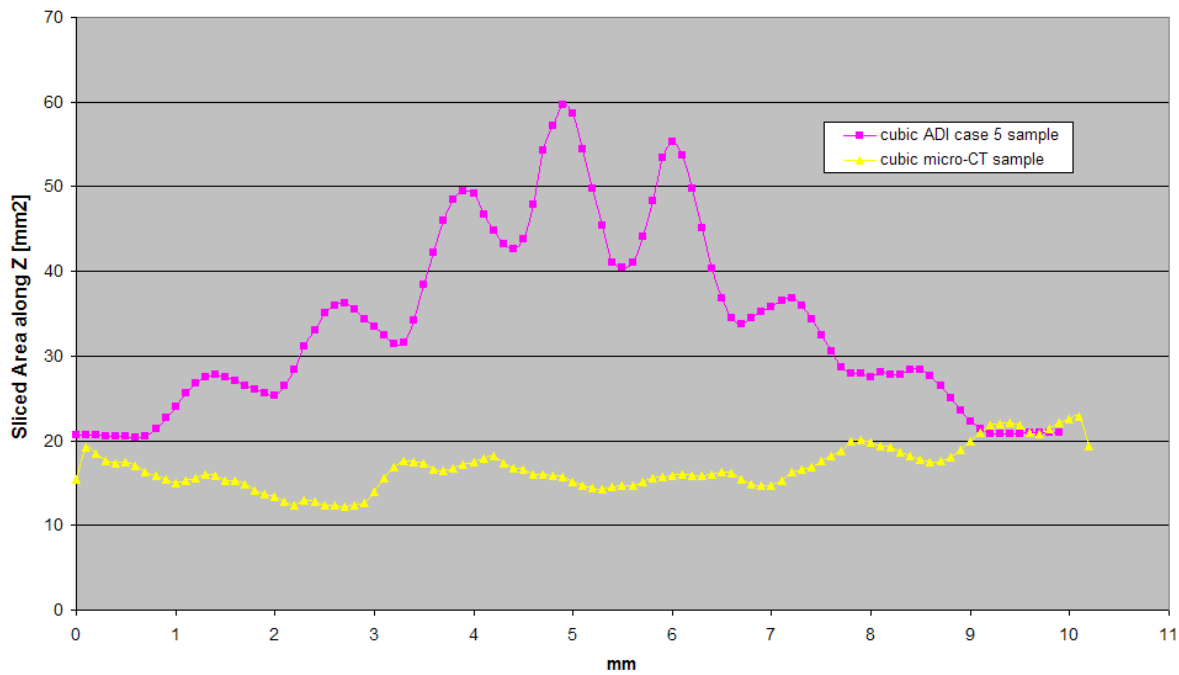


**Fig. 5.50** Comparison of sliced area along Z between the cubic ADI case 5 sample and cubic  $\mu$ CT sample

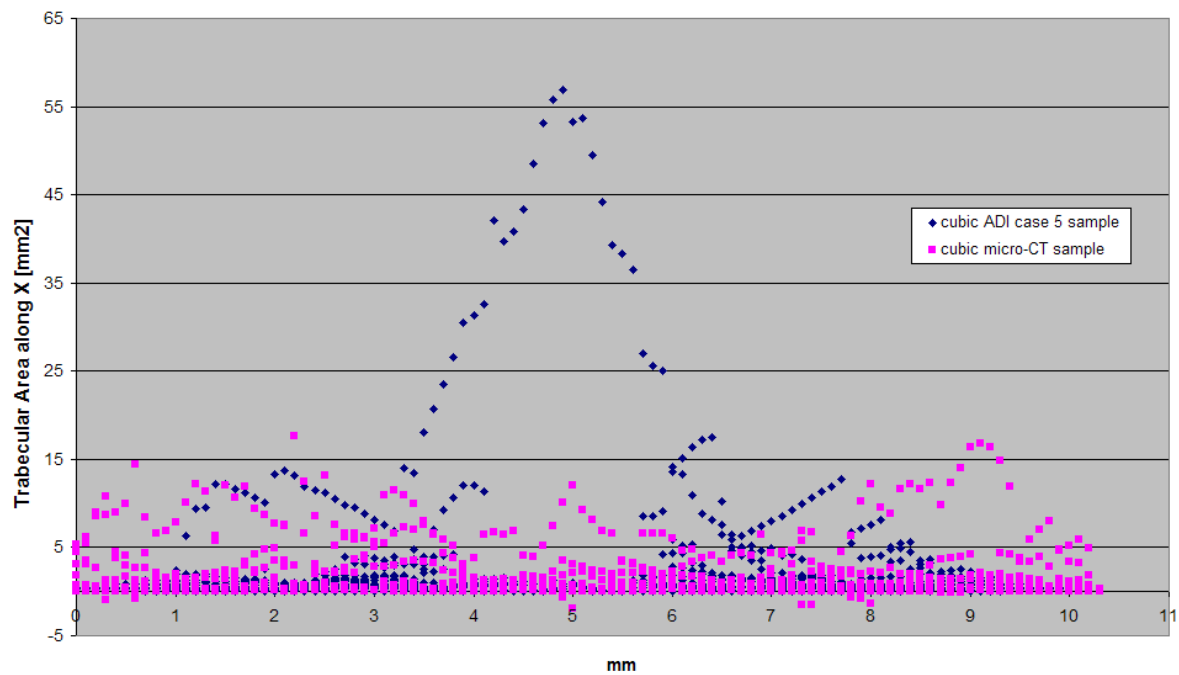


**Fig. 5.51** Comparison of trabecular area along X between the cubic ADI case 5 sample and cubic  $\mu$ CT sample

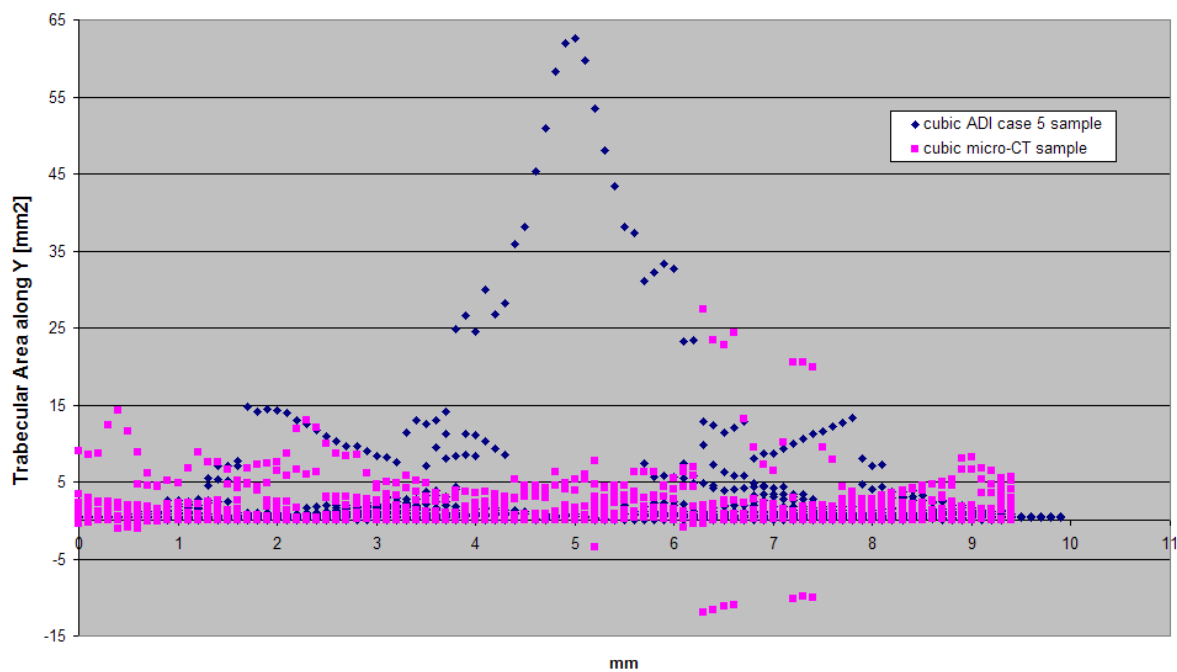


**Fig. 5.52** Comparison of trabecular area along *Y* between the cubic ADI case 5 sample and cubic  $\mu$ CT sample

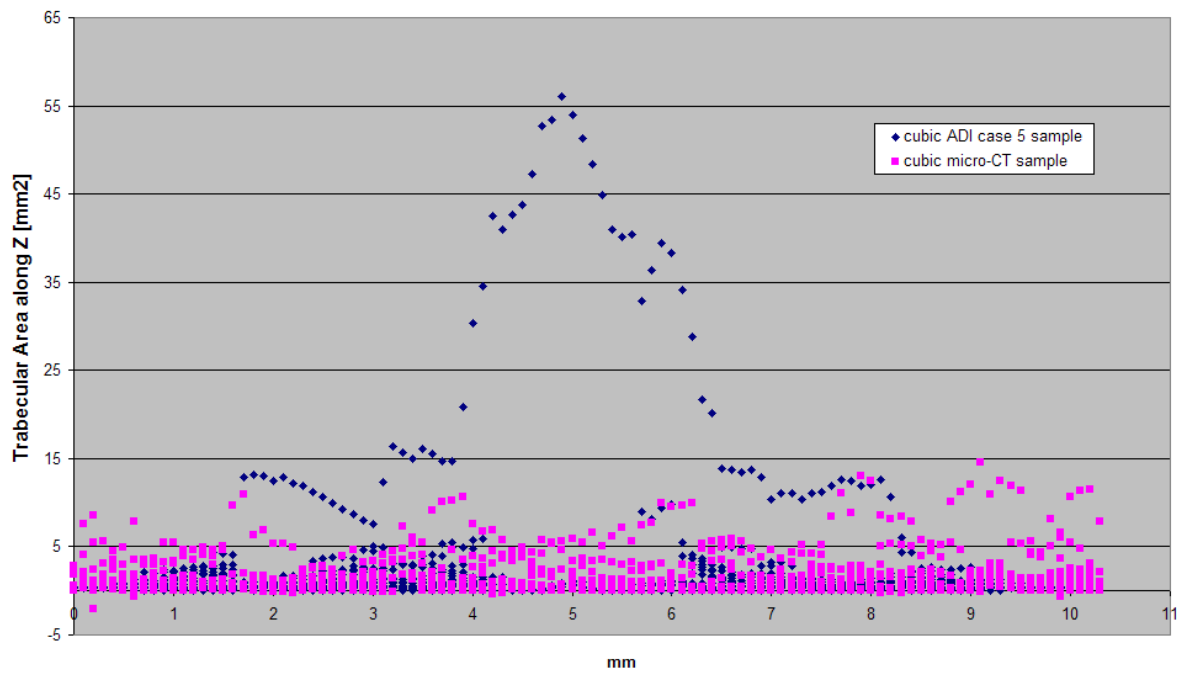


**Fig. 5.53** Comparison of trabecular area along *Z* between the cubic ADI case 5 sample and cubic  $\mu$ CT sample

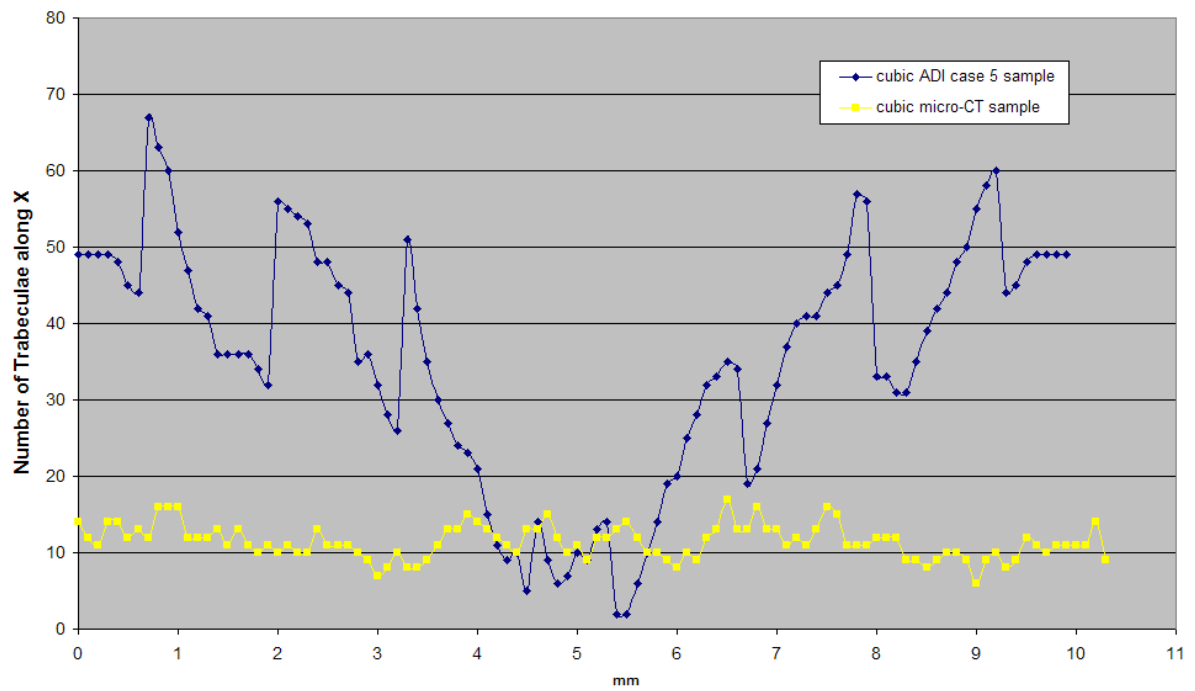


**Fig. 5.54** Comparison of number of trabeculae along  $X$  between the cubic ADI case 5 sample and cubic  $\mu$ CT sample

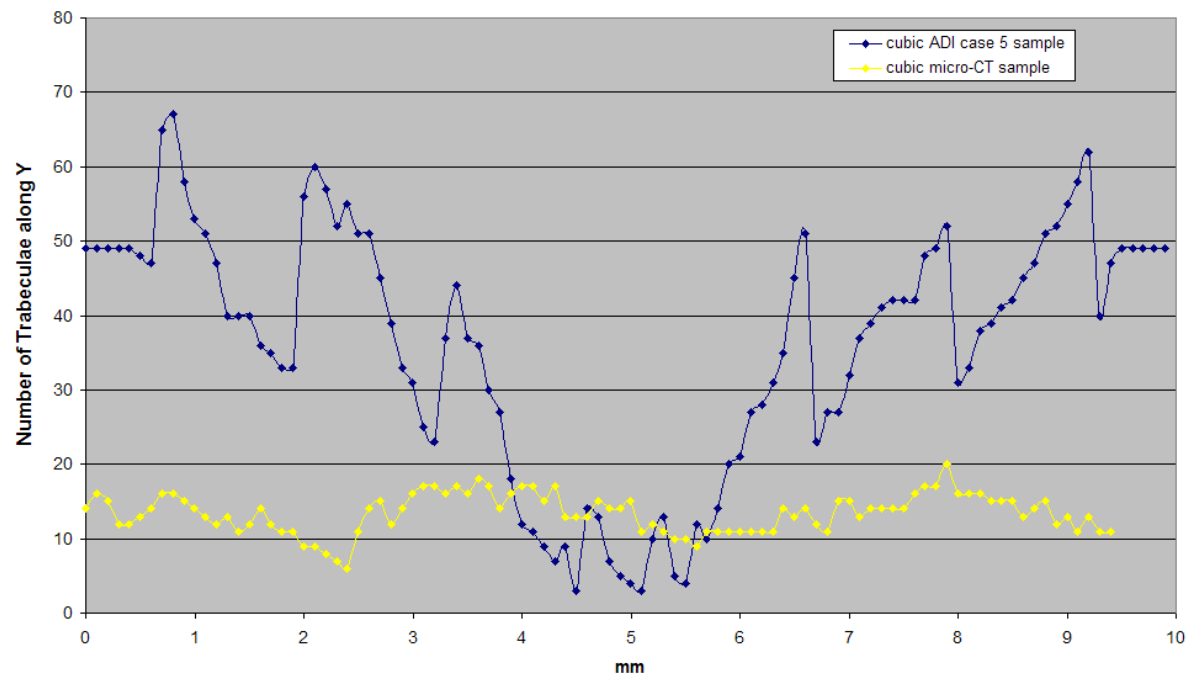


**Fig. 5.55** Comparison of the number of trabeculae along  $Y$  between the cubic ADI case 5 sample and cubic  $\mu$ CT sample



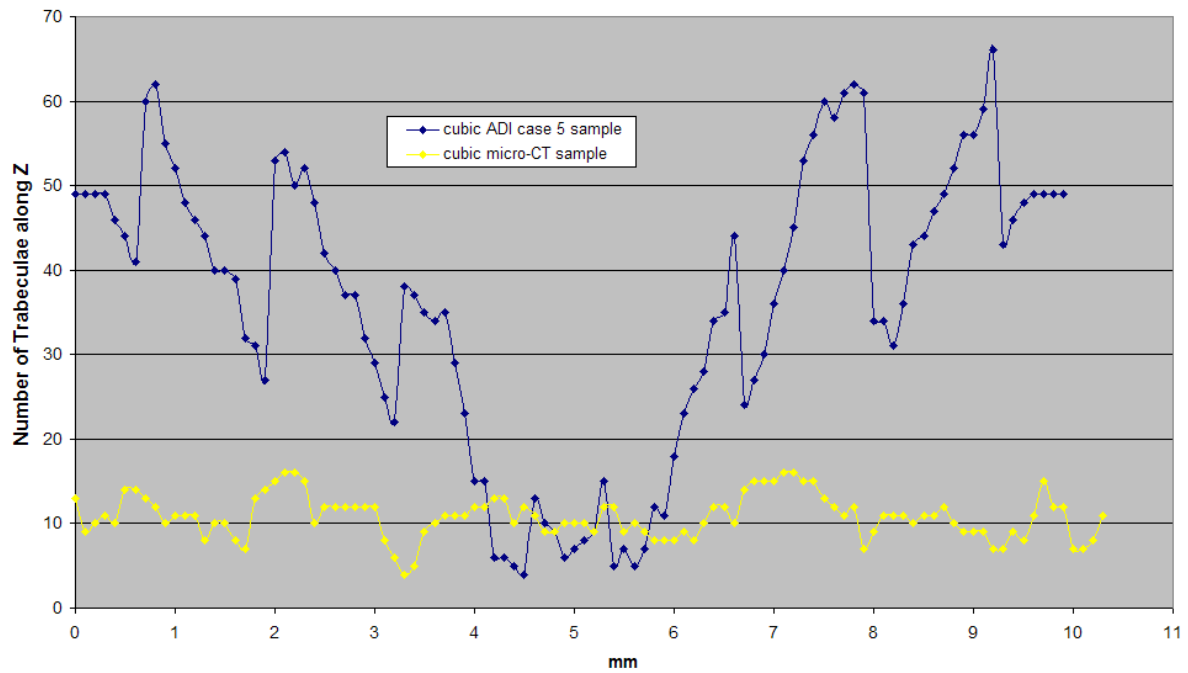


**Fig. 5.56** Comparison of the number of trabeculae along Z between the cubic ADI case 5 sample and cubic  $\mu$ CT sample

	X		Y		Z	
	cubic $\mu$ CT sample	cubic ADI case 5 sample	cubic $\mu$ CT sample	cubic ADI case 5 sample	cubic $\mu$ CT sample	cubic ADI case 5 sample
Total number of rods	504	1739	457	1830	278	1818
Total number of plates	684	1782	820	1765	850	1773
Trabecular Area Range (mm <sup>2</sup> )	-1.967 to 17.56	0.00018 to 56.96	-11.99 to 27.38	0.00011 to 62.58	-2.07 to 14.53	0.0002 to 56.12
Sliced area (mm <sup>2</sup> )	10.1 to 25.08	20.81 to 60.589	14.53 to 22.59	20.71 to 64.89	12.2 to 22.88	20.407 to 59.74

**Table 5.11** Differences between the cubic ADI case 5 sample and cubic  $\mu$ CT sample

#### 5.4.2 Comparison between Cubic ADI Case 6 Sample and Cubic $\mu$ CT Sample

The cubic  $\mu$ CT sample presents relatively uniform trends of sliced area, trabecular area and number of trabeculae in the three directions, mainly because it is only a section of a larger bone. In the ADI case 6 sample, however, the shape of the curves is a direct result of the channels being forced through a central region of the volume. As a result, it was expected to have several maximum peaks of sliced and trabecular areas, and several minimum peaks of

the number of trabeculae around the centre of the cube. For those reasons, the graphs were never likely to be similar.

The comparisons of sliced areas along the three axes between the cubic  $\mu$ CT sample and the cubic ADI case 6 sample, are depicted in Fig. 5.57 to Fig. 5.59. The sliced area in the middle section (5mm distance on each axis) was higher in the ADI case 6 sample by  $48\text{mm}^2$  along  $Z$ ,  $38\text{mm}^2$  along  $X$  and  $46\text{mm}^2$  along  $Y$ , and only three cross-sections on each axis presented the same sliced area. The differences in the ranges of sliced area were similar to those found in previous cases.

The trabecular areas on each axis are shown in Fig. 5.60 to Fig. 5.62. In the middle section, the differences between the two biggest contours were approximately  $33\text{mm}^2$  along  $X$ ,  $40\text{mm}^2$  along  $Y$  and  $49\text{mm}^2$  along  $Z$ . The trabecular area ranges were also different, with the lower value always negative for the cubic  $\mu$ CT sample and close to zero for the cubic ADI case 6 sample, where no voids were present in the geometry. The upper limits were also higher for the ADI sample - more than three times in  $X$ , twice in  $Y$  and approximately four times in  $Z$ .

The number of trabeculae along the three axes is shown in Fig. 5.63 to Fig. 5.65. In the ADI case 6 sample these numbers are much higher, except toward the centre of the cube, where the differences with the  $\mu$ CT sample become smaller. The number of trabeculae on the  $X$  axis presents a minimum at approximately 5.5mm, while on the other two axes there is no well-defined tendency, and the curves appear to have fractality due to the random interconnections. In addition, the two curves never intersect on the  $Z$  axis. As a consequence, only four sections had the same number of trabeculae on  $X$  and  $Y$ , and none on  $Z$ .

The number of polylines classified as 'rods' was much higher in the ADI sample (more than three, four and nine times higher on  $X$ ,  $Y$  and  $Z$  respectively), as well as the number of 'plates' (more than twice on each axis).

The main differences between these two geometries are summarised in Table 5.12.

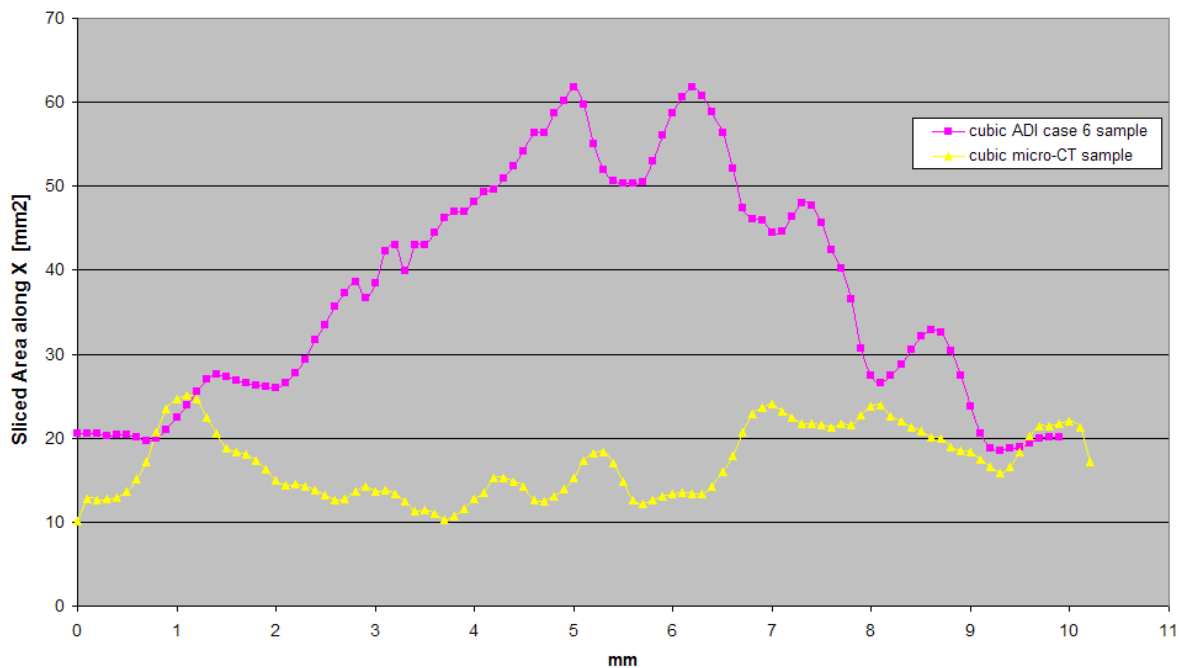


**Fig. 5.57** Comparison of sliced area along *X* between the cubic ADI case 6 sample and cubic  $\mu$ CT sample

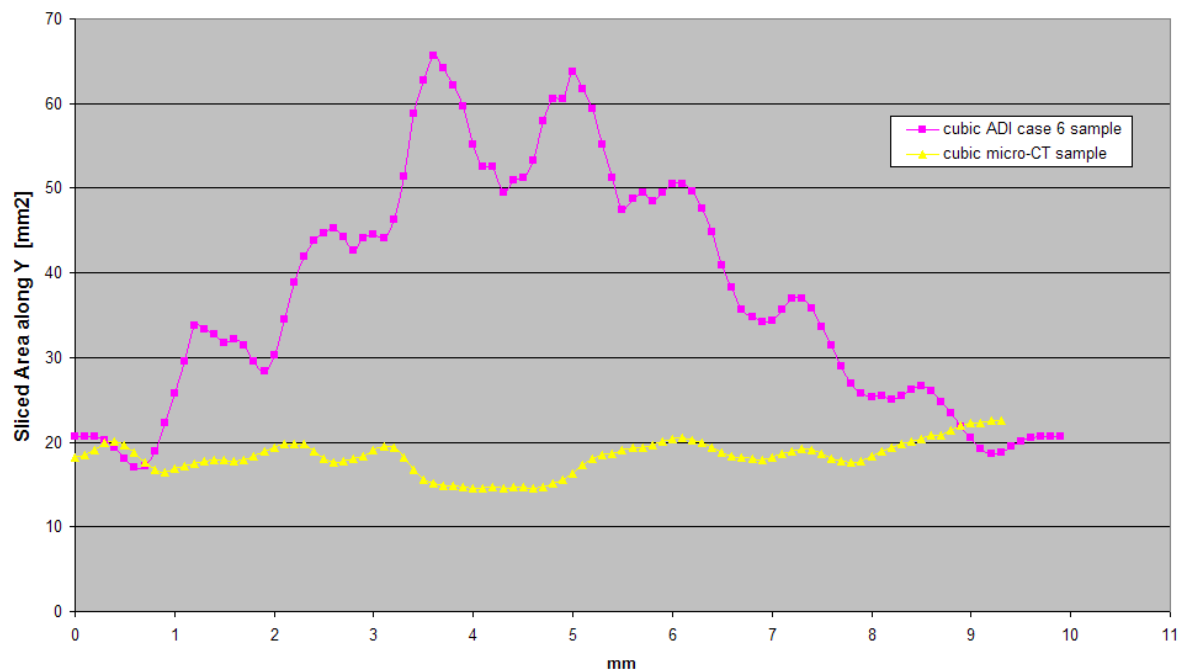


**Fig. 5.58** Comparison of sliced area along *Y* between the cubic ADI case 6 sample and cubic  $\mu$ CT sample

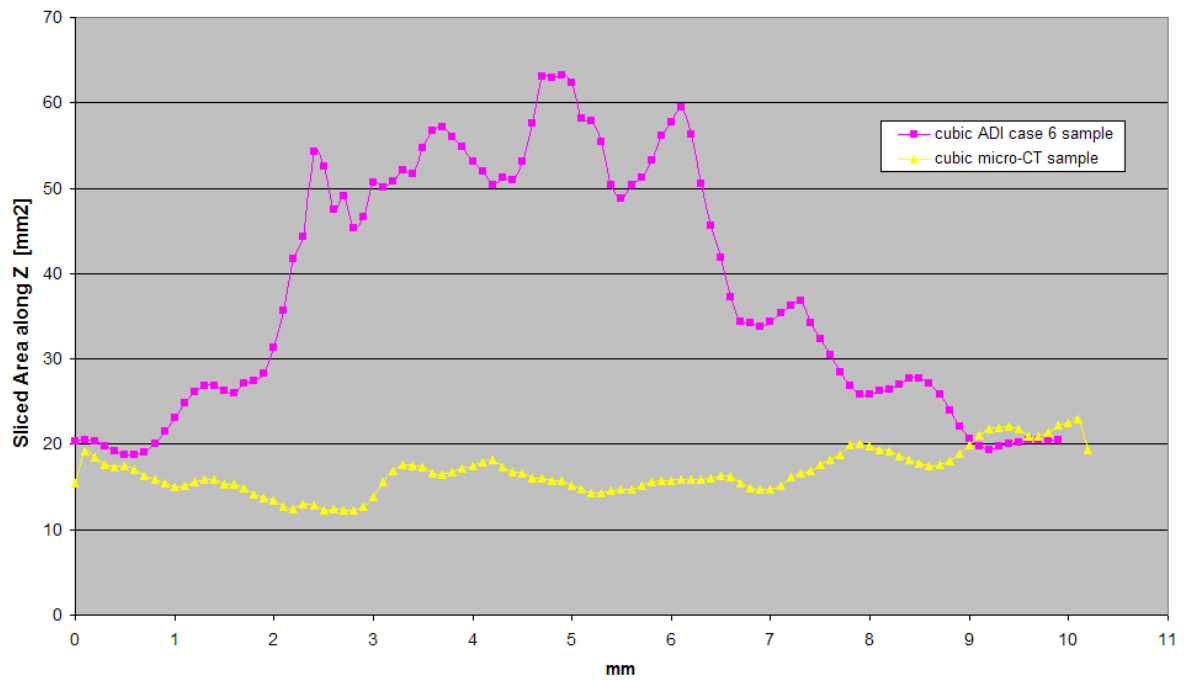


**Fig. 5.59** Comparison of sliced area along  $Z$  between the cubic ADI case 6 sample and cubic  $\mu$ CT sample

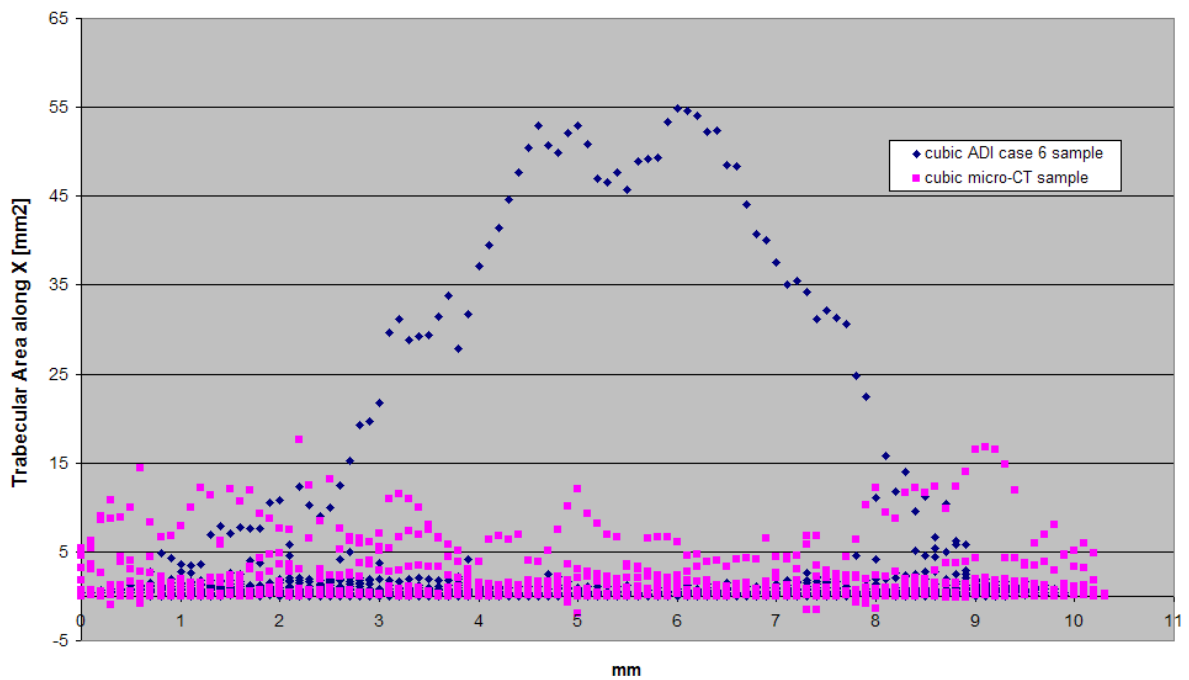


**Fig. 5.60** Comparison of trabecular area along  $X$  between the cubic ADI case 6 sample and cubic  $\mu$ CT sample

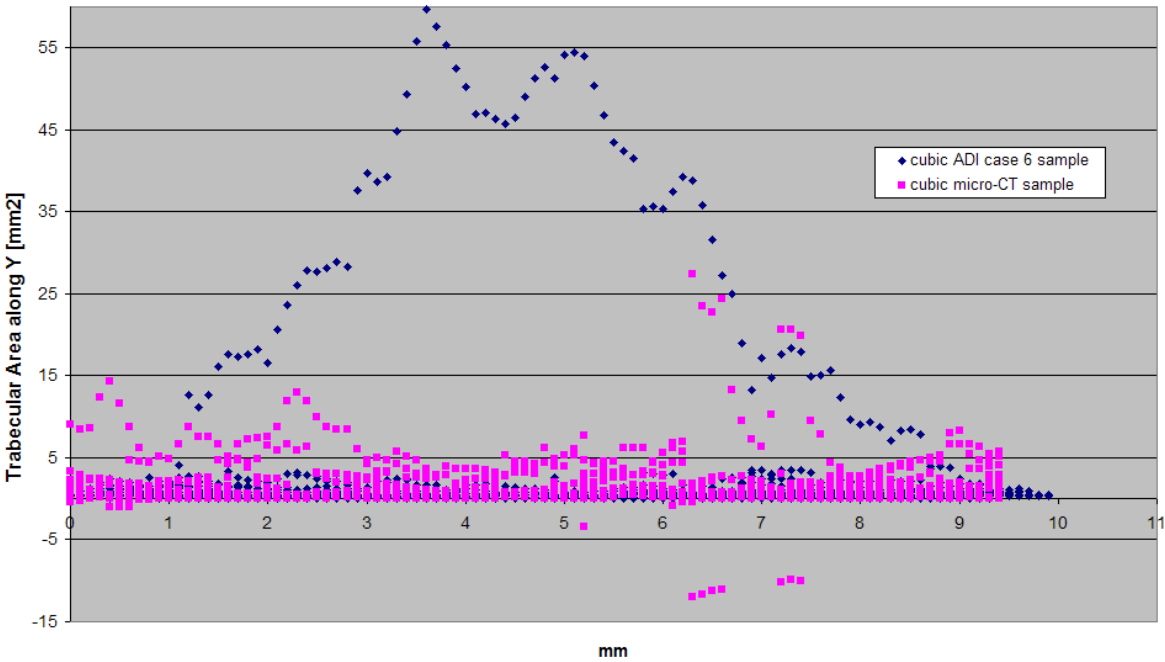


**Fig. 5.61** Comparison of trabecular area along *Y* between the cubic ADI case 6 sample and cubic  $\mu$ CT sample

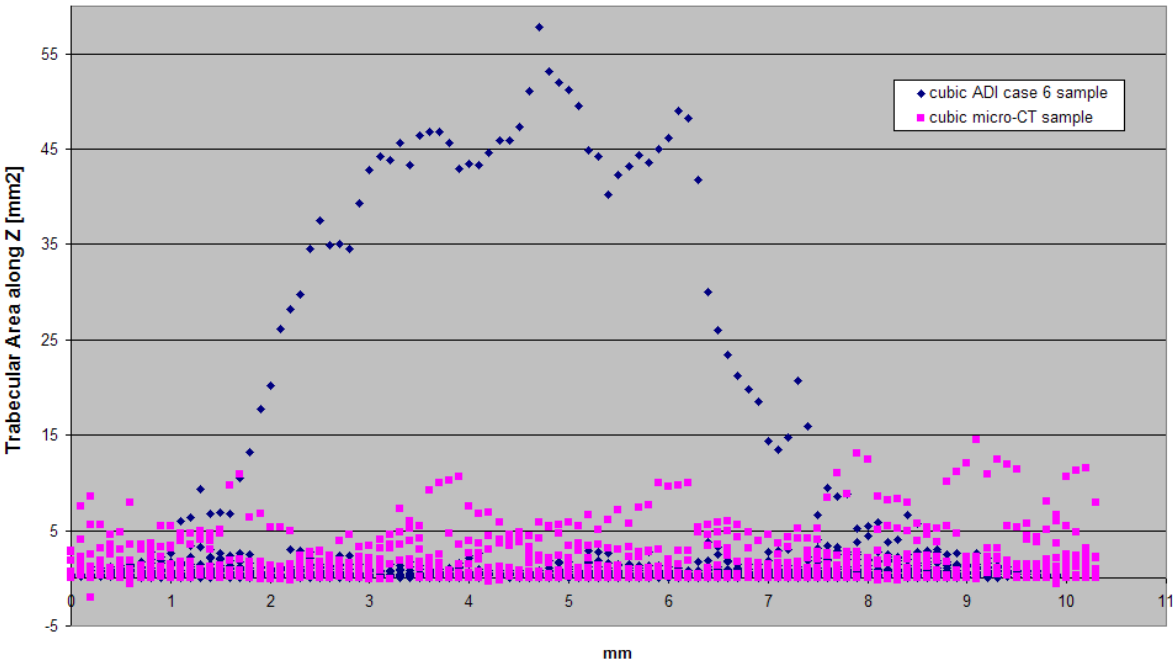


**Fig. 5.62** Comparison of trabecular area along *Z* between the cubic ADI case 6 sample and cubic  $\mu$ CT sample

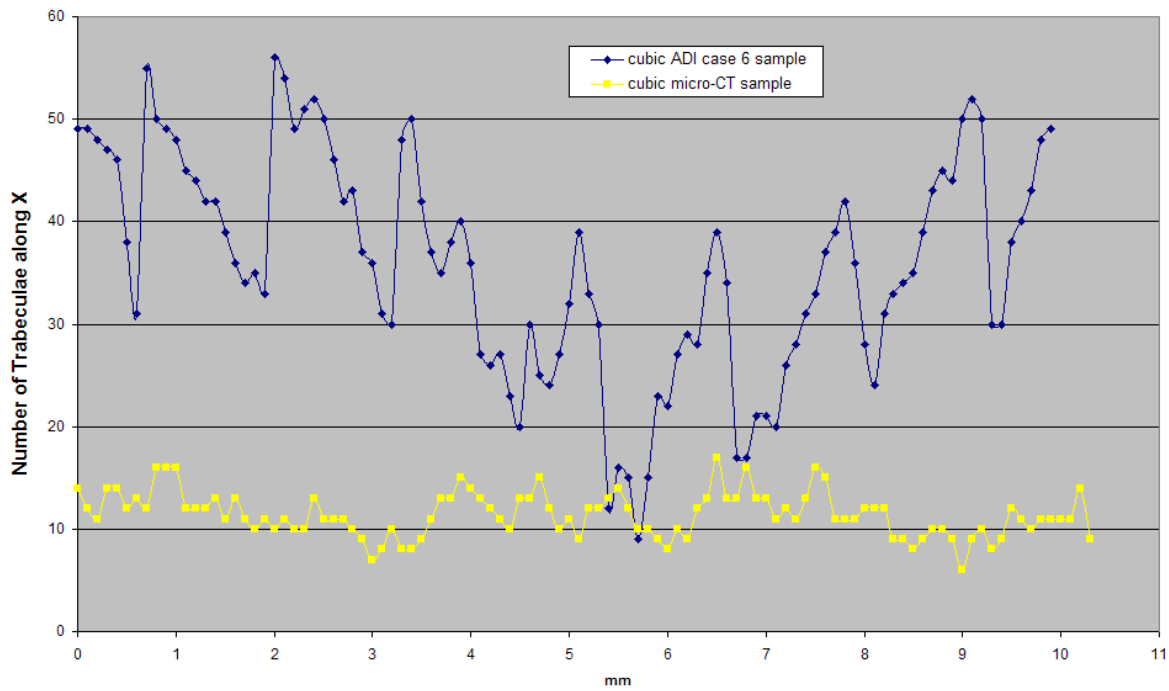


**Fig. 5.63** Comparison of the number of trabeculae along *X* between the cubic ADI case 6 sample and cubic  $\mu$ CT sample

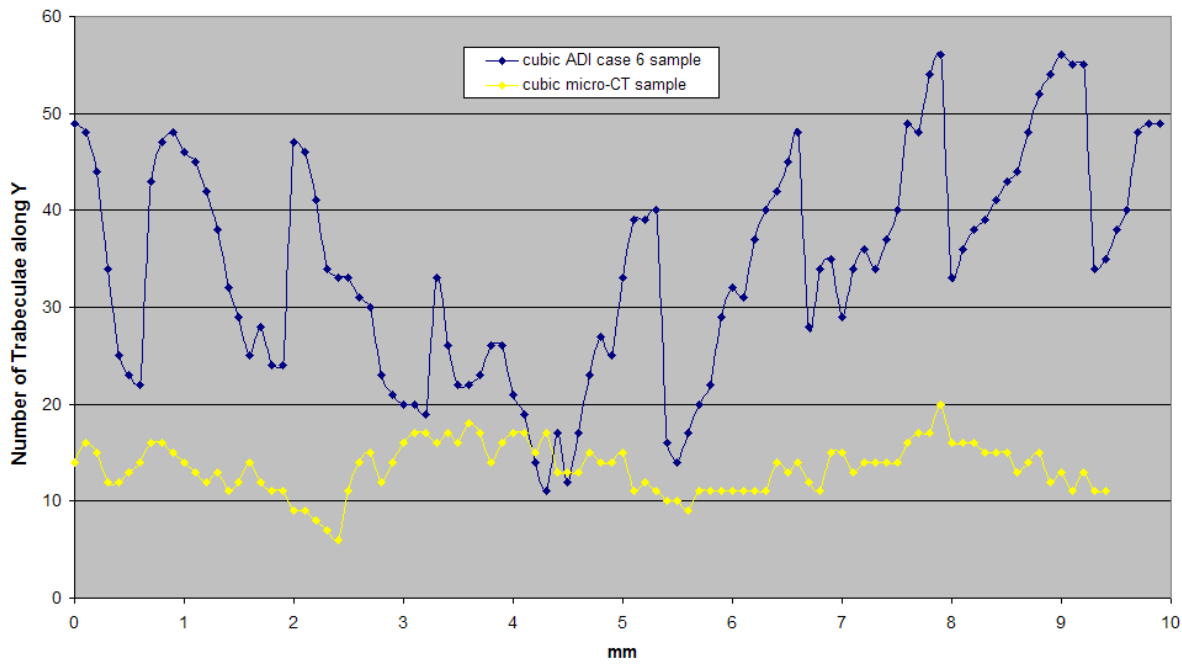


**Fig. 5.64** Comparison of the number of trabeculae along *Y* between the cubic ADI case 6 sample and cubic  $\mu$ CT sample

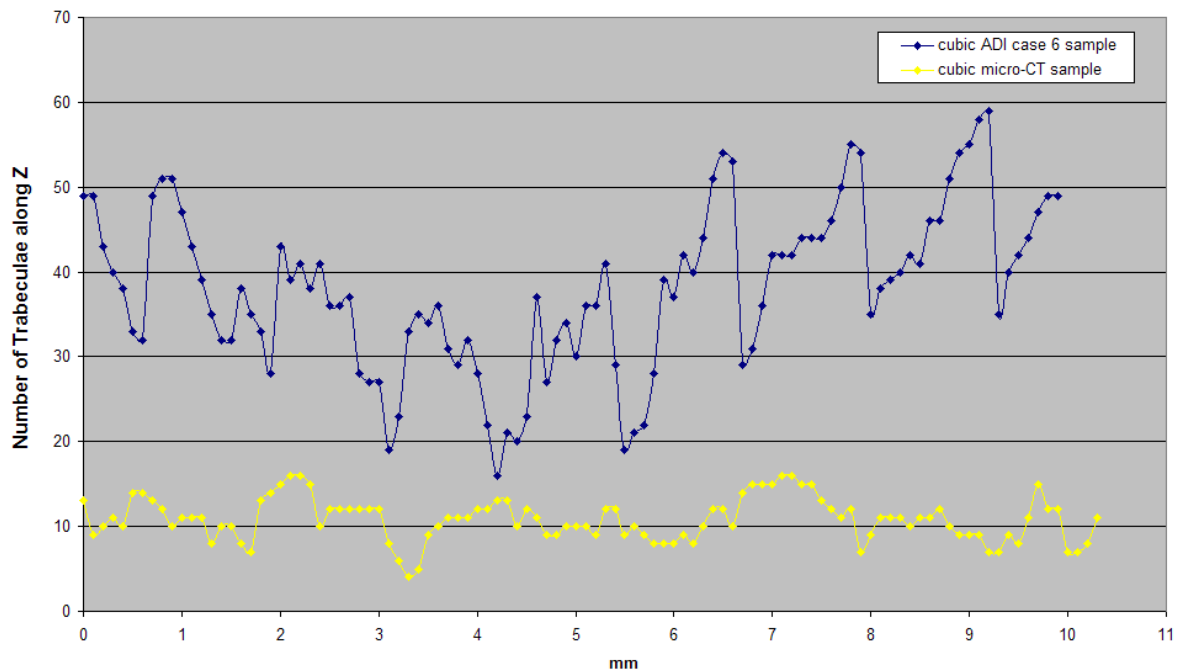


**Fig. 5.65** Comparison of the number of trabeculae along Z between the cubic ADI case 6 sample and cubic  $\mu$ CT sample

	X		Y		Z	
	cubic $\mu$ CT sample	cubic ADI case 6 sample	cubic $\mu$ CT sample	cubic ADI case 6 sample	cubic $\mu$ CT sample	cubic ADI case 6 sample
Total number of rods	504	1733	457	1686	278	1913
Total number of plates	684	1851	820	1737	850	1900
Trabecular Area Range (mm <sup>2</sup> )	-1.967 to 17.56	0.00047 to 54.917	-11.99 to 27.38	0.0003 to 59.77	-2.07 to 14.53	0.0001 to 57.78
Sliced area (mm <sup>2</sup> )	10.1 to 25.08	18.49 to 61.818	14.53 to 22.59	17.06 to 65.7	12.2 to 22.88	18.705 to 63.245

**Table 5.12** Differences between the cubic ADI case 6 sample and cubic  $\mu$ CT sample

### 5.4.3 Comparison between ADI Mouse Humerus Sample and $\mu$ CT Mouse Humerus Sample

In the  $\mu$ CT mouse humerus sample there are several peaks of sliced area, which are located in those sections where the bone is thickest. The same sections present peak values in the trabecular area and number of trabeculae (in all directions), suggesting that they are formed by a few big rods/plates and a large number of small rods/plates.

In the ADI mouse humerus sample, the trabecular and sliced areas present several maximum peaks around the centre in all directions, as a result of the design assumptions adopted. For the same reasons, the number of trabeculae also presents several minimum peaks around the centre of the volume.

The comparisons of sliced areas along the three axes, between the  $\mu$ CT mouse humerus sample and the relative ADI sample, are depicted in Fig. 5.66 to Fig. 5.68. From these figures it can be observed that the distributions present analogies, in particular along the  $X$  and  $Y$  axes, where the curves present similar shapes.

There are no great differences in the numerical values, and the amount of excess material in some areas of the ADI sample is compensated by the lack of material in others, showing an overall balance in the material distributions. That balance is well reflected by the sliced area ranges, which appeared to be close in all three directions ( $0.069 \text{ mm}^2$  to  $81.837 \text{ mm}^2$  and  $0.182 \text{ mm}^2$  to  $65.095 \text{ mm}^2$  on  $X$ ,  $0.09 \text{ mm}^2$  to  $74.31 \text{ mm}^2$  and  $0.2165 \text{ mm}^2$  to  $73.295 \text{ mm}^2$  on  $Y$ , and  $0.0125 \text{ mm}^2$  to  $61.765 \text{ mm}^2$  and  $0.028 \text{ mm}^2$  to  $46.346 \text{ mm}^2$  on  $Z$ ). In the ADI mouse humerus sample, most of the material tends to be concentrated at the centre of the structure as a result of the design approach adopted, which constrained the multi-section solids to pass through a central volume.

In the real bone structure, the material appears to be concentrated in one area along the  $Z$  axis and not located at the centre, but where the bone is thickest. In the middle section, the sliced area was the same in the  $X$  direction ( $36.7 \text{ mm}^2$ ), and lower by  $21 \text{ mm}^2$  and  $5 \text{ mm}^2$  along  $Z$  and  $Y$  respectively, whereas some other sections showed the same values (eighteen in  $X$ , three in  $Y$  and twelve in  $Z$ ).

A similar tendency was observed for the trabecular area in the three directions, as shown in Fig. 5.69 to Fig. 5.71. In the middle section, the differences between the two biggest contours were approximately  $3.5 \text{ mm}^2$  along  $X$ ,  $20 \text{ mm}^2$  along  $Y$  and  $6.5 \text{ mm}^2$  along  $Z$ .

The trabecular area ranges were very close in both the lower and the upper limits, in all three directions ( $-6.24 \text{ mm}^2$  to  $55.25 \text{ mm}^2$  and  $-10.175 \text{ mm}^2$  to  $53.884 \text{ mm}^2$  along  $X$ ,  $-3.37 \text{ mm}^2$  to  $56.987 \text{ mm}^2$  and  $-6.93 \text{ mm}^2$  to  $55.79 \text{ mm}^2$  for the  $Y$  axis, and  $-5.55 \text{ mm}^2$  to  $46.7 \text{ mm}^2$  and  $-2.335 \text{ mm}^2$  to  $40.095 \text{ mm}^2$  for the  $Z$  axis). The ADI mouse humerus presented significant



negatives values for the lower limits, meaning that voids of that maximum area were present in the geometry.

The number of trabeculae on the three axes is shown in Fig. 5.72 to Fig. 5.74. Along *X*, the ADI sample initially presents more contours - double in some sections - than the  $\mu$ CT sample, but the values become closer around the central area. Beyond that area, the values in the  $\mu$ CT mouse humerus become much higher, at some points even double. Along *Y*, the  $\mu$ CT mouse humerus has more trabeculae in all cross-sections, although with small differences in some points. Interestingly, the two curves present similar shapes. In the *Z* direction, the  $\mu$ CT sample presented an area with a much higher number of polylines (350 vs. 65), where most of the material is concentrated. That area corresponds to the interval around the maximum sliced area. Outside this portion of the diagram, the number of trabeculae in the ADI sample was always higher, despite it being very close at some points. As a consequence, only eight sections presented the same number of trabeculae along *X*, three along *Y*, and three along *Z*.

In the ADI mouse humerus, the numbers of polylines classified as 'rods' were always bigger (double in *Z*, 50% more in *X* and similar in *Y*), while the numbers of plates were significantly lower (up to three times less) than the respective values on the  $\mu$ CT sample.

The main differences between these two geometries are summarised in Table 5.13.

The comparison between the ADI and the  $\mu$ CT mouse humerus shows that the ADI geometry is a good approximation of the natural sample, and closer results would have been achieved by forcing the channels to converge to those sections where the natural bone is thickest. Since such sections are different in each direction, several converging points would be required on *X*, *Y*, and *Z*.

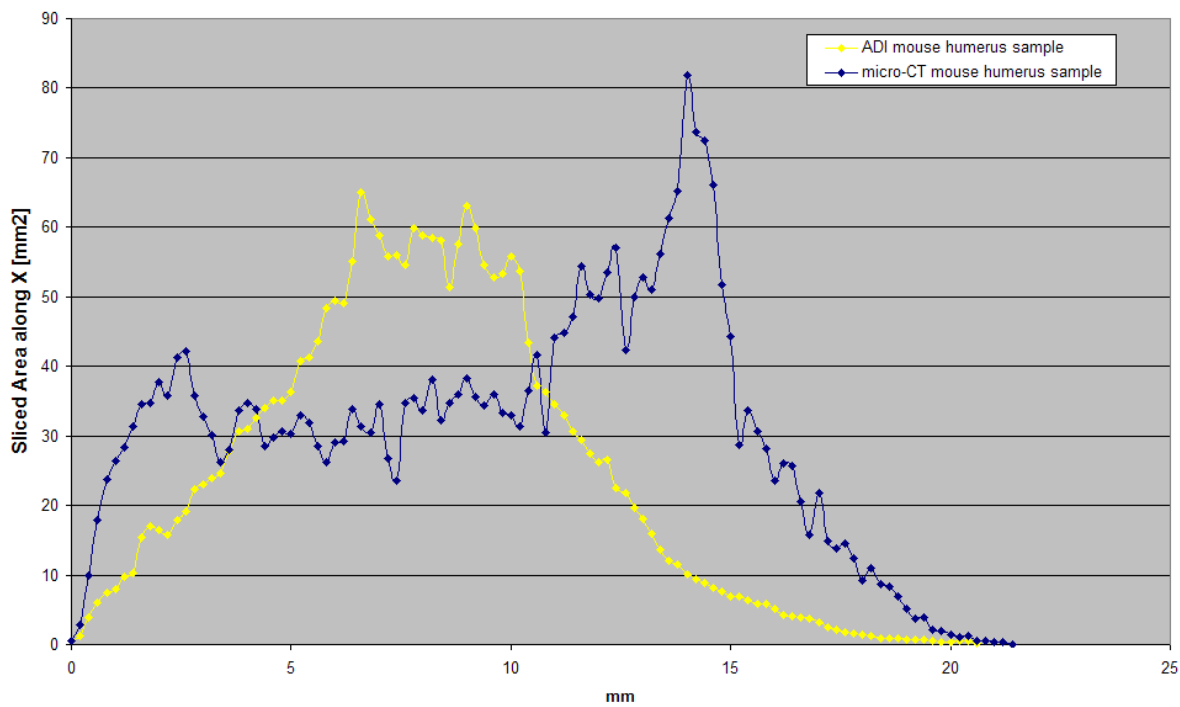


**Fig. 5.66** Comparison of the sliced area along X between the ADI mouse humerus and  $\mu$ CT mouse humerus

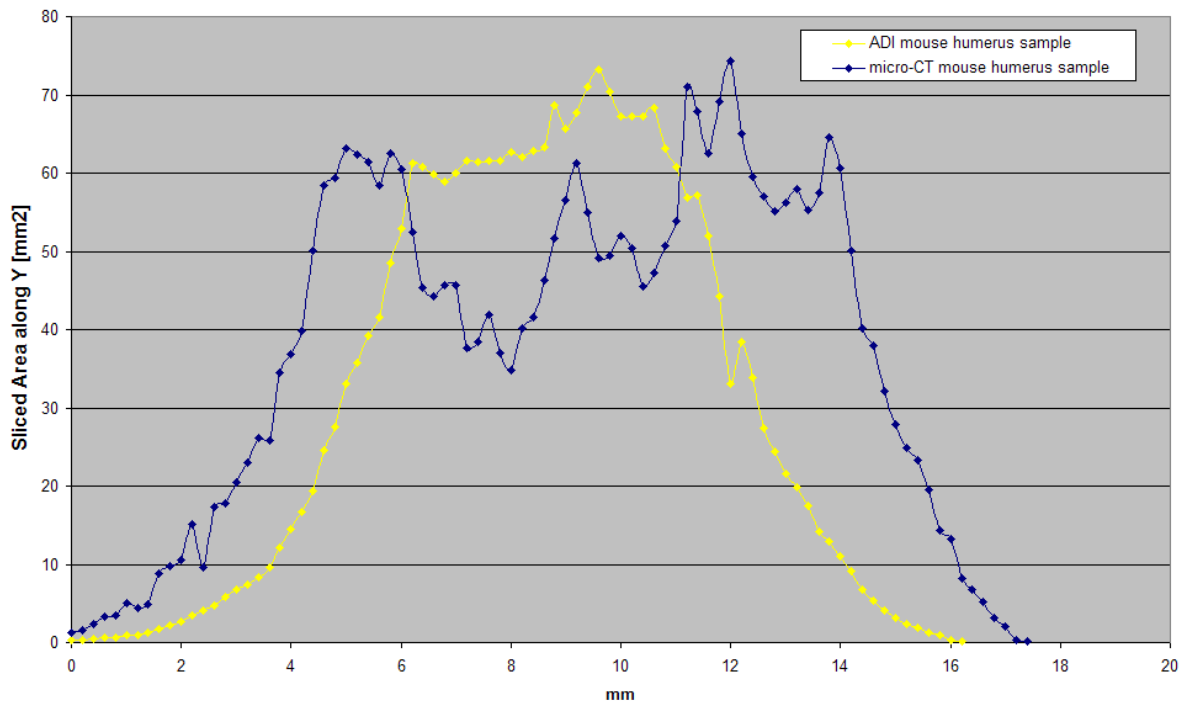


**Fig. 5.67** Comparison of the sliced area along Y between the ADI mouse humerus and  $\mu$ CT mouse humerus

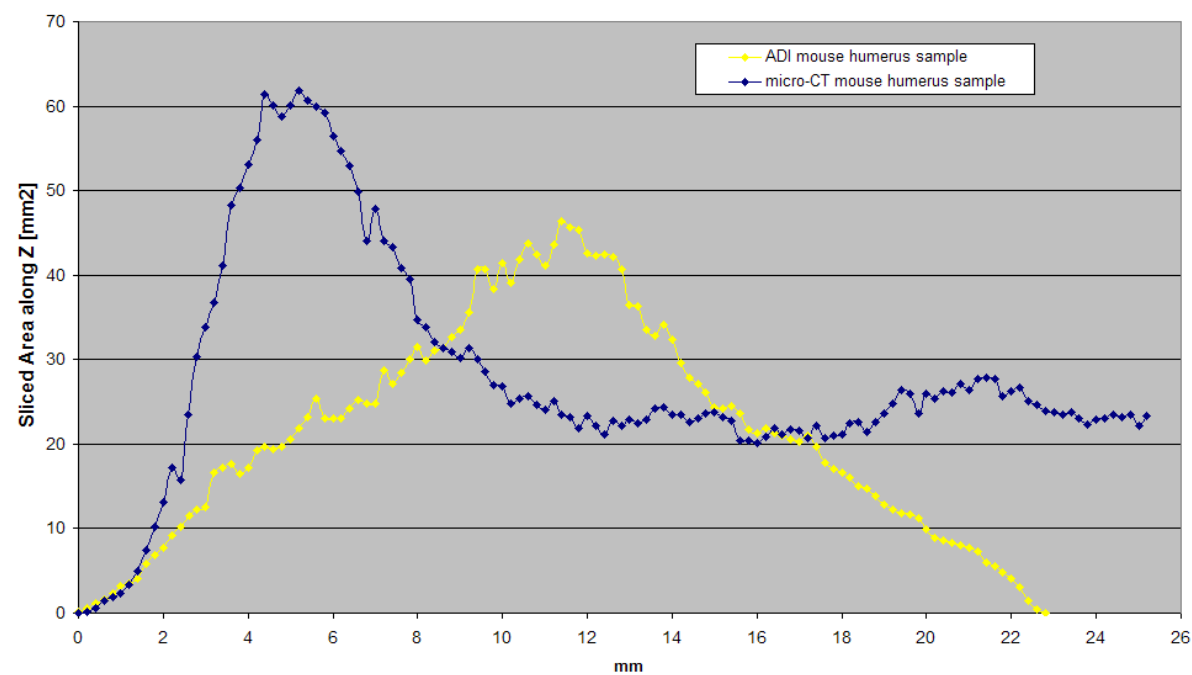


**Fig. 5.68** Comparison of the sliced area along Z between the ADI mouse humerus and  $\mu$ CT mouse humerus

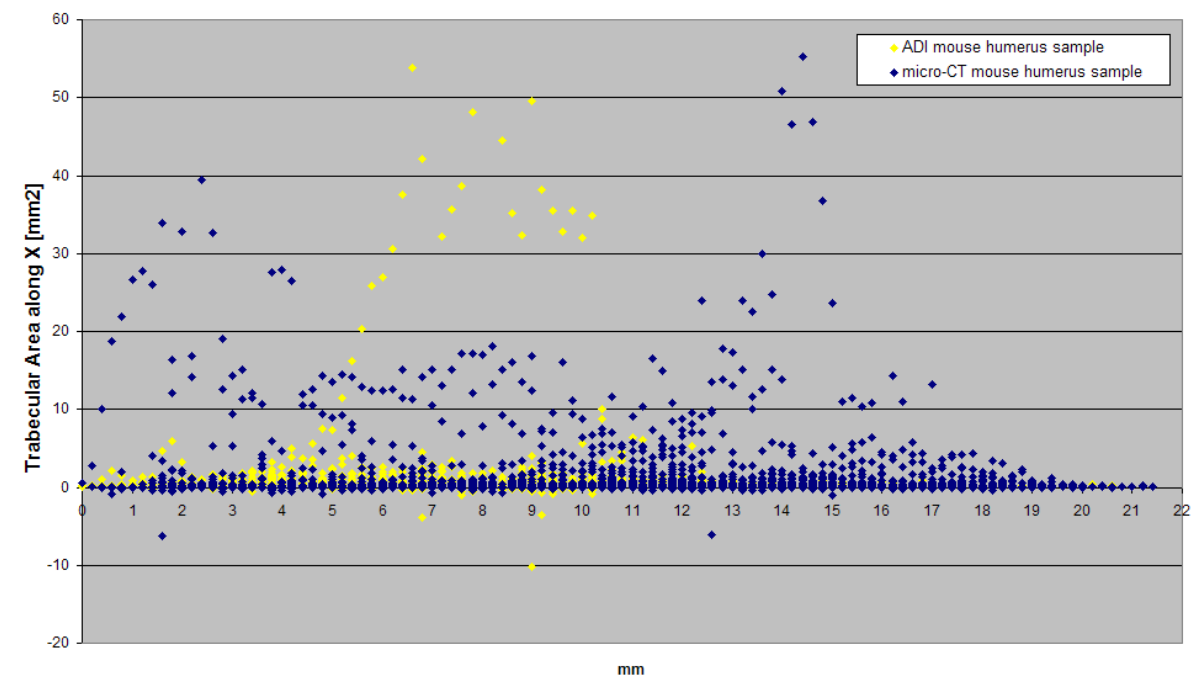


**Fig. 5.69** Comparison of the trabecular area along X between the ADI mouse humerus and  $\mu$ CT mouse humerus

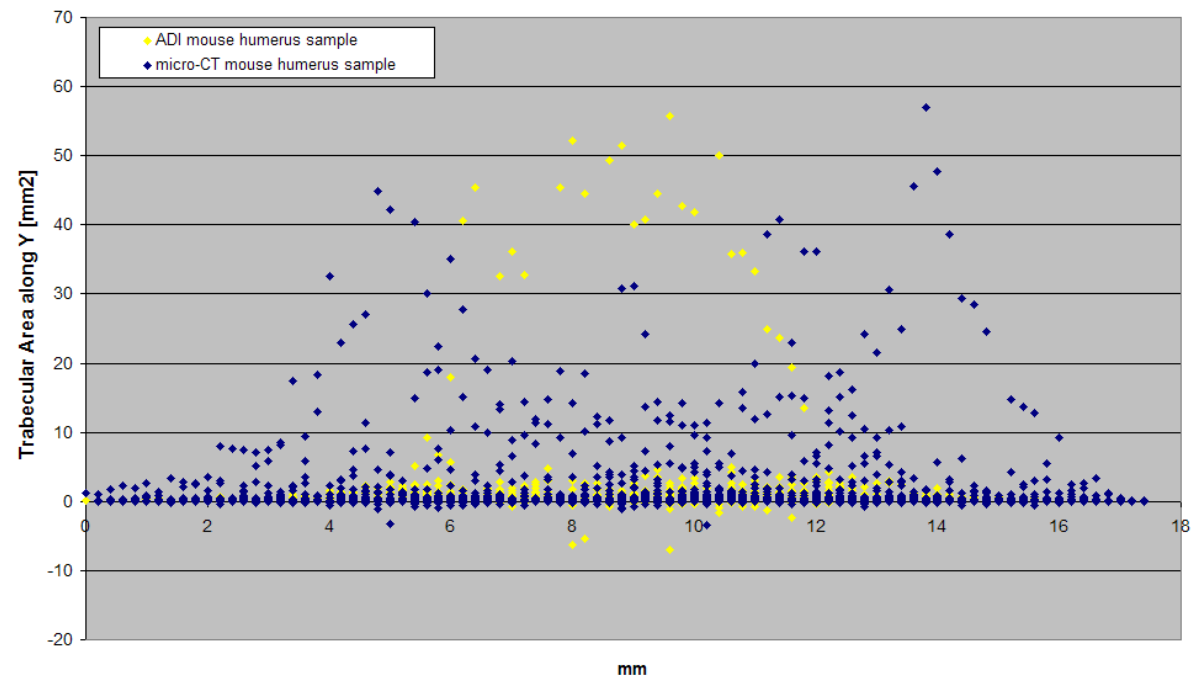


**Fig. 5.70** Comparison of the trabecular area along Y between the ADI mouse humerus and  $\mu$ CT mouse humerus

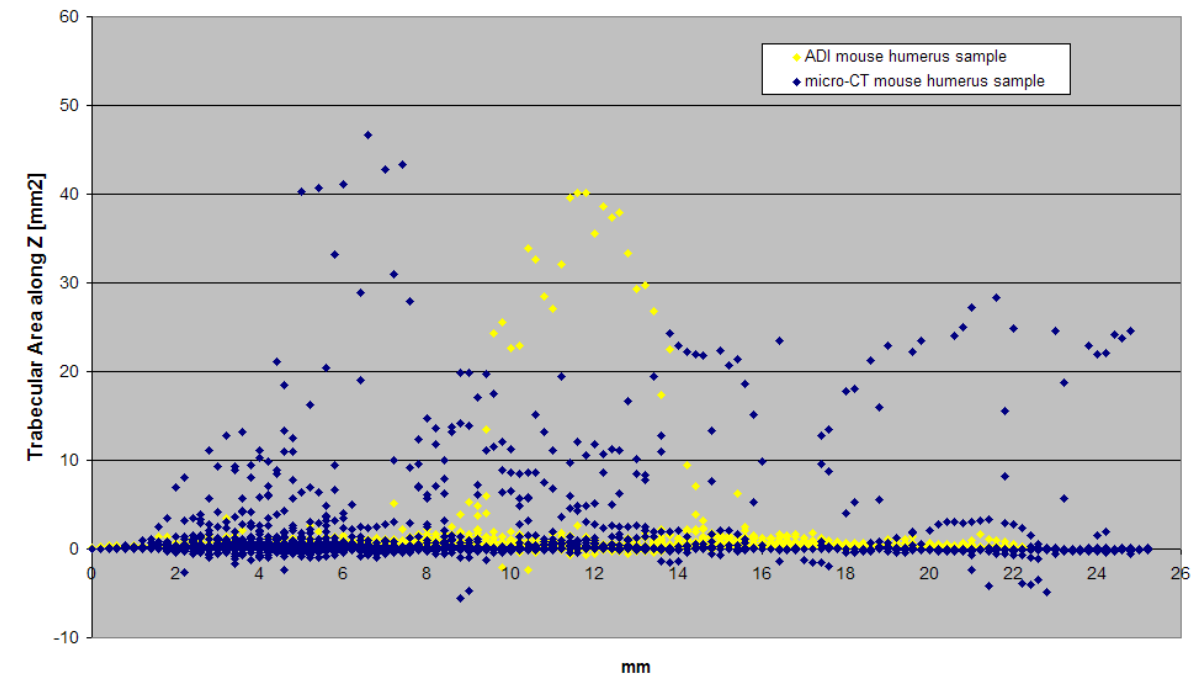


**Fig. 5.71** Comparison of the trabecular area along Z between the ADI mouse humerus and  $\mu$ CT mouse humerus

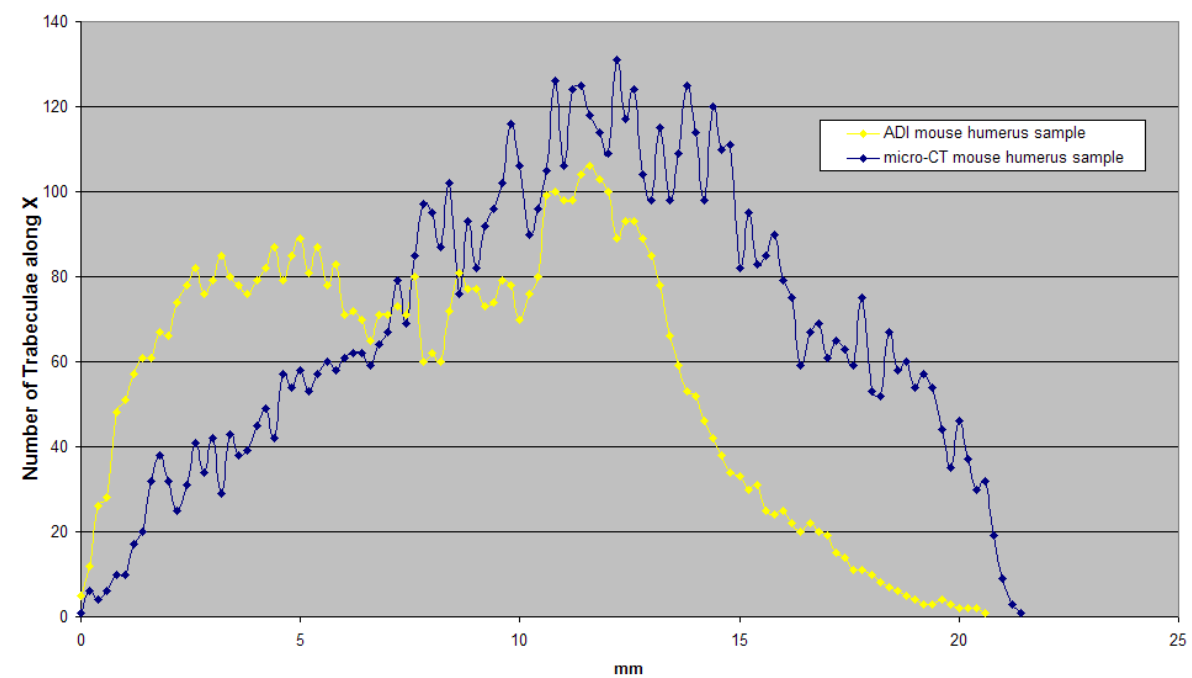


**Fig. 5.72** Comparison of the number of trabeculae along  $X$ , between the ADI mouse humerus and  $\mu$ CT mouse humerus

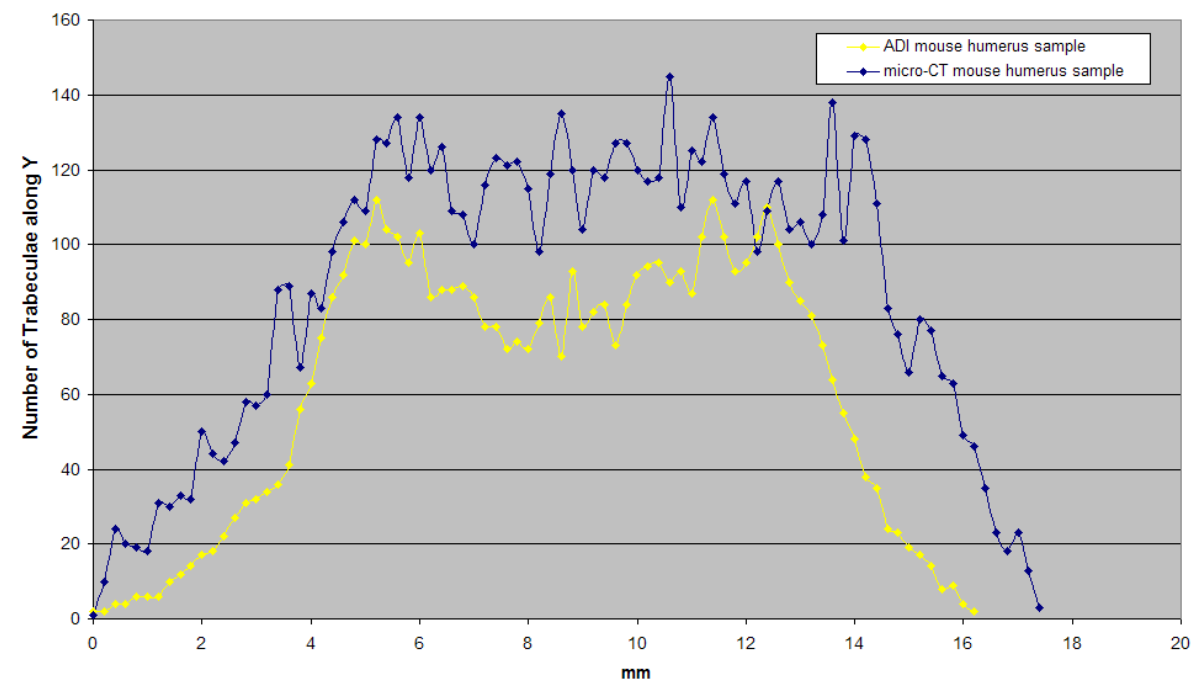


**Fig. 5.73** Comparison of the number of trabeculae along  $Y$ , between the ADI mouse humerus and  $\mu$ CT mouse humerus

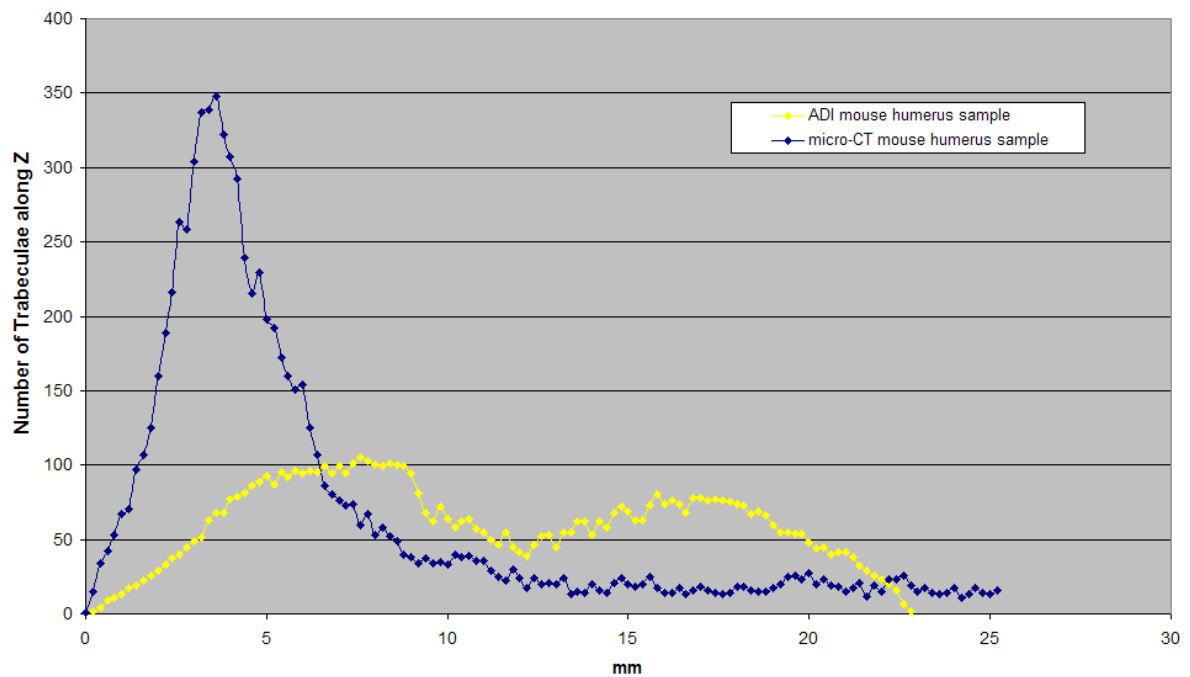


**Fig. 5.74** Comparison of the number of trabeculae along Z, between the ADI mouse humerus and  $\mu$ CT mouse humerus

	X		Y		Z	
	$\mu$ CT mouse humerus sample	ADI mouse humerus sample	$\mu$ CT mouse humerus sample	ADI mouse humerus sample	$\mu$ CT mouse humerus sample	ADI mouse humerus sample
Total number of rods	2428	3683	2653	2934	1406	4680
Total number of plates	4859	2107	5038	2075	6956	2216
Trabecular Area Range (mm <sup>2</sup> )	-6.24 to 55.25	-10.175 to 53.884	-3.37 to 56.987	-6.93 to 55.79	-5.55 to 46.7	-2.335 to 40.095
Slice area (mm <sup>2</sup> )	0.069 to 81.837	0.182 to 65.095	0.09 to 74.31	0.2165 to 73.295	0.0125 to 61.765	0.028 to 46.346

**Table 5.13** Differences between the ADI mouse humerus and the  $\mu$ CT mouse humerus

## 5.5 Review

The comparisons carried out in this chapter show that although the automated design methodology explained in chapter 2 and implemented in chapters 3 and 4 is efficient in terms of automation, the structures designed could be different to a greater or lesser extent in respect of a target geometry - in this case, trabecular bone architectures.

The ADI samples were designed according to the relatively small number of TE scaffolds requirements available in the literature, while the comparison involved more specific

quantitative requirements relative to specific biological trabecular geometries. The lack of knowledge about such quantitative requirements is a major limitation of the development of any design technique. The comparison between the two mouse humerus structures showed that ADI samples can be close to target geometries in some properties and distributions. This can be achieved by modifying parameters such as pore size, shape, rod paths and number of rods, as well as by moving the centroid region and using different converging points.

The cubic  $\mu$ CT sample presented relatively uniform trends of the analysed properties, as it was a portion of a larger bone. In both ADI case 5 and 6 samples, however, the channels converged to one or more points within the cubic volume. Since these network arrangements focused on the cubic volume alone, and not as a part of a larger geometry, the graphs produced were never likely to be the same.

For cubic ADI samples, the comparison also depends on the origin, location and orientation (relative to the cubic ADI samples) of the cubic  $\mu$ CT sample. Therefore, the analysed cubic ADI samples may present properties that are closer to other cubic  $\mu$ CT samples, from different locations, orientations and origins. More similar properties may also be achieved by modifying pore size, shape, rod paths and number of rods, as well as the number and location of the converging points in the ADI methodology.

The ADI mouse humerus geometry was a good approximation of the natural sample, and by modifying the parameters and the converging points of the channels, an even closer approximation would have been possible. However, that would require a lot of trial and error attempts, as the user would have to make arbitrary judgements on which variables to alter and by how much. That would take up a lot of the user's time which is contrary to the overall aims of the study. In addition, the converging points (located in those sections where the bone is thickest) would have to be selected for the particular  $\mu$ CT sample adopted, so that a trial and error approach would have to be repeated for each bone sample analysed.

Even designing ADI samples that match only the distributions of sliced areas in three orthogonal directions, without considering the other properties, can be an extremely time-consuming process.

For those reasons, based on the new quantitative requirements found in this chapter, a novel methodology of bio-mimetic automated design is presented in the following chapter. Instead

---

of being a based on re-iterative design, it will focus on the mathematical description of the problem and on its solutions.



## CHAPTER 6

### - AUTOMATED BIO-MIMETIC DESIGN INTEGRATION (ABDI) -

#### 6.1 Introduction

Chapter 5 has illustrated that although the design methodology introduced in chapters 3 and 4 represents an efficient and fully automated approach for designing complex and intricate features, it becomes impractical when topologies dictated by target geometries are required. In the previous chapter, the gradients of topological characteristics, for both designed and target geometries, showed differences both quantitatively and qualitatively. Therefore, when such topological properties are to be integrated in the automated design, a new approach is required.

In this chapter, a novel methodology of bio-mimetic automated design is described. This methodology, termed Automated Bio-mimetic Design Integration (ABDI), utilises the concept of discrete topology to describe the volume in which the simulated structure is created. A discrete volume can be associated to any geometry of any size and shape, by considering the smallest prism that surrounds it (referred to as ‘envelope’). This external envelope is subsequently divided into a finite number of small units (referred to as cells or voxels), of a predefined size, which can be either a cube or a prism. In theory, any other envelope with different shapes and sizes (i.e. spherical, cylindrical, etc) could be selected, as well as any shape and size for the unit cell. The smallest envelope size limits computational time and resources, because adding more cells than necessary does not provide any additional information on the geometry, but significantly increases the number of iterations in the algorithms. Therefore, minimum prismatic envelopes were used in this chapter, in order to test the design methodology, and also because other shapes would have required a more complex mathematical description of the problem, without providing any practical advantage.

Cubic unit cells of the same size were adopted in order to have a uniform description of the geometry with the same precision at any point and direction in the volume (all cells will be of equal importance in the final geometry, independent of their location).

While chapter 5 investigated three important topological aspects (trabecular and sliced areas, number of trabeculae, in three orthogonal directions) of the analysed structures, the ABDI methodology explained in this chapter has been developed to automatically design structures with the same gradients of sliced area as those found in target geometries, without taking the other two properties, trabecular area distributions and number of trabeculae, into account. As a consequence, the structures produced by using the ABDI approach will present biomimetic distributions of sliced areas, in three orthogonal directions, but with different trabecular areas and number of trabeculae. At this stage the attention was focused only on this topological property and on prismatic  $\mu$ CT samples. As such a novel methodology would require several steps of progressive development.

## 6.2 Methodology

The methodology introduced in this chapter has been explained in several steps, which can be summarised as follows:

- Discretisation of the sliced area in three orthogonal directions from a cubic (or prismatic)  $\mu$ CT sample of trabecular bone. The sliced areas analysed in chapter 5 are rounded from real to integer values, so that they are transformed into number of dense voxels. The total number of voxels has to be the same for the three axes, and the aim is to design structures with a predefined numbers of voxels in each layer along  $X$ ,  $Y$  and  $Z$ . This step is explained in section 6.2.1.
- Mathematical definition of the problem in terms of linear Diophantine equations. Two systems of such equations are required to fully describe the problem, one for the  $XZ$  distributions and one for the  $YZ$  distributions. The two systems are also expressed in matrix form, which provides a more intuitive visualisation of the problem. In such a matrix, each layer in  $Z$  is associated to a row, and each layer in  $X$  (or  $Y$ ) is associated to a column. The sum of the elements of the matrix by row or by column gives the required number of voxels for the corresponding layer. This step is explained in section 6.2.2.

- In order to estimate the number of solutions for each system, three different types of linear Diophantine equations are presented, each with different constraints on the integer variables, so that the number of solutions for each type is progressively reduced. The last type involves the presence of both a maximum and a minimum value for each variable, and is the one found in the systems. This step is explained in section 6.2.2.1.
- In order to solve the two systems of equations, a numerical algorithm is proposed. First, it involves the computation of the maximum and minimum values for each variable on a given Diophantine equation, which is subsequently solved. After one random solution is found, the remaining numbers of voxels are updated and the algorithm is repeated until the last Diophantine equation is solved. This step is explained in section 6.2.3.
- The solutions found for the two systems are subsequently combined to generate a template in which the design of the dense voxels is implemented. An estimation of the number of possible designs is also provided, as well as two conditions that must not be satisfied by the two solutions in order to be compatible (i.e. to allow at least one possible design). This step is explained in section 6.2.4.
- In order to verify that the two solutions are compatible, a particular design strategy called ‘minimum zero propagation design’ is proposed. This step is explained in section 6.2.4.1. Other design strategies are also mentioned in section 6.2.4.2, while section 6.2.4.3 presents some remedies to avoid the incompatibility of the solutions for the two systems.

Fig. 6.1 illustrates each of these steps.

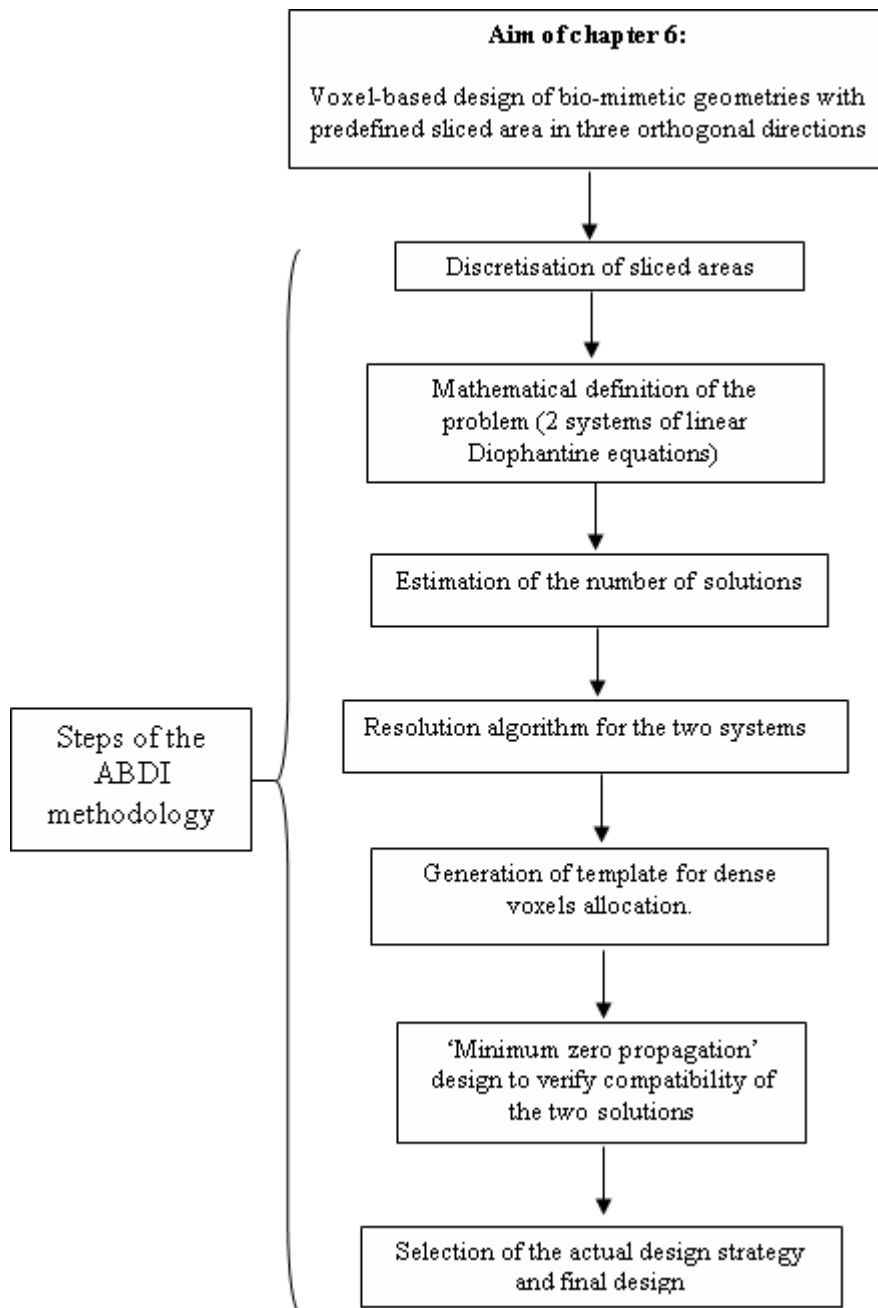


**Fig. 6.1** Scheme of the ABDI methodology introduced in this chapter.

### 6.2.1 Discretization of Sliced Area from a Cubic $\mu$ CT Sample

The cubic  $\mu$ CT sample investigated is the same as that presented in chapter 5. Discretization of the sliced area in the three specified directions was made in the same Excel file generated by the analysis presented in chapter 5. It was performed using the Round function in Excel, which rounds up a number to a specified number of digits. The number approximated is the ratio between the real sliced area for a given slice and direction, and the squared value of the voxel size. The number of digits has to be zero, because a voxel can be considered as either fully dense or void. Therefore the number of voxels has to be an integer value. For a given layer  $i$  in the  $Z$  direction (the same for  $X$  and  $Y$ ), it will be:

$$number\_of\_voxels\_Z_i = Round\left(\frac{Real\_sliced\_area\_Z_i}{voxel\_size^2}, 0\right) \quad (6.1)$$

In this chapter, a voxel size of 0.1 mm was used, which was the same value used for the layer thickness. In order to maintain the association between layers in both the analysed and discrete geometries it is important for the voxel size to be the same as the layer thickness used in the analysis step. If the voxel size is smaller than the layer thickness, the target sliced areas in the intermediate layers of the discrete geometry must be interpolated, thus leading to more computations without improving the accuracy of the data. The opposite case would instead lose accuracy, as some of the target sliced area would not be represented in the discrete model.

By repeating the formula (6.1) for all layers in the three directions, the number of voxels for each direction is defined, and the relative values can be stored in three different columns either in the Excel file produced in the analysis, or in a new Excel file/spreadsheet. The formula (6.1) generates a difference due to the approximation of real numbers into integers – a difference that will vary for each direction. It can be quantified by considering the *tot\_number\_of\_voxels*, which is the target number of voxels necessary to represent the whole real area, and the total number of voxels in each direction (*tot\_number\_of\_voxels\_X*, *tot\_number\_of\_voxels\_Y* and *tot\_number\_of\_voxels\_Z*). The *Real\_sliced\_area\_tot* value is the sum of all the real sliced areas in one direction (and will be the same in the other two).

---


$$tot\_number\_of\_voxels = Round\left(\frac{Real\_sliced\_area\_tot}{voxel\_size^2}, 0\right)$$

$$tot\_number\_of\_voxels\_X = \sum_{i=1}^N number\_of\_voxels\_X_i;$$

$$tot\_number\_of\_voxels\_Y = \sum_{i=1}^M number\_of\_voxels\_Y_i;$$

$$tot\_number\_of\_voxels\_Z = \sum_{i=1}^P number\_of\_voxels\_Z_i;$$

Where:

$N$  = number of layers along  $X$ .

$M$  = number of layers along  $Y$ .

$P$  = number of layers along  $Z$ .

This would normally result in:

$$tot\_number\_of\_voxels\_X \neq tot\_number\_of\_voxels\_Y \neq tot\_number\_of\_voxels\_Z$$

These differences can be quantified by:

$$delta\_X = tot\_number\_of\_voxels - tot\_number\_of\_voxels\_X$$

$$delta\_Y = tot\_number\_of\_voxels - tot\_number\_of\_voxels\_Y$$

$$delta\_Z = tot\_number\_of\_voxels - tot\_number\_of\_voxels\_Z$$

These differences can be either positive or negative, and have to be reduced to zero by introducing a correction. This correction may be performed in several different ways.

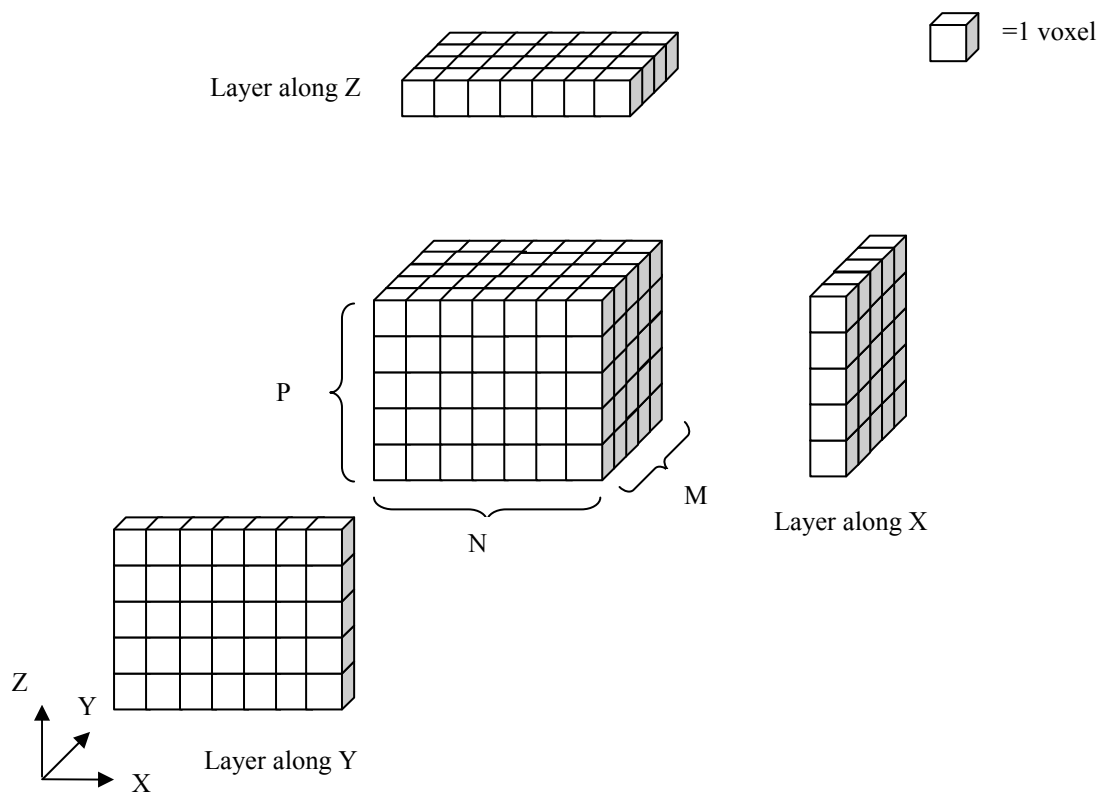
In this work the following approach has been proposed. It consists of selecting one random layer along  $X$  and then adding or subtracting (depending on the sign of  $delta\_X$ ) a value of '1' to the relative number of voxels. The random selection is then repeated for a number of times equal to  $delta\_X$ . The same operation is repeated in the other two directions, so that ultimately, the number of voxels in  $X$ ,  $Y$  and  $Z$  is the same and equal to the target value. Because the delta values are small compared to the total number of voxels, by using a random spread of voxels, the resulting sliced areas in the bio-mimetic structure will maintain an acceptable level of accuracy in respect of the real values of the  $\mu$ CT sample.

### 6.2.2 Mathematical Description of the Problem

After defining the number of voxels required in each direction (i.e. the sliced area required), the problem of designing a structure that satisfies these requirements can be mathematically described by two systems of linear Diophantine equations, which are polynomial equations defined in an integer domain (i.e. variables which only have integer and positive values). The term linear means that each monomial has a degree of zero or one.

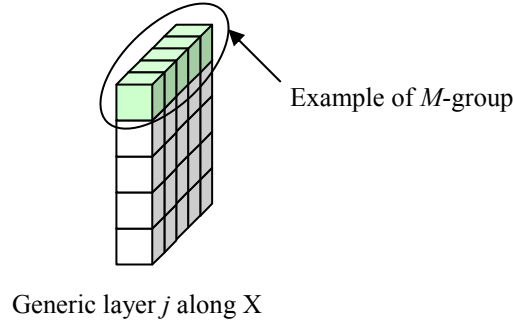
The volume in which the automated design is carried out, as stated in section 6.1, can be either a cube or a prism. This volume is subsequently divided into small cubic voxels of a given size. If the size of the prism is defined as ' $a \times b \times c$ ', where  $a$ ,  $b$ ,  $c$  are three real numbers that represent the envelope size of a  $\mu$ CT sample, the discretized volume will be composed of  $N \times M \times P$  layers in  $X$ ,  $Y$  and  $Z$  directions as a result of the slicing process explained in chapter 5.

Fig. 6.2 shows the discrete prismatic volume divided in  $N \times M \times P$  voxels.



**Fig. 6.2** Discretized prismatic volume and relative layers

By taking a generic layer along  $X$ , termed the letter  $j$ , it is evident that it can be described as a set of  $M$  cells for each of the  $P$  layers along  $Z$ . This is a convenient way to interpret the topology of this layer, as each  $M$ -group shows the effects that material distributions on a generic  $i$  layer in  $Z$  have on each layer along  $X$ . Fig. 6.3 highlights an  $M$ -group for a generic layer  $j$  on the  $X$  direction.



**Fig. 6.3** Example of an  $M$ -group in a generic layer  $j$  along  $X$ .

Each  $M$ -group can be considered as an integer variable in the Diophantine equation that describes the generic layer  $j$  along  $X$ . This equation takes the form of:

$$\alpha_{j,0} + \alpha_{j,1} + \alpha_{j,2} + \alpha_{j,3} + \dots + \alpha_{j,P-1} = D_j \quad (6.2)$$

Where:

$\alpha_{j,i}$  =  $M$ -group relative to the layer  $i$  along  $Z$  in the layer  $j$  along  $X$ .

$D_j$  = number of voxels required for the layer  $j$  along  $X$ .

It should be noted that the indices  $i$  and  $j$  start from 0 and finish at  $P-1$  and  $N-1$  respectively, and that the axis system adopted is oriented as shown in Fig. 6.2.

By repeating the equation (6.2) for all the  $N$  layers along  $X$ , a system of  $N$  Diophantine equations will be obtained. However, since the  $M$ -groups also have an affect on the material distribution along  $Z$ , it is necessary to take into account this further constraint by adding other  $P$  Diophantine equations, stating that the sum of all  $M$ -groups in a generic layer  $i$  along  $Z$ , is equal to the number of voxels required for that layer. This formula is:

$$\alpha_{0,i} + \alpha_{1,i} + \alpha_{2,i} + \alpha_{3,i} + \dots + \alpha_{N-1,i} = C_i \quad (6.3)$$



Where:

$C_i$  = number of voxels required for the layer  $i$  along  $Z$ .

By repeating the equation (6.3) for all the  $P$  layers in  $Z$ , the resulting system will be composed of  $N + P$  Diophantine equations, which can be expressed as follows:

$$\left\{ \begin{array}{l}
 \alpha_{0,0} + \alpha_{0,1} + \alpha_{0,2} + \alpha_{0,3} + \dots + \alpha_{0,P-1} = D_0 \\
 \alpha_{1,0} + \alpha_{1,1} + \alpha_{1,2} + \alpha_{1,3} + \dots + \alpha_{1,P-1} = D_1 \\
 \alpha_{2,0} + \alpha_{2,1} + \alpha_{2,2} + \alpha_{2,3} + \dots + \alpha_{2,P-1} = D_2 \\
 \dots \\
 \alpha_{N-1,0} + \alpha_{N-1,1} + \alpha_{N-1,2} + \alpha_{N-1,3} + \dots + \alpha_{N-1,P-1} = D_{N-1} \\
 \alpha_{0,P-1} + \alpha_{1,P-1} + \alpha_{2,P-1} + \alpha_{3,P-1} + \dots + \alpha_{N-1,P-1} = C_{P-1} \\
 \dots \\
 \alpha_{0,3} + \alpha_{1,3} + \alpha_{2,3} + \alpha_{3,3} + \dots + \alpha_{N-1,3} = C_3 \\
 \alpha_{0,2} + \alpha_{1,2} + \alpha_{2,2} + \alpha_{3,2} + \dots + \alpha_{N-1,2} = C_2 \\
 \alpha_{0,1} + \alpha_{1,1} + \alpha_{2,1} + \alpha_{3,1} + \dots + \alpha_{N-1,1} = C_1 \\
 \alpha_{0,0} + \alpha_{1,0} + \alpha_{2,0} + \alpha_{3,0} + \dots + \alpha_{N-1,0} = C_0
 \end{array} \right. \quad (6.4)$$

This system expresses the sum of all the elements of the following matrix, by row and by column (the system of co-ordinates adopted is orientated as shown in Fig. 6.2):

$$\left( \begin{array}{cccccc}
 \alpha_{0,P-1} & \alpha_{1,P-1} & \alpha_{2,P-1} & \alpha_{3,P-1} & \dots & \alpha_{N-1,P-1} \\
 \alpha_{0,P-2} & \alpha_{1,P-2} & \alpha_{2,P-2} & \alpha_{3,P-2} & \dots & \alpha_{N-1,P-2} \\
 & & & & \dots & \\
 \alpha_{0,3} & \alpha_{1,3} & \alpha_{2,3} & \alpha_{3,3} & \dots & \alpha_{N-1,3} \\
 \alpha_{0,2} & \alpha_{1,2} & \alpha_{2,2} & \alpha_{3,2} & \dots & \alpha_{N-1,2} \\
 \alpha_{0,1} & \alpha_{1,1} & \alpha_{2,1} & \alpha_{3,1} & \dots & \alpha_{N-1,1} \\
 \alpha_{0,0} & \alpha_{1,0} & \alpha_{2,0} & \alpha_{3,0} & \dots & \alpha_{N-1,0}
 \end{array} \right) \begin{array}{l} = C_{P-1} \\ = C_{P-2} \\ \dots \\ = C_3 \\ = C_2 \\ = C_1 \\ = C_0 \end{array} \quad (6.5)$$

$$\begin{array}{cccccc}
 \parallel & \parallel & \parallel & \parallel & & \parallel \\
 D_0 & D_1 & D_2 & D_3 & \dots & D_{N-1}
 \end{array}$$

The sum of the elements in each row is equal to the number of voxels required along  $Z$  in the corresponding layer. Similarly the sum of the columns is equal to the number of voxels

required along  $X$ , in the layer corresponding to that column. Therefore, the matrix (6.5), or equivalently the system (6.4), defines the problem of designing a structure with a given sliced area distribution along both  $Z$  and  $X$ . A similar system will then be required to match the distribution along  $Y$ , with the only difference being that each variable in the Diophantine equation will be an  $N$ -group (i.e. formed by  $N$  voxels), as shown in Fig. 6.4.

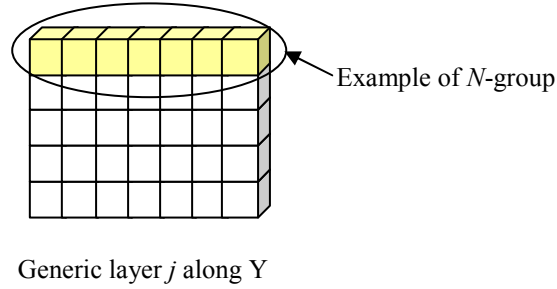


**Fig. 6.4** Example of an  $N$ -group, in a generic layer  $j$  along  $Y$ .

Therefore, referring to the  $N$ -groups with the notation  $\beta$ , the Diophantine equation that describes the generic layer  $j$  along  $Y$  can be expressed as:

$$\beta_{j,0} + \beta_{j,1} + \beta_{j,2} + \beta_{j,3} + \dots + \beta_{j,P-1} = E_j \quad (6.6)$$

Where:

$\beta_{j,i}$  =  $N$ -group relative to the layer  $i$  in  $Z$  and the  $j$  layer in  $Y$ .

$E_j$  = number of voxels required for the layer  $j$  along  $Y$ .

Again, the indices  $i$  and  $j$  start from 0 and end at  $P-1$  and  $M-1$  respectively.

Similarly, since the sum of all  $N$ -groups in a generic layer  $i$  along  $Z$  is equal to the number of voxels required for that layer in the same direction, each  $\beta_{j,i}$  has to satisfy the following equation:

$$\beta_{0,i} + \beta_{1,i} + \beta_{2,i} + \beta_{3,i} + \dots + \beta_{M-1,i} = C_i \quad (6.7)$$

Where:

$C_i$  = number of voxels required for the layer  $i$  along  $Z$ .

By repeating the equation (6.6) for all the  $M$  layers along  $Y$ , and equation (6.7) for all the  $P$  layers along  $Z$ , a system of  $M+P$  linear Diophantine equations will be obtained that is similar to the system (6.4) produced for the distributions in  $X$  and  $Z$ .

$$\left\{ \begin{array}{l}
 \beta_{0,0} + \beta_{0,1} + \beta_{0,2} + \beta_{0,3} + \dots + \beta_{0,P-1} = E_0 \\
 \beta_{1,0} + \beta_{1,1} + \beta_{1,2} + \beta_{1,3} + \dots + \beta_{1,P-1} = E_1 \\
 \beta_{2,0} + \beta_{2,1} + \beta_{2,2} + \beta_{2,3} + \dots + \beta_{2,P-1} = E_2 \\
 \dots \\
 \beta_{M-1,0} + \beta_{M-1,1} + \beta_{M-1,2} + \beta_{M-1,3} + \dots + \beta_{M-1,P-1} = E_{M-1} \\
 \beta_{0,P-1} + \beta_{1,P-1} + \beta_{2,P-1} + \beta_{3,P-1} + \dots + \beta_{M-1,P-1} = C_{P-1} \\
 \dots \\
 \beta_{0,3} + \beta_{1,3} + \beta_{2,3} + \beta_{3,3} + \dots + \beta_{M-1,3} = C_3 \\
 \beta_{0,2} + \beta_{1,2} + \beta_{2,2} + \beta_{3,2} + \dots + \beta_{M-1,2} = C_2 \\
 \beta_{0,1} + \beta_{1,1} + \beta_{2,1} + \beta_{3,1} + \dots + \beta_{M-1,1} = C_1 \\
 \beta_{0,0} + \beta_{1,0} + \beta_{2,0} + \beta_{3,0} + \dots + \beta_{M-1,0} = C_0
 \end{array} \right. \quad (6.8)$$

As with the previous problem, this system expresses the sum of all the elements of the following matrix, by row and by column:

$$\begin{array}{cccccc}
 \left( \begin{array}{cccccc}
 \beta_{0,P-1} & \beta_{1,P-1} & \beta_{2,P-1} & \beta_{3,P-1} & \dots & \beta_{M-1,P-1} \\
 \beta_{0,P-2} & \beta_{1,P-2} & \beta_{2,P-2} & \beta_{3,P-2} & \dots & \beta_{M-1,P-2} \\
 & & & & \dots & \\
 \beta_{0,3} & \beta_{1,3} & \beta_{2,3} & \beta_{3,3} & \dots & \beta_{M-1,3} \\
 \beta_{0,2} & \beta_{1,2} & \beta_{2,2} & \beta_{3,2} & \dots & \beta_{M-1,2} \\
 \beta_{0,1} & \beta_{1,1} & \beta_{2,1} & \beta_{3,1} & \dots & \beta_{M-1,1} \\
 \beta_{0,0} & \beta_{1,0} & \beta_{2,0} & \beta_{3,0} & \dots & \beta_{M-1,0}
 \end{array} \right) & \begin{array}{l}
 = C_{P-1} \\
 = C_{P-2} \\
 \dots \\
 = C_3 \\
 = C_2 \\
 = C_1 \\
 = C_0
 \end{array} & (6.9) \\
 \begin{array}{cccccc}
 \parallel & \parallel & \parallel & \parallel & & \parallel \\
 E_0 & E_1 & E_2 & E_3 & \dots & E_{M-1}
 \end{array}
 \end{array}$$

The sum of the elements in each row is equal to the relative number of voxels required along  $Z$ , while the sum of the columns is equal to the relative number of voxels required along  $Y$ .

Therefore, the matrix (6.9), or equivalently the system (6.8), defines the problem of designing a structure with a given sliced area distribution along both  $Z$  and  $Y$ .

From the mathematical model described, it is clear that the general problem of designing a structure with predefined gradients of a sliced area in three orthogonal directions can be addressed by solving two systems of linear Diophantine equations, one for  $XZ$  and one for  $YZ$  distributions. In section 6.2.3, a numerical method of solving the above systems will be presented.

Finally, as described in section 6.2.1, the total number of voxels along the three directions must be the same, after the corrections due to discretization. Therefore it will be:

$$D_0 + D_1 + D_2 + \dots + D_{N-1} = C_0 + C_1 + C_2 + \dots + C_{P-1} = E_0 + E_1 + E_2 + \dots + E_{M-1}$$

### 6.2.2.1 Linear Diophantine Equations

When a generic equation of the systems (6.4) or (6.8) is considered individually, i.e. not as part of a system with other equations, it will be in the form:

$$\begin{cases} X_1 + X_2 + X_3 + \dots + X_k = n \\ X_1 \geq 0 \\ X_2 \geq 0 \\ X_3 \geq 0 \\ \dots \\ X_k \geq 0 \end{cases} \quad (6.10)$$

Where  $X_1, X_2, X_3, \dots, X_k, n \in \mathbb{N}$  are natural numbers smaller or equal to  $n$ . In general, the number of solutions to the problem (6.10) can be expressed by the following formula (Zwillinger, 2002):

$$\frac{(n+k-1)!}{n!(k-1)!} \quad (6.11)$$

When the same equation is considered as part of the systems (6.4) or (6.8), but without the constraint of belonging to an  $M$  or  $N$ -group (i.e. the variables can assume values greater than  $M$  or  $N$ ), it will be in the form:

$$\begin{cases} X_1 + X_2 + X_3 + \dots + X_k = n \\ 0 \leq X_1 \leq \min(n, l_1) \\ 0 \leq X_2 \leq \min(n, l_2) \\ 0 \leq X_3 \leq \min(n, l_3) \\ \dots \\ 0 \leq X_k \leq \min(n, l_k) \end{cases} \quad (6.12)$$

Where  $l_1, l_2, l_3, \dots, l_k \in \mathbb{N}$  are natural numbers bigger or smaller than  $n$ . In the problems (6.4) and (6.8), these values are  $D_0, D_1, D_2, \dots, D_{N-1}$  and  $E_0, E_1, E_2, \dots, E_{M-1}$  respectively, if the equation considered is one row of the matrices (6.5) and (6.9).

The number of solutions for the equation (6.12) will be a subset of that in (6.11), whose dimensions will depend on the actual values of  $k, n, l_1, l_2, l_3, \dots, l_k$ . This subset, termed  $O$ , can be composed of several elements, although in some cases the equation (6.12) can admit one or zero solutions.

When the constraint of belonging to an  $M$  group (or similarly to an  $N$ -group) is introduced, the same equation will assume the following form:

$$\begin{cases} X_1 + X_2 + X_3 + \dots + X_k = n \\ t_1 \leq X_1 \leq \min(n, l_1, M) \\ t_2 \leq X_2 \leq \min(n, l_2, M) \\ t_3 \leq X_3 \leq \min(n, l_3, M) \\ \dots \\ t_K \leq X_k \leq \min(n, l_k, M) \end{cases} \quad (6.13)$$

Where  $t_1, t_2, t_3, \dots, t_k \in \mathbb{N}$  are natural numbers that represent the minimum value for each variable (which can also be equal to zero). This constraint is a direct consequence of introducing a limitation in the volume (i.e. number of voxels) available, which is represented by  $M$ . When  $M$  is smaller than  $l$  and  $n$  ( $l$  is a generic term of  $l_1, l_2, l_3, \dots, l_k$ ), as in the cases presented in this chapter, it acts to limit the volume available, restricting the number of solutions. The minimum value is necessary because it is possible that at some point the volume required becomes bigger than the volume available (as a consequence of distributing too little material in other layers), leading to an impossible situation in the design. Therefore,

$M$  will limit both the maximum and minimum values of the variables, but only if its value is smaller than  $l$  and  $n$  ( $l$  and  $n$  represent the volumes required, while  $M$  to the volume available). This point is further explained in section 6.2.3 which describes the resolution algorithm for the systems (6.5) and (6.9). It will also be shown that the values of  $t_1, t_2, t_3, \dots, t_k$  depends on  $M$  (and similarly, for the  $YZ$  distribution, on  $N$ ).

The number of solutions for a problem of the (6.13) type will be a subset of  $O$ , which is the group of solutions for the (6.12) problem. This subset, denoted as  $Q$ , can be composed of several elements, although in some cases the equation (6.13) can admit one or zero solutions. To quantify the number of solutions for an equation of the (6.10) type relative to the  $\mu$ CT sample analysed in chapter 5, the values relative to the layer in  $Z$  with smaller number of voxels are used:

$n = 1220$  (minimum number of voxels in  $Z$ , corresponding to layer 28)

$k = 103$  (number of layers in  $Z$ )

$$n\_solutions\_layer\_28 = \frac{(1220 + 103 - 1)!}{1220!(103 - 1)!} = 4.4203988131209354383761238186198e + 154$$

Since the number of solutions for a problem of the (6.10) type are very high, the sizes of subsets  $O$  and  $Q$  would be expected to be of similar magnitude (when  $l$  and  $n$  are of the same order, like in the sample analysed, and when  $N$  and  $M$  are not too restrictive).

The number of solutions for each individual equation (6.13) will then affect the number of solutions of the whole system. In section 6.2.4 it will be shown that not all the solutions of the two systems can be coupled to produce a bio-mimetic geometry, because they must satisfy a condition of 'compatibility'. This condition of compatibility will further reduce the number of solutions for each of the two systems.

Since the data that required changing were dependant on the  $\mu$ CT sample analysed, each sample will still be described by equations of the (6.13) type, but with different values of  $l_1, l_2, l_3, \dots, l_k$ ,  $t_1, t_2, t_3, \dots, t_k$ ,  $M$ ,  $n$  and  $k$ . That will therefore result in the number of solutions depending on the particular  $\mu$ CT sample analysed.

### 6.2.3 Implementation of a Resolution Algorithm

The proposed algorithm to solve the two systems (6.5) and (6.9) is sequential and based on the generation of a solution for one row, which will then affect the requirements for the

following row and so on, until the last row is solved. Each row of the matrices (6.5) and (6.9) is therefore considered as an equation of the (6.13) type, and subsequently resolved. The algorithm presented will be applied to the first system only, since it will work in the same way for the second.

To define each row as an equation of the (6.13) type, it is first necessary to define the values of  $l_1, l_2, l_3, \dots, l_k, t_1, t_2, t_3, \dots, t_k, M, n$  and  $k$ . For a generic row  $i$  in the matrix (6.5), it will be:

$$\left\{ \begin{array}{l} \alpha_{0,i} + \alpha_{1,i} + \alpha_{2,i} + \alpha_{3,i} + \dots + \alpha_{N-1,i} = C_i \\ t_{0,i} \leq \alpha_{0,i} \leq \min(C_i, D_0, M) \\ t_{1,i} \leq \alpha_{1,i} \leq \min(C_i, D_1, M) \\ t_{2,i} \leq \alpha_{2,i} \leq \min(C_i, D_2, M) \\ \dots \\ t_{N-1,i} \leq \alpha_{N-1,i} \leq \min(C_i, D_{N-1}, M) \end{array} \right. \quad (6.14)$$

As stated in the previous section,  $t_{0,i}, t_{1,i}, t_{2,i}, \dots, t_{N-1,i}$  represent the minimum values for each variable in the row  $i$ . These values can also be zero for some or all the variables in a given row. Their value is defined by comparing the remaining number of voxels required along  $X$  (equal to the initial number of voxels required minus the number of voxels already located in the previous layers) and the remaining number of voxels available. The remaining number of voxels required along  $X$  for a variable  $\alpha_{j,i}$  is equal to:

$$D_j - \sum_{k=0}^{i-1} \alpha_{j,k} \quad (6.15)$$

While the remaining number of voxels available after the variable  $\alpha_{j,i}$  is  $M$  multiplied by the number of rows remaining:

$$(P-i-1)*M \quad (6.16)$$

If:

$$D_j - \sum_{k=0}^{i-1} \alpha_{j,k} \leq (P-i-1)M$$

Then  $t_{j,i} = 0$

While if:

$$D_j - \sum_{k=0}^{i-1} \alpha_{j,k} > (P-i-1)M$$

Then  $t_{j,i}$  is the value at which the two areas are equal:

$$D_j - \sum_{k=0}^{i-1} \alpha_{j,k} - t_{j,i} = (P-i-1)M \rightarrow t_{j,i} = D_j - \sum_{k=0}^{i-1} \alpha_{j,k} - (P-i-1)M \quad (6.17)$$

After defining each row of the matrix (6.5) as an equation of the (6.13) type, the resolution algorithm can be implemented. Fig. 6.5 shows the flow chart followed by this algorithm.

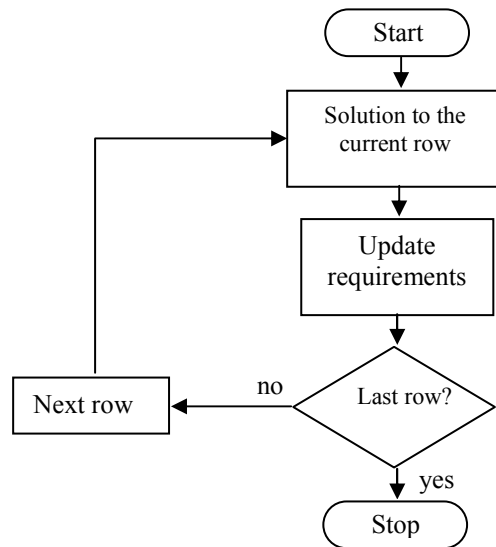


**Fig. 6.5** Flow chart of the proposed resolution algorithm



Starting from the first row of the matrix (6.5), which is the one at the bottom according to the system of co-ordinates in Fig. 6.2, the algorithm will find a solution for this row respecting the constraints defined by the relative (6.13) equation.

It will start by selecting a random value between 0 and  $N-1$ . This number identifies a variable in the row, to which a unit value will be added, provided that this addition does not breach the constraints. At this point, the initial values for all the variables in the row will be equal to their minimum values  $t_{0,0}, t_{1,0}, t_{2,0}, \dots, t_{N-1,0}$ , computed as previously explained, and therefore the constraint of minimum value is already satisfied.

The algorithm was written in Visual Basic within Excel, and the command used to select this random number 'j' is:

$$j = \text{int}(N * \text{rnd})$$

Where:

$\text{rnd}$  = Visual Basic 'random' function.

Afterwards, the program will verify that the constraint of maximum value for the variable  $\alpha_{j,0}$  ( $j$  is the random number just selected) is satisfied, by the following inequality:

$$\alpha_{j,0} + 1 \leq \min(D_j, M) \quad (6.18)$$

It should be noted that even though in the equation (6.14)  $C_0$  is included in the term on the right side of the inequality, by using an incremental approach (where the initial value of the variables is equal to the minimum value) such as that proposed in this section, it is implicit that  $\alpha_{j,0} + 1 \leq C_0$ , and therefore the maximum value can only be limited by  $D_j$  or  $M$ . If condition (6.18) is satisfied, the value of  $\alpha_{j,0}$  will be effectively increased by 1 and the process will be repeated a number of times, until the sum of the value of all variables is equal to  $C_0$ . If the condition is not satisfied, it means that  $\alpha_{j,0} + 1$  is exceeding the maximum value allowed, and therefore the value of  $\alpha_{j,0}$  will not be increased by 1, and the random selection repeated.

After the necessary number of successful random selections, the final values of  $\alpha_{0,0}, \alpha_{1,0}, \alpha_{2,0}, \alpha_{3,0}, \dots, \alpha_{N-1,0}$  will form a compatible solution for the equation (6.14),

relative to the first row. The same process is then repeated for the second row. To determine the minimum values, the algorithm will compute the remaining number of voxels required along  $X$  by using the (6.15), and the remaining number of voxels available by using the (6.16), both with  $i=1$ .

Afterwards, it will update the constraint related to the maximum value for the variables in the row, since the remaining numbers of voxels required along  $X$  have changed because of the solution found for the first row.

For a generic term  $\alpha_{j,1}$  of the second row, it will be:

$$\alpha_{j,1} + 1 \leq \min(D_j - \alpha_{j,0}, M)$$

That means that the number of voxels required along  $X$  must be updated after every row is solved. In conclusion, the algorithm will solve  $P-1$  equations of the (6.13) type, which will be:

$$\left\{ \begin{array}{l} \alpha_{0,0} + \alpha_{1,0} + \alpha_{2,0} + \alpha_{3,0} + \dots + \alpha_{N-1,0} = C_0 \\ t_{0,0} \leq \alpha_{0,0} \leq \min(D_0, M) \\ t_{1,0} \leq \alpha_{1,0} \leq \min(D_1, M) \\ t_{2,0} \leq \alpha_{2,0} \leq \min(D_2, M) \\ \dots \\ t_{N-1,0} \leq \alpha_{N-1,0} \leq \min(D_{N-1}, M) \end{array} \right.$$

$$\left\{ \begin{array}{l} \alpha_{0,1} + \alpha_{1,1} + \alpha_{2,1} + \alpha_{3,1} + \dots + \alpha_{N-1,1} = C_1 \\ t_{0,1} \leq \alpha_{0,1} \leq \min(D_0 - \alpha_{0,0}, M) \\ t_{1,1} \leq \alpha_{1,1} \leq \min(D_1 - \alpha_{1,0}, M) \\ t_{2,1} \leq \alpha_{2,1} \leq \min(D_2 - \alpha_{2,0}, M) \\ \dots \\ t_{N-1,1} \leq \alpha_{N-1,1} \leq \min(D_{N-1} - \alpha_{N-1,0}, M) \end{array} \right.$$

$$\begin{cases}
 \alpha_{0,2} + \alpha_{1,2} + \alpha_{2,2} + \alpha_{3,2} + \dots + \alpha_{N-1,2} = C_2 \\
 t_{0,2} \leq \alpha_{0,2} \leq \min(D_0 - \alpha_{0,0} - \alpha_{0,1}, M) \\
 t_{1,2} \leq \alpha_{1,2} \leq \min(D_1 - \alpha_{1,0} - \alpha_{1,1}, M) \\
 t_{2,2} \leq \alpha_{2,2} \leq \min(D_2 - \alpha_{2,0} - \alpha_{2,1}, M) \\
 \dots \\
 t_{N-1,2} \leq \alpha_{N-1,2} \leq \min(D_{N-1} - \alpha_{N-1,0} - \alpha_{N-1,1}, M)
 \end{cases}$$

...

$$\begin{cases}
 \alpha_{0,P-2} + \alpha_{1,P-2} + \alpha_{2,P-2} + \alpha_{3,P-2} + \dots + \alpha_{N-1,P-2} = C_{P-2} \\
 t_{0,P-2} \leq \alpha_{0,P-2} \leq \min(D_0 - \alpha_{0,0} - \alpha_{0,1} - \dots - \alpha_{0,P-3}, M) \\
 t_{1,P-2} \leq \alpha_{1,P-2} \leq \min(D_1 - \alpha_{1,0} - \alpha_{1,1} - \dots - \alpha_{1,P-3}, M) \\
 t_{2,P-2} \leq \alpha_{2,P-2} \leq \min(D_2 - \alpha_{2,0} - \alpha_{2,1} - \dots - \alpha_{2,P-3}, M) \\
 \dots \\
 t_{N-1,P-2} \leq \alpha_{N-1,P-2} \leq \min(D_{N-1} - \alpha_{N-1,0} - \alpha_{N-1,1} - \dots - \alpha_{N-1,P-3}, M)
 \end{cases}$$

The last row, numbered as  $P$ , will be automatically solved, as the sum of the minimum values for its variables will be equal to the number of voxels required for that row:

$$\begin{cases}
 \alpha_{0,P-1} + \alpha_{1,P-1} + \alpha_{2,P-1} + \alpha_{3,P-1} + \dots + \alpha_{N-1,P-1} = C_{P-1} \\
 \alpha_{0,P-1} = (D_0 - \alpha_{0,0} - \alpha_{0,1} - \dots - \alpha_{0,P-3} - \alpha_{0,P-2}) \\
 \alpha_{1,P-1} = (D_1 - \alpha_{1,0} - \alpha_{1,1} - \dots - \alpha_{1,P-3} - \alpha_{1,P-2}) \\
 \alpha_{2,P-1} = (D_2 - \alpha_{2,0} - \alpha_{2,1} - \dots - \alpha_{2,P-3} - \alpha_{2,P-2}) \\
 \dots \\
 \alpha_{N-1,P-1} = (D_{N-1} - \alpha_{N-1,0} - \alpha_{N-1,1} - \dots - \alpha_{N-1,P-3} - \alpha_{N-1,P-2})
 \end{cases}$$

In addition, the values of  $\alpha_{0,P-1}, \alpha_{1,P-1}, \alpha_{2,P-1}, \alpha_{3,P-1}, \dots, \alpha_{N-1,P-1}$  will automatically result to be  $\leq M$ .

The template for the system (6.5) can be an Excel spreadsheet, where the values of  $D_0, D_1, D_2, \dots, D_{N-1}$  are stored in the first row (starting from the second column), while  $C_0, C_1, C_2, \dots, C_{P-1}$  are stored in the first column, with the first and last elements,  $C_0$  and  $C_{P-1}$  located in rows  $P+1$  and 2 respectively, following the order presented in the matrix (6.5). Fig. 6.6 shows an example of template structured in this way.

The same procedure will apply for the system (6.9).

	$D_0$	$D_1$	$D_2$	...	$D_{N-1}$
$C_{P-1}$	$\alpha_{0,P-1}$	$\alpha_{1,P-1}$	$\alpha_{2,P-1}$	...	$\alpha_{N-1,P-1}$
$C_{P-2}$	$\alpha_{0,P-2}$	$\alpha_{1,P-2}$	$\alpha_{2,P-2}$	...	$\alpha_{N-1,P-2}$
$C_{P-3}$	$\alpha_{0,P-3}$	$\alpha_{1,P-3}$	$\alpha_{2,P-3}$	...	$\alpha_{N-1,P-3}$
...	...	...	...	...	...
$C_1$	$\alpha_{0,1}$	$\alpha_{1,1}$	$\alpha_{2,1}$	...	$\alpha_{N-1,1}$
$C_0$	$\alpha_{0,0}$	$\alpha_{1,0}$	$\alpha_{2,0}$	...	$\alpha_{N-1,0}$

**Fig. 6.6** Example of structured template in Excel for system (6.5).

#### 6.2.4 Design Implementation

The algorithm presented in the preceding section can be written in any programming language, but Visual Basic and Excel were used as they provided a suitable template for solving systems of linear Diophantine equations expressed in matrix form.

In addition, Excel is also suitable for performing voxel-based design, as each cell can be associated to a voxel and a spreadsheet to a particular layer in a specified direction.

Therefore, it is possible to write a routine in Visual Basic to generate a template where the actual voxel based design will be implemented. The template proposed in this chapter is structured so that there are  $P$  spreadsheets, representing the layers in  $Z$ , each containing the solutions  $\alpha_{0,i}, \alpha_{1,i}, \alpha_{2,i}, \alpha_{3,i}, \dots, \alpha_{N-1,i}$  and  $\beta_{0,i}, \beta_{1,i}, \beta_{2,i}, \beta_{3,i}, \dots, \beta_{M-1,i}$  to the relative row in the systems (6.5) and (6.9), with  $i$  representing a generic layer in  $Z$ . Fig. 6.7 shows an example of this template. It should be noted that  $\alpha_{0,i}, \alpha_{1,i}, \alpha_{2,i}, \alpha_{3,i}, \dots, \alpha_{N-1,i}$  are written in the first row, starting from the second column, while the values for  $\beta_{0,i}, \beta_{1,i}, \beta_{2,i}, \beta_{3,i}, \dots, \beta_{M-1,i}$  are written in the first column, with the first and last elements,  $\beta_{0,i}$  and  $\beta_{M-1,i}$  located in the row number  $M+1$  and 2 respectively, according to the system of co-ordinates shown in Fig. 6.2. This is the template adopted in this work, although alternative configurations are possible.

	$\alpha_{0,i}$	$\alpha_{1,i}$	$\alpha_{2,i}$	$\alpha_{3,i}$	...	$\alpha_{N-1,i}$
$\beta_{M-1,i}$						
...						
$\beta_{3,i}$						
$\beta_{2,i}$						
$\beta_{1,i}$						
$\beta_{0,i}$						

**Fig. 6.7** Example of proposed template for a generic layer  $i$  in  $Z$ .

After all the templates for the  $P$  layers have been drawn, the actual assignment of the material locations (i.e. of the dense voxels) can start.

In general, if an individual row  $j$  of the template in Fig. 6.7 is considered, the number of possible designs for that row is given by the number of  $k$ -combinations from a set of  $n$  elements, i.e. by the number of combinations without repetitions (Zwillinger, 2002):

$$\frac{n!}{k!(n-k)!} \rightarrow \frac{N!}{\beta_{j,i}!(N-\beta_{j,i})!} \quad (6.19)$$

That is also the number of solutions for a problem of the (6.12) type, when all the variables are limited between 0 and 1. The matrix shown in Fig. 6.7 is of the same type of the matrices (6.5) and (6.9), since the nature of the problem expressed by them is the same. The only difference is that the Diophantine variables in Fig. 6.7 can assume only two values, 0 and 1, while in the other problems, all the variables present different maximum and minimum values.

Assuming  $N=103$ , as in the sample investigated in this chapter, and a value of 50 for  $\beta_{j,i}$ , the formula (6.19) will give a value of:

$$6.61663757117201961728631646556 \text{ e } +29$$

This shows that the number of solutions for each individual row can be very high, when taken apart from the system. However, when the same row is considered as part of the system in Fig. 6.7, the number of solutions may be greatly reduced. The number of solutions for each individual row will also affect the number of solutions of the whole system.

In some cases, the system in Fig. 6.7 presents no solutions, depending on the number of zeros 'v' and 'u' in the two sequences  $\alpha_{0,i}, \alpha_{1,i}, \alpha_{2,i}, \alpha_{3,i}, \dots, \alpha_{N-1,i}$  and  $\beta_{0,i}, \beta_{1,i}, \beta_{2,i}, \beta_{3,i}, \dots, \beta_{M-1,i}$ . When some zeros are present in these sequences, they will reduce the actual number of voxels available for design, from  $N$  to  $(N - v)$  for the first sequence, and from  $M$  to  $(M - u)$  for the second. In this case, the number of possible designs will be less than before. For an individual equation in the rows, the formula (6.19) will become:

$$\frac{(N - v)!}{\beta_{j,i}!(N - v - \beta_{j,i})!} \quad (6.20)$$

Depending on the value of  $v$ , if the condition:

$$\text{Max}(\beta_{0,i}, \beta_{1,i}, \beta_{2,i}, \beta_{3,i}, \dots, \beta_{M-1,i}) > (N - v) \quad (6.21)$$

is verified by layer  $i$ , the design becomes impossible, because the term on the left represents the number of voxels to be allocated, while  $(N - v)$  the number of voxels available. It should be noted that the maximum value of the sequence  $\beta$  will be automatically less or equal to  $N$ , as that was a constraint in the equation (6.13) applied for the system (6.9).

Similarly, if the condition:

$$\text{Max}(\alpha_{0,i}, \alpha_{1,i}, \alpha_{2,i}, \alpha_{3,i}, \dots, \alpha_{N-1,i}) > (M - u) \quad (6.22)$$

is verified, the design becomes impossible.

If one or both the conditions (6.21) and (6.22) occur, there are two possible causes:

1) The solutions  $\alpha_{0,i}, \alpha_{1,i}, \alpha_{2,i}, \alpha_{3,i}, \dots, \alpha_{N-1,i}$  and  $\beta_{0,i}, \beta_{1,i}, \beta_{2,i}, \beta_{3,i}, \dots, \beta_{M-1,i}$  found for

---

the two systems (6.5) and (6.9) are incompatible, and cannot be coupled.

2) The particular design strategy adopted does not present any solution.

The two causes are explained in sections 6.2.4.1 and 6.2.4.2, while remedies to avoid such incompatibilities are described in section 6.2.4.3.

#### **6.2.4.1 Minimum Zeros Propagation Strategy**

When the first cause occurs, other solutions for the systems (6.5) and (6.9) have to be found by repeating the algorithm explained in section 6.2.3. To verify that this is the actual cause of conditions (6.21) or (6.22), a design strategy called 'minimum zeros propagation' has to be adopted. This strategy minimises the number of zeros in one of the two sequences, by allocating the required number of voxels in the elements, of the other sequence, with more voxels. It is not important which of the two sequences is selected to minimise the number of zeros, as if no solution is found by minimizing  $v$ , then no solution will be found by minimizing  $u$ , and vice versa. The use of this strategy is necessary to verify that for a given layer  $i$ , the two solutions  $\alpha_{0,i}, \alpha_{1,i}, \alpha_{2,i}, \alpha_{3,i}, \dots, \alpha_{N-1,i}$  and  $\beta_{0,i}, \beta_{1,i}, \beta_{2,i}, \beta_{3,i}, \dots, \beta_{M-1,i}$  are compatible. Therefore, it defines a necessary condition which, if satisfied, means that one or more designs are possible. If not satisfied, it means that no design will exist with those two solutions (i.e. they are incompatible). That is because any other strategy adopted to allocate the dense voxels will produce a greater quantity of zeros.

If, for instance,  $v$  is the parameter to be minimised and both conditions (6.21) and (6.22) are initially not satisfied, this design strategy will start by selecting the minimum non-zero value in the sequence  $\beta_{0,i}, \beta_{1,i}, \beta_{2,i}, \beta_{3,i}, \dots, \beta_{M-1,i}$ , referred as  $\beta_{\min,i}$ . Afterwards, it will take the  $\beta_{\min,i}$  elements with more voxels in the sequence  $\alpha_{0,i}, \alpha_{1,i}, \alpha_{2,i}, \alpha_{3,i}, \dots, \alpha_{N-1,i}$  and will reduce their value by 1. The new numbers of zeros in the two directions,  $v'$ ,  $u'$  and the two new sequences  $\alpha'_{0,i}, \alpha'_{1,i}, \alpha'_{2,i}, \alpha'_{3,i}, \dots, \alpha'_{N-1,i}$  and  $\beta'_{0,i}, \beta'_{1,i}, \beta'_{2,i}, \beta'_{3,i}, \dots, \beta'_{M-1,i}$  are then computed. It should be noted that  $u' = u + 1$ , since the row that has been just solved will become a new zero.

The new sequence  $\alpha'_{0,i}, \alpha'_{1,i}, \alpha'_{2,i}, \alpha'_{3,i}, \dots, \alpha'_{N-1,i}$  will be equal to the previous one, except for the  $\beta_{\min,i}$  elements involved, which will be reduced by 1.  $\beta'_{0,i}, \beta'_{1,i}, \beta'_{2,i}, \beta'_{3,i}, \dots, \beta'_{M-1,i}$  will be also equal to the previous one, except for the row relative to  $\beta_{\min,i}$ , which will now

be zero. After these values have been updated, both conditions (6.21) and (6.22) are tested again. If they are not satisfied, the new  $\beta'_{\min,i}$  value will be selected among  $\beta'_{0,i}, \beta'_{1,i}, \beta'_{2,i}, \beta'_{3,i}, \dots, \beta'_{M-1,i}$  and 1 will be subtracted from the  $\beta'_{\min,i}$  elements with more voxels in the sequence  $\alpha'_{0,i}, \alpha'_{1,i}, \alpha'_{2,i}, \alpha'_{3,i}, \dots, \alpha'_{N-1,i}$ . The tests are then repeated for  $M-1$  times before each iteration, as the last iteration, referred as  $\beta_{\max,i}$  will result in one solution. Fig. 6.8 shows an example of minimum zeros propagation design, applied to minimise  $v$ .

If at some point of the iteration process, one or both of the two conditions are satisfied, it means that the two solutions  $\alpha_{0,i}, \alpha_{1,i}, \alpha_{2,i}, \alpha_{3,i}, \dots, \alpha_{N-1,i}$  and  $\beta_{0,i}, \beta_{1,i}, \beta_{2,i}, \beta_{3,i}, \dots, \beta_{M-1,i}$  for the layer  $i$  are incompatible, and other solutions for the systems (6.5) and (6.9) have to be found. Fig. 6.9 shows an example of incompatible solutions, by using minimum zeros propagation design, applied to minimise  $v$ .



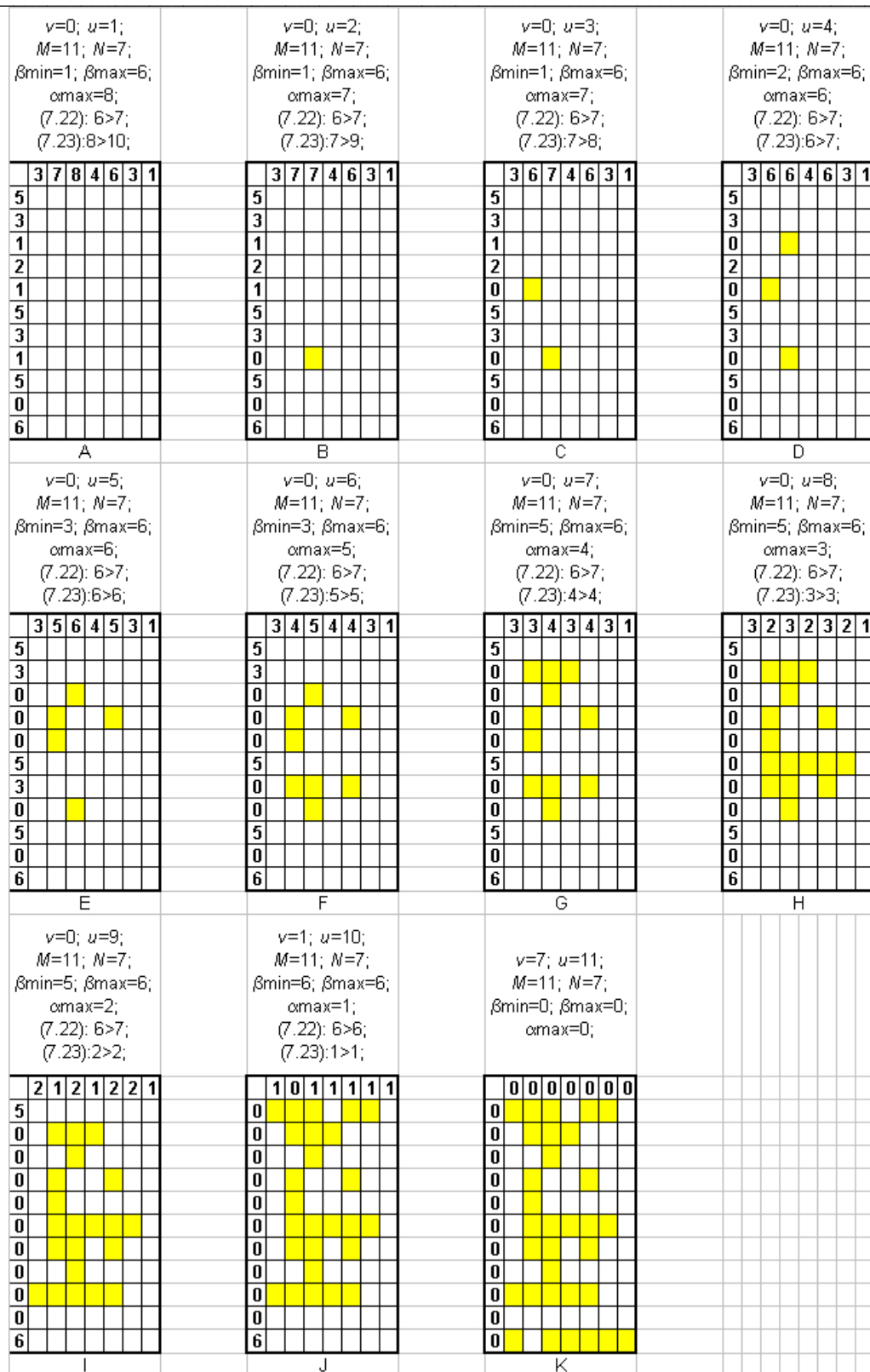


**Fig. 6.8** Example of minimum zeros propagation design applied to minimise  $v$ . It should be noted that the conditions (6.21) and (6.22) are never satisfied. Each step is presented, from initial template (A) to final design (K).

$v=1; u=1;$ $M=11; N=7;$ $\beta_{\min}=1; \beta_{\max}=6;$ $\alpha_{\max}=10;$ (7.22): $6>6;$ (7.23): $10>10;$	$v=1; u=2;$ $M=11; N=7;$ $\beta_{\min}=1; \beta_{\max}=6;$ $\alpha_{\max}=9;$ (7.22): $6>6;$ (7.23): $9>9;$	$v=1; u=3;$ $M=11; N=7;$ $\beta_{\min}=1; \beta_{\max}=6;$ $\alpha_{\max}=9;$ (7.22): $6>6;$ (7.23): $8>8;$	$v=1; u=4;$ $M=11; N=7;$ $\beta_{\min}=2; \beta_{\max}=6;$ $\alpha_{\max}=8;$ (7.22): $6>6;$ (7.23): $8>7;$																																																																																																																																																																																																																																																																																																																																																																																																
<table><tr><td></td><td>3</td><td>10</td><td>8</td><td>4</td><td>6</td><td>0</td><td>1</td></tr><tr><td>5</td><td></td><td></td><td></td><td></td><td></td><td></td><td></td></tr><tr><td>3</td><td></td><td></td><td></td><td></td><td></td><td></td><td></td></tr><tr><td>1</td><td></td><td></td><td></td><td></td><td></td><td></td><td></td></tr><tr><td>2</td><td></td><td></td><td></td><td></td><td></td><td></td><td></td></tr><tr><td>1</td><td></td><td></td><td></td><td></td><td></td><td></td><td></td></tr><tr><td>5</td><td></td><td></td><td></td><td></td><td></td><td></td><td></td></tr><tr><td>3</td><td></td><td></td><td></td><td></td><td></td><td></td><td></td></tr><tr><td>1</td><td></td><td></td><td></td><td></td><td></td><td></td><td></td></tr><tr><td>5</td><td></td><td></td><td></td><td></td><td></td><td></td><td></td></tr><tr><td>0</td><td></td><td></td><td></td><td></td><td></td><td></td><td></td></tr><tr><td>6</td><td></td><td></td><td></td><td></td><td></td><td></td><td></td></tr></table> A		3	10	8	4	6	0	1	5								3								1								2								1								5								3								1								5								0								6								<table><tr><td></td><td>3</td><td>9</td><td>8</td><td>4</td><td>6</td><td>0</td><td>1</td></tr><tr><td>5</td><td></td><td></td><td></td><td></td><td></td><td></td><td></td></tr><tr><td>3</td><td></td><td></td><td></td><td></td><td></td><td></td><td></td></tr><tr><td>1</td><td></td><td></td><td></td><td></td><td></td><td></td><td></td></tr><tr><td>2</td><td></td><td></td><td></td><td></td><td></td><td></td><td></td></tr><tr><td>1</td><td></td><td></td><td></td><td></td><td></td><td></td><td></td></tr><tr><td>5</td><td></td><td></td><td></td><td></td><td></td><td></td><td></td></tr><tr><td>3</td><td></td><td></td><td></td><td></td><td></td><td></td><td></td></tr><tr><td>0</td><td></td><td></td><td></td><td></td><td></td><td></td><td></td></tr><tr><td>5</td><td></td><td></td><td></td><td></td><td></td><td></td><td></td></tr><tr><td>0</td><td></td><td></td><td></td><td></td><td></td><td></td><td></td></tr><tr><td>6</td><td></td><td></td><td></td><td></td><td></td><td></td><td></td></tr></table> B		3	9	8	4	6	0	1	5								3								1								2								1								5								3								0								5								0								6								<table><tr><td></td><td>3</td><td>8</td><td>8</td><td>4</td><td>6</td><td>0</td><td>1</td></tr><tr><td>5</td><td></td><td></td><td></td><td></td><td></td><td></td><td></td></tr><tr><td>3</td><td></td><td></td><td></td><td></td><td></td><td></td><td></td></tr><tr><td>1</td><td></td><td></td><td></td><td></td><td></td><td></td><td></td></tr><tr><td>2</td><td></td><td></td><td></td><td></td><td></td><td></td><td></td></tr><tr><td>0</td><td></td><td></td><td></td><td></td><td></td><td></td><td></td></tr><tr><td>5</td><td></td><td></td><td></td><td></td><td></td><td></td><td></td></tr><tr><td>3</td><td></td><td></td><td></td><td></td><td></td><td></td><td></td></tr><tr><td>0</td><td></td><td></td><td></td><td></td><td></td><td></td><td></td></tr><tr><td>5</td><td></td><td></td><td></td><td></td><td></td><td></td><td></td></tr><tr><td>0</td><td></td><td></td><td></td><td></td><td></td><td></td><td></td></tr><tr><td>6</td><td></td><td></td><td></td><td></td><td></td><td></td><td></td></tr></table> C		3	8	8	4	6	0	1	5								3								1								2								0								5								3								0								5								0								6								<table><tr><td></td><td>3</td><td>7</td><td>8</td><td>4</td><td>6</td><td>0</td><td>1</td></tr><tr><td>5</td><td></td><td></td><td></td><td></td><td></td><td></td><td></td></tr><tr><td>3</td><td></td><td></td><td></td><td></td><td></td><td></td><td></td></tr><tr><td>0</td><td></td><td></td><td></td><td></td><td></td><td></td><td></td></tr><tr><td>2</td><td></td><td></td><td></td><td></td><td></td><td></td><td></td></tr><tr><td>0</td><td></td><td></td><td></td><td></td><td></td><td></td><td></td></tr><tr><td>5</td><td></td><td></td><td></td><td></td><td></td><td></td><td></td></tr><tr><td>3</td><td></td><td></td><td></td><td></td><td></td><td></td><td></td></tr><tr><td>0</td><td></td><td></td><td></td><td></td><td></td><td></td><td></td></tr><tr><td>5</td><td></td><td></td><td></td><td></td><td></td><td></td><td></td></tr><tr><td>0</td><td></td><td></td><td></td><td></td><td></td><td></td><td></td></tr><tr><td>6</td><td></td><td></td><td></td><td></td><td></td><td></td><td></td></tr></table> D		3	7	8	4	6	0	1	5								3								0								2								0								5								3								0								5								0								6							
	3	10	8	4	6	0	1																																																																																																																																																																																																																																																																																																																																																																																												
5																																																																																																																																																																																																																																																																																																																																																																																																			
3																																																																																																																																																																																																																																																																																																																																																																																																			
1																																																																																																																																																																																																																																																																																																																																																																																																			
2																																																																																																																																																																																																																																																																																																																																																																																																			
1																																																																																																																																																																																																																																																																																																																																																																																																			
5																																																																																																																																																																																																																																																																																																																																																																																																			
3																																																																																																																																																																																																																																																																																																																																																																																																			
1																																																																																																																																																																																																																																																																																																																																																																																																			
5																																																																																																																																																																																																																																																																																																																																																																																																			
0																																																																																																																																																																																																																																																																																																																																																																																																			
6																																																																																																																																																																																																																																																																																																																																																																																																			
	3	9	8	4	6	0	1																																																																																																																																																																																																																																																																																																																																																																																												
5																																																																																																																																																																																																																																																																																																																																																																																																			
3																																																																																																																																																																																																																																																																																																																																																																																																			
1																																																																																																																																																																																																																																																																																																																																																																																																			
2																																																																																																																																																																																																																																																																																																																																																																																																			
1																																																																																																																																																																																																																																																																																																																																																																																																			
5																																																																																																																																																																																																																																																																																																																																																																																																			
3																																																																																																																																																																																																																																																																																																																																																																																																			
0																																																																																																																																																																																																																																																																																																																																																																																																			
5																																																																																																																																																																																																																																																																																																																																																																																																			
0																																																																																																																																																																																																																																																																																																																																																																																																			
6																																																																																																																																																																																																																																																																																																																																																																																																			
	3	8	8	4	6	0	1																																																																																																																																																																																																																																																																																																																																																																																												
5																																																																																																																																																																																																																																																																																																																																																																																																			
3																																																																																																																																																																																																																																																																																																																																																																																																			
1																																																																																																																																																																																																																																																																																																																																																																																																			
2																																																																																																																																																																																																																																																																																																																																																																																																			
0																																																																																																																																																																																																																																																																																																																																																																																																			
5																																																																																																																																																																																																																																																																																																																																																																																																			
3																																																																																																																																																																																																																																																																																																																																																																																																			
0																																																																																																																																																																																																																																																																																																																																																																																																			
5																																																																																																																																																																																																																																																																																																																																																																																																			
0																																																																																																																																																																																																																																																																																																																																																																																																			
6																																																																																																																																																																																																																																																																																																																																																																																																			
	3	7	8	4	6	0	1																																																																																																																																																																																																																																																																																																																																																																																												
5																																																																																																																																																																																																																																																																																																																																																																																																			
3																																																																																																																																																																																																																																																																																																																																																																																																			
0																																																																																																																																																																																																																																																																																																																																																																																																			
2																																																																																																																																																																																																																																																																																																																																																																																																			
0																																																																																																																																																																																																																																																																																																																																																																																																			
5																																																																																																																																																																																																																																																																																																																																																																																																			
3																																																																																																																																																																																																																																																																																																																																																																																																			
0																																																																																																																																																																																																																																																																																																																																																																																																			
5																																																																																																																																																																																																																																																																																																																																																																																																			
0																																																																																																																																																																																																																																																																																																																																																																																																			
6																																																																																																																																																																																																																																																																																																																																																																																																			

**Fig. 6.9** Example of incompatible solutions for the systems (6.5) and (6.9), by using minimum zeros propagation design to minimise  $v$ . After a few iterations, the design becomes impossible as the condition (6.22) becomes true.

#### 6.2.4.2 Other Design Strategies

The minimum zeros propagation design is necessary to verify the compatibility of the requirements for layer  $i$ , but this is not the only design possible. The number of possible allocations for the dense voxels is equal to the number of solutions to the system shown in Fig. 6.7. If this system admits only one solution, then this solution will have to coincide with the solution obtained by the minimum zeros propagation design, either on rows or columns. Even when the system in Fig. 6.7 admits several solutions, it is also possible that by using a particular design strategy, one or both conditions (6.21) and (6.22) can become true, meaning that a valid design cannot be obtained by using that strategy. In these cases, the sequences  $\alpha_{0,i}, \alpha_{1,i}, \alpha_{2,i}, \alpha_{3,i}, \dots, \alpha_{N-1,i}$  and  $\beta_{0,i}, \beta_{1,i}, \beta_{2,i}, \beta_{3,i}, \dots, \beta_{M-1,i}$  are still valid, but other design strategies will have to be adopted.

Fig. 6.10 shows an example of a wrong strategy, which leads to an impossible design, even though the matrix admits some solutions (as shown in Fig. 6.8 and Fig. 6.11).

Finally, Fig. 6.11 illustrates another design strategy that is different from the minimum zeros propagation, which produces a valid design.

$v=0; u=1;$ $M=11; N=7;$ $\beta_{\min}=1; \beta_{\max}=6;$ $\alpha_{\max}=8;$ $(7.22): 6>7;$ $(7.23): 8>10;$		$v=1; u=2;$ $M=11; N=7;$ $\beta_{\min}=1; \beta_{\max}=6;$ $\alpha_{\max}=8;$ $(7.22): 6>6;$ $(7.23): 8>9;$		$v=1; u=3;$ $M=11; N=7;$ $\beta_{\min}=1; \beta_{\max}=6;$ $\alpha_{\max}=8;$ $(7.22): 6>6;$ $(7.23): 8>8;$		$v=1; u=4;$ $M=11; N=7;$ $\beta_{\min}=1; \beta_{\max}=6;$ $\alpha_{\max}=8;$ $(7.22): 6>6;$ $(7.23): 8>7;$
3 7 8 4 6 3 1		3 7 8 4 6 3 0		3 7 8 4 5 3 0		2 6 8 3 4 2 0
5		5		5		5
3		3		3		3
1		1		1		1
2		2		2		2
1		1		0		0
5		5		5		5
3		3		3		3
1		0		0		0
5		5		5		0
0		0		0		0
6		6		6		6
A		B		C		D

**Fig. 6.10** The use of wrong design strategies will lead to impossible design, even though the matrix does admit solutions.

#### 6.2.4.3 Remedies to Incompatibility of Solutions

The conditions of compatibility for the sequences  $\alpha_{0,i}, \alpha_{1,i}, \alpha_{2,i}, \alpha_{3,i}, \dots, \alpha_{N-1,i}$  and  $\beta_{0,i}, \beta_{1,i}, \beta_{2,i}, \beta_{3,i}, \dots, \beta_{M-1,i}$ , should be included as constraints in the systems (6.5) and (6.9). So far, these two systems have been treated as completely independent from one another, given that no mathematical constraints were set across the two. Some constraints regarding conditions (6.21) and (6.22) need to be included in the mathematical description of the two systems. However, these additions could significantly complicate both the mathematical models and the algorithms of resolution.

A feasible method to reduce the risk of incompatibilities in the solutions consists of 'artificially' limiting the maximum values for the sequences  $\alpha_{0,i}, \alpha_{1,i}, \alpha_{2,i}, \alpha_{3,i}, \dots, \alpha_{N-1,i}$  and  $\beta_{0,i}, \beta_{1,i}, \beta_{2,i}, \beta_{3,i}, \dots, \beta_{M-1,i}$ . The current geometrical limits for these values are  $M$  and  $N$  respectively, as each  $\alpha_{j,i}$  is an  $M$ -group, while each  $\beta_{j,i}$  is an  $N$ -group. By reducing the maximum values, for instance from  $M$  to  $M/2$ , and from  $N$  to  $N/2$ , there will be a double effect to aid avoiding the conditions (6.21) and (6.22) from occurring. It will limit the terms on the left side of the two inequalities, and at the same time reduce the number of zeros  $v$  and  $u$ , by distributing the dense voxels across the volume more uniformly. Therefore, it will

reduce the risk of voids and dense voxels being too concentrated in some areas. This approach has been successfully adopted in this chapter.

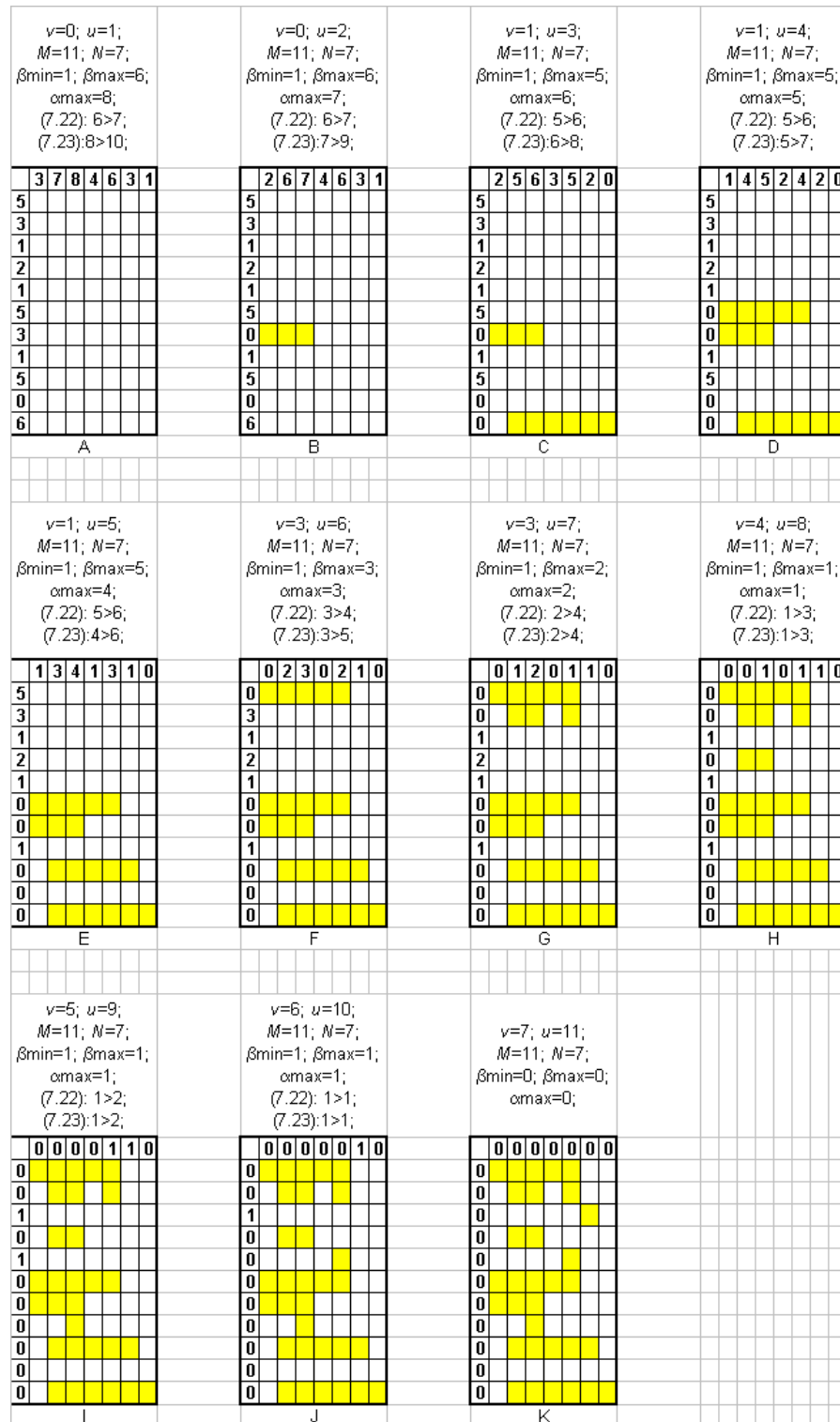


**Fig. 6.11** Design obtained by adopting a design strategy different from the minimum zeros propagation. It produces a valid design.

### 6.2.5 Computational Time and File Size

The time required to solve the two systems (6.5) and (6.9) was measured by using the VB 'Time' function, at the beginning and at the end of the resolution algorithm explained in section 6.2.3.

The same VB function was adopted to measure both the design time for generating all the  $P$  templates shown in Fig. 6.7 and for the relative voxels allocations.

The size of the Excel file containing the solutions of the two systems (6.5) and (6.9) and the designed  $P$  layers was obtained from the operative system.

### 6.2.6 Export to CAD

Once the  $P$  layers have been designed in Excel, they may be exported to a CAD application. In this section, a methodology to export the allocated voxels to CatiaV5R16 is presented.

The approach adopted involves the identification of the boundaries for each layer. A boundary is a side of a dense voxel connected to a void, and therefore a dense voxel can present up to four boundaries.

Boundaries for each layer will include the bottom and top sides of the dense voxels located in the first and last layers along Y respectively, and the left and right sides of the dense voxels located in the first and last layers along X respectively, according to the Excel template shown in Fig. 6.7. An example of boundary identification for a given layer is shown in Fig. 6.12.

Once each boundary has been identified, the coordinates of its vertexes are computed according to the axis system shown in Fig. 6.2. Points with those same coordinates are then designed onto a planar sketch in Catia V5R16, which corresponds to a given layer along Z. Finally, a line connecting the two vertexes of each boundary are drawn. For a given layer along Z, all these lines form the outer shape of the cross section.

The CAD representation of all dense voxels is not necessary and would be more demanding in terms of computational time and file size, as each voxel would require four points and four lines to be represented.

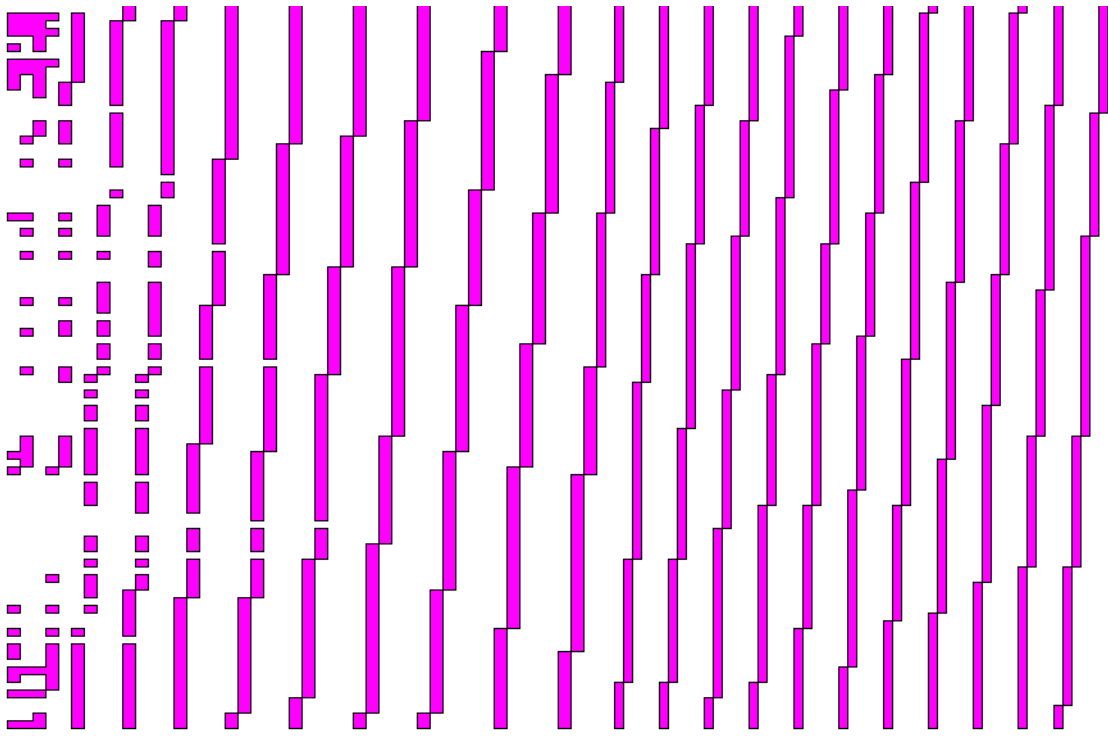


**Fig. 6.12** Example of boundary identification for a given layer along Z.

### 6.3 Results

The ABDI methodology has been used to produce two bio-mimetic structures based on the cubic  $\mu$ CT sample analysed in chapter 5. The discretization of the sliced area required in the three directions was made by considering a voxel size of 0.1mm, which was the same layer thickness used to analyse the proposed sample. By applying the formula defined in section 6.2.1, the following data were obtained:

$$Real\_sliced\_area\_tot = 1724.66 \text{ mm}^2 \quad (N = 103; M = 94; P = 103)$$

$$tot\_number\_of\_voxels = 172466$$

$$tot\_number\_of\_voxels\_X = 173642$$

$$tot\_number\_of\_voxels\_Y = 171924$$

$$tot\_number\_of\_voxels\_Z = 172466$$

$$delta\_X = -1176$$

$$delta\_Y = 542$$

$$delta\_Z = 0$$

The real and discretized sliced area distributions in  $Z$ ,  $X$ , and  $Y$  are shown in Fig. 6.13, 6.14 and 6.15 respectively. It should be noted that the effects of the real to integer approximation is more evident along  $X$ , as this axis presented the biggest value, in modulus, of delta.

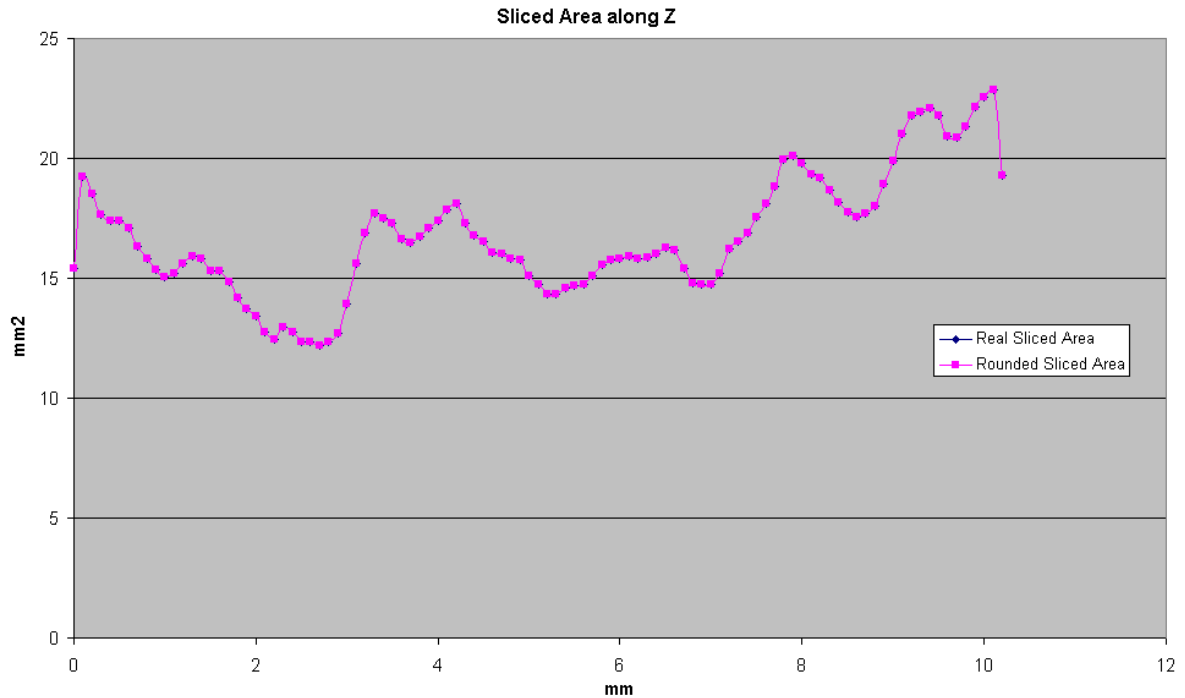


**Fig. 6.13** Real and discretized sliced area distribution along  $Z$ .

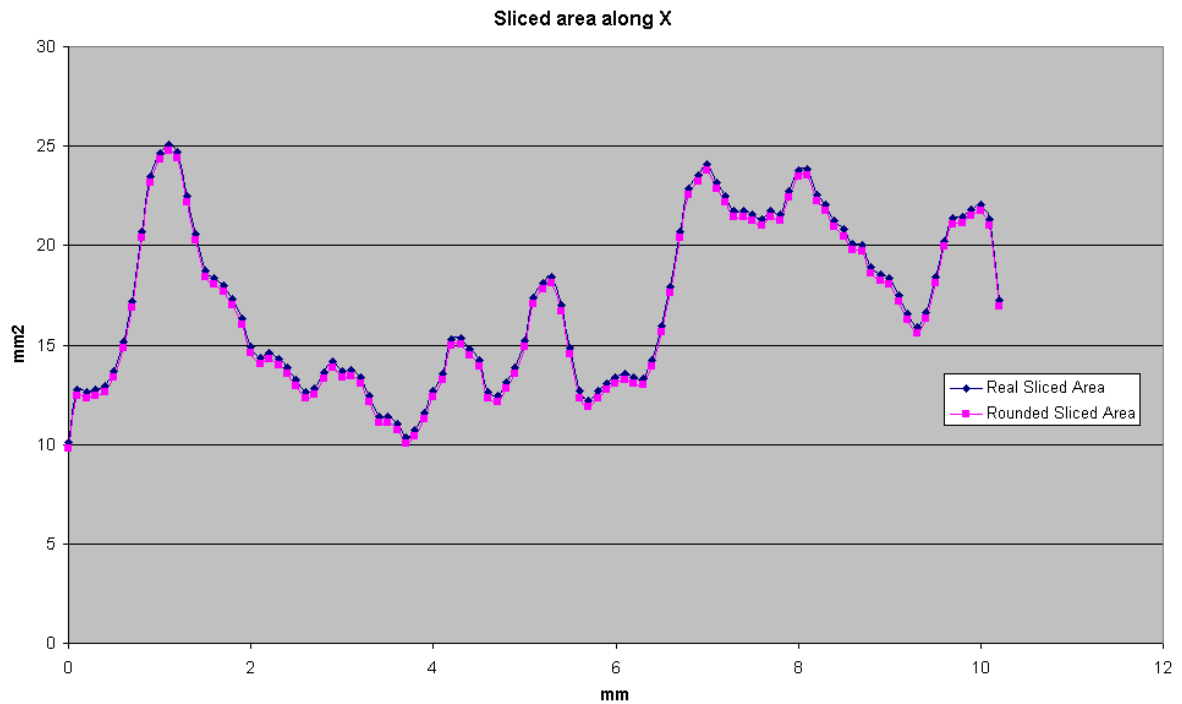


**Fig. 6.14** Real and discretized sliced area distribution along  $X$ .

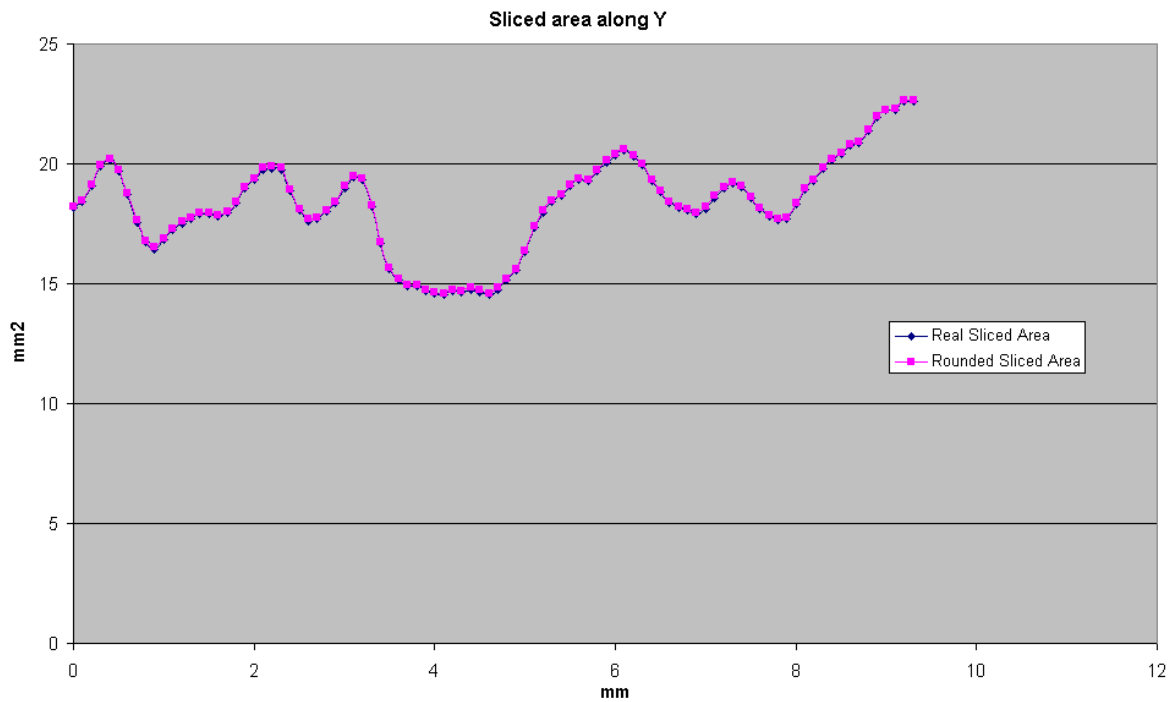


**Fig. 6.15** Real and discretized sliced area distribution along  $Y$ .

### 6.3.1 ABDI Geometry - Case 1 -

In this first case, two compatible solutions for the systems of equations (6.5) and (6.9) have been found by setting an 'artificial' maximum value, for all the  $\alpha$  and  $\beta$  variables, of 40 instead of  $M=94$  and  $N=103$ . As explained in section 6.2.4.3, this will reduce the number of zeros  $v$  and  $u$  and, at the same time, limit the value of the terms in the left side of the inequalities (6.21) and (6.22). The design strategy adopted was the minimum zeros propagation design, used to minimise  $u$ . Figures from 6.16 to 6.27 show every tenth layer along  $Z$ , starting from  $Z=0$ . The sliced area distributions along the three directions were the same as the discrete curve shown in Fig. 6.13, 6.14 and 6.15. The planar system of coordinates ( $X$ ,  $Y$ ) was the same for each cross-section, and was orientated as shown in Fig. 6.16.

The time required to solve the systems (6.5) and (6.9) were 94 and 90 seconds respectively, while the time required to design all the templates and allocated voxels was 1198 seconds. The size of the Excel file containing all the designed layers and the solutions to the systems (6.5) and (6.9) was 6.58 MB.



The export to CAD routine was able to design only three layers in Catia V5R16, due to the high number of geometrical elements required. This was caused by the large number of non-connected voxels, each of which required four vertexes and four lines to be designed.

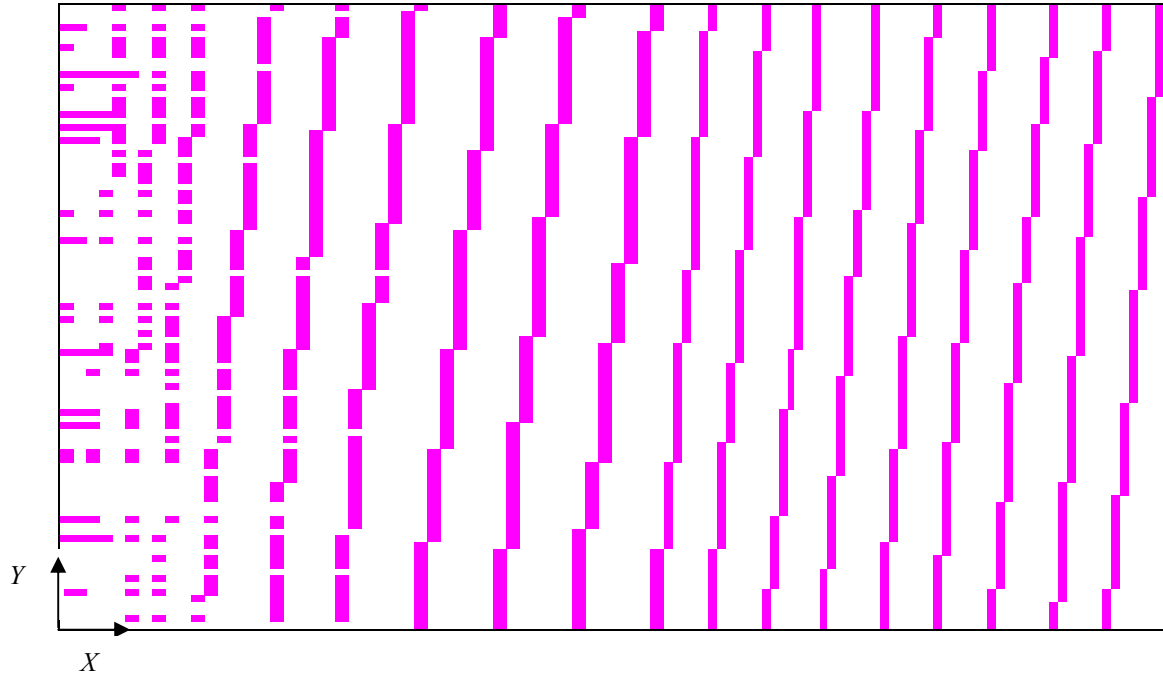


**Fig. 6.16** ABDI geometry, case 1. Layer number 0 in Z, corresponding to  $Z=0.0$  mm.

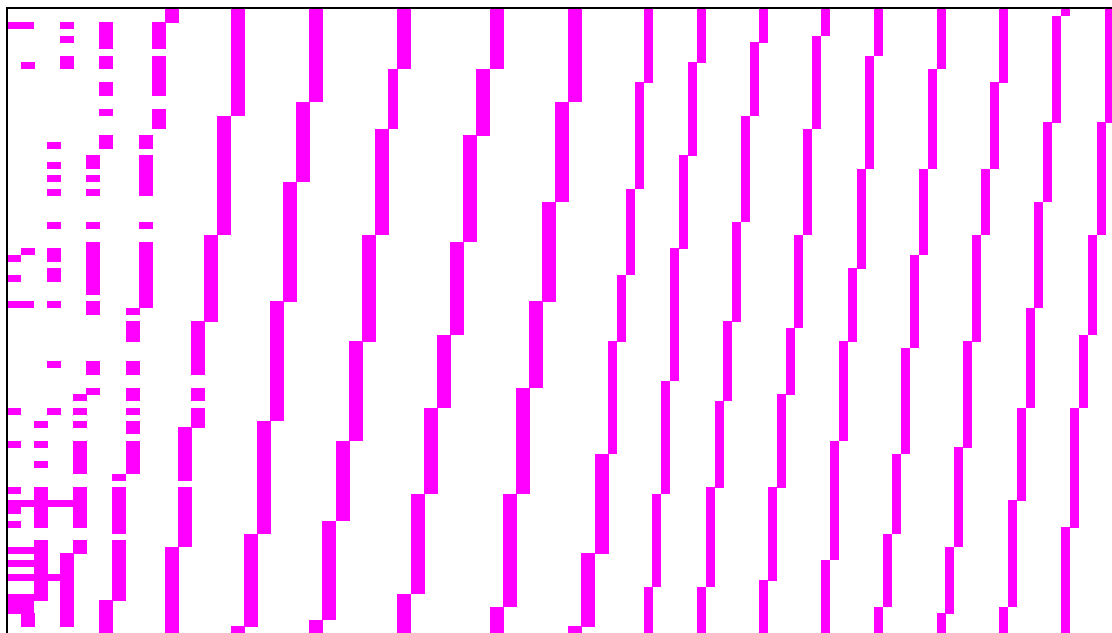


**Fig. 6.17** ABDI geometry, case 1. Layer number 10 in Z, corresponding to  $Z=1.0$  mm

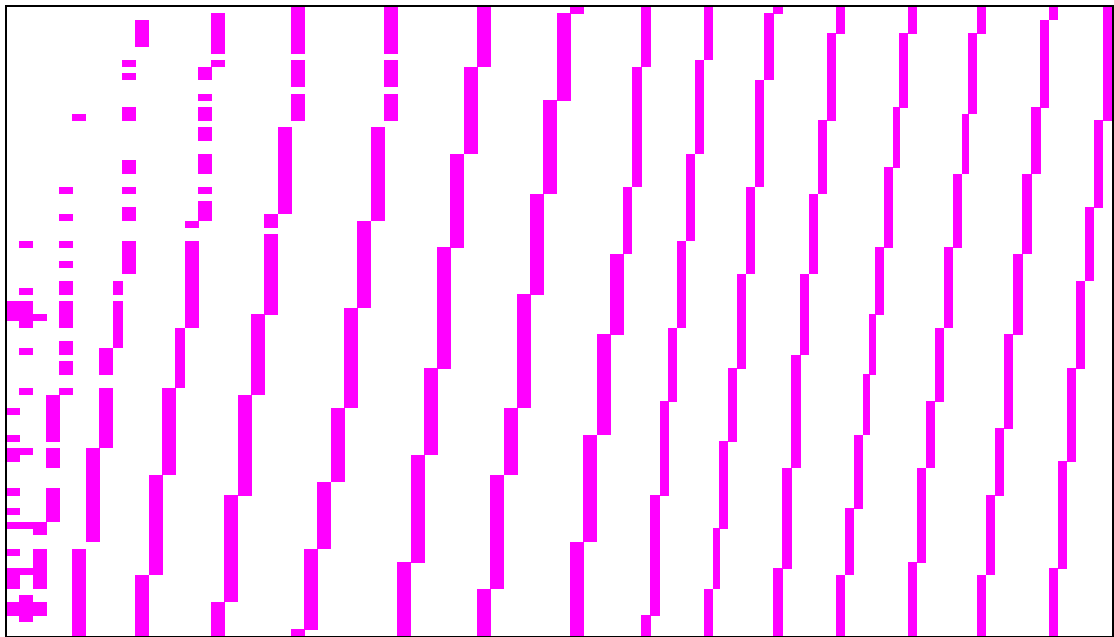


**Fig. 6.18** ABDI geometry, case 1. Layer number 20 in  $Z$ , corresponding to  $Z=2.0$  mm

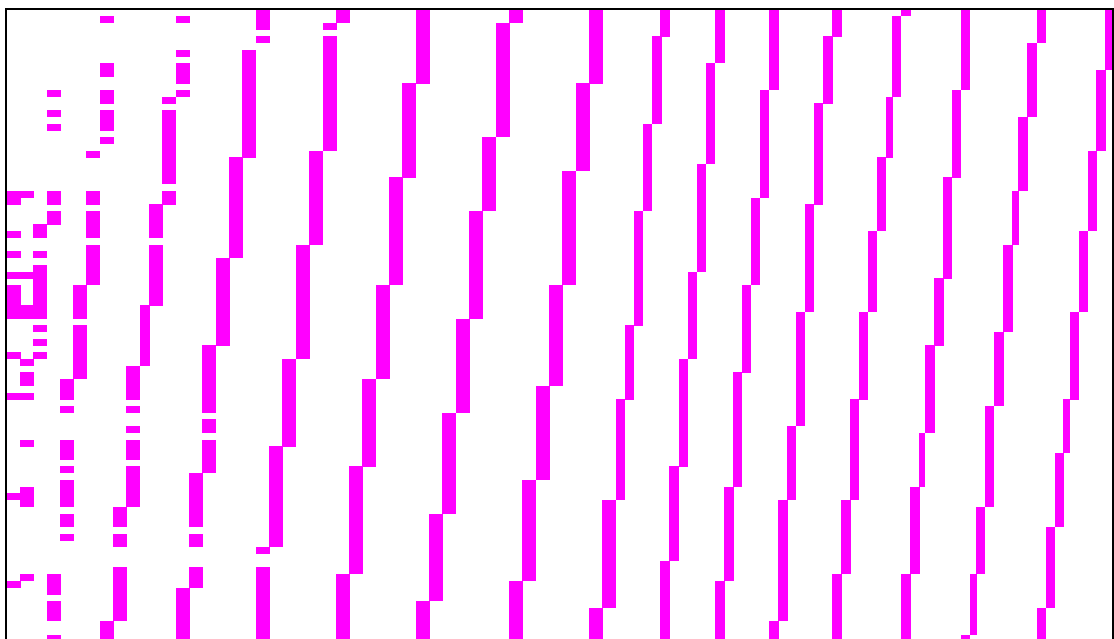


**Fig. 6.19** ABDI geometry, case 1. Layer number 30 in  $Z$ , corresponding to  $Z=3.0$  mm

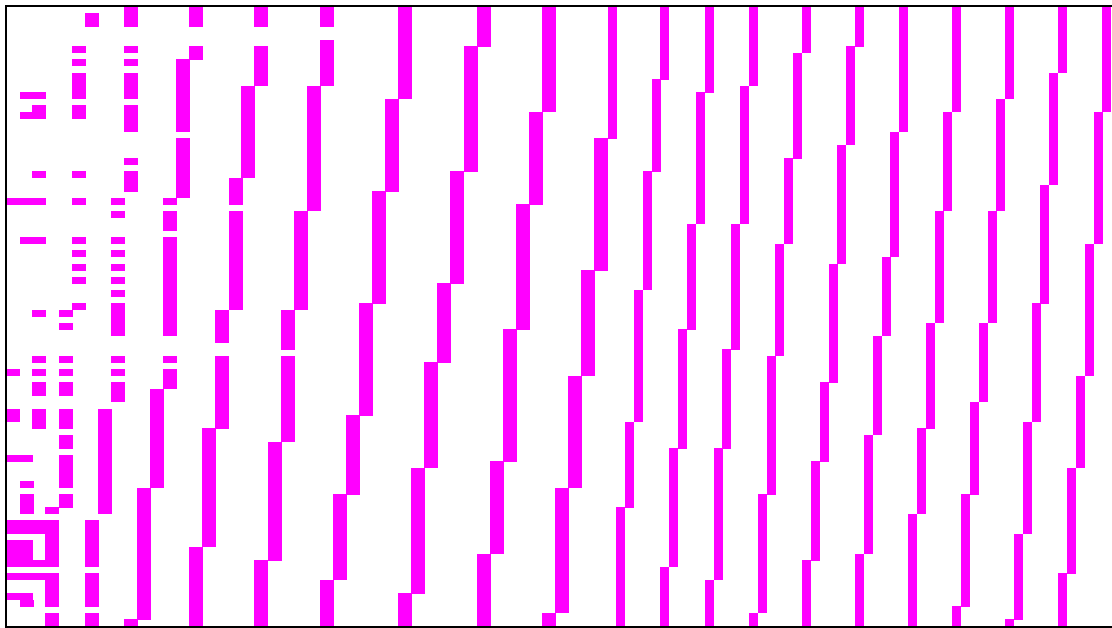


**Fig. 6.20** ABDI geometry, case 1. Layer number 40 in  $Z$ , corresponding to  $Z=4.0$  mm

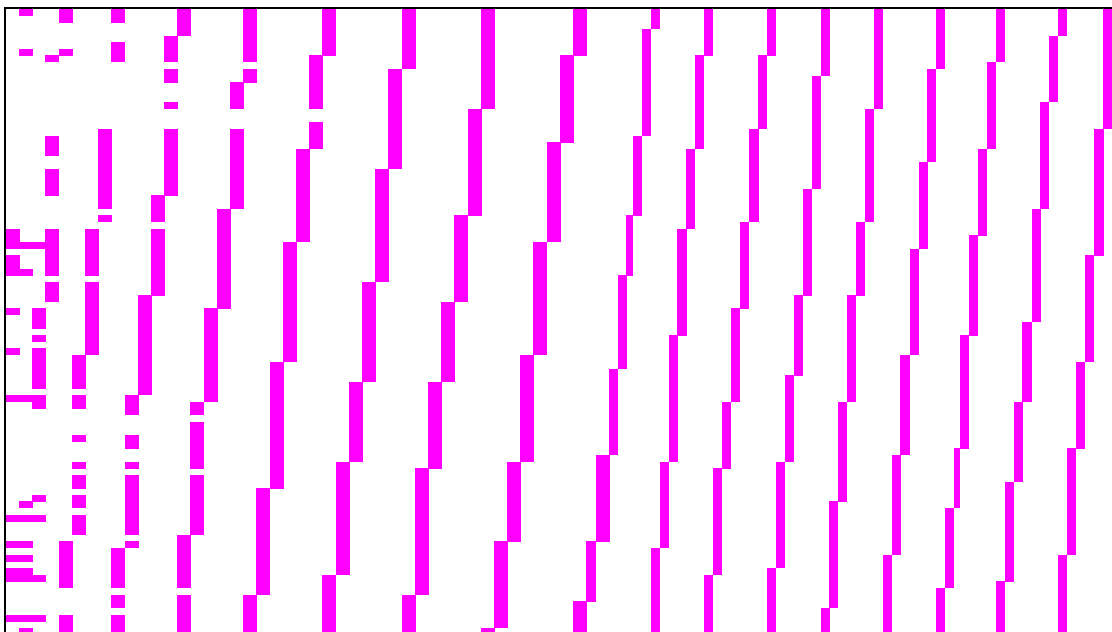


**Fig. 6.21** ABDI geometry, case 1. Layer number 50 in  $Z$ , corresponding to  $Z=5.0$  mm

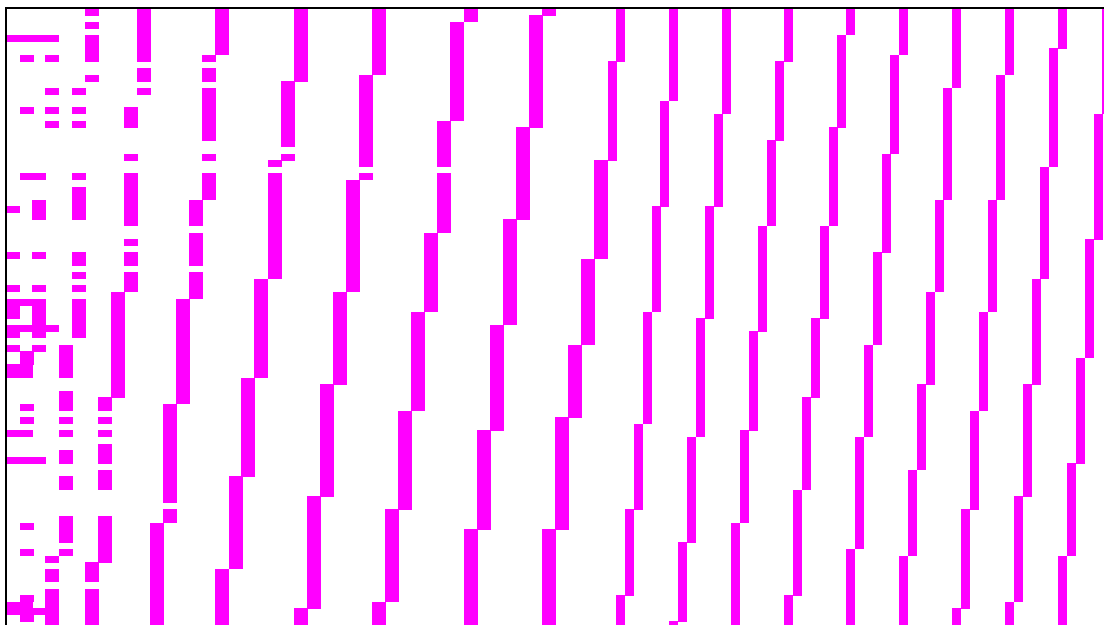


**Fig. 6.22** ABDI geometry, case 1. Layer number 60 in  $Z$ , corresponding to  $Z=6.0$  mm

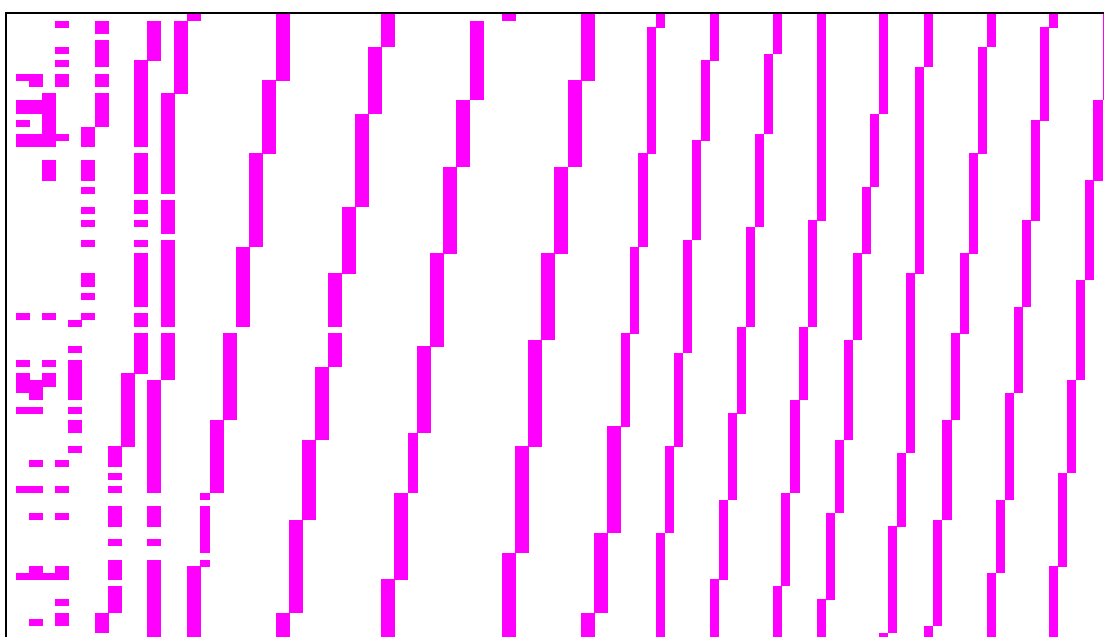


**Fig. 6.23** ABDI geometry, case 1. Layer number 70 in  $Z$ , corresponding to  $Z=6.0$  mm

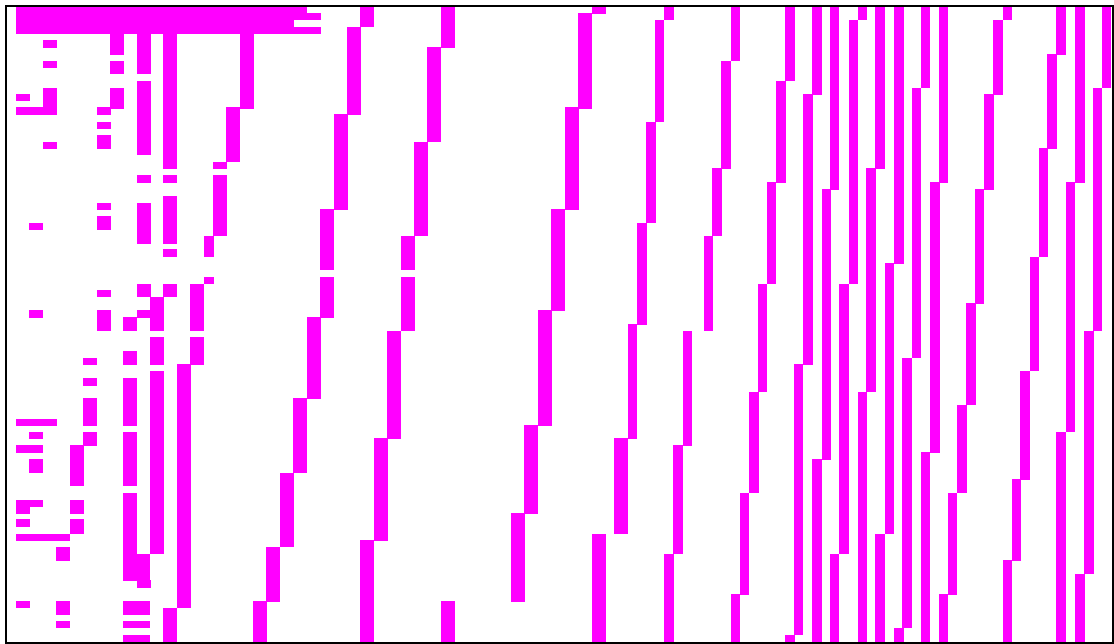


**Fig. 6.24** ABDI geometry, case 1. Layer number 80 in Z, corresponding to  $Z=8.0$  mm

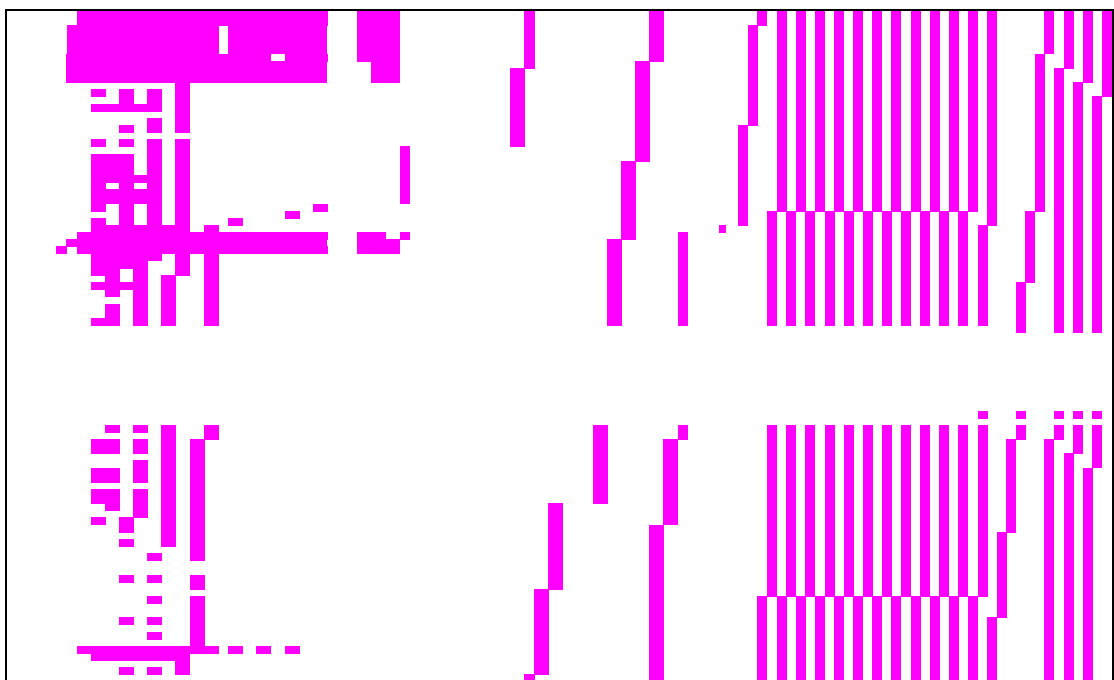


**Fig. 6.25** ABDI geometry, case 1. Layer number 90 in Z, corresponding to  $Z=9.0$  mm

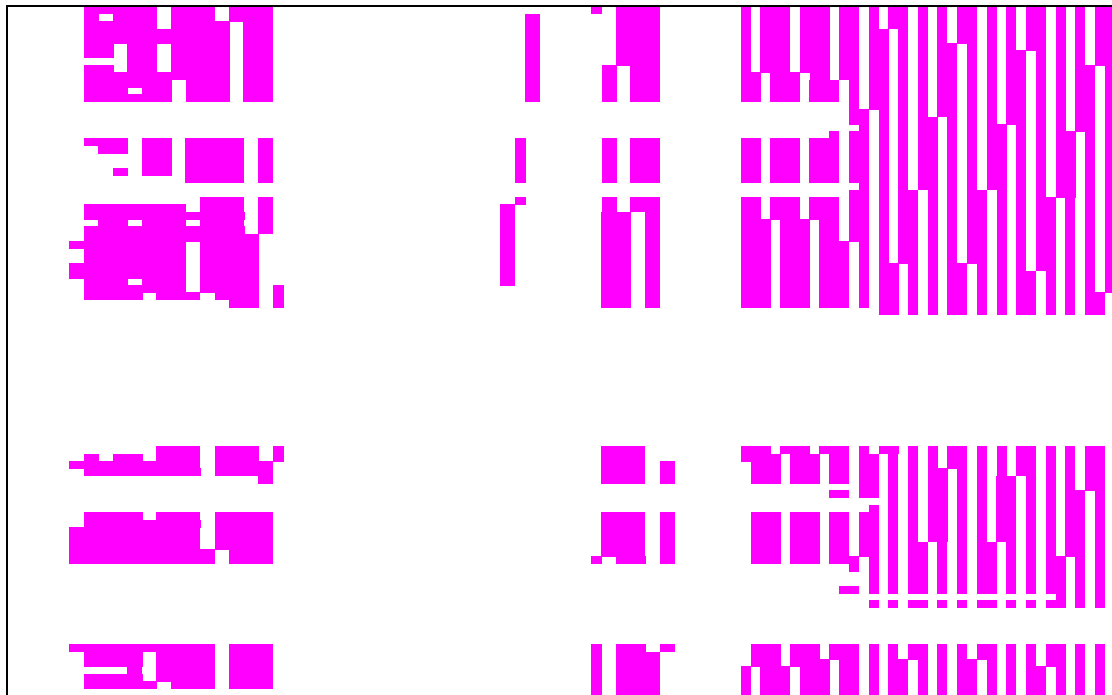


**Fig. 6.26** ABDI geometry, case 1. Layer number 100 in  $Z$ , corresponding to  $Z=10.0$  mm

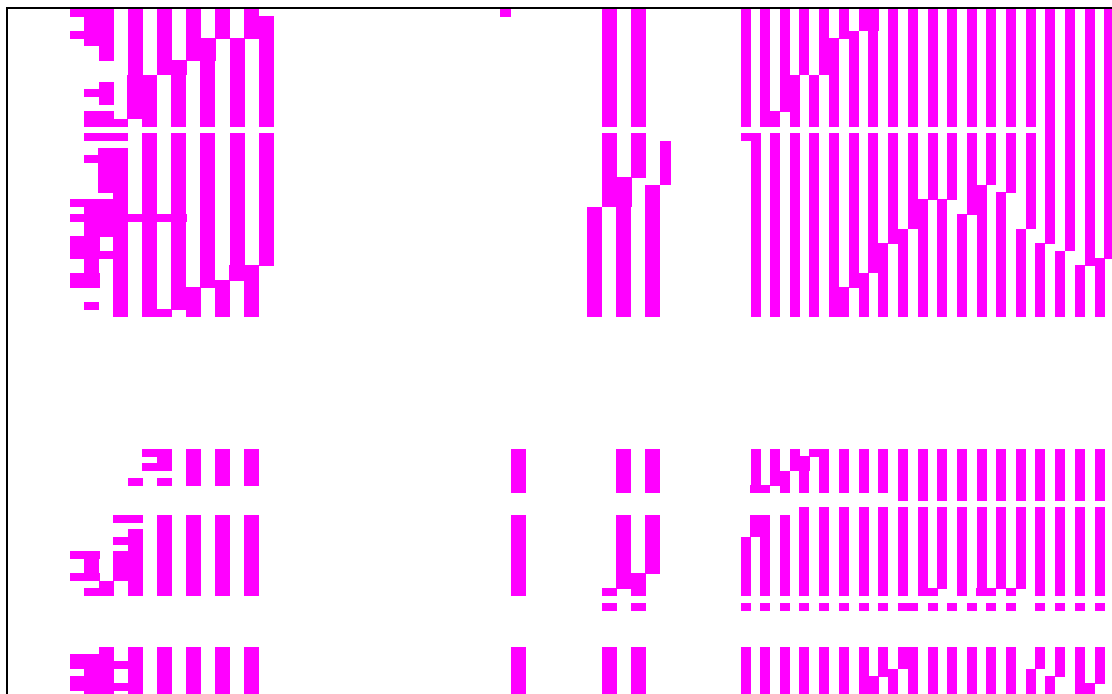


**Fig. 6.27** ABDI geometry, case 1. Layer number 102 in  $Z$ , corresponding to  $Z=10.2$  mm

### 6.3.2 ABDI Geometry - Case 2 -

In the second case, two compatible solutions for the systems of equations (6.5) and (6.9) were found by setting an 'artificial' maximum value for all the  $\alpha$  and  $\beta$  variables of 30 instead of  $M=94$  and  $N=103$ . As explained in section 6.2.4.3, this will reduce the number of zeros  $v$  and  $u$  and, at the same time, limit the value of the terms on the left side of the inequalities (6.21) and (6.22). The design strategy adopted was derived from the minimum zeros propagation design, used to minimise  $u$ , but with some changes. Instead of taking the minimum non-zero value in the sequence  $\alpha_{0,i}, \alpha_{1,i}, \alpha_{2,i}, \alpha_{3,i}, \dots, \alpha_{N-1,i}$  at each iteration it adopted a sequential approach where  $\alpha_{0,i}$  was the first value to be considered, followed by  $\alpha_{1,i}, \alpha_{2,i}, \alpha_{3,i}, \dots, \alpha_{N-1,i}$ .

Figures from 6.28 to 6.39 show every tenth layer along  $Z$ , starting from  $Z=0$ . The sliced area distributions along the three directions were the same as the discrete curve shown in Fig. 6.13, 6.14 and 6.15. The planar system of co-ordinates ( $X, Y$ ) was the same for each cross-section, and was orientated as shown in Fig. 6.28.

The time required to solve the systems (6.5) and (6.9) were 115 and 108 seconds respectively, while the time required to design all the templates and allocated voxels was 1217 seconds. The size of the Excel file containing all the designed layers and the solutions to the systems (6.5) and (6.9) was 6.66 MB.

As in the previous case, the export to CAD routine was able to design only three layers in Catia V5R16, due to the high number of geometrical elements required. This was caused by the large number of non-connected voxels, each of which required four vertexes and four lines to be designed.

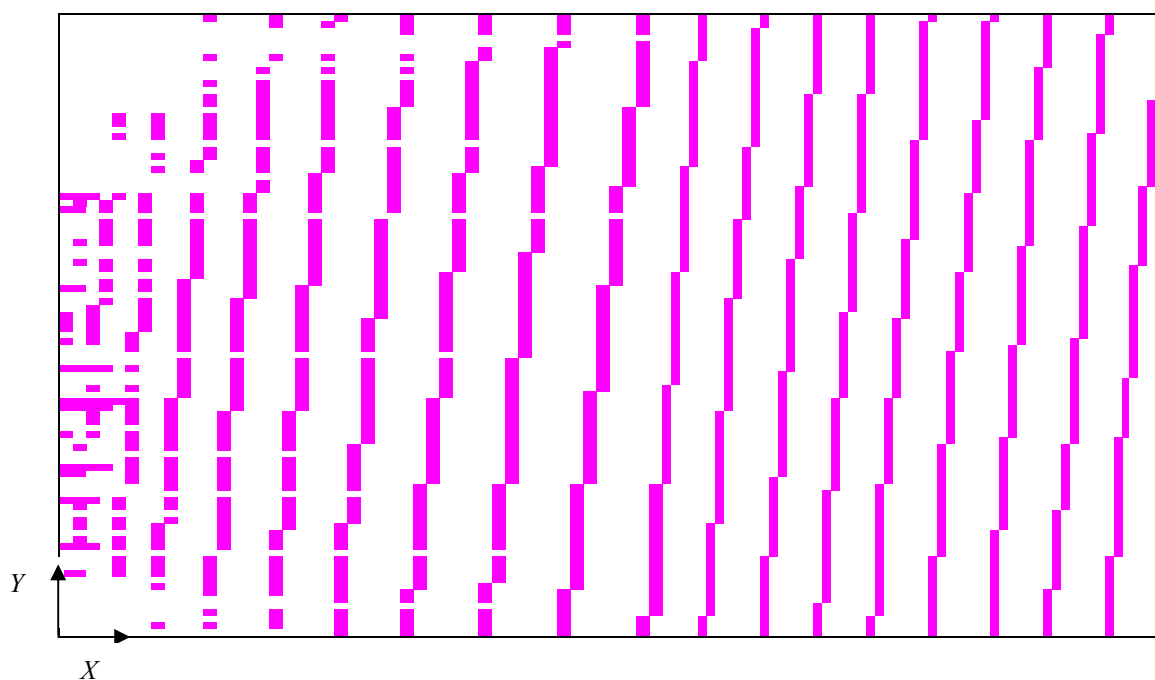


**Fig. 6.28** ABDI geometry, case 2. Layer number 0 in Z, corresponding to  $Z=0.0$  mm.

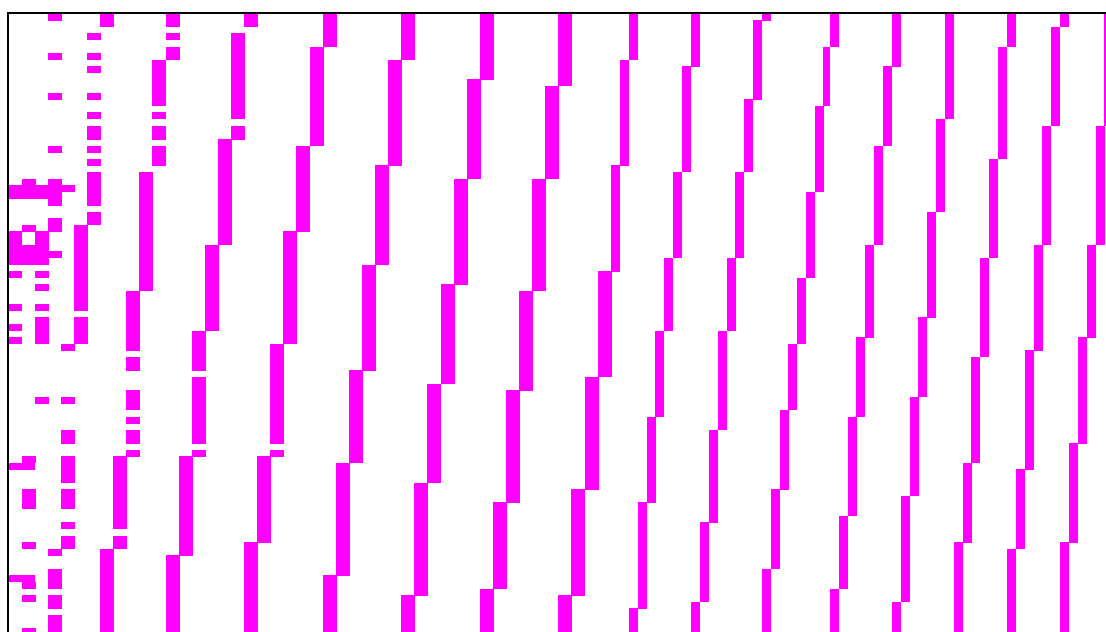


**Fig. 6.29** ABDI geometry, case 2. Layer number 10 in Z, corresponding to  $Z=1.0$  mm



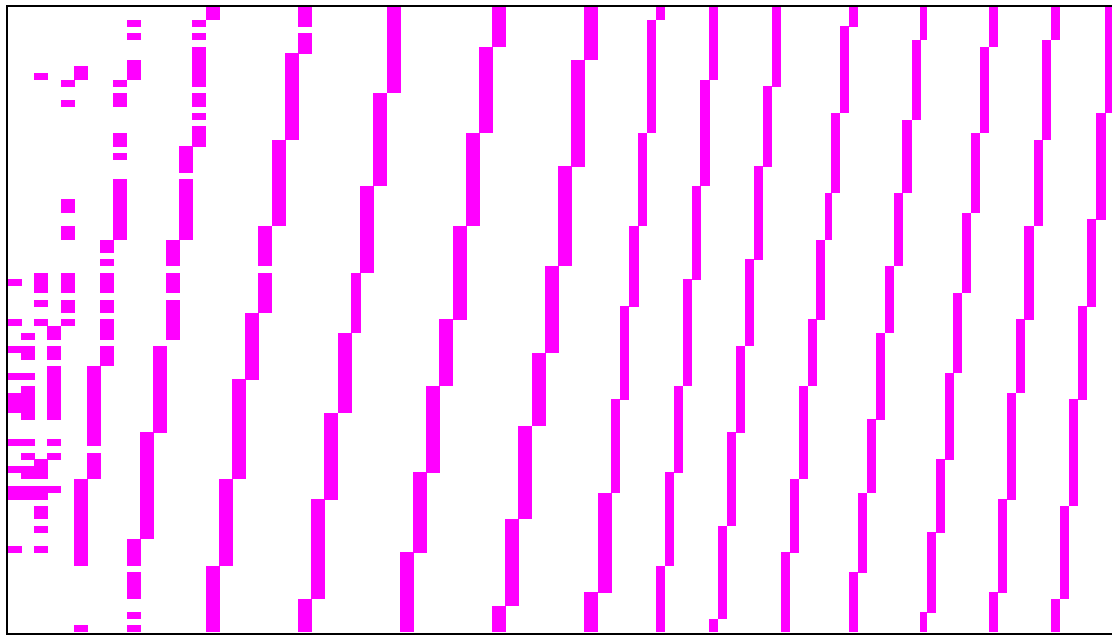


**Fig. 6.30** ABDI geometry, case 2. Layer number 20 in  $Z$ , corresponding to  $Z=2.0$  mm

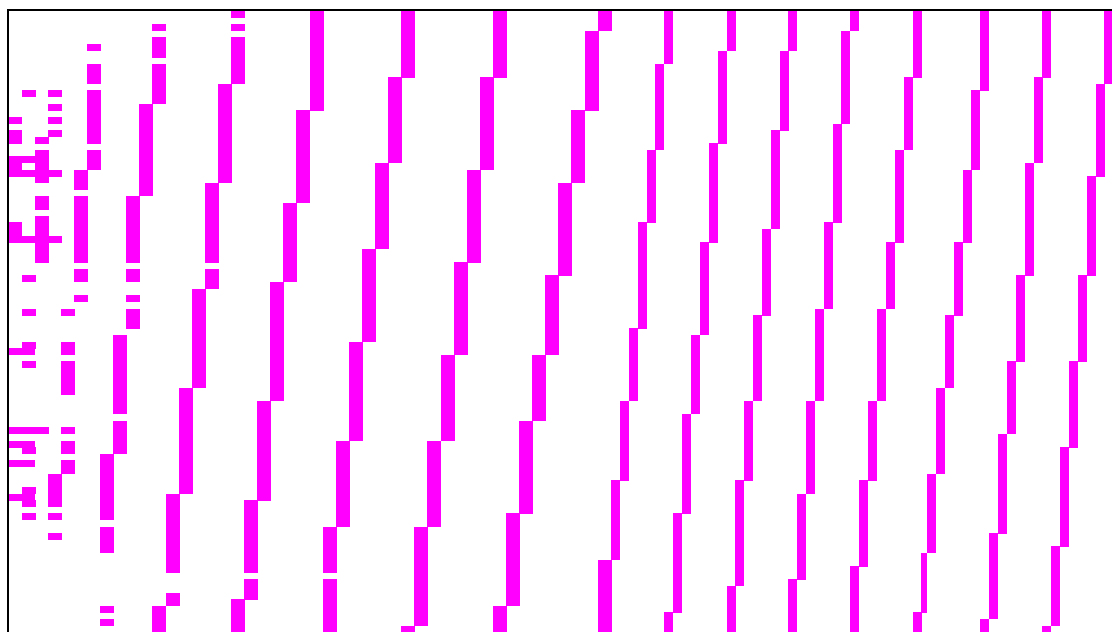


**Fig. 6.31** ABDI geometry, case 2. Layer number 30 in  $Z$ , corresponding to  $Z=3.0$  mm

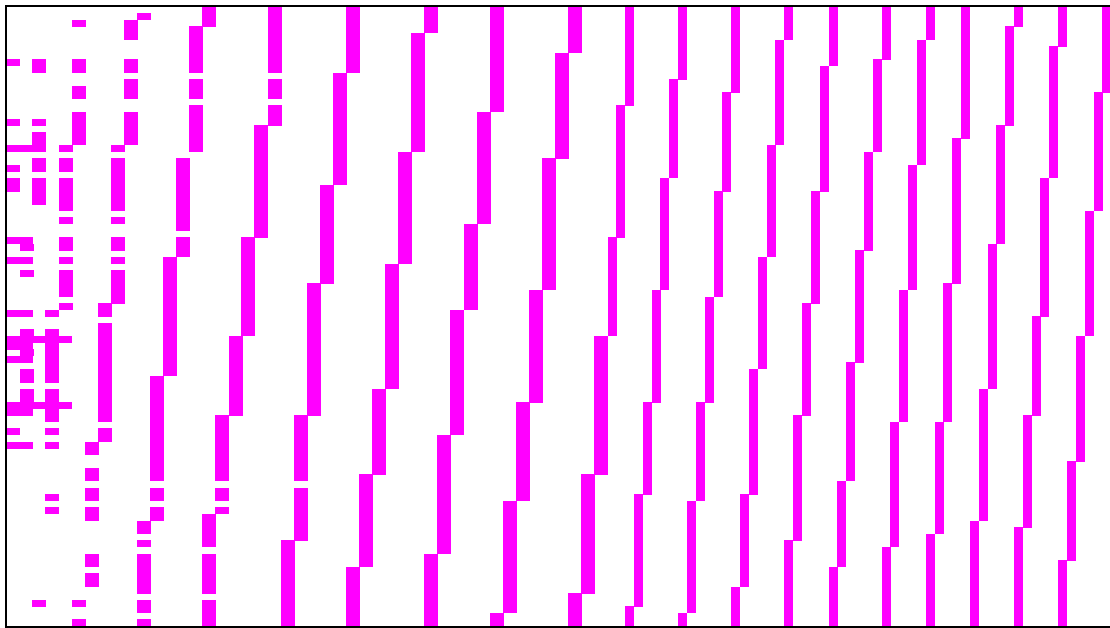


**Fig. 6.32** ABDI geometry, case 2. Layer number 40 in  $Z$ , corresponding to  $Z=4.0$  mm

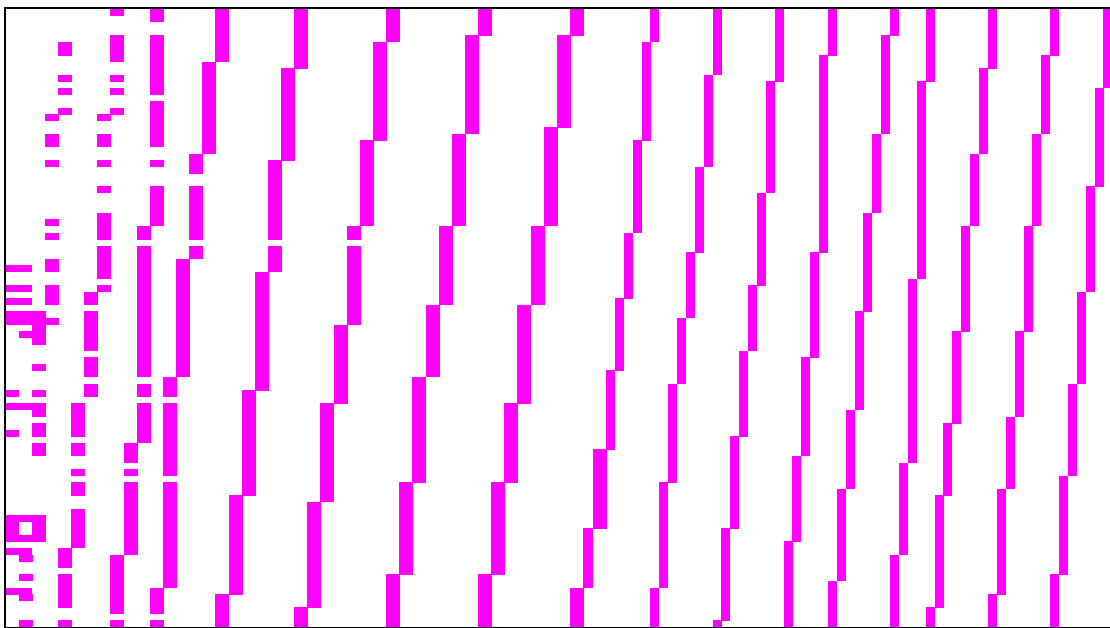


**Fig. 6.33** ABDI geometry, case 2. Layer number 50 in  $Z$ , corresponding to  $Z=5.0$  mm

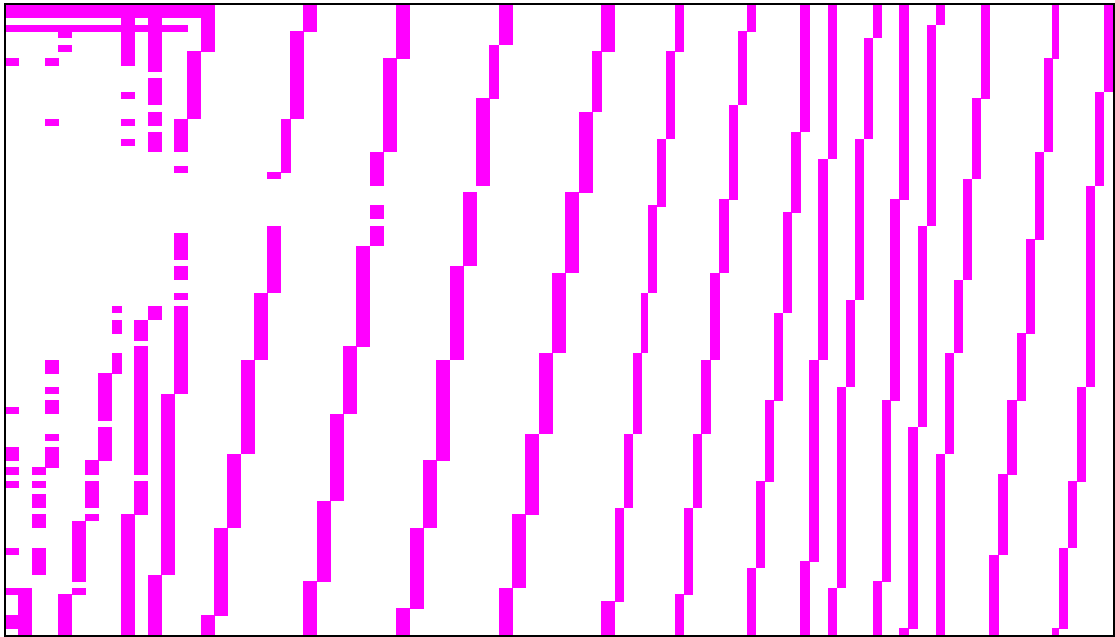


**Fig. 6.34** ABDI geometry, case 2. Layer number 60 in  $Z$ , corresponding to  $Z=6.0$  mm

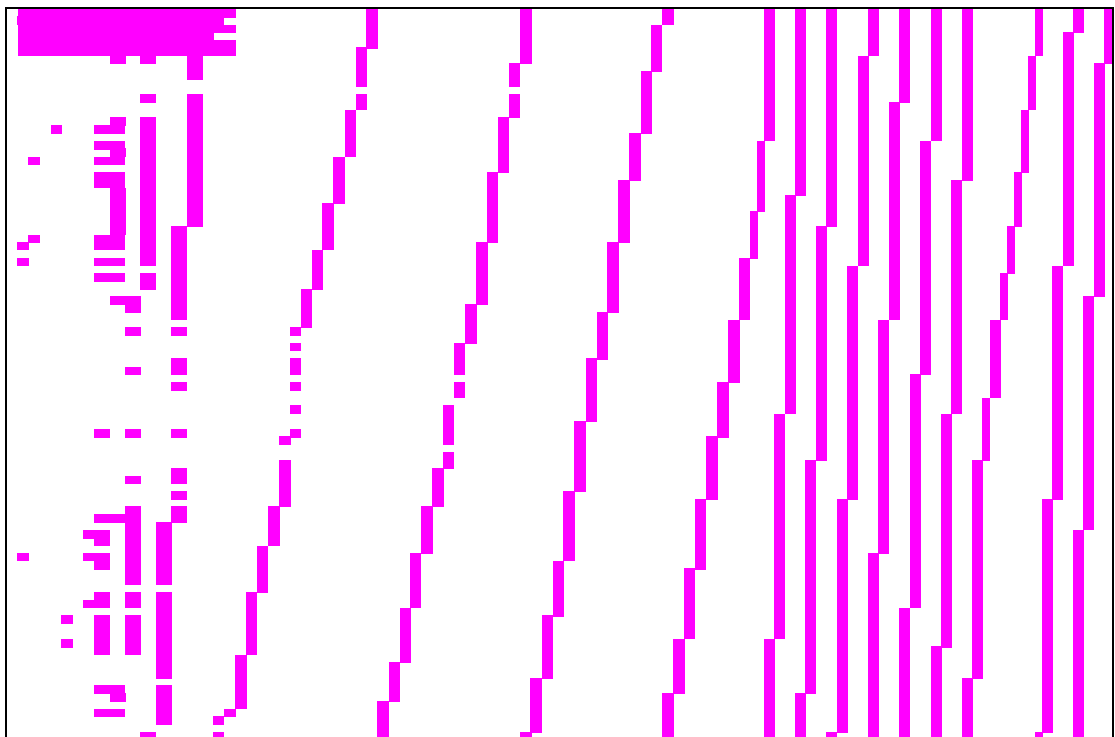


**Fig. 6.35** ABDI geometry, case 2. Layer number 70 in  $Z$ , corresponding to  $Z=6.0$  mm

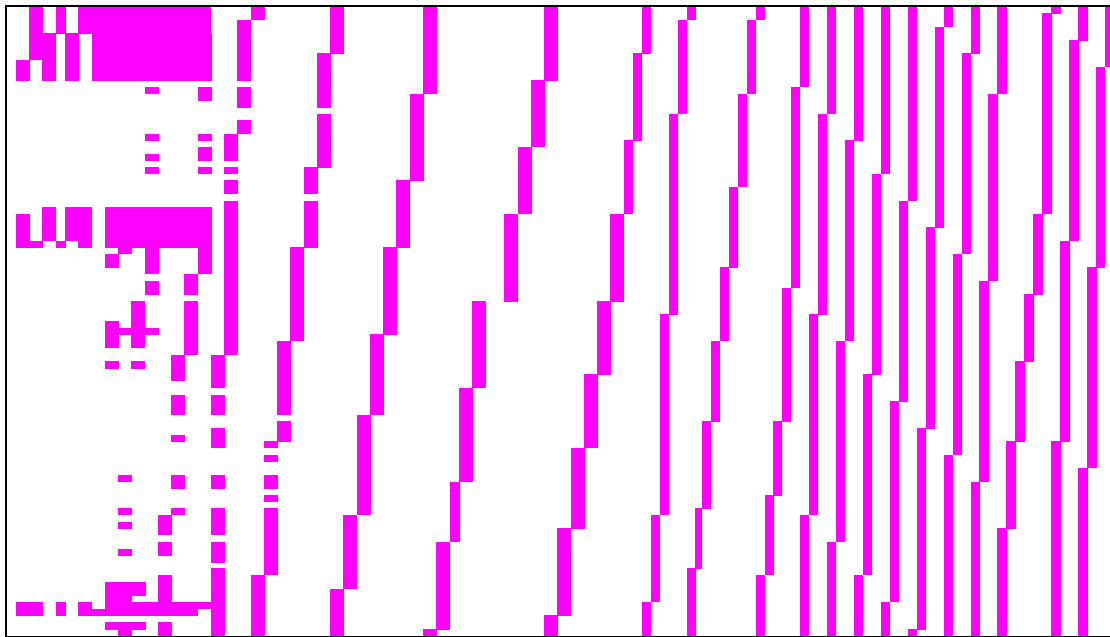


**Fig. 6.36** ABDI geometry, case 2. Layer number 80 in  $Z$ , corresponding to  $Z=8.0$  mm

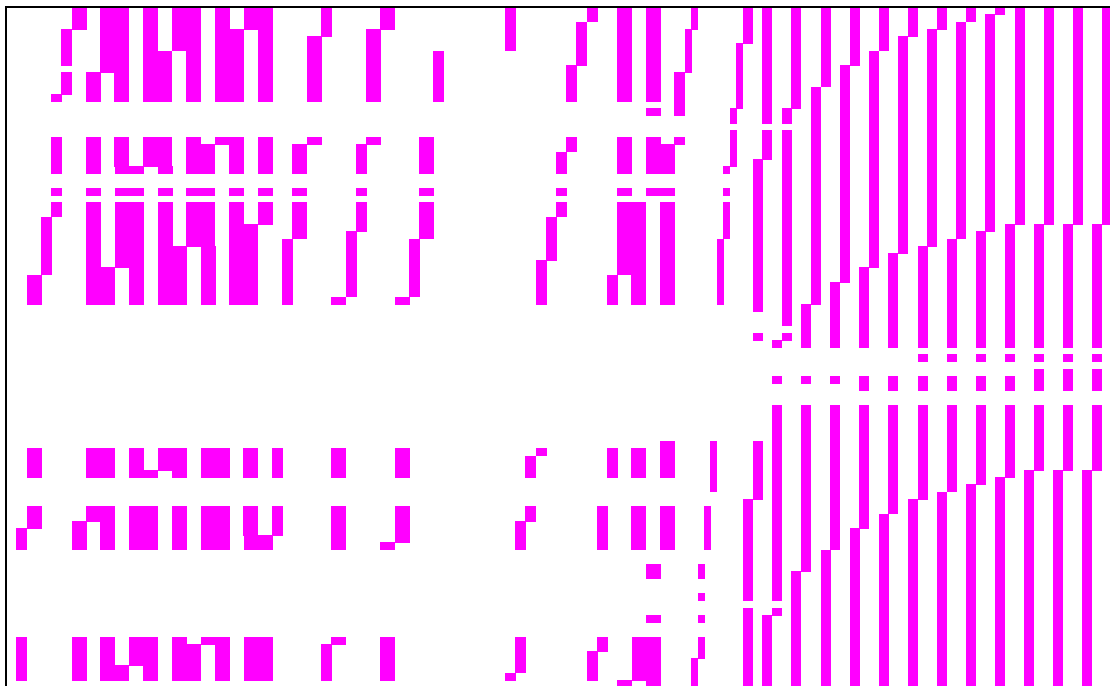


**Fig. 6.37** ABDI geometry, case 2. Layer number 90 in  $Z$ , corresponding to  $Z=9.0$  mm

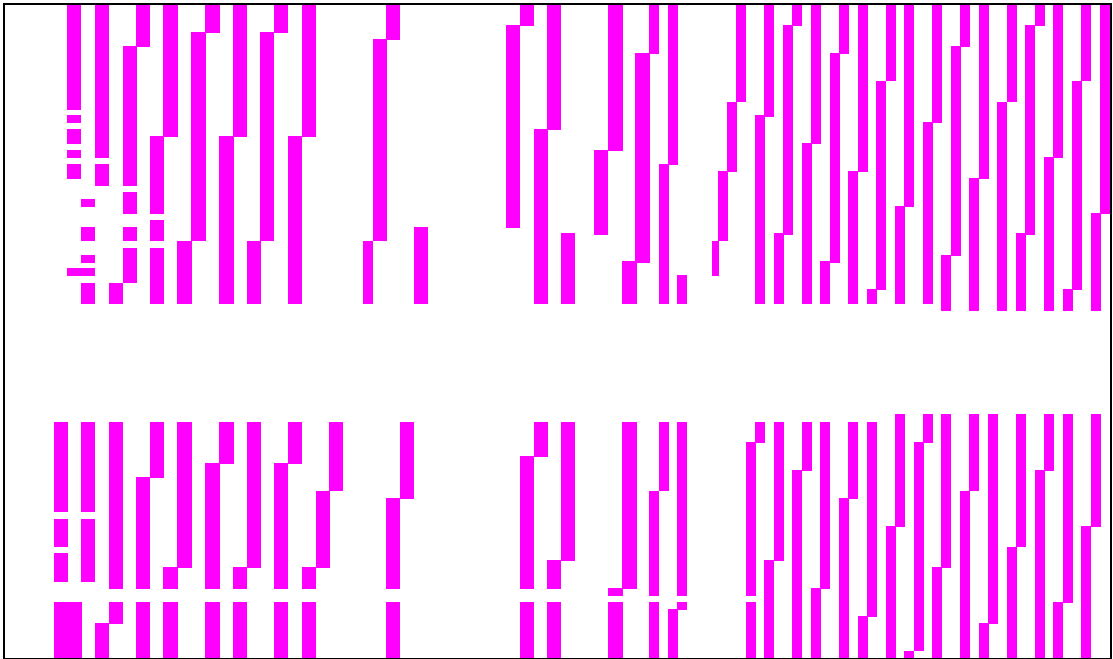


**Fig. 6.38** ABDI geometry, case 2. Layer number 100 in Z, corresponding to  $Z=10.0$  mm

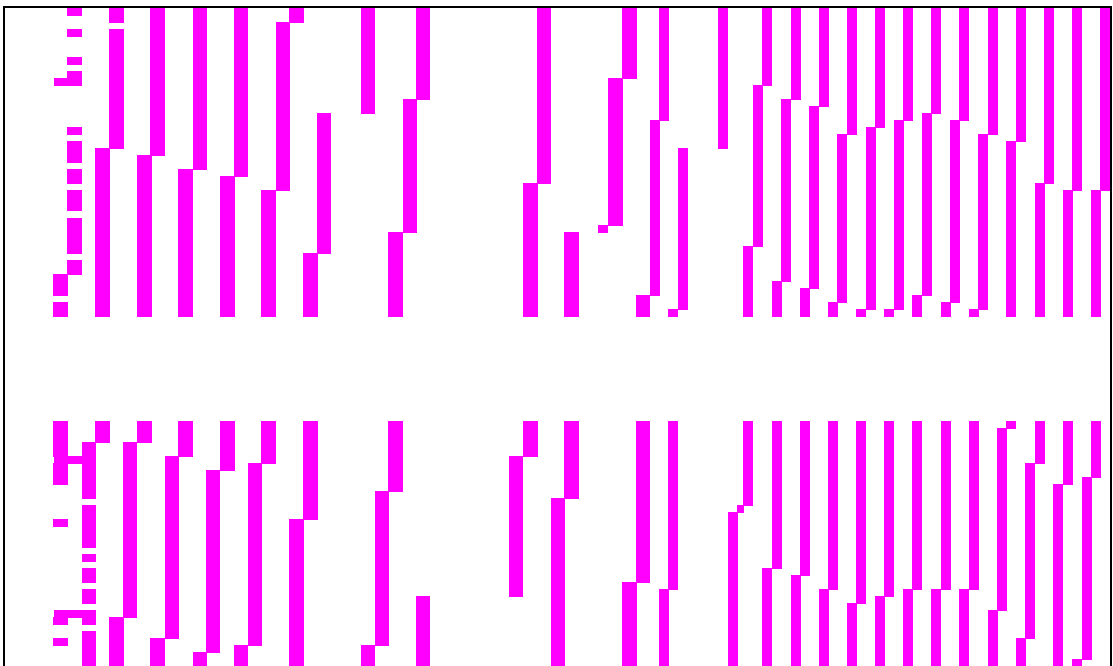


**Fig. 6.39** ABDI geometry, case 2. Layer number 102 in Z, corresponding to  $Z=10.2$  mm

## 6.4 Review

The ABDI methodology presented in this chapter was able to design two bio-mimetic geometries, with the same sliced area in three orthogonal directions as the  $\mu$ CT trabecular bone sample analysed in chapter 5.

To verify that the two geometries presented the same sliced areas as the  $\mu$ CT sample analysed in chapter 5, the number of dense voxels in the three directions were computed by a separate routine. In both cases, the curves obtained were exactly the same as the discrete curves shown in Fig. 6.13, 6.14 and 6.15, proving that these geometries are bio-mimetic in terms of sliced area (i.e. porosity). The discrete curves shown in these three figures present a very close match with those relative to the  $\mu$ CT sample analysed, as the maximum difference between the two was  $0.31 \text{ mm}^2$  in the  $X$  axis.

Neither the resolution algorithm nor the layer design presented processing delays or storage difficulties for standard specification computers. To solve the systems (6.5) and (6.9), the slowest run was for (6.5) in the second case study (since the maximum  $M$  for this case was 30 instead of 40, there will be more minimum values different from zero, and therefore more computation (6.17) will be required), which required 115 seconds to complete. The slowest run for completing the design of all layers was 1217 seconds, in the second case study (less values for  $v$  and  $u$  requires more computations). The biggest Excel file size containing all the layers was 6.66 MB, which included the data relative to the solutions found for the systems (6.5) and (6.9).

Therefore, the design methodology explained in this chapter did not require any excessive computational requirements, as it could be run on a current conventional computer.

In both the proposed designs, the pixel patterns created by the design strategies start distributed seemingly at random as might be expected but then settle into stripes or blocks which clearly do not replicate the desired trabecular structure. These patterns are a consequence of both design strategies adopted, which involved the minimisation of  $u$  that is the number of zeros in the sequence  $\beta_{0,i}, \beta_{1,i}, \beta_{2,i}, \beta_{3,i}, \dots, \beta_{M-1,i}$  relative to the layer  $i$  on  $Z$ . Therefore, since all the columns in Fig. 6.7 are progressively solved in the numerical algorithm, the dense voxels appear to be allocated in near vertical stripes, which eventually intersect to form blocks. In addition, the artificial limitation on the maximum values of all

$\alpha$  and  $\beta$  variables also affected the pixel patterns produced, as in both cases the voxels seemed to be distributed uniformly throughout the volume, with a low number of interconnections.

In their current form, because of the low interconnectivity of the dense voxels and the presence of floating material, the produced geometries could not be applied to TE.

The presence of non-connected voxels required a high number of boundaries, which prevented the complete export of the designed layers into CAD. The creation of CAD B-Rep entities from the pixel data produced was inefficient and potentially unnecessary as alternative methods of applying the data could be employed. A 3D representation of the pixel data could have been reconstructed in the same manner as CT data by using software such as Simpleware (by Simpleware Ltd., Exeter, UK) or Mimics (by Materialise N. V. Leuven, Belgium). In addition, pixel data/bitmaps have the potential for direct input to AM systems such as PolyJet modelling (by Objet Inc., Rehovot, Israel), digital light processing (Perfactory, by EnvisionTEC GmbH, Gladbeck, Germany) or 3D printing (by Z Corp).

Detailed descriptions of the presented bio-mimetic geometries are provided in section 7.5.

## CHAPTER 7

### - DISCUSSION -

This chapter contains a discussion of the findings from each stage of the experiments. Critical evaluation of the results, as well as the reasons behind the project decisions and directions are also included. In order to elucidate the rationale for the research and its progression, discussions in the form of a review have been included in some of the previous chapters where necessary. For those chapters, a summary of the previous reviews is provided.

#### 7.1 ADI Methodology (chapter 2)

From the literature review, it emerged that three geometrical parameters are critical for bone TE scaffolds, pore interconnectivity, size and shape. This chapter aimed to develop an automated design method for complex and irregular structures in conventional CAD software, which present random variability on those three key parameters in both regular and anatomical volumes. Although the same structures can be designed manually in CAD, due to the level of complexity, each design would require a significant amount of time - in the order of hours or days. The methodology explained in this chapter overcomes this limitation by introducing automation in the design process, so that complex and irregular structures can be designed in minutes instead of the hours - or even days - required by manual design.

Although this work focused on bone tissue and on only two kinds of trabecular bone morphologies, other tissues and morphologies can be introduced using the same design method through the use of parametric features and the definition of new geometrical elements. This work focused on Type I and Type IIa of bones (according to the trabecular bone classification proposed by Singh, 1978) because those types are widespread and most TE scaffold research efforts are oriented towards representations of rod networks.



The basic element used to represent complex and irregular rod networks was a multi-section solid with either one or two cross-sections, which were defined by using a closed four control-points curve. Such control-points were arranged as vertices of a square in order to provide an estimation of the pore size, while pore shape was controlled by modifying the values of the tangents at each control-point. Different numbers of cross-sections, each with different allocation of the control-points, as well as a more precise computation of pore size, could have been used. In addition, the pore shape could have been further modified by randomly changing the coordinates of the control-points. The proposed layout was adopted in order to provide a basic definition of irregular rod networks, to assess the feasibility of the automated design method, and to limit the computational time and resources required. The intention behind using this basic definition of rod networks was to provide a foundation from which more complex networks could be defined, which may eventually require more demanding computational resources.

The pore location model adopted for cubic volumes used the same number of rods and border distances in each direction and face of the cube, thus producing regular pore distributions. This limitation applied only to cubic volumes, but since they were chosen as reference volumes to test the design method and were not the target volumes for the method, there was no need to produce different pore locations on cubic volumes, so as to achieve irregular distributions. The pore location model adopted for anatomical volumes (which were the target volumes of the method) produced irregular distributions.

Curved paths were defined by either three control-points curves or two control-points curves with specified tangential directions and values. In the case of three control-points curves, the second point was defined either in the centroid or centroid region of the volume. Different converging points or regions could have been used in order to obtain more irregular geometries. The purpose of focusing on the centroid or centroid region was to achieve a basic model of random variation in pore interconnectivity, as this parameter mostly depends on rod paths. In addition, the intention was to increase the porosity at the centre of the scaffold, which may promote tissue regeneration deeper into thick section geometries, overcoming the limit of 500  $\mu\text{m}$  indicated by Ishaug-Riley *et al.* (1997). The proposed model of pore interconnectivity around the centroid or centroid region provides a foundation from which more complex models of pore interconnectivity – those based on different converging points, for instance - may be defined.

In both cubic and anatomical volumes, the surface pairs were arbitrarily selected by the user to be opposite, or approximately opposite in the case of anatomical volumes. That was done to increase interconnectivity throughout the volume (and not only on limited portions of it), which may enhance the flow of nutrients inside the scaffold from all the surrounding boundaries. Due to the interconnectivities among the rods, all surfaces, including those not directly paired, resulted as interconnected by the end of the design process.

The efficiency of the ADI method was measured by comparing the automated design time with the estimated time for manual design. The estimated figures for manual design were chosen by considering the average values for each design step, as in some cases the actual time will be higher, while in others it will be lower. The proposed values aimed to provide average values that could be used consistently throughout this work, and independently on each case study. These figures also assume that any random combination of parameters found by the user does not produce any error in the geometry, and that the manual design is carried out without interruption. In addition, anatomical volumes would require a much longer time, as pore locations are irregular and the settings used to define them differ from surface to surface.

Random variation of parameters has been proposed in this work in order to increase irregularities in the produced networks and allow the algorithms to design different structures at each run. In addition, routines were written to design the rod networks first, which were later converted into channels. The reason for that was because the rod structures were easier to inspect visually, and as such they were particularly suitable to assess the level of geometrical complexity during the development of the ADI methodology. However, if the method were fully developed it would be used to generate channels directly on the required volume, and would therefore be even more efficient.

Finally, the evaluation of CAD software was conducted in 2007 and some features may have changed over time. Newer versions of other CAD softwares may also satisfy the requisites for the ADI methodology, although the use of any other suitable CAD software will not affect the proposed methodology.

## 7.2 Automated Design on Regular Volumes (chapter 3)

This chapter aimed to develop and test basic forms of automated design in conventional CAD software. At this stage, the attention was focused on the feasibility aspects of CAD automation (algorithms and programming), rather than on those related to the target volume. For that reason, a cubic reference volume was proposed. There was no particular requirement to use a cubic shape - any other reference geometry could have been used - but this provided a regular volume to assess the effect of the variable parameters, aside from the location of each channel. The level of complexity achieved in the proposed rod networks was increased at each step by the progressive introduction of more variables in the design. Although other more complex networks could have been defined, the initial tests ended with case 6, because it presented random variation in all the key parameters for bone TE scaffolds - pore size, shape and interconnectivity. The proposed cases mainly presented differences in pore interconnectivity, while the variability in pore size and shape was achieved from case 2.

The estimated pore size range used in this chapter was from 0.2 to 0.8 mm for all six cases, as this range has been identified as suitable for bone regeneration in the literature available to date. The size of 10 mm for the cubic volume was proposed because the resultant structures could be compared with  $\mu$ CT cubic samples of approximately the same size.

The number of rods was increased from 5 to 7 for each direction, starting from case 3 in order to almost double the number rods on each face of the cube, thus increasing the number of computations. This increase in number of rods did not present any processing difficulties for a standard specification computer, showing little difference in both computational time and file size.

ASCII STL files were used because CATIA V5R16 does not allow the user either to select the parameters used to generate STL files, or the file format, and therefore the standard settings had to be used (CATIA V5R16 has a dedicated module for advanced STL manipulation, which was not available for this project). Although ASCII STL format requires larger space to store the same data (in some cases up to 50% more), it was used in this chapter as the file sizes involved did not present any problem or difficulties for standard specification computers.

The purpose of each case study can be summarised as follows:

- Case 1 → testing the automated design of a basic rod structure.
- Case 2 → testing the automated design of a rod structure with different size and shape.
- Cases 3 and 4 → testing the automated design of more complex linear rod networks, with different size, shape and cross-sections.
- Case 5 → testing the automated design of a basic curved rods network, with different size and shape.
- Case 6 → testing the automated design of a complex curved rods network of different size and shape, with random interconnections.

The use of Boolean operations to merge the produced cubic structures with anatomical volumes was inefficient because of the large computational time required and the presence of non-manifold edges, as well as the loss of control over the final geometry of the scaffold. Therefore the methodology required further development in order to be used with anatomical volumes.

### **7.3 Automated Design on Anatomical Volumes (chapter 4)**

The experiments presented in this chapter consisted of the development of a set of routines to achieve the automated design of several networks of interconnected rods in anatomical volumes, within conventional CAD software. The approach was similar to that in the previous chapter, but focused on the integration process of rods/channel networks within irregular volumes.

The proposed anatomical volumes were chosen according to the project needs. The craniofacial implant was limited in size because it was a segment of a larger bone, and therefore less relevant than the mouse humerus sample, which represented an entire bone structure and not only a portion of it. For this reason, the basic curved network shown in case 5 was used for the craniofacial implant, while the more complex and irregular network shown in case 6 was used for the mouse humerus. Since case 6 presented fractality and random variations on all the three key parameters for bone TE scaffolds (pore size, shape and interconnectivity), the resultant ADI mouse humerus represented the most complex

geometry produced by the ADI method in this project, which could also be assessed in more detail through a comparison with the relative  $\mu$ CT sample. The mouse humerus geometry was selected due to the limited number of samples available.

Pore size ranges were set from 0.2 to 0.8 mm and from 0.2 to 0.4 mm for the first and second case study respectively. The values used in the second case study were chosen in order to assess the effects of a smaller pore size, which mainly reduced the scaffold porosity to 30.15%, well below the minimum target value of 50%. However, the use of a smaller pore size had the secondary effect of increasing the number of rods, thus producing a more complex structure that required more computational resources.

The rod paths were modified after a run-time error because that was the most effective way of solving the impossible geometrical situations incurred. The modification of the tangent values on the two cross-sections was often not sufficient to solve geometrical errors with anatomical volumes, even after a large number of attempts.

In both case studies, different values for spatial resolutions and border distances were used on each surface, in order to generate approximately uniform distributions of pores on all surfaces, and maximise their number. These settings are user defined and dependant on the particular anatomical volume adopted.

In the first case study, the connections between the two surfaces were not necessary, and if the methodology were used properly, these surfaces would not be used to produce channels. In the second case study, only the two lateral surfaces were selected because the real  $\mu$ CT bone sample presented a hollow shape at the top end in Z. That also limited the computational time and file size of the resultant ADI structure.

As in chapter 3, ASCII file format was used in this chapter as it was the default setting for CATIA V5R16, which also did not allow the user to set any parameter related to the STL geometry (for this purpose, a dedicated module, which was not available in this project, would have to be used). Although ASCII STL format requires larger space to store the same data (in some cases up to 50% more), it was used in this chapter because the file sizes involved did not present any problem or difficulties for standard specification computers.

The efficiency of the ADI methodology was related to design time and based on a comparison with estimated manual design time. The results presented in this chapter proved the efficiency of the ADI methodology, which also eliminated the need for Boolean operations, and the feasibility of the automated design of complex networks of interconnected rods of different pore size and shape, into generic anatomical volumes obtained from CT scan data. An example of a resultant theoretical implant and fit of the produced networks is shown in Fig. 7.1 and 7.2.

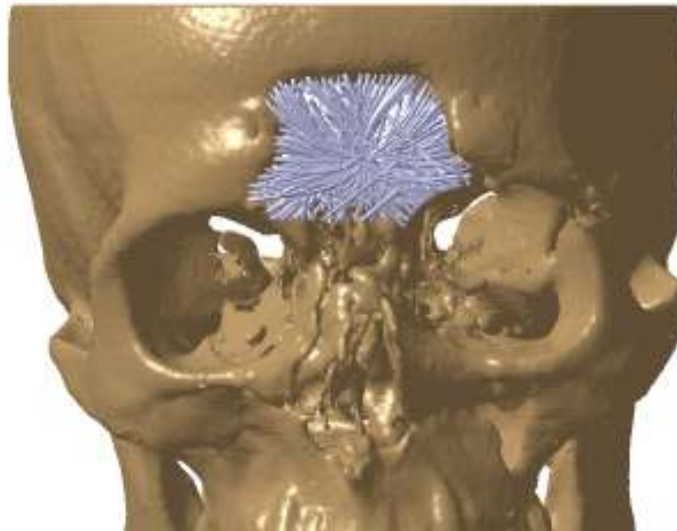


**Fig. 7.1** Fitting of ADI rod networks at an anatomical defect site.

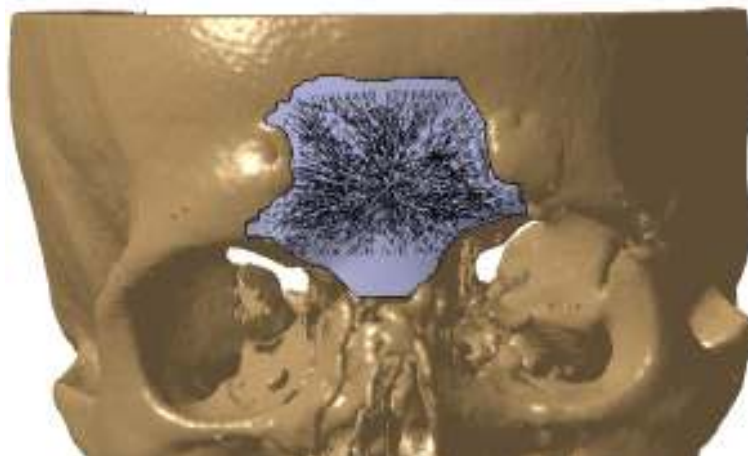


**Fig. 7.2** Fitting of ADI rod networks within a theoretical implant at the anatomical defect site.

The ADI methodology only allows for the quantification of the total porosity to characterise a scaffold geometry, while in reality the porosity of a bone varies across its sections. Therefore, if a structure is to be designed to match a given variation in porosity for a given bone or bone location, a method of ascertaining that porosity variation is required.

#### **7.4 Evaluation and Assessment of Automated Designed Structures (chapter 5)**

This chapter consisted of investigating a novel methodology of analysis for trabecular bone structures. The analysis of trabecular bone geometries involved the use of STL representations rather than the pixel data from which STL geometries are derived. That was because computerised 3D descriptions of trabecular bone allow the direct study of such architectures with no restrictive assumptions, as well as the direct quantification of any parameter pertaining to the internal architectures (Odgaard, 1997). The analysis of bitmaps would have required assumptions on bone morphology which may be difficult to verify (Odgaard, 1997).

STL representations are also more suitable to assess CAD design methodologies, as they always produce computerised descriptions of geometries. As a result, it would not be practical to compare pixel data of target structures with STL representations of the proposed CAD geometries, whose slices are mathematically described by polygons rather than pixels. In order to compare the designs produced with the required target structures, the same type of data and representation should be used. In addition, since the comparison involves the quantification of the two geometries, mathematical representations are required for both structures.

STL files of target structures from  $\mu$ CT scans were provided externally, and therefore there was no opportunity to modify the quality parameters used to generate them. In addition, they were supplied in binary format, as CT scans usually generate a very large amount of data, and binary format requires approximately 50% less space than ASCII format.

The precision and accuracy of the data produced in these analyses greatly depended on the volumetric representation of the geometry in STL format, as well as the slicing parameters. A compromise between the level of detail and correspondent file size was necessary, because file size increased enormously with small increases of the resolution.



For instance, if the  $\mu$ CT mouse humerus sample data were acquired with a pixel size of 3.4  $\mu\text{m}$ , the resultant STL file size would be more than 250 MB, which would not be practical to handle with current conventional computing facilities. By halving the resolution from 3.4 to 6.8  $\mu\text{m}$ , the smallest details were unavoidably lost, leading to a less precise but more manageable geometry (STL file of 100 MB).

When the study is focused on the macrostructure - as in the cases analysed in chapter 5 - the level of detail required is greater than 50  $\mu\text{m}$ , and therefore a more precise representation of the geometry is not necessary. In addition, according to existing literature, the smallest pore size suitable for bone regeneration is approximately 100  $\mu\text{m}$ . Therefore, for the purposes of bone TE scaffolds, smaller details are of limited interest, and a resolution of 6.8  $\mu\text{m}$  is more than acceptable.

Slicing parameters also affect the precision and accuracy of the data produced in these analyses. The parameters are controlled by the user and should be set to minimise the loss of precision. In this chapter, two slice thicknesses were used, 0.1 mm or 0.2 mm, depending on the case study. The second value was used for the mouse humerus  $\mu$ CT sample, due to the size of the volume and in particular to reduce the computational time in the Z axis. In both cases, the resultant data quality was compromised compared with the resolution of the scan data, and if the methodology were used properly a smaller value would be used. However, the proposed values were suitable for the purpose of testing and assessing the analysis methodology, as the use of bigger values does not affect the method, but only the computational time and file sizes.

ASCII code SSL slicing format was used in this chapter because the rest of the programming in this project was done using ASCII code, and because binary format would need decoding, which could also affect accuracy due to numerical conversions.

The longest slicing time was 170 seconds (for the ADI mouse humerus sample, along Z), while the shortest was 25 seconds (for the cubic  $\mu$ CT sample, along Z). In all cases, the analysis time was much longer, due to the slicing settings aimed at maintaining the highest level of accuracy from the STL geometry. The longest analysis time was 4541 seconds (for the ADI mouse humerus sample, along Z), and the shortest was 1266 seconds (for the cubic  $\mu$ CT sample, along Z).

The sizes of the files involved in these analyses were also reasonable. STL files ranged from 13.5 MB (in binary format, for the cubic  $\mu$ CT sample) to 100 MB (in binary format, for the



$\mu$ CT mouse humerus sample), while SSL files ranged from 2.14 MB (for the cubic  $\mu$ CT sample, along  $Y$ ) to 12.2 MB (for the  $\mu$ CT mouse humerus sample, along  $Z$ ).

The computational time and file sizes involved did not present processing delays or storage difficulties for standard specification computers.

Trabecular area, sliced area and number of trabeculae have been investigated as they represent the gradients of pore size, porosity and number of pores in each direction. The ratio between the area of a polyline and the area of its bounding box, which provides an estimated indication of the rod/plate topology, has also been analysed. In this work, a threshold of 0.6 was proposed for this ratio, although this value is only indicative and any other value could have been used in the routines.

The results presented in this chapter show that the ADI structure is a good approximation of the natural bone sample, and by modifying the parameters and the converging points for the channels, an even closer approximation would have been possible. However, that would require a lot of trial and error attempts, as the user would have to make arbitrary judgements on which variables to alter and by how much. That would take up a lot of the user's time, which is contrary to the overall aims of the study. Therefore, an alternative method for designing structures that match a given variation in porosity for a given bone or bone location is required.

### **7.5 Automated Bio-mimetic Design (chapter 6)**

The voxel based design method introduced in this chapter allows the mathematical description of the problem of designing prismatic structures with predefined gradients of sliced area in three orthogonal directions, in terms of linear Diophantine equations. At this stage, only prismatic volumes and sliced area were considered, as such a novel methodology would require several steps of progressive development. The value of this method will only be fully realised when the solution is achieved to combine multiple factors including porosity gradients with other factors such as Young's modulus or tensile strength. The proposed ABDI method is only in its very early stages and provides a foundation for further development. The method should theoretically work with anatomical volumes, as they would be contained and analysed within a prismatic volume (bounding box) where empty space would not affect the results.

In the discretization process, the total number of voxels has been defined by the discrete area obtained by the sum of all the real sliced area in  $X$ ,  $Y$ , or  $Z$ , because this value did not depend on the particular orientation adopted.

The proposed mathematical description of the problem does not include the condition of compatibility between the two systems of equations, and at the current stage each pair of solutions has to be tested in order to verify compatibility. The main reason for that was because this chapter focused on developing a basic mathematical model of the problem, in order to assess the feasibility and validity of the method, which provides a foundation for further development.

The number of solutions for each system of Diophantine equations has not been provided and requires more investigation. Similarly, the number of possible designs for a given pair of compatible solutions has not been computed, as at this stage the attention has focused mainly on the mathematical definition of the problem and on the algorithms to solve it, in order to produce examples of bio-mimetic geometries.

The proposed algorithm to solve the two systems obtains random solutions for each system. It is not the only possible algorithm, but it has the advantage of finding different solutions at each run, thus allowing the investigation of a large number of bio-mimetic designs.

The artificial limitation of the maximum values of all  $\alpha$  and  $\beta$  variables was proposed in order to reduce the risk of incompatibility in the solutions found by the algorithm. Although the condition of compatibility would have to be included in the mathematical formulation of the problem, such artificial limitation represented a viable solution to the problem, and allowed the design of the proposed structures without the need to re-run the algorithm and find other pairs of solutions to the two systems. This artificial limitation also affected the produced pixel patterns, as in both cases the voxels seemed to be distributed uniformly throughout the volume, with low interconnections.

The minimum zero propagation design has been proposed in order to verify the compatibility of each pair of solutions. It has also been tested in the two ADBI geometries, where it produced several unconnected vertical stripes and blocks, which clearly do not replicate the desired trabecular structure. The use of other strategies to allocate the dense voxels may have produced more interconnected geometries, resembling trabecular bone geometries. For this

purpose, it may also be necessary to introduce other parameters into the model, such as mechanical properties and number of trabeculae.

The export to CAD routine was proposed in order to assess the generation of CAD B-Rep data from the produced ABDI structures. Alternative 3D representations of such geometries from pixel/bitmap data would have been possible in the same way as CT data by using software such as Simpleware or Mimics.

### **7.5.1 Description of the ABDI geometries**

The geometries shown in section 6.3 presented some similarities. As explained in section 6.4, the produced pixel patterns are a consequence both of the design strategies adopted (which involved the minimisation of  $u$ ) and the artificial limitation of the maximum values of all  $\alpha$  and  $\beta$  variables. These settings produced pixel patterns that started out distributed seemingly at random, as might be expected, but then settled into stripes or blocks which clearly did not replicate the desired trabecular structure.

In the first design, the initial layers (from 0 to 60) were mainly composed of near vertical lines, whose thickness and distance increased when the co-ordinate  $Y$  decreased. Afterwards, up to layer 80, the lines on the left side started to present some interruptions in their continuity, while those on the right started to become more vertical. From layers 81 to 85, the interruptions started to become more significant in size and number, involving more and more elements in the middle area. Towards the low values of  $Y$ , the voxels started to agglomerate in two portions - one on the top left, and the other on the bottom left hand side of the sections. From layers 86 to 95, the lines in the middle progressively disappeared, as the voxels started to agglomerate more in the top and bottom areas. That was similar to the earlier occurrence on the left, where the two portions of dense voxels continued to grow. On the right hand side, the lines started to show central horizontal interruptions whose size increased layer after layer. By layer 98, two new portions of material had formed, again in the top and bottom ends.

Between layers 96 and 102, the 6 portions of materials (two on the left, two in the middle and two in the right) continued to grow until, towards the last layers, each group was made of small vertical lines.

In the second design, the initial layers (from 0 to 42) were composed of near vertical lines, whose thickness and distance, as in the first design, increased when the co-ordinate  $Y$  decreased. On the left side, numerous small, floating units were present. Afterwards, between layers 43 and 64, the lines on the left side started to reduce their distance, while the small floating units progressively extended towards the centre of the sections. Some lines in the middle also started to show small interruptions. Between layers 65 and 78, the lines on the left side were fragmented into small floating voxels, some of which agglomerated on the top left to form a compact group. Between layers 79 and 86, the lines in the middle also started to fragment, while the floating units on the left tended to agglomerate in other groups. Between layers 87 and 90, all the lines in the middle were fragmented into small floating units, which tended to form two areas, one at the top and one at the bottom. The lines on the right side also started to show several central interruptions of different size. Finally, between layers 91 and 102, two groups of small vertical lines, of similar distance, size and length, were formed. Those two groups extended across the whole length of the sections (across  $X$ ), one located on the top side, and one on the bottom.

The fact that two geometries were presented in this chapter means that both systems (6.5) and (6.9) have at least two solutions each. These resulted in four compatible solutions by setting an 'artificial' maximum value for the terms  $\alpha$  and  $\beta$ , smaller than  $M$  and  $N$ . As a result, it was proven that at least two distinct geometries present the same gradients of sliced area as those found in the  $\mu$ CT sample analysed, although it is likely that a large number of other structures may present the same characteristics. In this case, other engineering properties would have to be introduced into the model in order to fully describe trabecular bone geometries from an engineering point of view.

## CHAPTER 8

### - CONCLUSIONS -

- This work has shown the use of conventional computing facilities and CAD software in developing an automated, efficient and flexible design methodology of complex and irregular rod networks in regular (cubic) or anatomical volumes. This design methodology allows the CAD design of complex and irregular rod networks in minutes instead of the hours or even days that would be required by manual design for individual structures. The more irregular the geometry, the greater the time saved. In addition, the use of conventional CAD and computing facilities enhances applicability, flexibility and further developments of the methodology.
- This work has established a list of requirements that CAD software need to satisfy in order achieve such methodology, so that any CAD software other than the one used in this work can achieve the same automated design.
- This work has established a list of key parameters to define the geometry of rod networks into either regular (cubic) or anatomical volumes. Based on such representations, new parameters can be introduced in order to increase the complexity of the network, and parametric studies can be carried out in order to find the most sensitive parameters depending on the application.
- It has been shown that such key parameters can be varied in order to achieve irregularity and complexity in rod networks. Random variations have been proposed in order to increase irregularities in the network and allow the algorithms to design different structures at each run.

- 
- The experimental work has demonstrated how automation can hugely speed up the design of complex rod networks, compared with the estimated figures for manual design. Experimental geometries exhibiting a progressive increase in geometric variables and complexity, and the integration of the most irregular networks into anatomical volumes have demonstrated the efficiency and flexibility of the ADI methodology. That will allow the rapid and automated CAD generation of complex and irregular geometries for various applications other than TE.
  - An efficient alternative to Boolean operations for integrating internal architectures into anatomical volumes, which automatically detect and corrects non-manifold geometries, has been produced. This alternative method has the further advantage of allowing full control over the network geometry, particularly for the cross sections of each rod. This will allow the rapid and automated CAD design of complex and irregular architectures into any volume, independent of its shape.
  - An efficient alternative to Boolean operations for designing scaffold architecture and complementary geometry has been shown. This will allow the automated and efficient design of both scaffold architecture and theoretical shape of the regenerated bone. Although the scaffold structure represents the target geometry to be designed, the complementary geometry provides a better visualisation and assessment of the complexity of the internal network.
  - This work has highlighted the importance of quantitative data for driving the development of new design methodologies and assessing existing design methodologies. As a consequence, it has shown that detailed quantitative descriptions of target geometries are necessary, as the limited availability of such data can compromise the validity of any design method, irrespective of automation and efficiency. When detailed information is available, it can be used to define suitable design methods. This will contribute to the development of new forms of bio-mimetic design.
  - It has been shown that new quantitative data on target geometries can be acquired by using a novel analysis methodology based on the analysis of slices produced from 3D

volumetric representations (STL). All geometries available in that format, either from CAD or reverse engineering, can be analysed and assessed by using this method. This is particularly relevant for those applications where the design of structures that mimic certain properties of a target geometry is required.

- This work has established a list of key properties for the characterisation of trabecular bone structures represented in 3D volumetric (STL) format. These properties may be consistently analysed, and could become an alternative to those parameters typically analysed in traditional bone histomorphometry, which have the disadvantage of being based on assumptions that should be carefully verified before interpreting data (Odgaard, 1997). According to this author, the real problem related to 3D representations of trabecular bone structures is that of defining the properties to be measured, due to the high variability and irregularities of such geometries. The suggested properties may constitute a set of parameters used to better characterise bone structures.
- It has been shown that the ADI methodology can design rod networks on anatomical volumes with similar geometrical properties and distributions to those found in trabecular bone structures. This means that although the ADI methodology did not produce precisely the same geometrical characteristics as the  $\mu$ CT mouse humerus, it was capable of reproducing similar properties. Therefore, this method may be used in those applications that require the design of structures with similar properties (although not exactly the same) as those found in target geometries. Further refinement of the methodology may be possible so as to produce even better approximations of target structures, based on a trial and error approach.
- The systematic use of this analysis methodology to investigate the proposed properties (and eventually other characteristics) can make a significant contribution to the understanding and assessment of trabecular bone structures, and of any irregular and complex structure that can be represented in 3D volumetric (STL) format. This could also include investigations into how bone diseases affect trabecular bone structures.

- A new bio-mimetic automated design methodology has been defined, based on the allocation of dense voxels in discrete prismatic volumes. The voxels are allocated so that the resultant structures present the same gradients of sliced area (in three orthogonal directions) as those dictated by target geometries, such as prismatic  $\mu$ CT samples. This method can be used to design prismatic structures with predefined gradients of sliced area (i.e. porosity) in three orthogonal directions, as well as to investigate how voxels are allocated in natural structures and thus the natural topology from an engineering point of view.
- It has been shown that sliced areas in three orthogonal directions can be converted into requirements in terms of numbers of (cubic) voxels of a given size. This will allow the discretisation of the porosity distributions on all target geometries that can be represented in STL format, which ultimately defines the requirements for the ABDI method. The proposed discretisation method reduces the differences during the real to integer conversions, by randomly spreading the differences in each direction, thus allowing a very close approximation of the real values.
- In this work, a mathematical description of the problem of designing structures with specified gradients of sliced areas in three orthogonal directions, along with an algorithm to solve it, have been developed. This model has shown that the bio-mimetic allocation of dense voxels can be described by using two systems of Diophantine equations, which provide a foundation for investigating how the material is distributed in natural structures and which engineering properties are necessary to fully describe trabecular bone geometries.
- The ABDI methodology has shown that several geometries can present the same gradients of sliced area in three orthogonal directions, apart from the target geometry (trabecular bone structure). Although the number of such geometries has not been computed, the estimations show a very large number of possible topologies, suggesting that other engineering properties are necessary to fully describe trabecular bone geometries. These properties may include the trabecular area, the number of trabeculae and Young's modulus (or tensile strength), and they would have to be



introduced as constraints in the systems of equations, to further reduce the number of solutions. Ideally, the systems should be constrained to admit only one solution - the trabecular bone structure analysed - as the potential application of the method would be the identification of the set of engineering properties necessary to fully describe trabecular bone geometries, in order to understand them from an engineering point of view. The simple use of trabecular bone geometries from  $\mu$ CT scans for several applications would not provide any information on their engineering properties, while their full characterisation would allow engineers to design sophisticated structures that possess combinations of those properties, as required by a particular application (for instance, Young's modulus and gradients of sliced area, or gradients of sliced area and number of trabeculae).

## CHAPTER 9

### - RECOMMENDATIONS FOR FURTHER WORK-

- Parametric studies on ADI case 5 and case 6 samples with the purpose of matching the properties of the cubic  $\mu$ CT sample analysed. This would assess the best parameter configurations for the two networks, and investigate how well such cases can match the properties of the cubic  $\mu$ CT sample analysed.
- Implementation of new cases for cubic rod networks, with relative parametric studies and comparisons with the cubic  $\mu$ CT sample analysed. The development of new networks would further extend the level of complexity achieved in this work, with particular focus on pore size, shape and interconnectivity. It would also allow the assessment of the network configuration that best approximates the properties of the cubic  $\mu$ CT sample analysed.
- Parametric studies on ADI mouse humerus geometry with the purpose of achieving an even better approximation of the  $\mu$ CT mouse humerus sample analysed in this work. This would allow an assessment of how well the case 6 network can approximate the properties of a whole bone sample.
- Extension of the ADI methodology to other types of trabecular structures (Type IIb, IIc, IIIa, IIIb and IIIc, according to the classification proposed by Singh, 1978), on both cubic and anatomical volumes. This would be particularly useful in order to model other forms of tissue, which would be represented in the ADI method by different geometrical elements (plates of different size and shape), including combinations with existing rod networks. That would allow the automated generation of complex and irregular structures other than in the form of rod networks.

- Analysis of different  $\mu$ CT samples of both cubic and anatomical volumes. This would provide additional data on target geometries, allowing a more general investigation of their properties and how those change from sample to sample.
- Comparisons between the newly analysed  $\mu$ CT samples and designed structures, in order to verify whether cubic and anatomical ADI geometries can better approximate samples other than those proposed in this work. This would also assess the general validity of the method.
- Investigations into other forms of variation for parameters, other than random. Random variations have the advantage of producing different geometries at each run, however they might not represent the best approximation of natural samples. These investigations would allow the verification of whether different variations of parameters can provide a better approximation of the  $\mu$ CT samples.
- Definition of new properties in the analysis methodology developed in chapter 5, for instance to quantify the interconnectivity of trabeculae. These properties would further extend the level of knowledge about target structures and dictate new quantitative requirements for bio-mimetic design methods.
- Investigation of the exact number of solutions for systems (6.5) and (6.9), as well as for the design implementations. This investigation would assess how many structures with predefined sliced areas in three orthogonal directions exist. It is, therefore, particularly relevant for engineering applications, as these structures may be used to design porous devices with controlled gradients of porosity in three directions, for medical and industrial applications.
- Introduction of the ‘condition of compatibility’ for the solutions of systems (6.5) and (6.9) in terms of constraint into these systems. In the current model, a pair of solutions is initially computed by the resolution algorithm, and subsequently their compatibility is verified. If they are not compatible, another pair of solutions is computed and the test repeated. This further development would provide a more

---

efficient way of finding compatible solutions and improving the existing mathematical model.

- Investigations into different design strategies to reduce the number of floating voxels in the ABDI designs. The design strategies adopted produced structures with unconnected stripes and blocks, which did not replicate the desired trabecular geometry. Therefore, new design strategies would have to be adopted in order to produce interconnected structures that are more similar to trabecular geometries. That would also increase the range of applications for the ABDI structures.
- Introduction of trabecular area, number of trabeculae, mechanical and newly defined properties into the mathematical formulation of the ABDI methodology. This would allow the restriction of the number of solutions to the two systems of Diophantine equations, and better identify the set of engineering properties necessary to fully describe trabecular bone geometries, in order to understand them from an engineering point of view.
- Extension of the ABDI methodology to anatomical volumes. This would provide an general version of the method to include any volume, independent of its size and shape, thus overcoming the current limit of prismatic shapes.
- Investigation into the manufacturability and mechanical properties of ADI and ABDI geometries. These investigations would be essential for those applications that require physical samples of the produced structures.
- Biological assessment of the ADI and ABDI structures. These investigations would be essential in the context of TE scaffolds, and would include both *in vitro* and *in vivo* tests. The level of regenerated tissue, its depth of penetration into the scaffolds structure and its mechanical properties, would ultimately dictate the suitability of the proposed geometries for the purposes of TE.

## PUBLICATIONS

### Journal Papers

- Published:

Ramin, E., and Harris, R. A. 2009. Advanced computer-aided design for bone tissue-engineering scaffolds. *Proc. IMechE, Part H: J. Engineering in Medicine*, 223 (3): 289-301.

- Submitted

Ramin, E., and Harris, R. A. 2010. Automated Design Integration of Computer Aided Designed Bone Tissue Engineering Scaffolds on Anatomical Volumes. *Submitted to Proc. IMechE, Part H: J. Engineering in Medicine on 26<sup>th</sup> February 2010.*

### Conference Papers:

Ramin, E., and Harris, R. A. 2007. Automated Design of Tissue Engineering Scaffolds by Advanced CAD. *Proceedings of 18th Solid Freeform Fabrication Symposium, Austin, Texas.*

### Conference Presentations:

Ramin, E., and Harris, R. A. 2008. Optimised Bio-mimetic Design of Ingrowth Scaffolds in Cranio-Facial Implants. *3rd International Conference of Advanced Digital Technology in Head and Neck Reconstruction, Cardiff, UK.*

Ramin, E., and Harris, R. A. 2006. Automated Design of Bio-Mimetic Structures. *Powder Technology in the Medical Device Industry, A Powdermatrix/MediTech Joint Meeting, Nottingham, UK.*

---

## References

- Ahn, S. H., M. Montero, D. Odell, S. Roundy, and P. K. Wright. 2002. Anisotropic material properties of fused deposition modelling ABS. *Rapid Prototyping Journal*, 8 (4): 248-257.
- Anderl, R. and R. Mendgen. 1996. Modelling with constraints: theoretical foundation and application. *Computer-Aided Design*, 28 (3): 155-168.
- Ault, H. K. 1999. 3-D geometric modelling for the 21st century. *Engineering Design Graphics Journal*, 63(2).
- Bartolo, P. J. S., H. Almeida, and T. Laoui. 2009. Rapid prototyping and manufacturing for tissue engineering scaffolds. *International Journal of Computer Applications in Technology*, 36 (1): 1-9.
- Bertoline, B. R., and E. N. Wiebe. 2002. Technical Graphics Communication, 3<sup>rd</sup> edition. *McGraw-Hill*: 318-319.
- Bezier, P. 1966. Definition numerique des courbes et surfaces I. *Automatisme*, XI: 625-623.
- Bezier, P. 1967. Definition numerique des courbes et surfaces II. *Automatisme*, XII: 17-21.
- Bhatia, S. N., and C. S. Chen. 1999. Tissue engineering at the micro-scale. *Biomedical Micro-devices*, 2 (2): 131-144.
- Bibb, R. and G. Sisias. 2002. Bone structure models using stereolithography: a technical note. *Rapid Prototyping Journal*, 8 (1): 25-29.
- Bibb, R., D. Eggbeer, R. Williams, and A. Woodward. 2006. Trial fitting of a removable partial denture framework made using computer-aided design and rapid prototyping techniques. *Proc. IMechE, Part H: J. Engineering in Medicine*, 220: 793-797

- 
- Bose, S., J. Darsell, H. L. Hosick, L. Yang, D. K. Sarkar, and A. Bandyopadhyay. 2002. Processing and characterization of porous alumina scaffolds. *Journal of Materials Science: Materials in Medicine*, 13 (1): 23-28.
- Bruder, S. P., K. H. Kraus, V. M. Goldberg, and S. Kadiyala. 1998. Critical-sized canine segmental femoral defects are healed by autologous mesenchymal stem cell therapy. *Transactions of the Annual Meeting of the Orthopaedic Research Society*, 44: 147.
- Buckley, C. T., and K. U. O'Kelly. Topics in Bio-Mechanical Engineering. *P.J. Prendergast, P.E. McHugh*. ISBN 0-9548583-0-1: 147-166.
- Capito, R. M., and M. Spector. 2003. Scaffold-based articular cartilage repair. *IEEE Engineering in Medicine and Biology Magazine*, 22 (5): 42.
- Chang, B. S., I. C. Lee, K. S. Hong, H. J. Youn, H. S. Ryu, S. S. Chung, and K. W. Park. 2000. Osteoconduction at porous hydroxyapatite with various pore configurations. *Biomaterials*, 21 (12): 1291-1298.
- Chappard, D., M. F. Baslé, E. Legrand, and M. Audran. 2008. Trabecular bone microarchitecture: A review. *Morphologie*, 92 (299): 162-170.
- Charriere, E., J. Lemaitre, and P. Zysset. 2003. Hydroxyapatite cement scaffolds with controlled macro-porosity: Fabrication protocol and mechanical properties. *Biomaterials*, 24 (5): 809-817.
- Chu, T. M. G., D. G. Horton, S. J. Hollister, S. E. Feinberg, and J. W. Halloran. 2002. Mechanical and in vivo performance of hydroxyapatite implants with controlled architectures. *Biomaterials*, 23 (5): 1283-1293.
- Chu, T. M. G., J. W. Halloran, S. J. Hollister, and S. E. Feinberg. 2001. Hydroxyapatite implants with designed internal architecture. *Journal of Materials Science: Materials in Medicine*, 12 (6): 471-478.
-

- Chua, C. K., K. F. Leong, C. M. Cheah, and S. W. Chua. 2003a. Development of a tissue engineering scaffold structure library for rapid prototyping. Investigation and classification. *International Journal of Advanced Manufacturing Technology*, 21 (4): 291-301.
- Chua, C. K., K. F. Leong, C. M. Cheah, and S. W. Chua. 2003b. Development of a tissue engineering scaffold structure library for rapid prototyping. Parametric library and assembly program. *International Journal of Advanced Manufacturing Technology*, 21 (4): 302-12.
- Chua C. K., K. F. Leong, and C. S. Lim. 2003. Rapid Prototyping: Principles and Applications in Manufacturing, second edition. *World Scientific Publishing*. ISBN-13: 9789812381200
- Colton, C. K. 1995. Implantable biohybrid artificial organs. *Cell Transplantation*, 4 (4).
- Coons, S. 1968. Rational bicubic surface patches. *Technical report, MIT, Project MAC*.
- Cooper, K. G. 2001. Rapid prototyping technology: selection and application. *CRC press*: 46.
- Cox, M. 1972. The numerical evaluation of B-splines. *J Inst. Maths. Applics.*, 10: 134-149.
- Cutkosky, M. R., J. M. Tenenbaum, and D. Muller. 1988. Features in process based design. *ASME Computers in engineering (CIE) conference, San Francisco, CA*: 557-62.
- Das S., and S. J. Hollister. 2003. Tissue Engineering Scaffolds. *Encyclopedia of Materials: Science and Technology*. ISBN 0-08-043152-6: 1-7.
- Das, S., S. J. Hollister, C. Flanagan, A. Adewunmi, K. Bark, C. Chen, K. Ramaswamy, D. Rose, and E. Widjaja. 2003. Freeform fabrication of Nylon-6 tissue engineering scaffolds. *Rapid Prototyping Journal*, 9 (1): 43-49
- De Boor, C. 1978. *A Practical Guide to Splines*. *Springer-Verlag*: 113–114.



- 
- De Boor, C. 1972. On calculating with B-splines. *J. Approx. Theory* 6: 50–62.
- De Casteljau, P. 1963. Courbes et surfaces à poles. *Technical Report, A. Citroen, Paris*.
- Dimas, E., and D. Briassoulis. 1999. 3D geometric modelling based in NURBS: a review. *Advances in engineering software*, 30: 741-751.
- Dobson C. A., G. Sias, R. Phillips, M. J. Fagan, and C. M. Langton. 2006. Three dimensional stereolithography models of cancellous bone structures from  $\mu$ CT data: testing and validation of finite element results. *Proc. IMechE, Part H: J. Engineering in Medicine*, 220.
- Downey, P. A., and M. I. Siegel. 2006. Perspectives - bone biology and the clinical implications for osteoporosis. *Physical Therapy*, 86 (1).
- Eggbeer, D., R. Bibb, and R. Williams. 2005. The computer-aided design and rapid prototyping fabrication of removable partial denture frameworks. *Proc. IMechE, Part H: J. Engineering in Medicine*, 219: 195–202.
- Eggbeer, D., P. L. Evans, and R. Bibb. 2006. A pilot study in the application of texture relief for digitally designed facial prostheses. *Proc. IMechE, Part H: J. Engineering in Medicine*, 220: 705-714.
- Farin, G. 1992, From Conics to NURBS: a tutorial and survey. *IEEE Computer Graphics and Applications*, 12 (5): 78-86.
- Foley, J. D., S. K. Feiner, and J. F. Hughes. 1997. Computer Graphics: Principles and Practice. *Addison-Wesley*: 533-561.
- Forrest, A., R. 1968. Curves and surfaces for computer-aided design. *Ph.D thesis, Cambridge*.

- 
- Fuh, J. Y. H., L. Lu, C. C. Tan, Z. X. Shen, and S. Chew. 1999. Curing characteristics of acrylic photopolymer used in stereolithography process. *Rapid Prototyping Journal*, 5 (1).
- Garrahan, N. J., Mellish, R. W. E., Vedi, S., and J. E. Compston, 1987. Measurement of mean trabecular plate thickness by a new computerized method. *Bone*, 8: 227-230.
- Gebhardt, A. 2003. Rapid Prototyping. *Hanser Gardner Publications*. ISBN-13: 9781569902813
- Gomes, A. J. P., and J. C. G. Teixeira. 1991. Form feature modelling in a hybrid CSG/BRep scheme. *Computers & Graphics*, 15 (2): 217-229.
- Gordon, W. J., and R. F. Riesenfeld. 1974. Bernstein-Bézier Methods for the computer-aided design of free-form curves and surfaces. *Journal of the ACM*, 21 (2): 293-310.
- Hague, R., G. D'Costa, and P. M. Dickens. 2001. Structural design and resin drainage characteristics of QuickCast 2.0. *Rapid Prototyping Journal*, 7 (2): 66-73.
- Hieu, L. C., E. Bohez, J. Vander Sloten, H. N. Phien, E. Vatcharaporn, P. H. Binh, P. V. An, and P. Oris. 2003. Design for medical rapid prototyping of cranioplasty implants. *Rapid Prototyping Journal*, 9 (3): 175-186.
- Hoffmann, C. M., and R. J. Arinyo. 1998. On user-defined features. *Computer-Aided Design*, 30 (5): 321-332.
- Hoffmann, C. M. and R. J. Arinyo. 2002. Parametric Modelling. *Handbook of Computer-Aided Geometric Design*: 519-541.
- Hollister, S. J., C.Y. Lin, E. Saito, R. D. Schek, J. M. Taboas, and J. M. Williams. 2005. Engineering craniofacial scaffolds. *Orthodontics & Craniofacial Research*, 8 (3): 162-173.
-

- Hollister, S. J., R.D. Maddox, and J. M. Taboas. 2002. Optimal design and fabrication of scaffolds to mimic tissue properties and satisfy biological constraints. *Biomaterials*, 23: 4095-4103.
- Hulbert S. F., F. A. Young, R. S. Mathews, J. J. Klawitter, C. D. Talbert, and F. H. Stelling. 1970. Potential of ceramic materials as permanently implantable skeletal prostheses. *Journal of Biomedical Material Research*, 4 (3):433-56.
- Hutmacher, D. W., T. Schantz, I. Zein, K. W. Ng, S. H. Teoh, and K. C. Tan. 2001. Mechanical properties and cell cultural response of polycaprolactone scaffolds designed and fabricated via fused deposition modelling. *Journal of Biomedical Materials Research*, 55 (2): 203.
- Hutmacher, D. W., M. Sittinger and M. V. Risbud. 2004. Scaffold-based tissue engineering: rationale for computer-aided design and solid free-form fabrication systems. *Trends in biotechnology*, 22 (7): 354-62.
- Ishaug-Riley, S. L., G. M. Crane, A. Gurlek, M. J. Miller, A. W. Yasko, M. J. Yaszemski, and A. G. Mikos. 1997. Ectopic bone formation by marrow stromal osteoblast transplantation using poly (DL-lactic-co-glycolic acid) foams implanted into the rat mesentery. *Journal of Biomedical Materials Research*, 36 (1): 1.
- Itala, A. I., H. O. Ylanen, C. Ekholm, K. H. Karlsson, and H. T. Aro. 2001. Pore diameter of more than 100 micron is not requisite for bone ingrowth in rabbits. *Journal of Biomedical Materials Research*, 58: 679-683.
- Jaecques, S. V. N., L. Muraru, C. Van Lierde, E. De Smet, H. Van Oosterywck, M. Wevers, I. Naert, and J. Vander Sloten. 2004. In vivo micro-CT-based FE models of guinea pigs with titanium implants: an STL-based approach. *International Congress Series*, 1268: 579-583.
- Jin, Q. M., H. Takita, T. Kohgo, K. Atsumi, H. Itoh, and Y. Kuboki. 2000. Erratum - effects of geometry of hydroxyapatite as a cell substratum in BMP-induced ectopic bone formation. *Journal of Biomedical Materials Research*, 52 (4): 841.

- 
- Jinnai, H., H. Watashiba, T. Kajihara, Y. Nishikawa, M. Takahashi, and M. Ito. 2002. Surface Curvatures of Trabecular Bone Micro-architecture. *Bone*, 30 (1): 191-194.
- Johnson, T. 1963. Sketchpad III: a computer program for drawing in three dimensions. *Proceedings of the Spring Joint Computer Conference, Detroit, Michigan, Spartan Books*, 23: 348.
- Karageorgiou, V., and D. Kaplan. 2005. Porosity of 3D biomaterial scaffolds and osteogenesis. *Biomaterials*, 26 (27): 5474-5491.
- Knapp, L. 1979. A design scheme using coons surfaces with non-uniform basis B-spline curves. *Ph.D thesis, Syracuse University*.
- Kohn, D. H., M. Sarmadi, J. I. Helman, and P. H. Krebsbach. 2002. Effects of pH on human bone marrow stromal cells in vitro: Implications for tissue engineering of bone. *Journal of Biomedical Materials Research*, 60 (2): 292.
- Kruyt, M. C., J. D. de Bruijn, C. E. Wilson, F. C. Oner, C. A. van Blitterswijk, and A. J. Verbout. 2003. Viable osteogenic cells are obligatory for tissue-engineered ectopic bone formation in goats. *Tissue Engineering*, 9(2): 327-36.
- Kruth, J. P. 1991. Material in-process manufacturing by rapid prototyping technologies. *CIRP Annals*, 2: 603-614.
- Kuboki, Y., Q. Jin, M. Kikuchi, J. Mamood, and H. Takita. 2002. Geometry of artificial ECM: Sizes of pores controlling phenotype expression in BMP-induced osteogenesis and chondrogenesis. *Connective Tissue Research*, 43 (2-3): 529-3.
- Kuboki, Y., Q. Jin, and H. Takita. 2001. Delivery systems for the BMPs - Scientific Article - Geometry of carriers controlling phenotypic expression in BMP-induced osteogenesis and chondrogenesis. *Journal of Bone and Joint Surgery*, 83 (1): 105.
-

- Lal, P., and W. Sun. 2004. Computer modeling approach for microsphere-packed bone scaffold. *Computer-Aided Design*, 36 (5): 487.
- Langer, R., and J. P. Vacanti. 1993. Tissue engineering. *Science*, 260: 920-926.
- Lin, C. Y., N. Kikuchi, and S. J. Hollister. 2004. A novel method for biomaterial scaffold internal architecture design to match bone elastic properties with desired porosity. *Journal of Biomechanics*, 37 (5): 623-636.
- Mallepre, T., and D. Bergers. 2009. Advanced Pre-Surgery Planning by Animated Biomodels in Virtual Reality. *13th International Conference on Biomedical Engineering*, 23: 399-401.
- Manjubala, I., A. Woesz, C. Pilz, M. Rumpler, N. Fratzl-Zelman, P. Roschger, J. Stampfl, and P. Fratzl. 2005. Biomimetic mineral-organic composite scaffolds with controlled internal architecture. *Journal of Materials Science, Materials in Medicine*, 16 (12): 1111-1119.
- Marks, S. C., and D. C. Hermey. 1996. The structure and development of bone: in Bilezikian, J. P., L. G. Raisz, and G. A. Rodan, eds. *Principles of Bone Biology*. Calif: Academic Press, San Francisco: 3-14.
- Miller, Z. and M. B. Fuchs. 2005. Effect of trabecular curvature on the stiffness of trabecular bone, *Journal of Biomechanics*, 38: 1855-1864.
- Mironov, V., T. Boland, T. Trusk, G. Forgacs, and R. R. Markwald. 2003. Organ printing: Computer-aided jet-based 3D tissue engineering. *Trends in Biotechnology*, 21 (4): 157.
- Monedero, J. 2000. Parametric design: a review and some experiences. *Automation in Construction*, 9 (4): 369-377.
- Mooney, D. J., D. F. Baldwin, N. P. Suh, and J. P. Vacanti. 1996. Novel approach to fabricate porous sponges of poly (D,L-lactic-co-glycolic acid) without the use of organic solvents. *Biomaterials*, 17 (14): 1417.

- 
- Mortenson, M. E. 1999. Mathematics for Computer Graphics Applications. *Industrial Press*: 226-240.
- Naing, M. W., C. K. Chua, K. F. Leong, and Y. Wang. 2005. Fabrication of customised scaffolds using computer-aided design and rapid prototyping techniques. *Rapid Prototyping Journal*, 11 (4): 249.
- Nazarian, A., B. D. Snyder, D. Zurakowski, and R. Müller. 2008. Quantitative micro-computed tomography: a non-invasive method to assess equivalent bone mineral density. *Bone*, 43 (2): 302-311.
- Odgaard, A. 1997. Three-dimensional methods for quantification of cancellous bone architecture, *Bone*, 20 (4): 315-328.
- Ono, I., T. Ohura, E. Narumi, K. Kawashima, I. Matsuno, S. Nakamura, N. Ohhata, Y. Uchiyama, Y. Watanabe, F. Tanaka, and T. Kishinami. 1992. Three-dimensional analysis of craniofacial bones using three-dimensional computer tomography. *Journal of Cranio-Maxillofacial Surgery*, 20 (2): 49-60.
- Parfitt, A. M., C. H. E. Mathews, A. R. Villaneuva, M. Kleerekoper, B. Frame, and D. S. Rao. 1983. Relationships between surface, volume, and thickness of iliac trabecular bone in aging and in osteoporosis. *J Clin Invest*, 72: 1396-1409.
- Parsons, J. R. 1998. Cartilage. In: Black, J., and Hastings, G., eds. Handbook of Biomaterials Properties. *Chapman & Hall*. ISBN 0412603306: 40-46.
- Piegl, L. A., and W. Tiller. 1987. Curve and surface constructions using rational B-splines. *Computer Aided Design*, 19(9): 485-98.
- Piegl, L. A., and W. Tiller. 1997. The NURBS book. *Springer-Verlag, New York Second Edition*. ISBN 3-540-61545-8.
-

- 
- Pham, D. T., and S. S. Dimov. 2003. Rapid prototyping and rapid tooling-the key enablers for rapid manufacturing. *Proceedings of the IMECH E Part C Journal of Mechanical Engineering Science*, 217 (1): 1-23.
- Pham, D. T., and R. S. Gault. 1998. A comparison of rapid prototyping technologies. *International Journal of Machine Tools and Manufacture*, 38 (10-11): 1257-87.
- Pratt, M. J. 1988. Synthesis of an optimal approach to form feature modelling. *ASME Computers in engineering conference (CIE), San Francisco, CA*: 263-74.
- Pratt, M. J. 2001. Solid Modeling. *Encyclopaedia of Library and Information Science*, 69: 325-364.
- Rajpurohit, R., C. J. Koch, Z. Tao, C. M. Teixeira, and I. M. Shapiro. 1996. Adaptation of chondrocytes to low oxygen tension: Relationship between hypoxia and cellular metabolism. *Journal of Cellular Physiology*, 168 (2): 424-432.
- Rho, J. Y., L. Kuhn-Spearing, and P. Zioupos. 1998. Mechanical properties and the hierarchical structure of bone. *Medical Engineering & Physics*, 20 (2): 92.
- Riesenfeld, R. 1973. Applications of B-spline approximation to geometric problems of CAD. *Ph.D thesis, Syracuse University*.
- Ritman, E. L. 2004. Micro-Computed Tomography - current status and developments. *Annual Review of Biomedical Engineering*, 6: 185-208.
- Rogers, D. F. 2001. An introduction to NURBS. *Academic Press, San Diego*: 130.
- Roller, D. F. 1989. Design by features: an approach to high level shape manipulations. *Computers in Industry*, 12 (3): 185-191.
- Roller, D. F. 1991. An approach to computer-aided parametric design. *Computer-Aided Design*, 23 (5): 385-391.
-

- 
- Rooney, J., and P. Steadman. 1993. Principles of computer-aided design, *UCL Press*.
- Rose, F. R., L. A. Cyster, D. M. Grant, C. A. Scotchford, S. M. Howdle, and K. M. Shakesheff. 2004. In vitro assessment of cell penetration into porous hydroxyapatite scaffolds with a central aligned channel. *Biomaterials* 25: 5507-5514.
- Rosen, D. W., J. R. Dixon, and X. Dong. 1991. A methodology for conversions of feature based representations. *International Conference on Design Theory and Methodology DTM, ASME*, 31: 45-51.
- Roy, T. D., J. L. Simon, J. L. Ricci, E. D. Rekow, V. P. Thompson, and J. R. Parsons. 2003. Performance of degradable composite bone repair products made via three-dimensional fabrication techniques. *Journal of Biomedical Materials Research Part A*, 66 (2): 283-291.
- Ryan, G., A. Pandit, and D. P. Apatsidis. 2006. Fabrication methods of porous metals for use in orthopaedic applications. *Biomaterials*, 27 (13): 2651-2670.
- Sachlos, E., and J. T. Czernuszka. 2003. Making Tissue Engineering scaffolds work. Review on the application of Solid Freeform Fabrication technology to the production of Tissue Engineering scaffolds. *European Cells and Materials*, 5: 29-40.
- Salomons, O. W., F. J. A. M. Van Houten, and H. J. J. Kals. 1993. Review of research in feature-based design. *Journal of Manufacturing Systems*, 12 (2): 113-132.
- Sang, H. L., and L. Kunwoo. 2001. Partial entity structure: a compact non-manifold boundary representation based on partial topological entities, *ACM Symposium on Solid and Physical Modelling, proceedings of the sixth ACM symposium on solid modelling and applications*: 159-170.
- Savchenko, V., and A. Pasko. 2002. Shape Modeling. *Encyclopaedia of Computer Science and Technology*, 45 (30): 311-346.
-



- Schaaf, H., P. Streckbein, M. Obert, B. Goertz, P. Christophis, H. P. Howaldt, and H. Traupe. 2008. High resolution imaging of craniofacial bone specimens by flat-panel volumetric computed tomography. *Journal of Cranio-Maxillofacial Surgery*, 36 (4): 234-238.
- Schoenberg, J. 1946. Contributions to the problem of approximation of equidistant data by analytic functions. *Quart. Appl. Math.*, 4: 45–99 and 112–141.
- Sekou S., L. Dichen, L. Bingheng, L. Yanpu, G. Zhenyu, and L. Yaxiong. 2004. Design and fabrication of custom mandible titanium tray based on rapid prototyping. *Medical Engineering & Physics*, 26 (8): 671-676.
- Selimovic, I. 2006. Improved algorithms for the projection of points on NURBS curves and surfaces. *Computer Aided Geometric Design*, 23 (5): 439-445.
- Shah, J. J., and M. T. Rogers. 1988. Expert form feature modelling shell. *Computer Aided Design*, 20 (9): 515-24.
- Sharma, B., and J. H. Elisseeff. 2004. Engineering structurally organized cartilage and bone tissues. *Annals of Biomedical Engineering*, 32 (1): 148.
- Sheu, L., and J. T. Lin. 1993. Representation scheme for defining and operating form features, *Computer-Aided Design*, 25 (6): 333-347.
- Singh, I. 1978. The architecture of cancellous bone. *Journal of Anatomy*, 127 (2): 305–310.
- Sisias, G. R., C. A. Phillips, M. F. Dobson, M. J. Fagan, and C. M. Langton. 2002. Algorithms for accurate rapid prototyping replication of cancellous bone voxel maps. *Rapid Prototyping Journal*, 8 (1): 6-24.
- Sommerfeldt, D., and C. Rubin. 2001. Biology of bone and how it orchestrates the form and function of the skeleton, *European Spine Journal*, 10 (0): 86 - 95.

- Sriram, V., K. Wood, D. Bourell, and J. J. Beaman. 2003. Selective laser sintering of DuraFormTM polyamide with small-scale features. *Solid Freeform Fabrication Proceedings*: 585-595.
- Starly, B., W. Lau, T. Bradbury, and W. Sun. 2006. Internal architecture design and freeform fabrication of tissue replacement structures. *Computer Aided Design*, 38 (2): 115-124.
- Starly, B., J. Nam, W. Lau, and W. Sun. 2002. Layered Composite Model for Design and Fabrication of Bone Replacement. *Proceedings of 13th Solid Freeform Fabrication Symposium, Austin, Texas*: 24-34.
- Stauber, M., and R. Müller. 2006. Volumetric spatial decomposition of trabecular bone into rods and plates - A new method for local bone morphometry. *Bone*, 38: 475-484.
- Sutherland, I. 1963. Sketchpad, a man-machine graphical communication system. *PhD thesis, MIT, Dept. of Electrical Engineering*.
- Taboas, J. M., R. D. Maddox, P. H. Krebsbach, and S. J. Hollister. 2003. Indirect Solid Freeform Fabrication of local and global porous, Biomimetic and composite 3-D polymer-ceramic scaffolds. *Biomaterials*, 24 (1): 181-194.
- Tan, K. H., C. K. Chua, K. F. Leong, M. W. Naing, and C. M. Cheah. 2005. Fabrication and characterization of three-dimensional poly(ether-ether-ketone)/-hydroxyapatite biocomposite scaffolds using laser sintering. *Proceedings - Institution of Mechanical Engineers Part H Journal of Engineering in Medicine*, 219: 183-194.
- Tellis, B. C., J. A. Szivek, C. L. Bliss, D. S. Margolis, R. K. Vaidyanathan, and P. Calvert. 2008. Trabecular scaffolds created using micro CT guided fused deposition modeling. *Materials Science and Engineering*, 28 (1): 171-178
- Tiller, W. 1983. Rational B-splines for curve and surface representation. *IEEE Computer Graphics and Applications*, 3 (6).

- Tomlins, P., P. Grant, S. Mikhalovsky, L. Mikhalovska, S. James, and P. Vadgama. 2006. Characterisation of polymeric tissue scaffolds. *NPL Measurement Good Practice Guide*, 89.
- Truscott, M., D. de Beer, G. Vicatos, K. Hosking, L. Barnard, G. Booyesen and I. R. Campbell. 2007. Using RP to promote collaborative design of customised medical implants. *Rapid Prototyping Journal*, 13 (2): 107-114
- Tsang, V. L., and S. N. Bhatia. 2004. Three-dimensional tissue fabrication. *Advanced Drug Delivery Reviews*, 56: 1635-1647
- Uchiyama, T., T. Tanizawa, H. Muramatsu, N. Endo, H. E. Takahashi, and T. Hara. 1999. Three-dimensional micro-structural analysis of human trabecular bone in relation to its mechanical properties. *Bone*, 25 (4): 487.
- Ulrich, D., B. Rietbergen, A. Laib, and P. R  egsegger. 1998. Mechanical analysis of bone and its micro-architecture based on in vivo voxel images. *Technology and Health Care*, 6 (5-6): 421.
- Vacanti, J. P., and R. Langer. 1999. Tissue Engineering: the design and fabrication of living replacement devices for surgical reconstruction and transplantation. *The Lancet*, 354: 32-34.
- Van Cleynenbreugel, T., J. Schrooten, H. Van Oosterwyck, and J. V. Sloten. 2006. Micro-CT-based screening of biomechanical and structural properties of bone tissue engineering scaffolds. *Med. Biol. Eng Comput.*, 44 (7): 517-25
- Van Emmerik, M. J. G. M., and F. W. Jansen. 1989. User interface for feature modelling. *Computer Applications in Production and Engineering*, edited by Kimura, F., and A. Rolstadas. Elsevier, IFIP.
- Van Rietbergen, B., S. Majumdar, W. Pistoia, D. C. Newitt, M. Kothari, A. Laib, and P. R  egsegger. 1998. Assessment of cancellous bone mechanical properties from micro-

- FE models based on micro-CT, pQCT and MR images. *Technology and Health Care*, 6 (5): 413-416.
- Venuvinod, P. K., and W. Ma. 2004. Rapid prototyping: laser-based and other technologies. *Springer*. ISBN 1402075774.
- Versprille, K. 1975. Computer-aided design applications of the rational B-spline approximation form. *Ph.D thesis, Syracuse University*.
- Viceconti, M., C. Zannoni, D. Testi, and A. Cappello. 1999. CT data sets surface extraction for biomechanical modeling of long bones. *Computer methods and programs in biomedicine*, 59 (3): 159-66.
- Wakamatsu, E., and H. A. Sissons. 1969. The cancellous bone of the iliac crest. *Calcif. Tissue Res.*, 4: 147-161.
- Wang, N., and T. M. Ozsoy. 1991. A scheme to represent features, dimensions and tolerances in geometric modelling. *Journal of Manufacturing Systems*, 10 (3): 233-40.
- Williams, J. M., A. Adewunmi, R. M. Schek, C. L. Flanagan, P. H. Krebsbach, S. E. Feinberg, S. J. Hollister, and S. Das. 2005. Bone tissue engineering using polycaprolactone scaffolds fabricated via selective laser sintering. *Biomaterials*, 26 (23): 4817-4827.
- Willows, A., Q. Fan, F. Ismail, C. M. Vaz, P. E. Tomlins, L. Mikhalovska, S. Mikhalovsky, S. James, and P. Vadgama. 2006. Electrochemical assessment of tissue scaffold degradation. *NPL Report DEPC-MPR*, 049.
- Woesz, A., M. Rumpler, J. Stampfl, F. Varga, N. Fratzl-Zelman, P. Roschger, K. Klaushofer, and P. Fratzl. 2005. Towards bone replacement materials from calcium phosphates via rapid prototyping and ceramic gel-casting. *Materials Science and Engineering*, 25: 181-186.

- 
- Woo, S. L., and R. E. Levine. 1998. Ligament, tendon and fascia. In: Black, J., and G. Hastings, eds. *Handbook of Biomaterials Properties*. *Chapman & Hall*. ISBN 0412603306: 59-65
- Xiang, L., D. Li, B. Lu, Y. Tang, L. Wang, and Z. Wang. 2005. Design and fabrication of CAP scaffolds by indirect solid free form fabrication. *Rapid Prototyping Journal*, 11 (5): 312-18.
- Yan, X., and P. Gu. 1996. A review of rapid prototyping technologies and systems. *Computer Aided Design*, 28 (4): 307-18.
- Yang, S., K. F. Leong, Z. Du, and C. K. Chua. 2001. The design of scaffolds for use in tissue engineering. Part I: traditional factors. *Tissue Engineering*, 7 (6): 679-689.
- Zhongzhong, C., Z. Remu, and L. Dichen. 2004. Fabrication of artificial bioactive bone using rapid prototyping. *Rapid Prototyping Journal*, 10 (5): 327-333.
- Zwillinger, D. 2002. *CRC Standard Mathematical Tables and Formulae*, 31st Edition. *Chapman & Hall*. ISBN 1584882913.